DISS. ETH NO. _18081_

Structural, petrological and geochemical constraints on transfer and evolution of arc magmas in the mafic-ultramafic Sapat Complex (Kohistan; Northern Pakistan)

A dissertation submitted to

ETH ZURICH

for the degree of
Doctor of Sciences

presented by

Pierre Bouilhol

Master in Earth Science (DEA), University of Montpellier (France)

Date of birth
10 November 1979

Citizen of France

accepted on the recommendation of

Jean-Pierre Burg (ETH)
Max W. Schmidt (ETH)
Peter B. Kelemen (Columbia University, USA)

2008

A mon Grand Père, Robert Salsé

"Society speaks and all men listen,
mountains speak and wise men listen"
John Muir

Table of Contents

Abstract

Kohistan refers to a Himalayan region in NW Pakistan. This geographical region, as big as Switzerland, is known among geologist to host one of the best exposures of Paleo-Island arcs. The Kohistan paleo-island arc formed in the Tethys Ocean above a north-dipping subduction during Mesozoic times. The paleo-arc is now delimited by two suture zones, the Indus Suture zone to the south and the Karakoram Suture to the north. The best known section of the Kohistan Paleo-island Arc is along the Karakoram Highway, which displays the arc from its roots, above the Indus Suture, to its sediments, in the footwall of the Karakoram-Kohistan Suture. The Sapat Complex lies directly above the Indus Suture in tributaries of the Kaghan Valley. It is one of these areas that have been little documented because working conditions (remote, high and steep valley) are not favourable. Literature mentioned the existence of ultramafic and mafic rocks but the area is best known for the occurrence of gem olivine.

This research work aimed elucidating the geodynamical setting of the Sapat Complex and characterizing the magmatic processes recorded in these rocks. For this purpose, field work, structural and petro-geochemical analyses and geochronological determination have been carried out. Results shed light on the forearc affiliation of the Sapat Complex and bring new insights on how arc-magmas are transferred and evolve in the mantle via porosity waves and in the crust via magmatic pipes.

Previously believed to represent a magmatic chamber of the arc, the Sapat Complex actually includes an upper mantle section and its overlying crust. The ultramafic mantle rocks are made of depleted meta-harzburgite showing in some places dunites and pyroxenites-gabbros that formed at the expense of the meta-harzburgites via melt-rock reactions. The formation of the dunite-pyroxenite is best explained by the percolation via porosity waves of primitive arc melt into the meta-harzburgites. The chemical characteristics of the melts and surroundings peridotites suggest that the dunite-pyroxenites formed in a forearc region. The presence of gem olivine and associated calcite + cr-clinochlore within the dunites testifies for the percolation of carbonated fluids. The chemical characteristics of these vein minerals show that they are not issued from late Himalayan metamorphism but are of subduction origin. Their peculiar chemistry (low Nb/Ta, low $\delta^{11}B$) shows that carbonated fluids would influence the behavior of high field strength element and B in the mantle wedge. The crustal part of the Sapat Comlex comprises series of meta-plutonic rocks enclosing pyroxenite bodies. These series represent a cumulative sequence issued from the same parental melt as those forming the dunite-pyroxenite association within the mantle. The isotopic characteristics of the series validate the cogenitic nature of all lithologies and strengthen the interpretation of forearc origin. They also show that the widespread fluid-assisted metasomatism affecting the rocks occurred during subduction. The pyroxenite bodies enclosed in the metaplutonic series represent magmatic pipes in which primitive melts have been transferred toward higher crustal levels and in which differentiation took place. These conduits are analogue to deep magmatic chambers used as melt highways within the crust. The Sapat Complex formed on a forearc region between 105 and 99 Ma, possibly favored by trenchward migration of the melting source region.

Résumé

Le Kohistan est une région Himalayenne au NW du Pakistan. Cette région, aussi grande que la Suisse, est connue parmi les géologues pour être l'un des paléo-arcs volcaniques les mieux exposés. Ce paléo-arc s'est formé dans la Téthys, au-dessus d'une subduction a vergence nord pendant le crétacé. Il est maintenant encadré par deux sutures, la suture de l'Indus au sud et la suture Karakorum-Kohistan au nord. La section la plus connue de l'arc du Kohistan est celle de la route du Karakorum; elle permet d'étudier l'arc depuis ses racines, au-dessus de la suture de l'Indus, jusqu'à ses sédiments, sous de la suture nord. Le complexe de Sapat se trouve au-dessus de la suture de l'Indus, dans des affluents de la vallée de Kaghan. Il s'agit de l'un des secteurs qui, en raison des conditions de travail (difficulté d'accès, altitude) ont été peu documentés. La littérature y avait mentionné l'existence de roches ultramafiques et mafiques, mais Sapat est particulièrement connu pour son olivine gemme.

Ce travail de thèse avait pour but d'élucider le cadre géodynamique du complexe de Sapat et de caractériser les processus magmatiques qui ont formé ces roches. Les travaux de terrain classiques ont donc été complétés par des analyses structurales, petro-géochimiques et géochronologiques. Les resultats permettent de déterminer l'affiliation d'avant-arc de Sapat et de documenter les processus de transfert des magmas d'arc dans le manteau par l'intermédiaire de vagues de porosité, et dans la croûte par l'intermédiaire de chenaux magmatiques.

Anciennement considéré comme une chambre magmatique dans l'arc, le complexe de Sapat représente en fait une section mantellique surmontée par sa croûte. Les roches ultramafiques du manteau sont principalement des méta-harzburgites appauvries au sein desquelles la percolation de magmas primitifs a généré des dunites et des pyroxénites-gabbros. Les caractéristiques géochimiques des magmas et des péridotites encaissantes montrent que les dunites-pyroxénites ce sont formées dans une région de forearc. La présence de veines à olivine gemme et de calcite + cr-clinochlore dans les dunites témoigne de la percolation de fluide carbonatés. Les caractéristiques chimiques de ces mineraux prouvent qu'ils ne ce sont pas formés à la faveur d'un événement métamorphique himalayen mais sont liés à la subduction. Leur chimie particulière (faible Nb/Ta et $\delta 11B$) indique que les fluides carbonatés influencent le comportement d'éléments lithophiles à fort potentiel ionique et du B dans le manteau.

La partie crustale du complexe de Sapat est une série de roches méta-plutoniques renfermant des corps pyroxénitique. Ces séries représentent une séquence cumulative issue d'un même magma parent et cogénétique avec les produits de fusion qui ont formé l'association dunites-pyroxénites du manteau. Les caractéristiques isotopiques des roches valident le caractère cogénétique de toutes les lithologies décrites et renforcent l'hypothèse d'une origine d'avant-arc. Elles prouvent également que la métasomatose affectant les séries plutoniques a eu lieu pendant la subduction. Les corps de pyroxénite dans les séries métaplutoniques représentent des conduits magmatiques dans lesquels des magmas primitifs ont été transféré vers les niveaux crustaux supérieurs, et dans lesquels une différentiation s'est produite. Ces conduits sont équivalents à des chambres magmatiques profondes jouant le rôle « d'autoroute magmatique ». Le complexe de Sapat s'est formé sur une région d'avant-arc entre 105 et 99 Ma à la faveur du deplacement vers la fosse des souces magmatiques.

I.   Introduction

Subduction zones are one of the major processes portraying the "Earth's face". Together with Mid Ocean Ridges, subduction zones are not only engines of plate tectonics, but also the major "factory" for magma production. The tremendous hazard of volcanic activity in island arcs has fascinated and attracted a large part of the humanity by providing goods in fertilizing grounds and taking them back during eruptions. To earth scientists, volcanoes have been of primary interest to understand magma compositions and genesis. The peculiarity of subduction volcanism (explosivity, calc-alkaline affinities) has highlighted the specificity of island arc processes. The genesis of magmas at convergent margins has been a matter of active debate, and if earth scientists have believed that the entire slab was melting below arc-volcanoes, the fundamental role of flux melting is now widely accepted as a fundamental process originating magmas in subduction zones.

Subduction - i.e. descent and recycling of lithosphere in the Earth mantle - is associated with volcanic activity. The subduction-related "volcanic island arcs" differ markedly from other mantle volcanites by their chemical composition, which is reminiscent of the continental crust composition. For this reason, several authors have suggested that repeated accretion of island arcs is the main mechanism of post-Archaean continental crustal growth (Taylor and McLennan, 1985; Kelemen, 1995; Rudnick and Fountain, 1995; Taylor and McLennan, 1996; Condie, 1997; Rudnick and Gao, 2003). This "andesite model", has been generally accepted as it builds up recognizable links between continental genesis and plate tectonics. However, the model faces the so-called "arc paradox": the continental crust has an andesitic major element composition similar to that of granodioritic plutonic rocks, but estimates of the composition of exposed island arcs and magmatic fluxes to the upper arc crust are basaltic and similar to plutonic gabbroic rocks (Pearcy et al., 1990; Kelemen et al., 2003). Whether and how oceanic arcs underwent changes during or after accretion to continents and attain the andesite bulk composition of the continental crust is barely understood. Some authors have been as far as stating that the continental crust actually is basaltic with a major cumulate counterpart below the seismic Moho (Kay and Kay, 1985). Other authors conceive that the andesitic crust formed through crustal differentiation of basaltic magma, with the mafic dense residue having delaminated and absorbed into the mantle (Jull and Kelemen, 2001; Kelemen et al., 2003). These discussions involve geochemical, petrological and tectonic processes together.

Obviously, a better understanding of island arc formation and accretion is a necessary step to improve our perception of the origin of continents. In fact, the assessment of delamination and differentiation processes is profoundly hindered by the lack of exposed deep levels of active island arcs. The delamination theory is nowadays favored to explain the lack of primitive cumulate rocks in the Talkeetna paleo-island arc, in Alaska (Jull and Kelemen, 2001; Kelemen et al., 2003). The Kohistan paleo-island arc is advantageously much better exposed than Talkeetna therefore offers important, complementary information. As such, new field and petro-structural information on the Sapat mafic-ultramafic rocks, in Kohistan, should be a valuable appendage to the data set concerning tectonic and petrogenetic processes in deep levels of island arcs and possibly the formation of the continental crust.

I.1.   Kohistan – An overview

The Kohistan Complex (North Pakistan, Fig. I.1) is one of the best exposed paleo-island arcs identified on the Earth. These few occurrences provide invaluable opportunities to observe exhumed, deep-seated arc rocks, which are otherwise imaged by geophysical signals only. The Kohistan intra-oceanic island arc formed during northward subduction of the Tethys Ocean in Mesozoic times (Tahirkheli, 1979; Bard, 1983; Coward et al., 1987). It is now tectonically pinched between the Karakoram (part of Asia) and Indian continents. It was obducted southward over the Indian plates, probably in Paleocene-Eocene times (Tahirkheli et al., 1979; Coward et al., 1987; Leech et al., 2005). The Indus Suture Zone (Fig. I.1, 2) is the boundary between India and Kohistan (Gansser, 1980). In Pakistan, it has often be referred to as the MMT, for Main Mantle Thrust, by reference to the ultramafic rocks particularly well exposed in the Jijal Complex (Tahirkheli, 1979; Tahirkheli et al., 1979; Jan and Howie, 1981; Coward and Butler, 1985; Coward et al., 1987; Treloar et al., 1996; Searle et al., 1999). Kohistan shows two main units on each side of the Chilas Complex (Fig. I.1, 2) regarded as a plutonic complex made of co-magmatic gabbronorite and ultrabasic intrusions.

 On the South of the Chilas complex, the ultramafic and mafic rocks of Jijal are overlain by the so called Southern Amphibolites (Treloar et al., 1990; Treloar et al., 1996). This unit comprises three domains (Zeilinger, 2002; Burg et al., 2005) which from south to north are: (i) The Patan complex, made of gabbros, garnet gabbros, diorites and meta-equivalent, representing the deep roots of the arc (Burg et al., 1998; Garrido et al., 2006; Dhuime et al., 2007). (ii) The Kiru amphibolites made of metagabbros, hornblendites and interlayered metadiorites and metalavas. (iii) The Kamila Amphibolites, separated from the Kiru by granitic sheets (97.1 ± 0.2 Ma; Schaltegger et al., 2002), are principally made of metaplutonic rocks with screens of metasediments and metavolvanics. The Kamila sequences are believed to represent the old oceanic crust on which the arc built (Khan et al., 1997). Ages through the whole Southern amphibolites are variable, from 110 Ma to 75 Ma and do not define any of the above domains, but reflect superimposed intrusions of different composition, at different depths.

The Northern part of Kohistan, the Kohistan Batholith, is principally made of granitoids (Petterson and Windley, 1985; Petterson and Windley, 1991; Crawford and Searle, 1992; Petterson et al., 1993; Khan et al., 1998; Searle et al., 1999). These granitoids represent the middle to upper crustal level of the Paleo-arc and have recorded 120 Ma of magmatic history (Schaltegger et al., 2003; Heuberger et al., 2007). Within the granitoids, meta-sediments and meta-volcanic rocks are of arc-to back-arc basins origin. On the far North of Kohistan the Yasin series represents unmetamorphosed back-arc sediments and lavas (Khan et al., 1996).
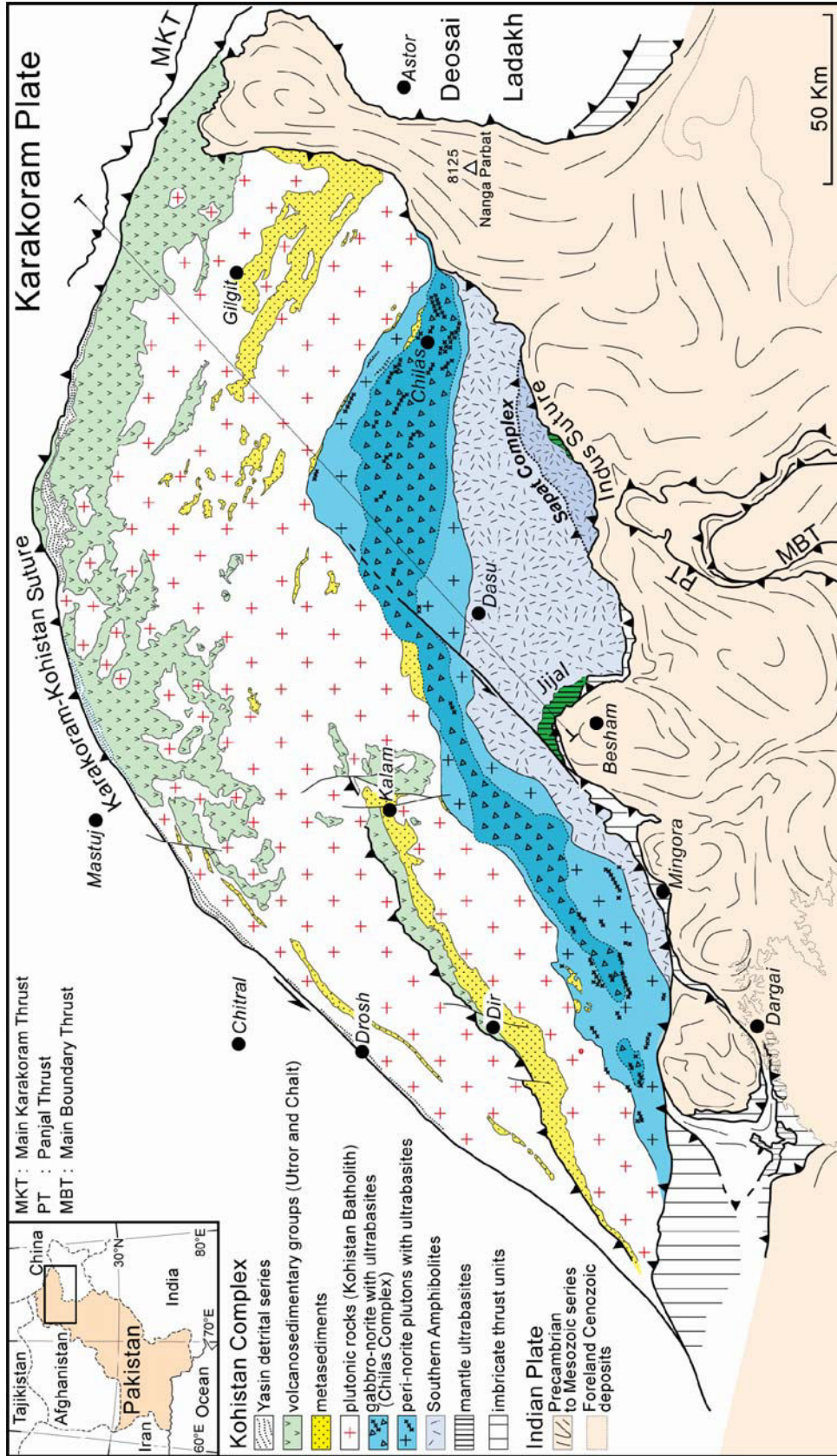
Figure I.1 : Geological map of the Kohistan Paleo-Island Arc. Built on Landsat 7ETM+
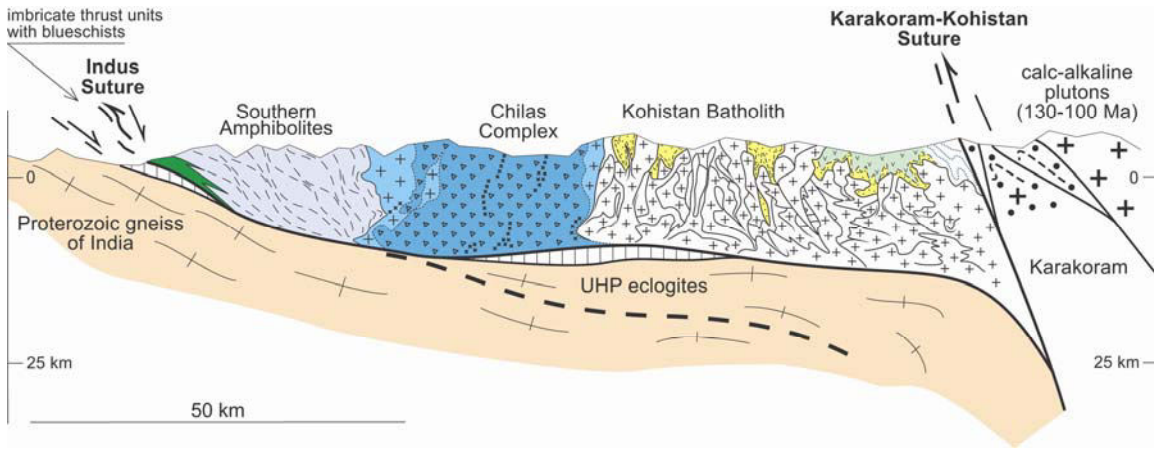
Figure I.2: Cross section through the Kohistan arc (Burg et al., 2006). Trace and legend on Fig. I.1.

I.2.   Geological setting of ultramafic complexes in Kohistan; introduction to the Sapat Complex

Two main ultramafic-mafic complexes within the Kohistan Paleo-Island arc have revealed to be very important in terms of deep magmatic processes within the arc: The Jijal Complex and the Chilas Complex. Their comparison emphasizes the key role of ultramafic rocks in island arcs, thus in understanding the structural and magmatic evolution of island arcs.

Jijal
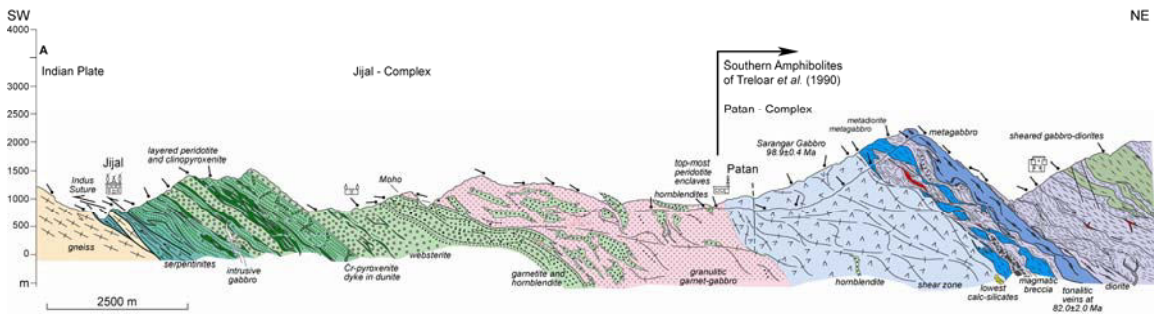
Figure I.3: Section through the Jijal complex and part of the overlying Patan complex (Burg et al., 2005). Ages: Yamamoto et al. (2005) and Schaltegger et al. (2002)

The more than 3 km thick ultramafic part of the Jijal complex (Fig. I.3) is composed of upper mantle peridotites, pyroxenites, garnetites and hornblendites (Jan and Howie, 1981; Jan and Windley, 1990). It is comprised of dunites and wehrlites interlayered with pyroxenites, and minor harzburgites, with an upward increasing proportion of pyroxenites, hornblendites and garnetites (Jan and Windley, 1990; Miller et al., 1991). The occurrence of elongated flames, streaks and wisps of dunite in websterites and garnet-hornblende pyroxenites towards the top of the exposed mantle section attest to

olivine- and melt-consuming reactions (Burg et al., 1998; Garrido et al., 2007). The mantle peridotites were modified and fertilized by percolating hydrous melts and fluids, hence crystallizing secondary pyroxene, hornblende and garnet. Burg et al. (1998) regarded these processes as having formed the fossile sub-arc mantle to crust transition under near-solidus conditions of the peridotite, atop the asthenospheric mantle where melts were channelized and eventually concentrated. Based on bulk rock chemistry and clinopyroxene analyses, the ultramafics have been recently interpreted as the Kohistan fore-arc crust-mantle transition zone (Dhuime et al., 2007; Garrido et al., 2007). Also, based on Sm/Nd ages of ultramafic separates, the ultramafic processes pinpointed by Dhuime et al. (2007) are dated at 117 ± 7 Ma. The garnet-hornblende pyroxenites border granulitic gabbros along a sharply defined boundary interpreted as the intrusive contact of crustal calc-alkaline gabbros into the reacted, hornblende-rich upper mantle. Recent studies (Garrido et al., 2006; Dhuime et al., 2007) point to crustal differentiation whereby the garnet granulites represent restites produced by dehydration melting of a hornblende-gabbronorite protolith and accompanied by variable extraction of hydrous granitic melts. At the opposite, some authors suggest that these rocks are igneous (Burg et al., 1998; Ringuette et al., 1999) and were formed by high pressure crystal fractionation of an hydrous andesitic melt (Muntener and Ulmer, 2006; Dessimoz et al., 2008; Muntener et al., 2008). Cooling of the garnet-bearing rocks below 700°C has been dated at 91.0 ± 6.3 Ma (Yamamoto and Nakamura, 1996).

Chilas
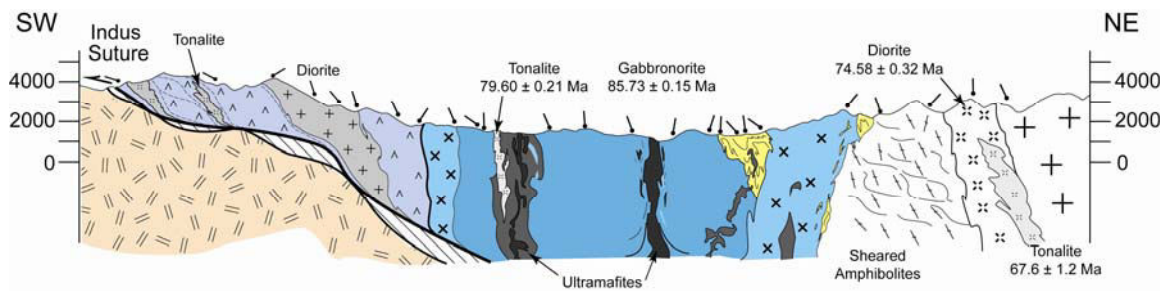
Figure I.4: Cross section through the Chilas complex from Jagoutz et al. (2007). Legend as Fig. I.1 and I.2. Ages from Jagoutz (2004) and Schaltegger et al. (2002).

The Chilas ultramafic and mafic rocks (Fig. I.4) represent apices of intra-arc mantle diapirs that served as porous flow conduits to feed the so-called Chilas gabbronorite, about 85 Ma ago (Burg et al., 1998; Schaltegger et al., 2002; Jagoutz et al., 2006; Jagoutz et al., 2007). The estimated bulk composition of the gabbronorite matches estimates of continental lower crust composition. Therefore, the km-scale melt conduits are interpreted as being an alternative to explain the X_{Mg} gap between bulk continental crust estimates and basaltic magmas (Jagoutz et al., 2006). In-situ mineral analyses on mineral of both ultramafics and co-genetic gabbronorites have constrained the petro-geochemical processes involved into this processes (Jagoutz et al., 2007). Structural relationships confirmed extension that geochemical arguments on the Chilas rocks had hinted (Burg et al., 2006; Jagoutz et al., 2006; Jagoutz et al., 2007). This clarification has had important consequences on the understanding of both the regional geodynamics and the arc

evolution. The Chilas suite of mantle diapirs records the splitting of the Kohistan arc, with rifting taking place within the island arc.

Sapat

The Sapat Complex (Fig. I.1, 5), about 70 km to the east of Jijal, lies directly above the Indus Suture and therefore shares the same structural level within Kohistan as Jijal. Drag folds and shear bands are particularly abundant in graphitic schists of the suture zone, indicating greenschist facies to very-low grade normal faulting, as reported in the Bhimbal Valley, approximately 15 km to the southwest of Sapat (Burg et al., 1996) and along several segments of the Indus Suture (Vince and Treloar, 1996; Anczkiewicz et al., 1998).
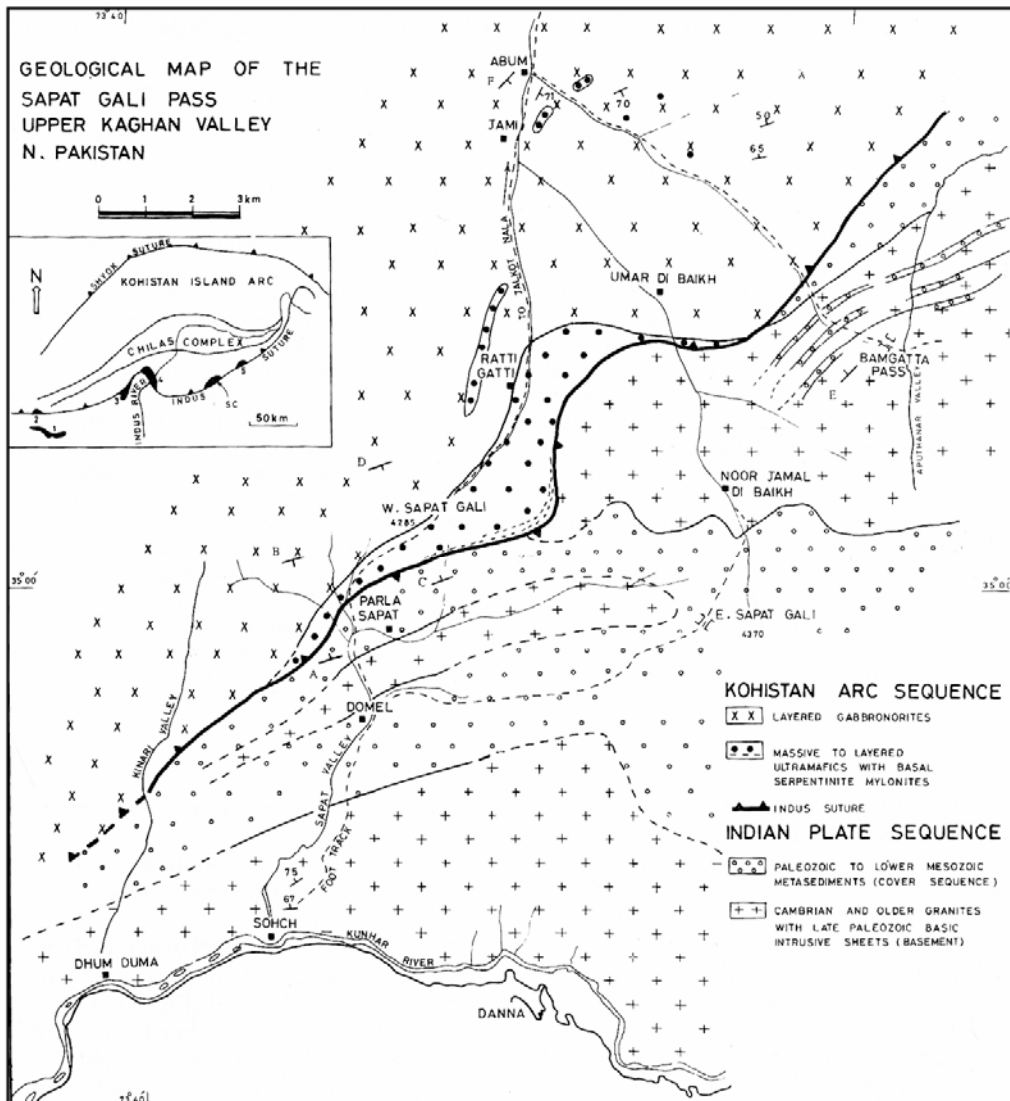
Figure I.5: Geological map of the Sapat Complex from Jan et al. (1993)

The Sapat Complex has attracted worldwide attention for the occurrence of exceptional gem olivine (Kane, 2004) interpreted as representing a late Himalayan metamorphic product (Jan et al., 1993). They occur in the Sapat ultramafic rocks, which were first interpreted as a "layered-type" complex (Fig. I.6) where the ultramafic rocks represent cumulates in a magmatic chamber of the arc (Jan et al., 1993; Arif and Jan, 2006) but were later attributed to ophiolitic sequences (Khan et al., 2004).
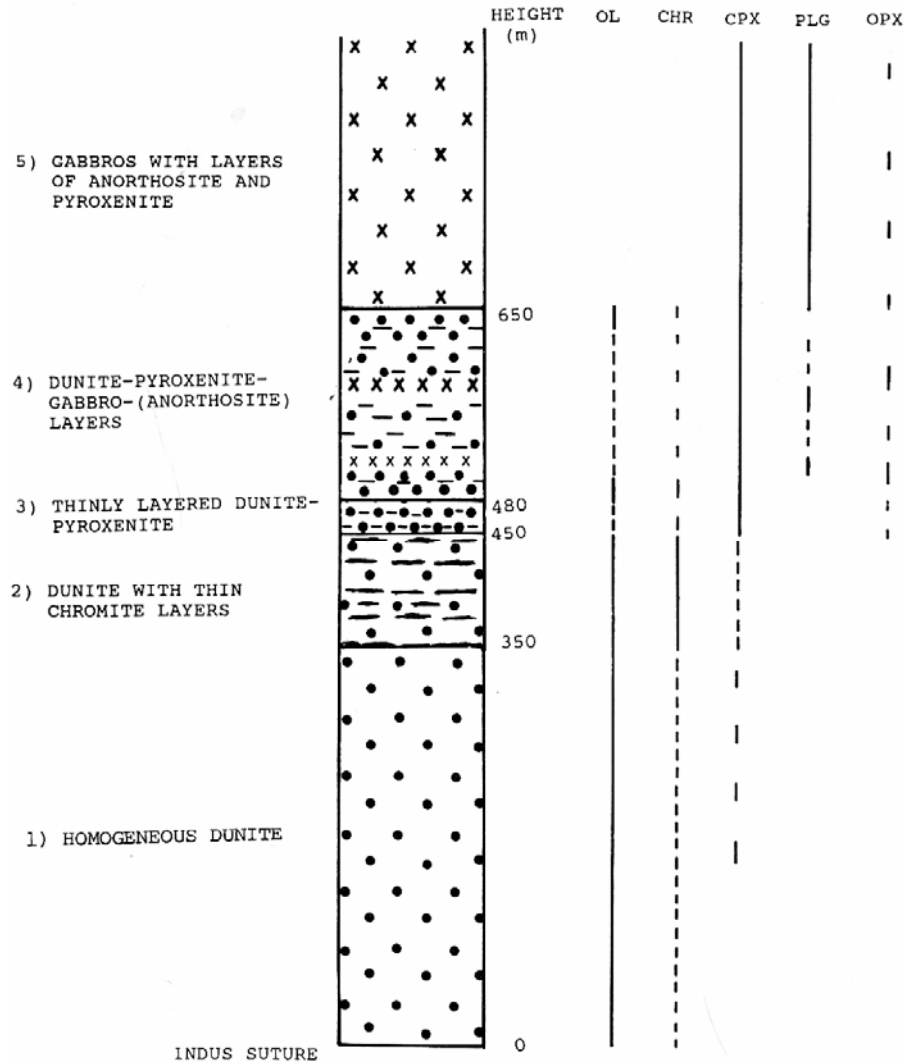
Figure I.6: Schematic log of Jan et al. (1993) through the Sapat Complex. Note the reference to "layers" thorough the description, relating a magmatic chamber origin

The mafic part of Sapat has been scantily described and referred to be mainly composed of folded (Fig. I.7) amphibolite-facies metagabbros (Khan et al., 1998). Ultramafic bodies within these mafic rocks were mentioned and thought to represent pyroxene-rich cumulate horizons within the magmatic chamber (Jan et al., 1993; Khan et al., 1998).
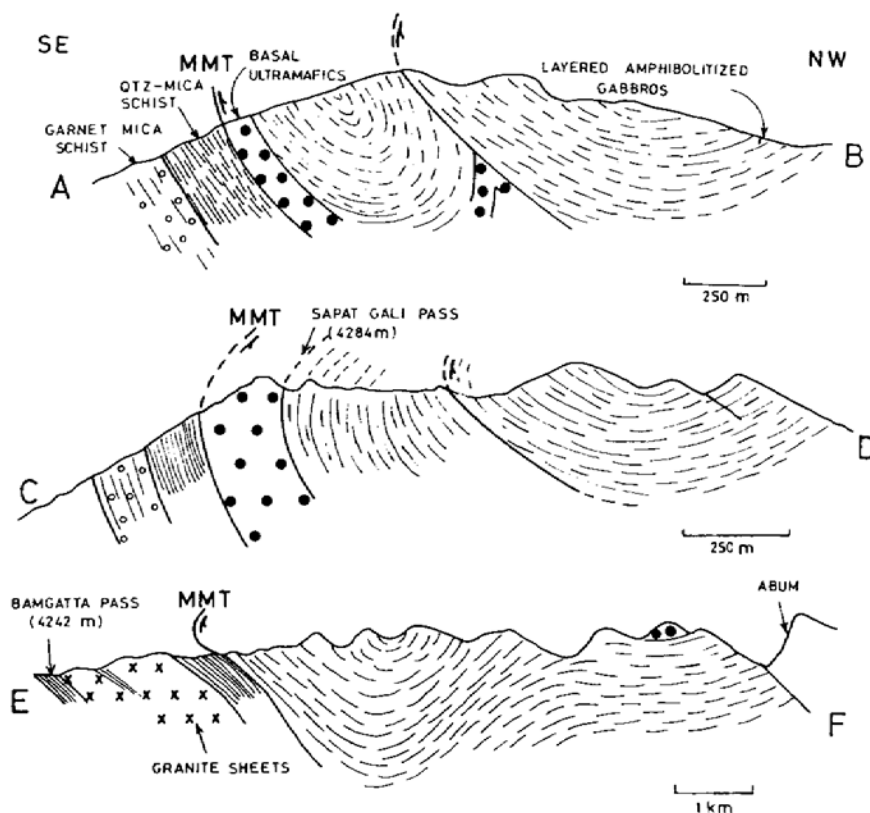
Figure I.7: Cross section through the Sapat Complex from Jan et al. (1993)

The Sapat Complex is one of these Himalayan areas that, due to their difficult working conditions (remote, strong relief at high altitude), has been little documented; it was therefore prone to offer unvisited outcrops and new clues to the evolution of the Kohistan island arc. Possibly documenting unrecognized mantle and lower crustal processes within the arc was the incentive to study this Complex.

I.3.   Goals, methods and outlines

The aims of this PhD work were several folds:

1) Elucidate the geodynamical setting to which the Sapat ultramafic rocks belong and to characterize the processes that are recorded in these rocks.

2) Clarify the origin and significance of gem olivine.

3) Characterize the Sapat mafic rocks, specify their origin and understand their significance with respect to the Jijal and Chilas ultramafic and mafic associations.

4) Capture the processes involved in the formation of the Sapat Complex and put forward the fundamental mechanisms that led to the characteristics of this complex.

5) Pinpoint to which evolutionary stage and geodynamical context Sapat belongs within the Kohistan paleo-island arc.

For these purpose we established a map of the Sapat Complex through field campaigns (<5 months over 2 years) complemented with satellite picture analysis (Landsat 7ETM+ and SPOT). Systematic sampling of the different units has yield more than a ton of rocks. Classical petrology (parageneses determination) combined with microprobe analyses have been the back bone of further geochemical analyses. Solution ICP-MS on bulk-rocks (conducted in Montpellier University with Jean-Louis Bodinier) have been done on all the different lithologies found in Sapat. Moreover, LA-ICP-MS measurements have been carried out on structurally controlled minerals, allowing detailed chemical determination. Isotopic data (Sr-Nd-Pb) on bulk rocks (conduct in Geneva with Massimo Chiaradia) have been carried out on the principal lithologies to attest for the source and co-geniticity of the lithologies. Likewise, isotopic data (C-O-B) have been measured on gem olivine and associated minerals (conducted at the ETH with Stephano Bernasconi and Lausanne with Benita Pullitz and Torsten Venneman) to understand their significance. Numerical modeling has been performed with James Connolly (ETH) in order to elucidate the mode of transport of magma within the mantle lithosphere, and constrains the observations made on the Sapat mantle. To better constrain the source of these rocks and their significance in the Kohistan Complex, zircons have been dated and their Hf isotopic compositions measured (in ETH and in Geneva, by Urs Schaltegger). Appendix 1 provides all the detailed analytical procedures.

The first section of this thesis is composed of three chapters dedicated to the ultramafic rocks of the Sapat Complex. Chapter II.1 presents the geological setting and compositions of the different ultramafic lithologies, and has been published in Lithos (Bouilhol et al., 2008). Our investigation shows that the Sapat ultramafic rocks mostly consist of meta-harzburgites representing ultra-depleted mantle that further reacted with primitive melts and volatile-rich fluids, leading to intra-mantle fractionation processes. We consider that the evolution of the Sapat ultramafic rocks reflects subcrustal processes in front of the island arc and represents the expansion of arc magmatism onto a forearc region. The percolation of carbonated fluid of subduction origin yielding vein olivine strengthens that interpretation. Chapter II.2 further investigates the origin of the gem olivine (+ calcite + cr-clinochlore). The trace element and isotopic compositions of the minerals show that the crystallization of the vein olivine parental fluids points to a "slab signature" and that carbonated fluids are a possible agent responsible for Nb/Ta variations and $\delta^{11}B$ and signature in the forearc region. Chapter II.3 describes a combined porous and channelized flow in the crust-mantle transition zone. In order to show that porosity waves are a viable mechanism for the transfer of arc-magmas through the lithosphere, we implemented the porosity wave model of Connoly and Podladchikov (2007) with temperature and mineral solubility in order to investigate the petrological consequences of such a mode of transfer. The model shows that porosity waves satisfy the structural and petrological observations in Sapat and that such a model should apply to the general transfer of arc-magmas in the top of the wedge.

The second section, composed of three chapters, treats of the crustal part of Sapat. Chapter III.1 is a detailed structural and petro-geochemical description of the metaplutonic series. It shows that the meta-plutonic series is made of metagabbros, meta-hornblendites and tonalites that host pyroxenite bodies. All of these rocks are cumulates derived from a common parental melt through fractional crystallization. The series

extensively re-equilibrated in amphibolite to greenschist facies, fluid-assisted metamorphism. From their chemical specificities, the meta-plutonic rocks of Sapat do not pertain to any of the known units within Kohistan. The isotopic and trace element bulk rock composition strengthens the interpretation that the ultramafic, mantle lithologies (except meta-harzburgites) and the crustal rocks are cogenetic. Isotopic compositions show that the metasomatic amphibolite facies re-equilibration is not due to a late Himalayan overprint, but occurred during subduction. Together with the fact that the mantle source region is heterogeneous and shows a depleted component interpreted as representing part of a 150 Ma old Tethyan lithosphere, the isotopic data reinforce the interpretation that the Sapat Complex formed on a forearc region. Chapter III.2 is dedicated to the detailed study of two of the mafic-ultramafic bodies intruding the meta-plutonic series. Their subvertical, internal magmatic structures, the relationships between the different lithologies and the host metaplutonic, along with the compositional mineralogical evolution, show that the kilometer sized bodies were magmatic pipes. Within these pipes, melts were migrating toward higher crustal levels and undergoing differentiation from primitive to evolved compositions. These conduits are of major importance in terms of magma transfer and evolution and, considering the existence of ultramafic conduits at Chilas, the Sapat pipes strengthen the process of magma transfer and differentiation as being closely linked to magmatic conduits. Chapter III.3 presents the chronological constraints obtained for the formation of the Sapat Complex. Precise zircon ages from tonalite dykes of different structural positions show that the complex formed between 106 and 99 Ma. Coupled with the Hf isotopic composition of dated zircon fraction, and the bulk isotopic composition of dated sample, we have reconstructed the temporal evolution of the source during the establishment of the Sapat Complex. The data show that melting initiated in a more depleted mantle source region (εHf ≈ 16) than the "normal" Kohistan mantle source (εHf ≈ 14). They also show that beginning of melting tapped heterogeneity within the source as Nd shows an enriched component whereas the other isotopic systems show a more depleted component. After melting initiation, the source steadily went back to the "Kohistan εHf" baseline values i.e a more enriched source. The more depleted starting source composition is interpreted, in accordance with data presented in the first section, as melting of a mantle forearc region.

In Conclusion, this study elaborates two levels of implications:

(i) On the regional scale, the investigation of the previously poorly documented Sapat Complex revealed that it corresponds to a yet unrecognized geodynamical setting within the Kohistan Paleo-island arc i.e a magmatic complex taking place on a forearc location between 106 and 99 Ma. The whole Complex does not correspond to a layered type magmatic chamber, but is subdivided into a basal mantle overlain by its corresponding crust. The geochemical characteristics of the cumulative crustal sequence do not correspond to any of the known Kohistan parts. Like the metasomatism responsible for the amphibolite facies re-crystallization of the series, the vein olivines do not correspond to a late Himalayan feature, but formed during on-going subduction.

(ii) Upon arc processes, this study sheds light on several aspects usually shadowed in nowadays active arcs due to the depth of which these processes occur, or due to scarcity of exhumed deep arc-root. It shows that pipe-like structures are important for the transfer and the evolution of arc magmas. First in the mantle where porosity waves allow the formation of a dunitic channel, in which further melt waves pass through to aliment the

crust in primitive magmas. Second, in the crust, where magmatic conduits act as magmatic chambers in which crystallization and reaction of primitive melt are critical for the evolution of arc-magmas.

The peculiar position of the Sapat magmatism i.e closer to the trench, show that fluids are omnipresent in the mantle but also in the crust, and that carbonated fluids in subduction regions participate in the elemental budget of specific elements (B and Ta for example).

II.   The Ultramafites

II.1.   The arc to fore-arc mantle of Kohistan

II.1.1.   Introduction

Studies of the production and evolution of magmas, of their migration and of their petrological and geochemical characteristics allow an understanding of the origin and growth of continental and oceanic lithosphere. Arc-processes are the main actors of continental crust formation (Rudnick, 1995), and lead to the chemical characteristics of the continental crust (depletion of Nb, Ti, enrichment in LREE and Pb; e.g. Kelemen et al., 2003). Early differentiation, thought to take place at the base of the arc crust, is an important stage in the evolution of arc magmas. However, the magmatic processes involved remain poorly documented because of the inaccessibility of present-day arc roots and the scarcity of exhumed ones. Two places on Earth offer the opportunity to study deep arc processes, namely the Talkeetna Arc in South Alaska (e.g. Debari and Coleman, 1989; Greene et al., 2006) and the Kohistan Arc in North Pakistan (e.g. Bard, 1983; Burg et al., 1998).

Studying arc roots, especially arc mantle lithosphere, is a prerequisite to specifying the first differentiation of primary arc melt compositions, the mode of transfer of primitive melts, and to recognizing the relationships between transferred melt and the host mantle. For this purpose, it is necessary to distinguish ultramafic rocks formed as cumulates from ultramafic rocks formed by melt-rock reactions or through precipitation from a cooling and depressurizing magma as arc-melts percolated through the mantle.

In this study, we investigate the Sapat Complex at the front of the Kohistan paleo-island-arc through detailed mapping, and by characterizing its mineral and bulk rock chemistry. Our goals are (1) to elucidate the origin of these ultramafic rocks, (2) to evaluate the imprint of melts passing through the ultramafics and (3) to characterize the melts involved. Our investigation shows that the Sapat ultramafic rocks mostly consist of meta-harzburgites representing ultra-depleted mantle that further reacted with primitive melts and volatile-rich fluids, leading to intra-mantle fractionation processes. We consider that the evolution of the Sapat ultramafic rocks reflect subcrustal processes in front of the island arc.

II.1.2.   Geology of the Sapat Complex

Two main lithological units were identified in the Sapat Complex (Fig. II.1): The ultramafic rocks (dunites, meta-harzburgites and pyroxenites) at the base of the complex are segmented into the large northern Sapat and the small southern Ledi bodies. These ultramafic lenses are overlain by meta-gabbros and tonalites-trondhjemites that include pyroxenite bodies ranging from wehrlites to plagioclase-bearing olivine-websterites. The contact between the ultramafic and metaplutonic units is a fault zone. Shear sense criteria in ductile and brittle shear zones indicate top-to the-north normal movement. These shear zones sliced the steeply foliated meta-gabbros whose foliation cuts the primary magmatic fabric marked by amphibole clusters and compositional layers. Graded layers and mesoscopic diapiric structures indicate that the magmatic sequence has a normal orientation. Shear zones are increasingly rare up-section, whereas the foliation flattens to an approximately constant 40°N dip within the 300 m thickness above the crust mantle
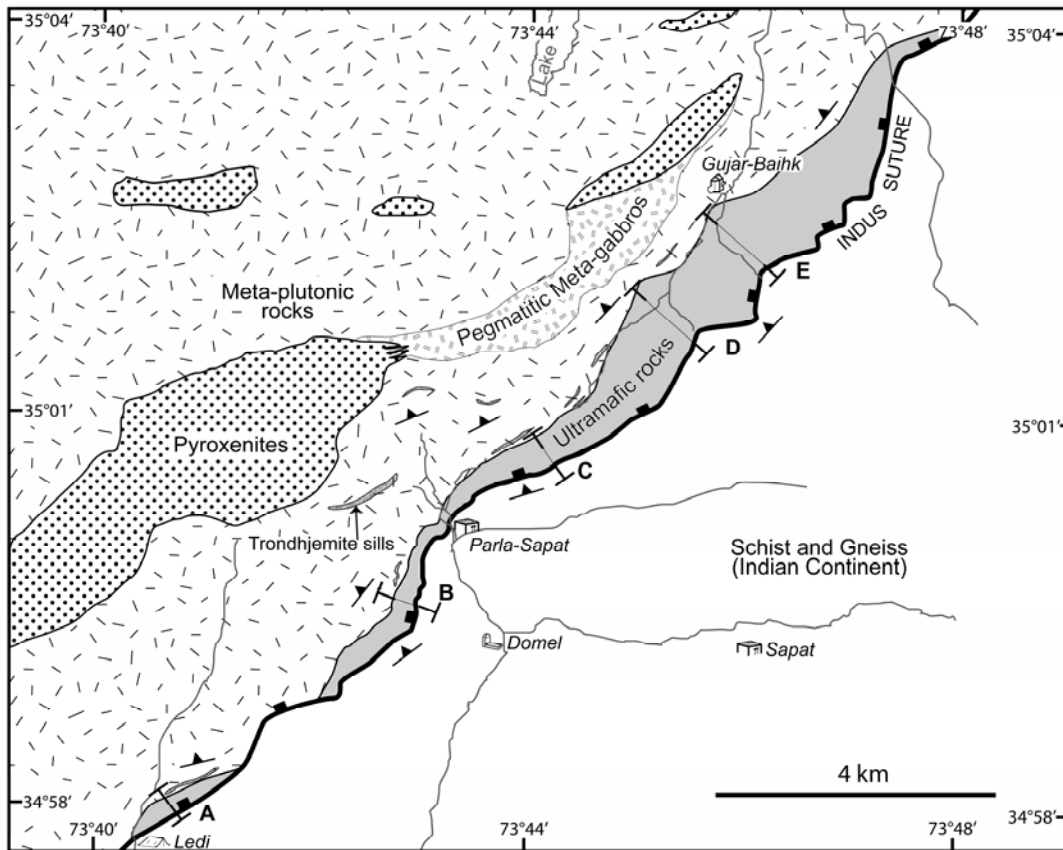
Figure II.1: Simplified geological map of the southeastern part of the Sapat Complex. A-E = location of "map-view" sections of figure II.2. The map has been elaborated from new field evidence reported on Landsat 7 ETM+ and SPOT satellite images.
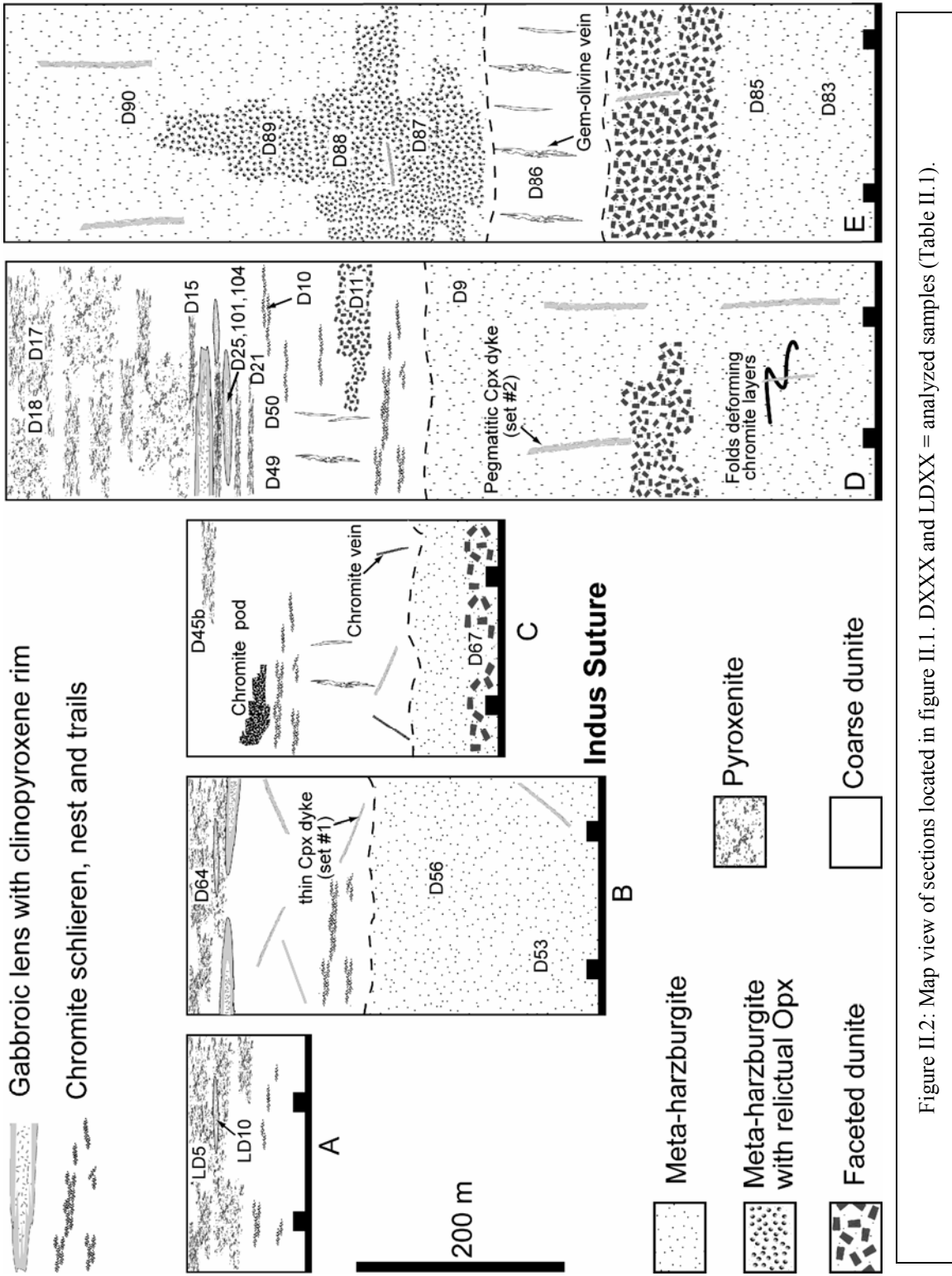
Figure II.2: Map view of sections located in figure II.1. DXXX and LDXX = analyzed samples (Table II.1).

| Samples | | Rock | | Paragenesis | | | |
Number	Location: Deg° Min' Sec"	unit	type	Primary Magmatic	Reactionnal	Subsolidus	Retrograde
D87	N 35°02'16.97" E 73°45'55.02"	Meta-harzburgite	meta-harzburgite	ol1-spl1-opx	ol2-spl2		ol-tlc-tr-chl
D11'	N 35°01'53.99" E 73°45'19.20"	Meta-harzburgite	facetted dunite	ol1-spl1(opx?)	ol2-spl2-hb		tr-srp
D90	N 35°02'20.15" E 73°45'50.22"	Meta-harzburgite	meta-harzburgite	ol1-spl1-opx	ol2-spl2		ol-tlc-srp-(tr?)
D89	N 35°02'19.55" E 73°45'51.96"	Meta-harzburgite	meta-harzburgite	ol1-spl1-opx	ol2-spl2		ol-tlc-srp
D67	N 35°00'41.27" E 73°43'57.30"	Meta-harzburgite	facetted dunite	ol1-spl1(opx?)	ol2-spl2-hb		tr-srp
D88	N 35°02'18.05" E 73°45'54.00"	Meta-harzburgite	meta-harzburgite	ol1-spl1-opx	ol2-spl2		ol-tlc-tr-srp-chl
D56	N 34°59'44.69" E 73°42'54.72"	Meta-harzburgite	meta-harzburgite	ol1-spl1-opx	ol2-spl2		ol-tlc-tr-srp
D55	N 34°59'44.69" E 73°42'54.72"	Meta-harzburgite	meta-harzburgite	ol1-spl1-opx	ol2-spl2		ol-tlc-tr-srp
D83	N 35°02'10.85" E 73°46'01.02"	Meta-harzburgite	meta-harzburgite	ol1-spl1-opx	ol2-spl2		tr-srp
D53	N 35°00'08.21" E 73°43'14.22"	Meta-harzburgite	meta-harzburgite	ol1-spl1-opx	ol2-spl2		ol-tlc-tr-srp
D85	N 35°02'16.61" E 73°46'03.12"	Meta-harzburgite	meta-harzburgite	ol1-spl1-opx	ol2-spl2		tr-srp-di
D9	N 35°01'43.25" E 73°45'23.82"	Meta-harzburgite	clinopyroxene-dunite	ol1-spl1	ol2-spl2-cpx	ol2(?)-cal	di-srp
D49	N 35°01'44.15" E 73°45'04.02"	Coarse dunite	dunite	ol-spl		ol2-cal	srp
D86	N 35°02'16.97" E 73°46'00.90"	Coarse dunite	dunite	ol-spl		ol2-cal-chl	srp
D50	N 35°01'43.01" E 73°45'04.08"	Coarse dunite	dunite	ol-spl		ol2-cal-chl	srp
D10	N 35°01'49.73" E 73°45'19.20"	Coarse dunite	chromite rich dunite	ol-spl			srp
D17	N 35°01'48.59" E 73°44'58.08"	Pyroxenite	ol-clinopyroxenite	ol-cpx-spl			tr-srp
D64	N 34°59'35.39" E 73°42'46.98"	Pyroxenite	ol-clinopyroxenite	ol-cpx-spl			tr-srp
LD5	N 34°57'57.88" E 73°40'45.30"	Pyroxenite	ol-clinopyroxenite	ol-cpx-spl			di-tr-srp-mag
D15	N 35°01'39.83" E 73°44'52.14"	Pyroxenite	clinopyroxenite_dyke	ol-cpx-spl			tr-srp
D18	N 35°01'48.59" E 73°44'58.08"	Pyroxenite	ol-clinopyroxenite	ol-cpx-spl			tr-srp-chl
D25	N 35°01'47.33" E 73°45'04.14"	Pyroxenite	meta-gabbro	cpx-hbl-pl(?)-spl			ep-tr-chl-grt
LD10	N 34°57'55.42" E 73°40'46.20"	Pyroxenite	meta-gabbro	cpx-ep-spl			chl-grt
D104	N 35°01'47.33" E 73°45'02.46"	Pyroxenite	meta-gabbro	cpx-hbl(?)-pl(?)			ep-tr-chl

Table II.1: Samples analyzed in this study. Minerals in brackets are minors. Mineral abbreviations from (Kretz, 1983)

transition. Field observation allows distinction of three main ultramafic lithologies (Fig. II.2): (1) meta-harzburgites s.l. (2) dunites and (3) pyroxenites. Since this work focuses on these ultramafic rocks, it will not describe in detail the metaplutonic units.

II.1.2.1. Meta-harzburgites

At the mesoscale meta-harzburgites display a fine-grained (sub-millimetric) texture with small, disseminated spinel grains. Locally, pinkish aggregates represent pseudomorphes of orthopyroxene (Fig. II.3a). Meta-harzburgites usually do not show any foliation, except in one place where open folds of spinel layers were observed. South of Gujar-Baihk (Figs. II.1 and II.2E) a 100m^2 patch of homogeneous, coarse-grained meta-harzburgite with relict orthopyroxene (Fig. II.3a) locally exhibits a sub-horizontal banding (Fig. II.3b).

II.1.2.2. Dunites

These principally differ from the meta-harzburgites by their coarser (millimeter-size) grains and their freshness. The dunites display higher modal abundance of spinel than the meta-harzburgites. Coarse spinel may be disseminated and unevenly distributed (Fig. II.3c), and locally forms nests, schlierens and trails of aligned crystals. Two ~ 5×5 m size chromite pods were found to the north of Parla-Sapat (Figs. II.1 and II.3d). These pods have a sharp angular contact with the fresh, coarse host dunite (Fig. II.3d) and contain millimeter to centimeter size spinels associated with kammererite (Cr-chlorite), calcite and serpentine. In addition to these pods, a few chromite dykes occur, containing strongly zoned spinel grains within a matrix of chlorite, calcite, sulfides of Ni, Fe, Cu and Ru, and native metals (Pt). Gem-quality olivine associated with magnetite, chlorite, calcite and serpentines crystallized in subvertical tension gashes and veins striking N160 within the coarse dunites.

These dunites clearly differs from "faceted" dunites, defined by randomly oriented, millimeter-sized olivine grains with shiny planes that resemble twin surfaces, and occur as vertical zones with diffuse boundaries within the meta-harzburgites.

II.1.2.3. Clinopyroxenites and olivine-clinopyroxenites

Clinopyroxenites occur (i) as homogeneous olivine-clinopyroxenites with rare sub-horizontal bands just below the sheared meta-plutonic rocks; (ii) in vertical clinopyroxene trails that develop into massive olivine-clinopyroxenites containing gabbro and tonalite-trondhjemite lenses in their core and with blurred boundaries to host dunites; and (iii) in dykes cross-cutting dunites and meta-harzburgites.

Clinopyroxenites in the small Ledi lens (Figs II.1 and II.2A) are dominantly homogeneous olivine-clinopyroxenites, with associated clinopyroxene trail zones. These lithologies are found in only three places of the Sapat body (sections B, C and D, Fig. II.2).

II.1.2.4. Homogeneous olivine-clinopyroxenites

This lithological domain has no clear contact. A variety of textures from randomly distributed clinopyroxene (Fig. II.3e) to alternating clinopyroxene-rich and clinopyroxene-poor bands are seen. In places clinopyroxene forms cockade-like aggregates, whilst
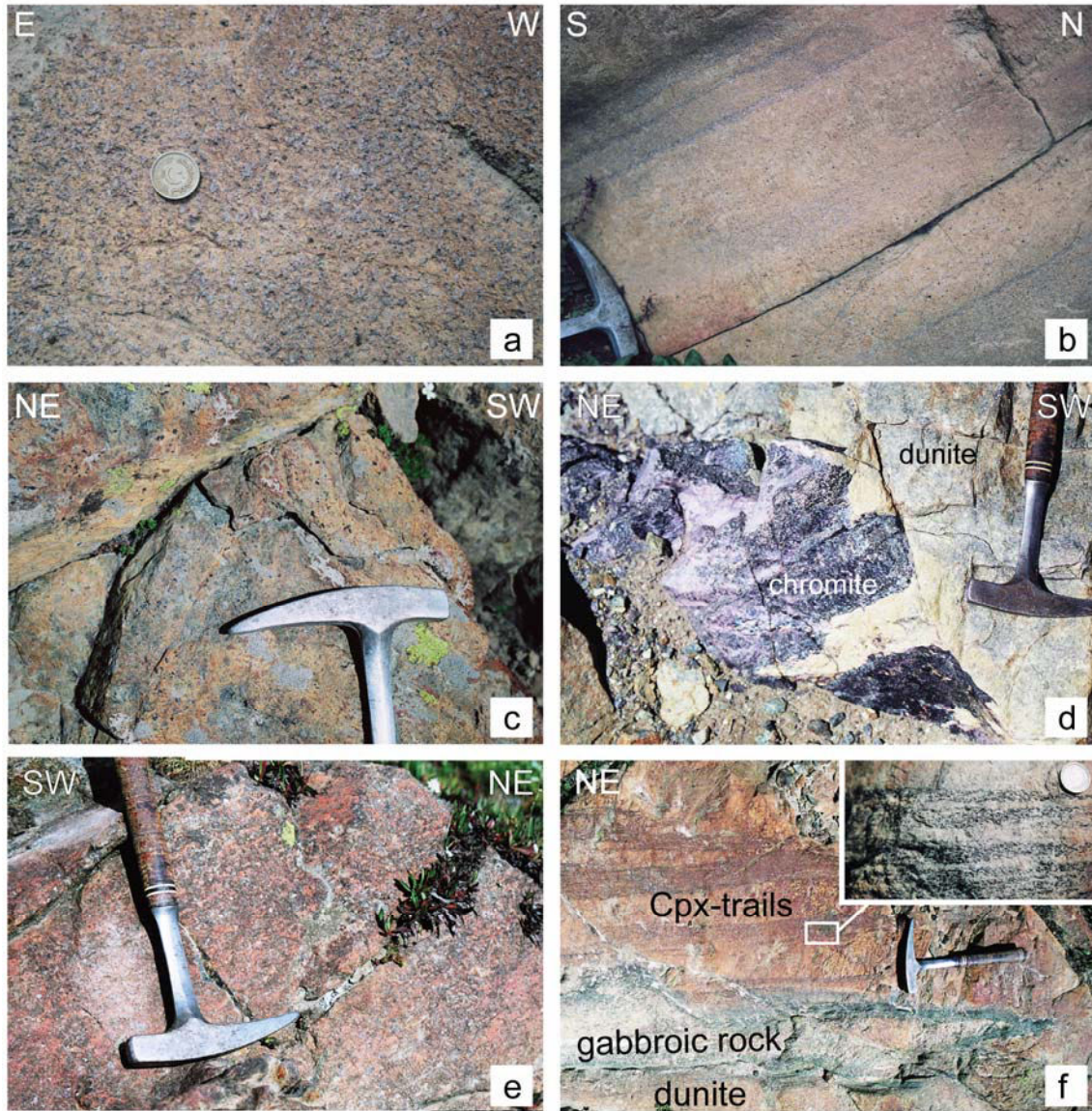
Figure II.3: a) Coarse-grained homogeneous meta-harzburgite with relict (pinkish globules) orthopyroxene (GPS: N35°02.277'-E073°46.052'). b) Banded meta-harzburgite (GPS: N35°02.594'-E073°45.802'). c) Coarse-grained dunite with evenly distributed euhedral spinel (black spots, sample D49, Fig. II.2D, Table II.1). d) Contact between a chromite pod and the host dunite, purple color of the pod due to kammererite. (GPS: N35°00.808'-E073°44.060'). e) Pyroxenite with coarse clinopyroxene homogeneously distributed in the olivine ground mass (sample D17, Fig. II.2D, Table II.1). f) Aligned clinopyroxene (Cpx) forming trails in dunite (Impregnated dunite) and associated gabbroic lens rimmed by a dark clinopyroxene rim. Note sub-parallelism between clinopyroxene trails and gabbroic lens (N35°01.715°-E073°45.069').

elsewhere clinopyroxene grains define flame structures, and isolated domains of wehrlites are found enclosed in olivine-clinopyroxenites. The homogeneous olivine-clinopyroxenites are directly linked to the "trail" zones.

II.1.2.5.   *"Clinopyroxene trail" zone*

Millimeter to centimeters sized clinopyroxene porphyroblasts define trails that sometimes coalesce to form flame- to banded-structures showing sharp contacts with the host dunites (Fig. II.3f). These mostly subvertical trails strike N015 and are clustered in elliptic zones tens to hundreds m^2 in size in map view. Some clinopyroxene bands evolve in their centres into lens-shaped gabbros (Fig. II.3f) composed of greenish clinopyroxene in a white polymineralic matrix, the former defining an internal fabric parallel to the contacts with the enclosing clinopyroxenite. This contact always contains a rim of clinopyroxene and chlorite that separates gabbros from the surrounding clinopyroxenites. Contacts between gabbroic lenses and pyroxenites are parallel to the regional trend defined by the clinopyroxene trails and bands in the dunites. One of these gabbroic lenses contains diffuse patches of a hornblende-bearing tonalite-trondhjemite pegmatite.

II.1.2.6.   *Clinopyroxenite dykes*

Two sets of clinopyroxenite dykes were identified (Fig. II.4). Set #1 is made of thin (0.5 to 5cm) fine-grained bodies approximately parallel to the regional trend of the Sapat Complex, and mostly found in the dunite. These are heterogranular, containing millimeter-scale, anhedral clinopyroxene and smaller subhedral olivine crystals. They have diffuse boundaries in thin section and the degree of replacement of the host ultramafic rocks is variable. At the dyke tips, but also intermittently along single dykes, clinopyroxene grains may pervade olivine grain boundaries and become more abundant, coalescing to form continuous structures. These thin dykes, together with micrometric, interstitial clinopyroxene in the wall dunites, exhibit a combination of infiltration and intrusion features attributed to percolative fractional crystallization (Harte et al., 1993).

The second set of clinopyroxenite dykes are pegmatitic, striking almost perpendicular to the trend of the Sapat Complex, and only found in the meta-harzburgite They are comprised of cm-scale clinopyroxene grains and are less abundant but larger than the first set. In thin section, the clinopyroxenes show secondary recrystallization to tremolite and diopside.

II.1.3.   **Petrography**

II.1.3.1.   *Meta-harzburgites*

The meta-harzburgites exhibit a wide range of textures and parageneses. All meta-harzburgites have a heterogranular texture with millimetre-sized olivine crystals (Ol_1) within a matrix of very small (µm-scale) olivine grains (Ol_2) often associated with amoeboid spinel and other phases. Ol_1 crystals display undulose extinction and subgrain boundaries, and have interlobate boundaries between each other and with rarely preserved orthopyroxene (Fig. II.5b). This indicates that the large Ol_1 grains are primary and that the non-deformed, fine-grained Ol_2 grains are secondary. Small (<1/10 mm) euhedral spinel crystals included in large primary olivine grains are also interpreted as a primary phase (Spl_1, Fig. II.5a). This contrasts with secondary, amoeboid spinel grains
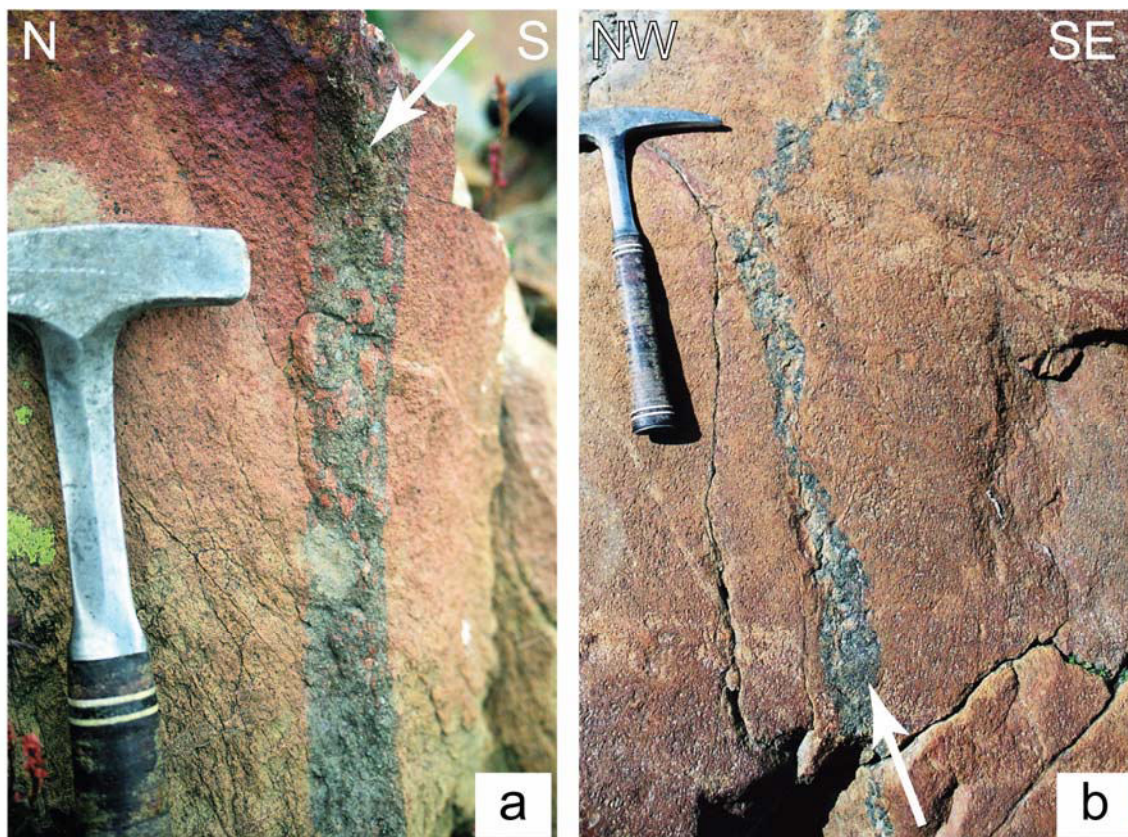
Figure II.4: a) Thin clinopyroxene-bearing dyke (set #1, arrowed) in dunite. (N34°59.404'-E073°42.849'). b) Pegmatitic dyke (set #2, arrowed) in meta-harzburgite (N35°01.178'-E073°44.707').

(Spl$_2$, Fig. II.5a) associated with Ol$_2$. The matrix olivine is associated with various orthopyroxene decomposition products made of Ol+Tlc±Tr. Olivine (Ol) locally mimics pyroxene cleavages (Fig. II.5c). Rarely, micrometer-size diopside associated with tremolite overgrows olivine (Ol). Chlorite may occur at any grain boundary and, in places, forms rims around spinel. In sample D9, the fine-grain matrix is composed of Ol$_2$+Spl$_2$+Cpx+Cal+Di (Fig. II.5d). In few samples, Ol$_2$ rims millimetre size diopside and tremolite aggregates, which are pseudomorphs after clinopyroxene.

II.1.3.2. *Dunites*

Dunites are usually equigranular and very fresh, with serpentinization restricted to grain boundaries. Millimeter-sized olivine grains with undulose extinction and subgrain boundaries are commonly tabular and imbricated. These grains are primary. Trails of interstitial, lobate to subhedral spinel are associated with smaller olivine in bands parallel to the long axis of the millimeter sized tabular olivine grains. Olivine is also found as inclusions in spinel and within spinel cracks. Small (ca. 0.1mm), secondary olivine (Ol$_2$) is associated with calcite, amoeboid spinel and occasionally with chlorite at grain boundaries and within cracks of primary olivine (Fig. II.5e). Calcite crystallized at grain boundaries of the dunite minerals (preferentially next to chromite trails), and commonly
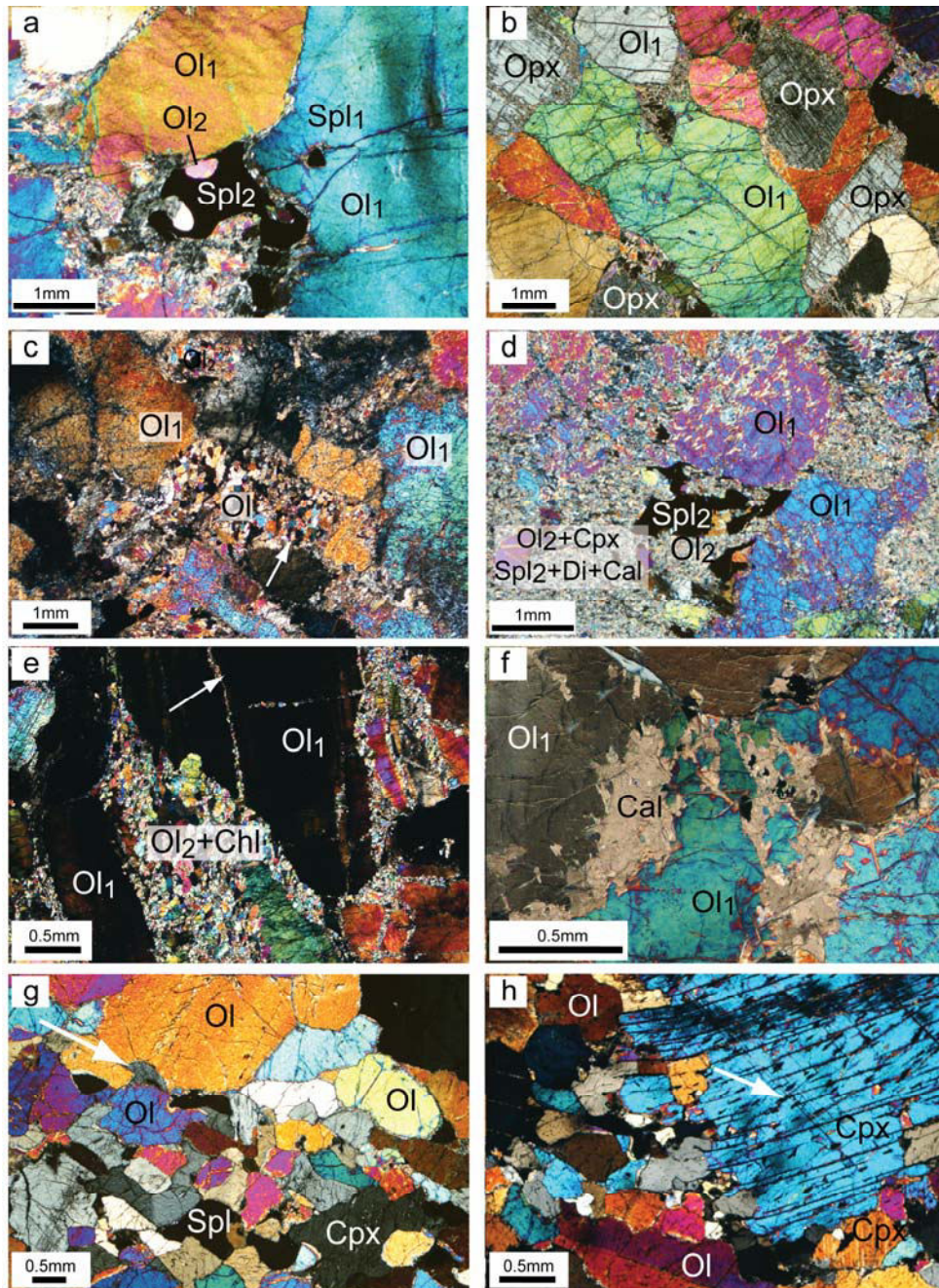
Figure II.5: a) Secondary amoeboid spinel (Spl_2) associated with secondary olivine (Ol_2) between large grains of strained, primary olivine (Ol_1) with spinel inclusions (Spl_1, sample D88, Fig. II.2E, Table II.1). b) Meta-harzburgite with well preserved orthopyroxene (Opx, sample D89, Fig. II.2E, Table II.1). c) Mosaic aggregates of metamorphic olivine (Ol) mimicking cleavages (white arrow) between serpentinized primary olivine (Ol_1, sample D83, Fig. II.2E, Table II.1). d) Serpentinized primary olivine (Ol_1) within matrix composed of secondary olivine (Ol_2), clinopyroxene, secondary spinel (Spl_2), diopside (Di) and calcite (Ca), sample D9, Fig. II.2D, Table II. 1. e) Strained olivine grains (Ol_1) in matrix of secondary olivine-chlorite±calcite (Ol_2+Chl); white arrow: matrix-containing crack. (Sample D65, GPS: N35°00.808'-E073°44.060'). f) Interstitial calcite (Ca) overgrowing olivine (Ol) (GPS: N35°01.067'-E073°44.762'). g) Ol-clinopyroxenite-spinel micro-vein in coarse dunite from the trail zone; arrow = vein boundary. h) Clinopyroxene porphyroblast (Cpx) with magnetite exsolution and amphibole inclusions (white arrow) in dunite (Ol = olivine).

overgrew olivine (Fig. II.5f). Serpentine overgrowing secondary olivine represents a late event. The several millimeter big Ol_1 of "faceted" dunites show an orthogonal network of planes whose origin is unclear.

II.1.3.3. *Trail zones and homogeneous olivine-clinopyroxenites*

Within the trail zone, fine grained (0.1-0.5 mm) olivine-clinopyroxene (± spinel) micro-veins are well defined in thin section (Fig. II.5g). They are aligned between anhedral, millimetre size, deformed olivine grains of the host dunite. Olivine grains have a globular shape whereas clinopyroxene is amoeboid and fills grain boundaries. The macroscopically well aligned, millimeter- to centimeter-sized clinopyroxene porphyroblasts forming trails have lobate boundaries (Fig. II.5h), pervade olivine grain boundaries and engulf and overgrow olivine grains (Fig. II.5h). Chlorite and hornblende are often associated with clinopyroxene, either as inclusions (Fig. II.5h) or at grain boundaries.

Within homogeneous olivine-clinopyroxenites, amoeboid, multi-millimeter sized clinopyroxene invades grain boundaries and engulf olivine. Clinopyroxene is also found as an intercumulus phase together with rounded olivine and anhedral spinel l. Strained olivine has lobate boundaries and is heterogranular, ranging from millimeter to micrometer in size. In some samples, tremolite and diopsidic rims around clinopyroxene document metamorphic recrystallisation. In the most retrogressed sample LD5 (Fig. II.2A), magnetite is found as an exsolution phase within clinopyroxene. The metamorphic matrix of olivine-clinopyroxenites often comprises serpentines and/or tremolite ± chlorites. Ni and Cu sulfides are common at grain boundaries in all pyroxenites.

II.1.3.4. Gabbroic lenses

Metagabbros in clinopyroxenite bands display a recrystallised texture. The metamorphic paragenesis consists of matrix chlorite, amphibole, epidote, Cr-rich garnet and tremolite occasionally corroding and replacing magmatic clinopyroxene (Fig. II.6). Millimetre-size magmatic clinopyroxene is closely associated with subhedral to euhedral epidote and may contain inclusions of hornblende. Clinopyroxene grains have thin, epitactic, irregular rims of diopside representing metamorphic re-equilibration. Feldspars are no longer present, with all of the Na_2O now incorporated in amphibole.

Figure II.6: a) relictual clinopyroxene (Cpx) in metamorphic matrix (Amph+Chl) (sample D25, Table II.1) b) Clinopyroxene (Cpx) and euhedral epidote (Ep); arrow = amphibole inclusions in clinopyroxene (sample LD10, Table II.1).

II.1.3.5.   Interpretation of textures

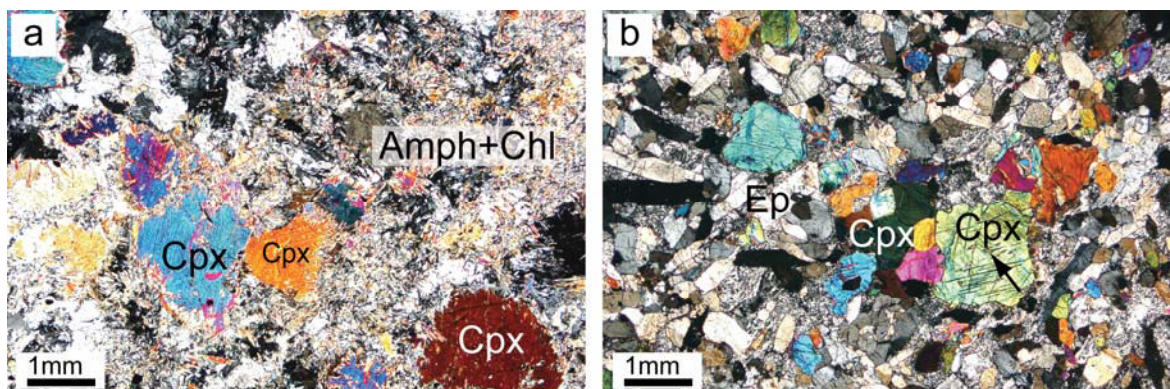Meta-harzburgites show partial amphibolite to greenschist facies re-equilibration and late serpentinization, contrasting with dunites which exhibit very limited serpentinization. The presence of both metasTable II. orthopyroxene, and its highly recrystallized metaproducts (Ol-Tr-Tlc) document fluid-assisted lower amphibolite facies re-equilibration. However, secondary olivine often crystallized together with secondary spinel, and sample D9 (Fig. II.2D) shows the presence of magmatic clinopyroxene within the fine-grained recrystallized matrix (+calcite+diopside). Relationships between meta-products and the olivine-spinel forming reactions indicate that the amphibolite facies re-equilibration affecting the meta-harzburgites has apparently overprinted magmatic reactions,

Spinel and clinopyroxene trails in dunite define melt percolation features (e.g. Harte et al., 1993). The porphyroblastic clinopyroxene forming trails growing at grain boundaries relate the formation of clinopyroxene to melt percolation. Olivine-clinopyroxene bearing micro-veins observed in the trail zone, in thin dykes, and in the homogeneous olivine-clinopyroxenites imply co-precipitation of these phases upon cooling. We accordingly interpret the clinopyroxenite areas as defining impregnated zones where melt-rock reactions and melt crystallization occurred.

In the field, dunites and associated pyroxenites represent the uppermost mantle levels of a mantle-crust transition zone. A partial amphibolite to greenschist facies re-equilibration affected the pyroxenitic domain. Microcracks and grain boundaries in dunite are filled with secondary olivine, chlorite, spinel and calcite and are considered the serpentine-free equivalent of the gem-olivine-bearing veins found in dunite in the same structural position. This paragenesis is interpreted has precipitates from fluids during cooling.

II.1.4.   Mineral compositions

II.1.4.1.   Olivine

Olivine grains (Table II.2) are generally unzoned with X_{Mg} ranging from 0.861 to 0.986 (Fig. II.7a). The highest X_{Mg} (~0.980-0.940) comes from olivine grains in chromite pods (never from grains in contact with spinel) and gem crystals. Meta-harzburgites contain olivine with $0.861 < X_{Mg} < 0.912$ which can be divided into two subgroups at ~ 0.870 and ~ 0.900. Coarse-grained dunites have a smaller X_{Mg} range of 0.894 to 0.930. In all pyroxenites, olivine ranges from X_{Mg}= 0.912 to 0.886 (except one value of 0.876). Olivine NiO contents range from 0.15 to 0.52 wt %. Primary olivine grains display the highest NiO values and secondary olivine generally contains less NiO. NiO contents in primary olivine grains decrease toward the rims and towards cracks filled with low Ni Ol_2 and Chl, indicating re-equilibration processes. MnO contents (Fig. II.7b) are negatively correlated with NiO and X_{Mg} variations. Generally, the most differentiated (lowest X_{Mg}) olivine grains have more MnO and less NiO. Gem-olivines have a wide range in X_{Mg} ($0.893<X_{Mg}<0.954$) and NiO content ($0.256<NiO$ wt%<0.457).

Ni content and X_{Mg} of olivine are positively correlated with Mo and negatively correlated with Ti, Sc, Co, Zn, and B contents (Fig. II.8, Table II.3) in olivine. These correlations do not apply for meta-harzburgite olivine, which has (i) significantly higher Mo contents (Mo>0.24 ppm) than olivine from the other rocks, (ii) Zn contents (~35 ppm) similar to those of low Ni olivine and (iii) low Ti contents (2-3 ppm). Secondary olivine has 10-20

fold higher concentrations of Cr, Sc, and B (up to 20-30 ppm) than other olivines. Nevertheless Cr does not show any correlation with Mg# or Ni content.
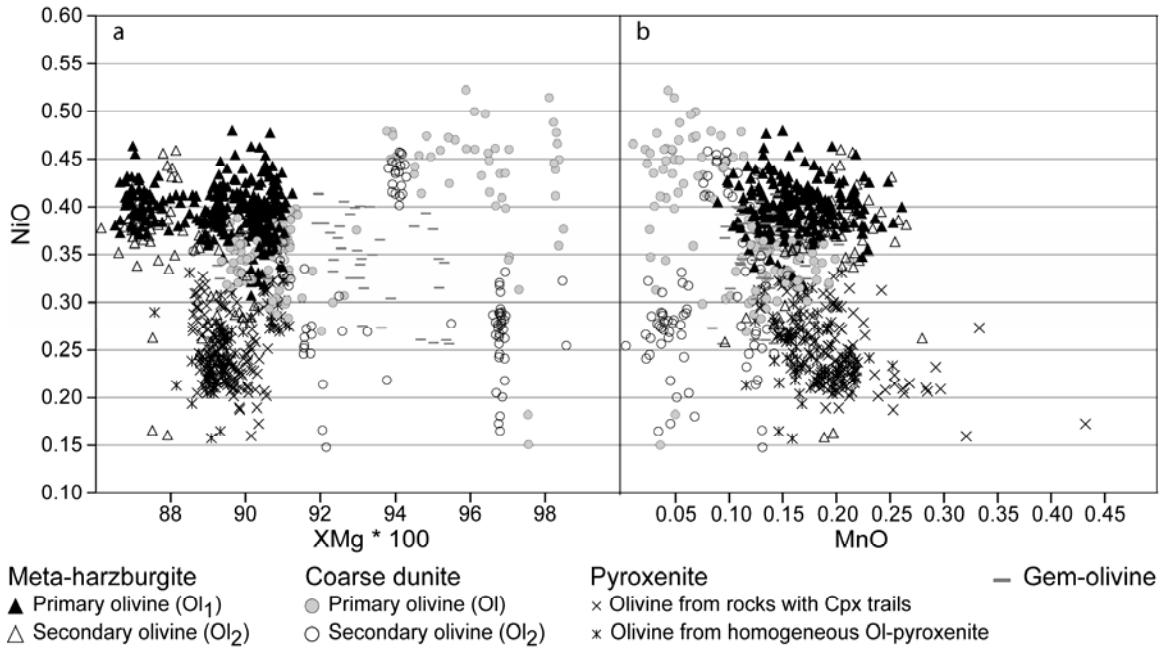

Figure II.7: Olivine chemistry: a) X_{Mg} versus NiO. b) X_{Mg} versus MnO wt%.
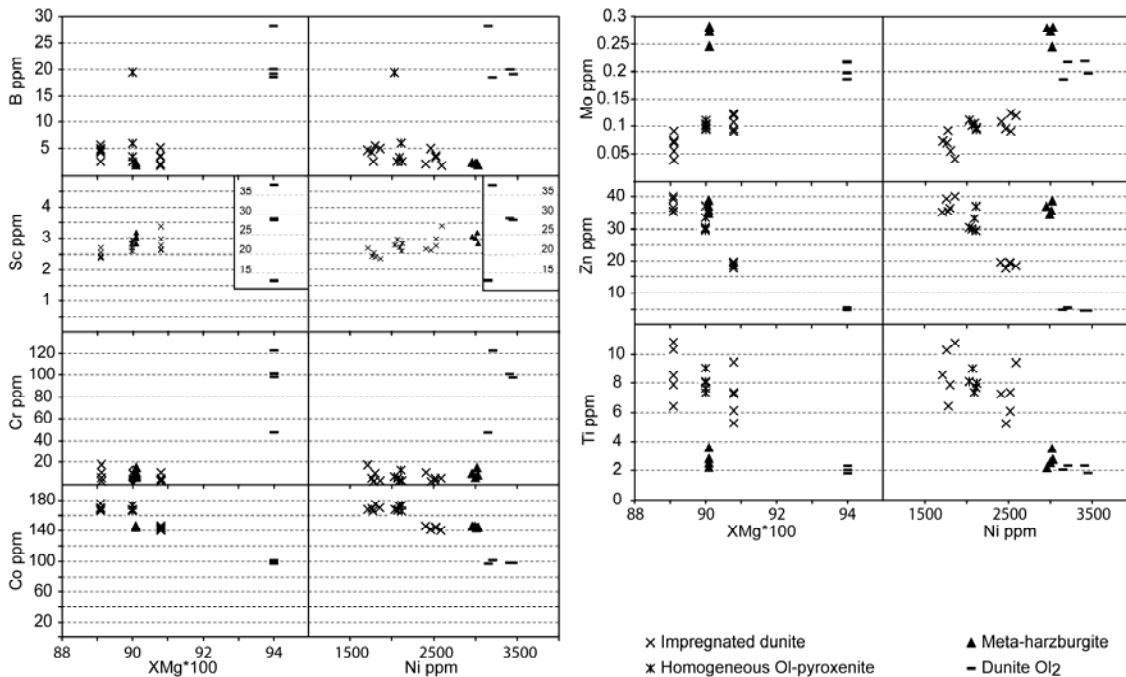

Figure II.8: Relationships between minor elements, X_{Mg} and Ni contents in olivine. X_{Mg} values are from E.P.M.A analysis; Ni content measured during laser ablation with the other minor elements.

Table 2

rock	dunite				Meta-Harzburgite						Faceted dunite		Homog. Pyroxenite	
Sample	D86		D39		D88				D85		D67		D64	
olivine	Ol	n=24	Ol2	n=20	Ol1	n=45	Ol2	n=3	Ol	n=28	Ol1	n=28	Ol	n=30
	Average	2σ	Average	2σ	Average	2σ	Average	2σ	Average	2σ	Average	2σ	Average	2σ
SiO_2	40.74	0.66	39.60	0.29	41.13	0.32	41.05	0.16	40.27	0.21	40.76	0.26	39.05	0.59
FeO	8.30	0.11	5.44	0.09	8.68	0.23	9.04	0.22	11.84	0.18	10.10	0.63	9.46	0.38
MnO	0.138	0.015	0.096	0.015	0.133	0.017	0.161	0.015	0.196	0.017	0.168	0.019	0.200	0.013
NiO	0.362	0.023	0.432	0.018	0.396	0.027	0.311	0.037	0.383	0.013	0.378	0.026	0.229	0.021
MgO	50.93	0.40	53.26	0.46	50.57	0.35	49.87	0.17	48.00	0.26	49.14	0.81	50.40	0.36
Total	100.52	0.63	98.87	0.58	100.94	0.47	100.48	0.30	100.82	0.31	100.61	1.33	99.41	0.83
Si	0.985	0.014	0.958	0.006	0.993	0.007	0.998	0.005	0.987	0.005	0.995	0.014	0.956	0.009
Fe	0.168	0.002	0.110	0.002	0.175	0.004	0.184	0.004	0.243	0.004	0.206	0.011	0.194	0.008
Mn	0.003	0.000	0.002	0.000	0.003	0.000	0.003	0.000	0.004	0.000	0.003	0.000	0.004	0.000
Ni	0.007	0.000	0.008	0.000	0.008	0.001	0.006	0.001	0.008	0.000	0.007	0.000	0.005	0.000
Mg	1.836	0.012	1.920	0.007	1.820	0.008	1.807	0.005	1.754	0.005	1.787	0.009	1.840	0.010
XMg	0.911	0.001	0.940	0.001	0.907	0.002	0.903	0.002	0.872	0.003	0.891	0.004	0.900	0.004

Table II.2: Representative E.P.M.A. analyses of olivine of the different lithologies.

Sample	D64 impregn. dunite		D21a impregn. dunite		D45b impregn. dunite		D89 Meta-harzburgite		D39 Gem-olivine	
Mineral	Ol	n=4	Ol	n=5	Ol	n=5	Ol1	n=4	Ol	n=4
	Average	2σ	Average	2σ	Average	2σ	Average	2σ	Average	2σ
B	3.74	1.59	4.50	1.10	3.29	1.32	2.36	0.20	21.50	4.59
Ca	73.1	22.7	264.0	257.5	133.2	39.0	127.1	178.2	17.4	5.5
Sc	2.78	0.16	2.49	0.13	2.88	0.32	3.03	0.15	27.00	10.24
V	0.376	0.177	0.774	0.575	0.196	0.113	0.750	0.135	0.647	0.424
Cr	6.83	4.63	8.26	6.15	5.82	3.12	10.52	3.79	92.04	31.78
Mn	1300	74	1360	34	1107	11	1018	24	770	26
Co	170	4	170	3	144	2	145	1	98	2
Ni	2097	24	1781	53	2502	69	3002	31	3306	149
Zn	32.6	3.5	37.5	2.1	19.0	0.9	36.7	1.8	4.8	0.3
Li	1.47	0.09	1.37	0.29	1.58	0.17	0.91	0.04	17.29	6.33
Mo	0.098	0.004	0.065	0.019	0.107	0.014	0.270	0.017	0.203	0.016
Ti	8.05	0.72	8.79	1.80	7.09	1.59	2.79	0.56	2.12	0.24

Table II.3: LA-ICP-MS composition in minor elements of olivine.

II.1.4.2. *Spinel*

Spinel chemistry (Table II.4) reflects the processes that affected the ultramafic rocks. Primary spinel, included in olivine of meta-harzburgites, is very low in TiO_2 (<0.50 wt %) and ranges in X_{Mg} from 0.50 to 0.25 with a Cr# (Cr/Cr+Al) between 0.50 and 0.68 (Fig. II.8a, b). Rims of primary spinel and amoeboid second stage spinel have lower X_{Mg} (0.13-0.24) and slightly higher TiO_2 (0.09-0.26). A significantly higher Cr# (0.84-0.96) is seen in grains with Fe^{3+} < 0.5 apfu.

Primary spinel from dunites shows a wide range of X_{Mg} (0.17 – 0.80) with the highest values in chromite pods. Ranges of TiO_2 and Cr# are typically restricted to approximately 0.20 wt % and 0.70, respectively. Nevertheless, several grains have very high Cr#, of 0.94 – 0.98. Late spinel and rims of primary crystals contain higher a TiO_2 content and Cr#, and lower X_{Mg}. Cores of anhedral spinel associated with melt percolation and pyroxenite formation have the same composition as primary spinel of dunites. Rims of anhedral spinel have low X_{Mg} (0.20-0.01) and high TiO_2 content (≤ 2.60).

Magnetite (lower left corner of figure II.8a) is found with metamorphosed pyroxene and along grain boundaries associated with serpentines in meta-harzburgites and dunites. Magnetite also forms rims on all spinel compositions and is associated with gem-olivine when embedded in serpentine. Magnetite is attributed to late serpentinization.
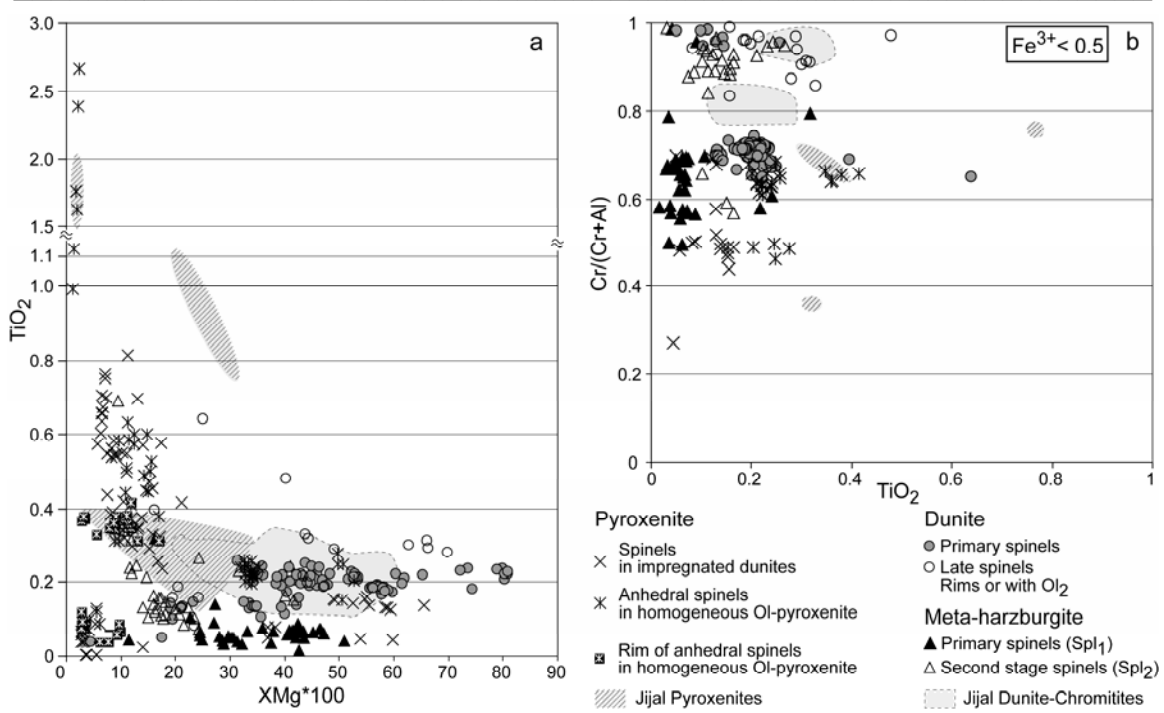
Figure II.8: Spinel chemistry a) TiO_2 wt% content versus X_{Mg}. b) Cr number versus TiO_2 wt% for low Fe^{3+} spinel (<0.5 cations pfu). Spinel from Jijal (Jan and Windley, 1990) shown for comparison.

rock	Dunite		Meta-Harzburgite				Homog. Pyroxenite	
Sample	D50		D87				D64	
Spinels	Spl	n=12	Spl1	n=8	Spl2	n=8	Spl	n=17
	Average	2σ	Average	2σ	Average	2σ	Average	2σ
TiO2	0.141	0.016	0.057	0.014	0.136	0.024	0.493	0.096
Cr2O3	53.08	2.64	51.48	3.36	62.28	1.90	23.53	5.44
Al2O3	12.30	5.17	16.68	4.03	4.75	1.35	0.22	0.18
FeO	27.68	4.12	24.88	1.81	28.61	0.34	67.98	5.50
MnO	0.0	0.0	0.0	0.0	0.0	0.0	0.651	0.185
NiO	0.042	0.015	0.031	0.020	0.019	0.013	0.310	0.051
MgO	6.52	1.56	7.45	1.77	3.24	0.17	2.28	0.43
Total	99.80	1.06	100.62	0.77	99.11	0.41	95.82	0.55
Ti	0.004	0.001	0.001	0.000	0.004	0.001	0.014	0.003
Cr	1.411	0.124	1.326	0.136	1.763	0.063	0.692	0.156
Al	0.479	0.195	0.634	0.138	0.200	0.056	0.009	0.008
Fe3+	0.101	0.098	0.035	0.009	0.027	0.008	1.249	0.161
Fe2+	0.680	0.068	0.642	0.076	0.830	0.009	0.866	0.022
Mn	0.000	0.000	0.000	0.000	0.000	0.000	0.020	0.006
Ni	0.001	0.000	0.001	0.000	0.001	0.000	0.009	0.002
Mg	0.323	0.068	0.359	0.076	0.173	0.008	0.127	0.023
XMg	0.322	0.067	0.358	0.076	0.172	0.008	0.123	0.022
Cr ≠	0.751	0.099	0.676	0.070	0.898	0.029	0.987	0.008

Table II.4: Representative E.P.M.A. analyses of spinel of the different lithologies.

II.1.4.3.   *Clinopyroxene*

Clinopyroxenes composition (Table II.5) shows a trend of increasing Al, Na, and Ti content with decreasing X_{Mg} (0.87 <X_{Mg}<0.98; 0.58 < Al_2O_3 < 3.70 wt %; 0.03 <TiO_2 < 0.24 wt %) (Fig. II.9a, b). This trend correlates with the structural position of the clinopyroxene, with a sequence from thin clinopyroxenite dykes, to clinopyroxene from grain boundaries in meta-harzburgites (sample D9), to trail zones and homogeneous olivine-clinopyroxenites, and finally to the meta-gabbros. Magmatic clinopyroxene which contains > 0.5 wt % Al_2O_3 and > 0.03 TiO_2 wt %, also contains between 0.15 and 1.23

Cr_2O_3 wt% and does not correlate with the Al, Na, Ti trend. Clinopyroxene is usually zoned with a slight decrease in Al, Cr and Ti toward rims corresponding to a slight increase in X_{Mg}. This zoning is attributed to late subsolidus re-equilibration controlled by negative tschermak substitution. The latest metamorphic rims and neoformed metamorphic clinopyroxenes from meta-harzburgites are close to pure diopside, with X_{Mg} > 0.96.
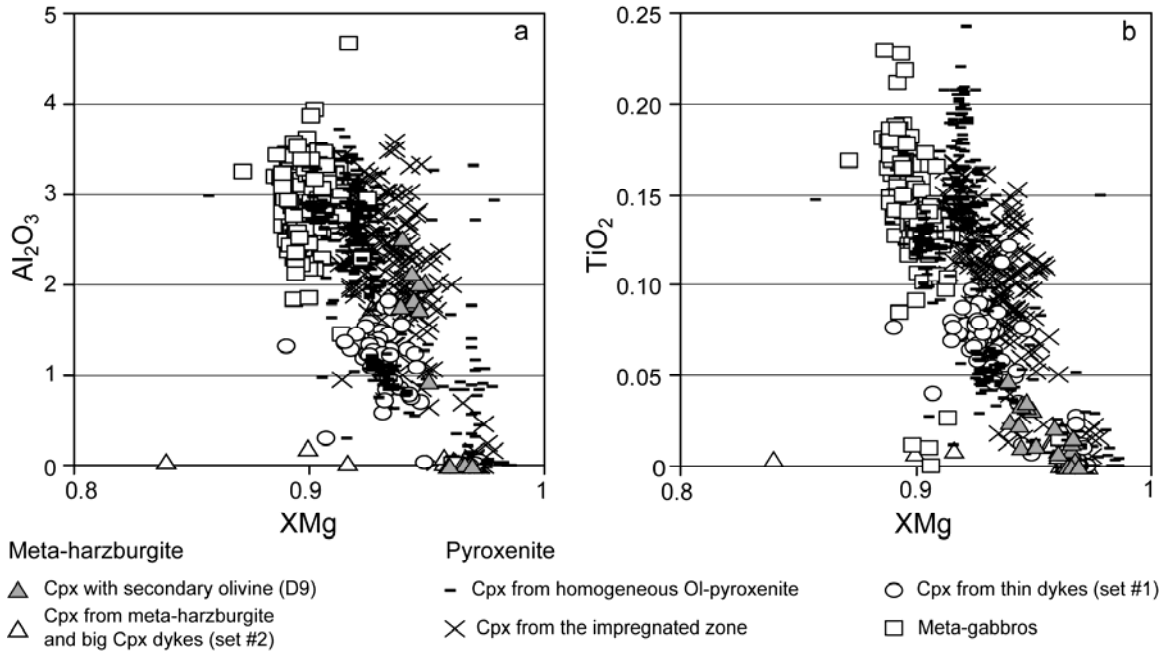
Figure II.9: Clinopyroxene chemistry a) Al_2O_3 wt% content versus X_{Mg}. b) TiO_2 wt% content versus X_{Mg}.
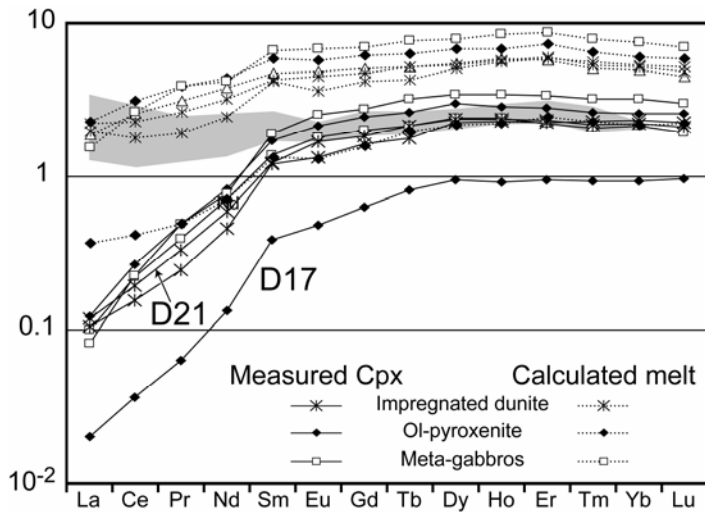
Figure II.10: Trace element composition of clinopyroxene. Chondrite normalized Rare Earth Element patterns and their calculated parental melts using Kd's of Hart and Dunn (1993). Grey array = parental melt of Jijal pyroxenites defined by Garrido et al. (2007). Chondritic from Sun and McDonough (1989).

We analyzed trace element compositions of clinopyroxene from the trail zones (impregnated dunites, samples D21-D45b, Fig. II.2C and D), from homogeneous ol-clinopyroxenites (samples D17, Fig. II.2D, and D64, Fig. II.2B) and from the meta-gabbros (D25, Fig. II.2D, and LD10, Fig. II.2A) (Table II.6). The chondrite normalized REE patterns (Fig. II.10) of all clinopyroxenes are similar, with a flat HREE segment

(0.89<Dy_N/Lu_N<1.41), a slightly fractionated MREE segment (0.29<Sm_N/Dy_N<0.69) and a strongly fractionated LREE segment (0.04<La_N/Sm_N<0.14). Samples from Ol-clinopyroxenite show the same absolute values as samples from the impregnated dunites and meta-gabbros, except for sample D17, which has approximately half the REE contents of the other samples, yet with the same pattern. Samples normalized to the primitive mantle have strong Zr-Hf and slight Ti negative anomalies, and positive Pb, Sr and Sm anomalies. Clinopyroxenes from the impregnated dunite have the highest concentrations in Th and U whereas clinopyroxenes from the olivine-clinopyroxenites and meta-gabbros have the lowest Th and U concentrations. We also notice a strong Nb/Ta fractionation (ca. Nb/Ta=2.5). The trace element concentrations of clinopyroxenes are similar to those observed for the bulk rock (paragraph II.1.5.2).

Table 5

rock	Peridotite		Big dyke		Thin dyke		Impregnated dunite		homogeneous Ol-pyroxenite				Meta-gabbros			
Sample	D9		D76		SAP12		D45		D17				D25			
cpx	cores	n=21	cores	n=6	cores	n=9	cores	n=11	rims	n=10	cores	n=5	rims	n=10	cores	n=6
	Average	2σ	Average	2σ	Average	2σ	Average	2σ	Average	2σ	Average	2σ	Average	2σ	Average	2σ
SiO2	53.76	0.94	55.78	0.21	53.46	0.77	54.106	0.514	53.85	0.62	53.41	0.18	52.80	0.42	52.34	1.14
TiO2	0.02	0.01	0.01	0.00	0.06	0.03	0.09	0.02	0.04	0.02	0.05	0.00	0.13	0.02	0.12	0.03
Cr2O3	0.38	0.35	0.25	0.11	0.59	0.31	0.69	0.10	0.43	0.19	0.58	0.01	0.81	0.10	0.79	0.16
Al2O3	0.80	0.98	0.03	0.04	1.13	0.56	1.94	0.27	0.89	0.33	1.12	0.07	3.13	0.19	4.05	1.25
FeO	1.41	0.35	1.31	0.09	1.90	0.42	1.78	0.21	2.49	1.02	2.38	0.10	2.99	0.20	2.96	0.31
MnO	0.05	0.03	0.04	0.00	0.09	0.03	0.05	0.02	0.10	0.04	0.10	0.01	0.09	0.01	0.08	0.01
NiO	0.04	0.02	0.02	0.02	0.04	0.02	0.03	0.01	0.02	0.01	0.02	0.01	0.03	0.02	0.03	0.01
MgO	17.59	0.37	17.73	0.20	17.69	0.25	17.36	0.50	18.63	2.87	17.64	0.13	16.02	0.39	15.99	0.46
CaO	26.09	0.72	26.34	0.22	25.11	0.65	24.49	0.63	23.64	4.45	24.85	0.14	24.60	0.33	23.57	1.67
Na2O	0.04	0.01	0.14	0.05	0.17	0.07	0.17	0.03	0.07	0.03	0.09	0.01	0.36	0.09	0.67	0.50
Total	100.18	0.45	101.64	0.30	100.25	0.36	100.720	0.465	100.16	0.53	100.25	0.25	100.96	0.65	100.60	0.83
Si	1.946	0.026	1.991	0.003	1.933	0.022	1.949	0.014	1.946	0.013	1.935	0.006	1.907	0.007	1.890	0.036
Ti	0.000	0.000	0.000	0.000	0.002	0.001	0.002	0.000	0.001	0.000	0.001	0.000	0.004	0.001	0.003	0.001
Cr	0.011	0.010	0.007	0.003	0.017	0.009	0.020	0.003	0.012	0.005	0.017	0.000	0.023	0.003	0.022	0.005
Al	0.034	0.042	0.001	0.002	0.048	0.024	0.083	0.011	0.038	0.014	0.048	0.003	0.133	0.008	0.172	0.054
Fe3+	0.042	0.010	0.019	0.007	0.057	0.013	0.010	0.013	0.059	0.013	0.066	0.007	0.049	0.007	0.059	0.019
Fe2+	0.000	0.001	0.020	0.005	0.000	0.001	0.044	0.015	0.016	0.026	0.006	0.008	0.041	0.010	0.031	0.017
Mn	0.002	0.001	0.001	0.000	0.003	0.001	0.002	0.000	0.003	0.001	0.003	0.000	0.003	0.000	0.002	0.000
Ni	0.001	0.001	0.001	0.000	0.001	0.000	0.001	0.000	0.000	0.000	0.001	0.000	0.001	0.000	0.001	0.000
Mg	0.949	0.017	0.943	0.008	0.954	0.011	0.932	0.027	1.003	0.148	0.952	0.005	0.862	0.017	0.860	0.025
Ca	1.012	0.024	1.007	0.009	0.973	0.023	0.945	0.024	0.916	0.174	0.964	0.005	0.952	0.014	0.912	0.063
Na	0.003	0.001	0.010	0.003	0.012	0.005	0.012	0.002	0.005	0.002	0.006	0.001	0.025	0.006	0.047	0.035
xMg(Fetot)	0.957	0.011	0.960	0.002	0.943	0.012	0.946	0.006	0.932	0.017	0.930	0.003	0.905	0.007	0.906	0.007

Table II. 5: Representative E.P.M.A analysis of clinopyroxene.

II.1.4.4. *Orthopyroxene*

The harzburgite orthopyroxenes (Appendix 2) have X_{Mg} values ranging from 0.894 to 0.918, Ca contents of 0.28 to 1.56 wt % and Al_2O_3 contents between 1.34 and 1.85 wt%. The freshest crystals have a weak zoning with a decrease in Al, Cr, Ni, and Ca from core to rim. This zoning is interpreted as reflecting cooling from mantle temperatures and metamorphic re-equilibration in amphibolite facies.

II.1.4.5. *Amphibole*

Amphibole crystals (Appendix 2) in ultramafic rocks are tremolitic, have negligible Cr contents, and relate to pyroxenes through metamorphic reactions. A few edenitic amphiboles (0.90 < X_{Mg} < 0.92, 0.97 < Cr_2O_3 < 1.91) are present in the trail zones and in homogeneous olivine-clinopyroxenites as inclusions in clinopyroxene.

rock	Homog. ol-clinopyroxenite				Impregnated dunite				Meta-gabbros			
Sample	D64	n=8	D17	n=6	D45b	n=5	D21	n=5	D25	n=5	LD10	n=4
	Average	2σ	Average	2σ	Average	2σ	Average	2σ	Average	2σ	Average	2σ
Cs	0.023	0.023	0.006	0.003	0.008	1/5	0.015	0.001	0.044	0.033	0.100	0.109
Rb	0.018	0.008	0.008	0.003	<0.0127	-	0.025	1/5	0.053	0.030	0.090	0.088
Ba	0.039	0.034	0.025	0.014	0.0267	0.0159	0.075	0.041	0.538	0.253	0.271	0.223
Th	0.0008	0.0004	0.0003	0.0003	0.0042	0.0011	0.0060	0.0016	0.0017	0.0010	0.0007	0.0007
U	0.0004	0.0003	<0.00021	-	0.0021	0.0011	0.0024	0.0015	0.0004	0.0003	0.0006	0.0003
Nb	0.0048	0.0020	0.0020	0.0005	0.0041	0.0026	0.0059	0.0021	0.0059	0.0012	0.0052	0.0011
Ta	0.0020	0.0001	0.0018	0.0007	0.0021	0.0001	0.0022	0.0006	0.0038	0.0021	0.0030	1/4
La	0.029	0.003	0.005	0.002	0.025	0.004	0.028	0.003	0.024	0.003	0.019	0.003
Ce	0.163	0.012	0.022	0.002	0.095	0.013	0.119	0.005	0.136	0.012	0.137	0.025
Pb	0.034	0.008	0.104	0.021	0.012	0.006	0.086	0.044	0.095	0.047	0.018	0.013
Pr	0.047	0.004	0.006	0.001	0.023	0.003	0.032	0.005	0.037	0.004	0.047	0.005
Sr	5.16	0.15	2.03	0.05	4.38	0.10	6.43	0.23	5.69	0.11	5.9	1.77
Nd	0.385	0.026	0.062	0.005	0.214	0.009	0.278	0.019	0.330	0.038	0.363	0.004
Sm	0.261	0.028	0.059	0.015	0.185	0.017	0.188	0.036	0.211	0.033	0.293	0.018
Zr	1.28	0.09	0.55	0.01	0.55	0.05	0.87	0.08	1.14	0.08	1.21	0.11
Hf	0.082	0.016	0.005	0.002	0.044	0.011	0.060	0.014	0.078	0.018	0.087	0.006
Eu	0.123	0.009	0.028	0.002	0.077	0.008	0.098	0.007	0.105	0.011	0.146	0.007
Gd	0.505	0.028	0.130	0.014	0.336	0.007	0.380	0.021	0.415	0.043	0.565	0.049
Tb	0.098	0.005	0.031	0.002	0.067	0.002	0.080	0.008	0.080	0.006	0.119	0.008
Dy	0.761	0.061	0.242	0.014	0.571	0.024	0.603	0.010	0.611	0.062	0.881	0.072
Y	4.03	0.19	1.34	0.06	3.24	0.06	3.32	0.11	3.36	0.23	4.91	0.32
Ho	0.160	0.009	0.052	0.003	0.129	0.005	0.135	0.007	0.136	0.009	0.195	0.009
Er	0.466	0.021	0.159	0.014	0.375	0.017	0.388	0.015	0.368	0.037	0.556	0.031
Ti	985	56	340	14	679	32	810	62	879	25	1130	65
Tm	0.067	0.005	0.024	0.003	0.058	0.007	0.055	0.004	0.053	0.005	0.082	0.008
Yb	0.439	0.022	0.160	0.019	0.394	0.028	0.377	0.054	0.363	0.035	0.546	0.066
Lu	0.065	0.004	0.024	0.002	0.058	0.004	0.054	0.009	0.049	0.001	0.077	0.006

Table II.6: Trace element composition of clinopyroxene from four samples. Element below detection limit are quoted with their detection limit (e.g. <0.00021=below D.L. of 0.00021).

II.1.4.6. *Chlorite*

Chlorite (Table II. 7) is present as chromium-rich clinochlore with up to 5.89 Cr_2O_3 wt % (Fig. II.11). The highest Cr contents are measured in matrix chlorite from chromite pods, in chlorite within Ol_2-bearing cracks, and grain boundaries in dunite. Chlorite has high Ni contents up to 0.47 wt% NiO, with a generally positive correlation of Cr and Ni. It becomes richer in Al^{VI} with decreasing Ni and Cr contents. Chlorite is also found as inclusions in clinopyroxene, either as patches or needle-like shape.
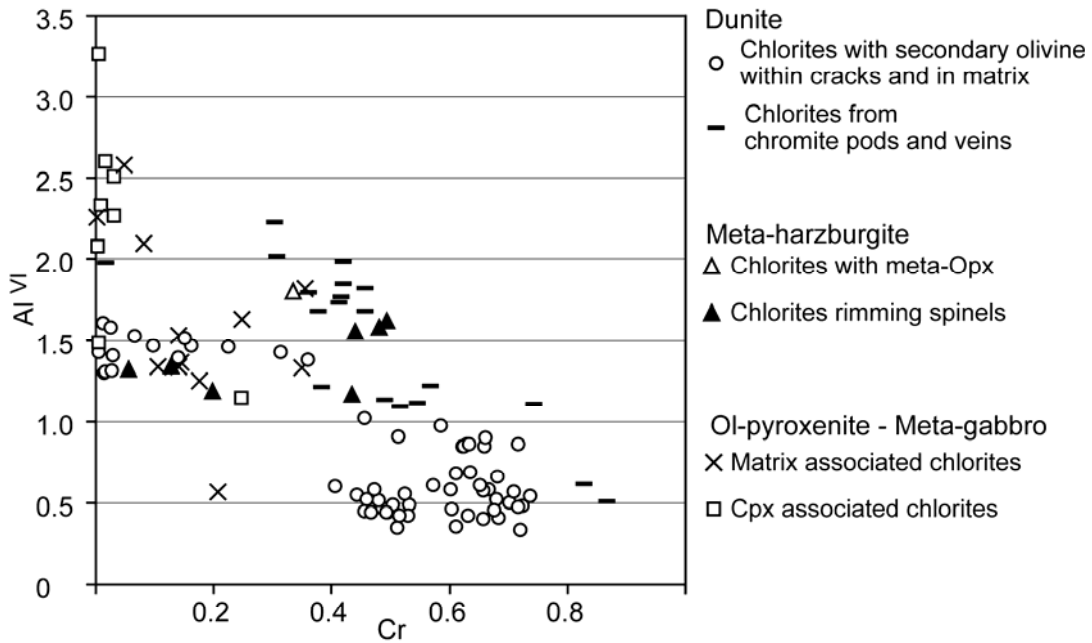

Figure II.11: Al^{VI} versus Cr contents (cations) of chlorites.

rock	veine		veine		chromite pod				chromite dyke		Meta-gabbro		impregnated dunite	
Sample	D39	with Ol2	D1	with Ol2	D65	with Ol2		matrix	D5	matrix	LD10	matrix	D21	within cpx
chlorite		n=21		n=7		n=13		n=8		n=7		n=8		n=3
	Average	2σ	Average	2σ	Average	2σ	Average	2σ	Average	2σ	Average	2σ	Average	2σ
SiO_2	35.35	0.99	32.64	0.87	33.77	0.43	34.24	2.01	35.76	0.49	29.39	0.76	33.12	3.90
Cr_2O_3	3.41	0.46	2.29	1.05	0.89	0.78	3.78	1.29	4.25	0.18	0.09	0.08	2.03	0.54
Al_2O_3	7.56	1.03	17.22	1.41	12.65	0.42	10.96	2.76	9.71	0.44	21.08	1.21	13.39	5.74
FeO	3.19	0.24	1.26	0.14	2.02	0.29	1.76	0.39	3.68	0.05	8.68	0.62	3.61	0.62
NiO	0.21	0.02	0.19	0.16	0.14	0.02	0.13	0.03	0.20	0.02	0.14	0.03	0.12	0.01
MgO	36.33	0.46	33.86	0.70	35.01	0.75	34.94	1.41	35.25	0.25	27.11	2.37	34.97	3.10
CaO	0.02	0.02	0.04	0.02	0.01	0.01	0.01	0.01	0.02	0.02	0.86	2.15	0.13	0.02
Na_2O	0.02	0.02	0.06	0.01	0.14	0.03	0.10	0.02	0.00	0.00	0.03	0.02	0.01	0.02
Total	86.12	0.64	87.57	0.58	84.65	0.89	85.94	2.03	88.90	0.53	87.48	1.12	87.40	0.40
Si	6.797	0.194	6.125	0.158	6.516	0.101	6.580	0.291	6.722	0.098	5.697	0.126	6.249	0.670
Cr	0.518	0.069	0.340	0.156	0.135	0.120	0.572	0.185	0.631	0.025	0.013	0.013	0.304	0.084
Al	1.714	0.231	3.809	0.303	2.876	0.086	2.490	0.643	2.152	0.092	4.817	0.271	2.989	1.300
Fe^{3+}	0.163	0.116	0.000	0.000	0.087	0.105	0.005	0.015	0.000	0.000	0.028	0.078	0.211	0.069
Fe^{2+}	0.350	0.140	0.197	0.021	0.239	0.085	0.279	0.069	0.579	0.007	1.379	0.120	0.359	0.095
Ni	0.032	0.003	0.028	0.024	0.022	0.003	0.020	0.005	0.030	0.003	0.022	0.005	0.018	0.002
Mg	10.411	0.113	9.469	0.174	10.067	0.130	10.008	0.217	9.878	0.041	7.833	0.680	9.836	0.770
Ca	0.004	0.002	0.007	0.004	0.002	0.001	0.002	0.002	0.003	0.003	0.178	0.446	0.026	0.005
Na	0.006	0.007	0.022	0.005	0.052	0.009	0.039	0.009	0.001	0.001	0.013	0.008	0.004	0.006

Table II.7: Representative E.P.M.A analyses of chlorite. Recalculation assuming 20 cations, 28Ox and 16 OH sites.

II.1.5. Bulk-rock compositions

II.1.5.1. Major elements and minor transition metals

There is no systematic variation of major elements as a function of the loss on ignition, which ranges from 0.3 to 5.6 wt% and is notably low in some of the olivine-rich rocks (Table II.8). X_{Mg} values in Meta-harzburgites and dunites overlap ($X_{Mg}^{harzburgites}$ = 0.913 – 0.923; X_{Mg}^{dunite} = 0.909 – 0.936), with the highest X_{Mg} in dunites (Fig. II.12). The coarse dunites of the crust-mantle transition zone are significantly higher in MgO content (47.3-50.3 wt %, in all samples except for D10 (Fig. II.2D) which has 43.8 wt %) than the 'faceted' dunites (42.3-45.2 wt %). Cr and Ti content are correlated with the proportion of spinel, with a maximum of 7.2 wt % Cr_2O_3 and 162 ppm Ti (sample D10). MnO and FeO contents are relatively constant with increasing MgO content, whereas Al_2O_3 and CaO are negatively correlated with MgO. Sc, V, Co, and Cu are negatively correlated with MgO content, whereas Ni contents increase with increasing MgO. Zn and Co concentrations are all approximately 50 ppm and ≤ 136 ppm, respectively (Fig. II.13).

Pyroxenites have a restricted range of X_{Mg} (0.889 – 0.906; Fig. II.12). Ca, Ti, and Fe contents vary dramatically between samples. Al, Cr and Mn vary to a far lesser extent. These variations reflect different modal proportions of clinopyroxene, olivine and spinel in pyroxenite and are also seen in the concentration of transitional metals Sc, V, Co, Cu, Zn and Ni (Fig. II.13).

Meta-gabbros are distinguished from all other rock types by lower X_{Mg} (0.816<$X_{Mg}^{meta-gabbro}$<0.897; Fig. II.12) and highest Al contents (around 17 wt% Al_2O_3). Ca, Al and Cr decrease gently with decreasing X_{Mg}, whereas Mn, and Fe content increase. Nevertheless, the high CaO and Al_2O_3 concentrations in combination with low SiO_2 values exclude that the gabbros represent true melt compositions, the original melt compositions being modified by cumulative and/or metasomatic processes. Transitional metals (Fig. II.13) have a different behaviour. Sc and V significantly increase with decreasing X_{Mg}, whereas Zn abruptly decreases between an X_{Mg} of 0.897 and 0.881 (from 38.8 to 19.4 ppm). Co and Ni are rather constant, and the high Cu content of the most differentiated meta-gabbro is probably due to an undetected Cu-phase. The most differentiated meta-gabbro (X_{Mg}=0.816) has a strong enrichment in Ti (1058 ppm), likely due to the presence of Ti-oxide.
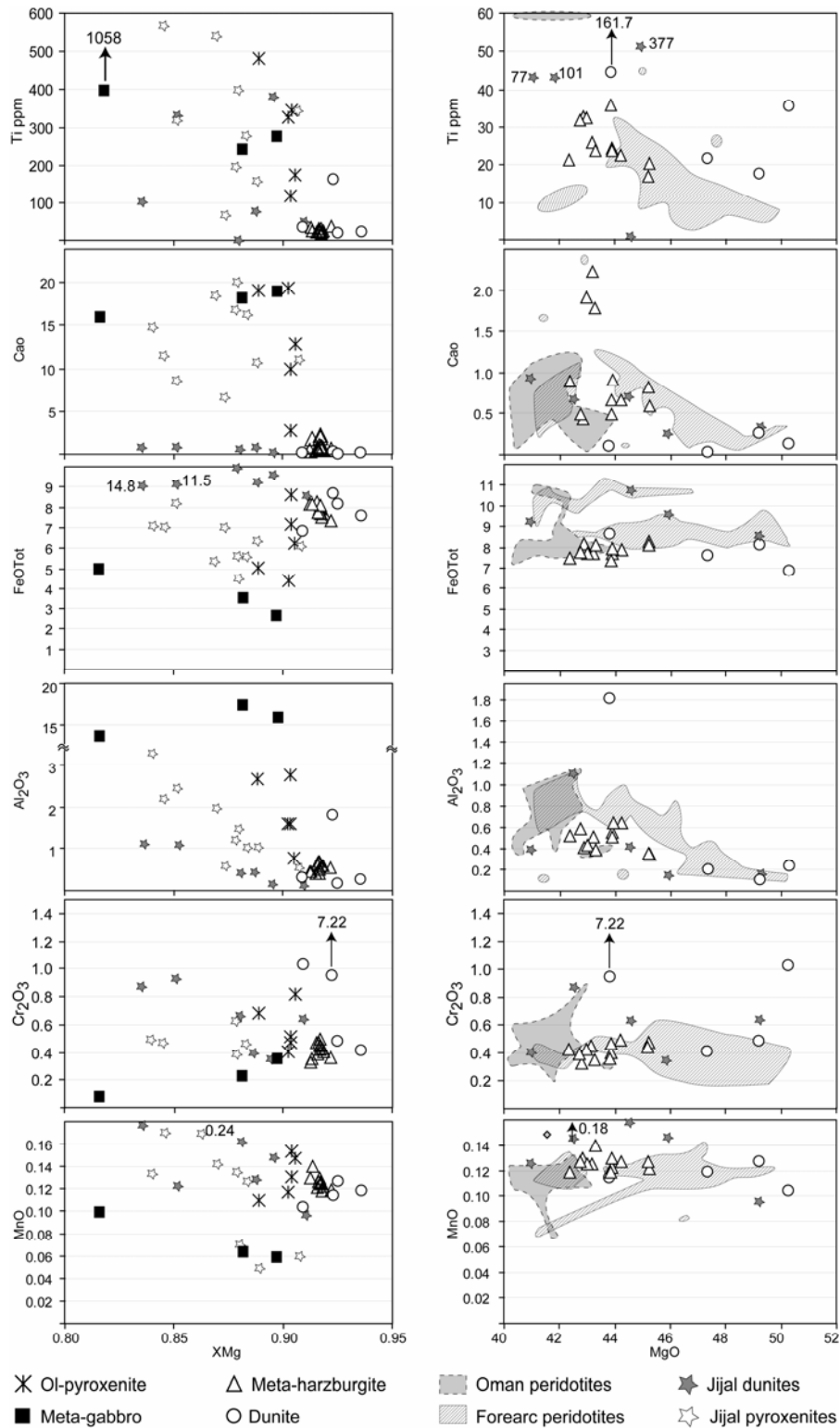
Figure II.12: Left: Bulk-rock major element compositions versus X_{Mg}. Right: Bulk-rock major element compositions versus MgO of Sapat meta-harzburgites and dunites. Other harzburgites and dunites: Forearc from the Sandwich Island (Pearce et al., 2000) and Marianna (Parkinson and Pearce, 1998); Oman ophiolites from Godard et al. (2000). Jijal samples are from Dhuime et al. (2007), pyroxenites = wehrlites, websterites and clinopyroxenites.
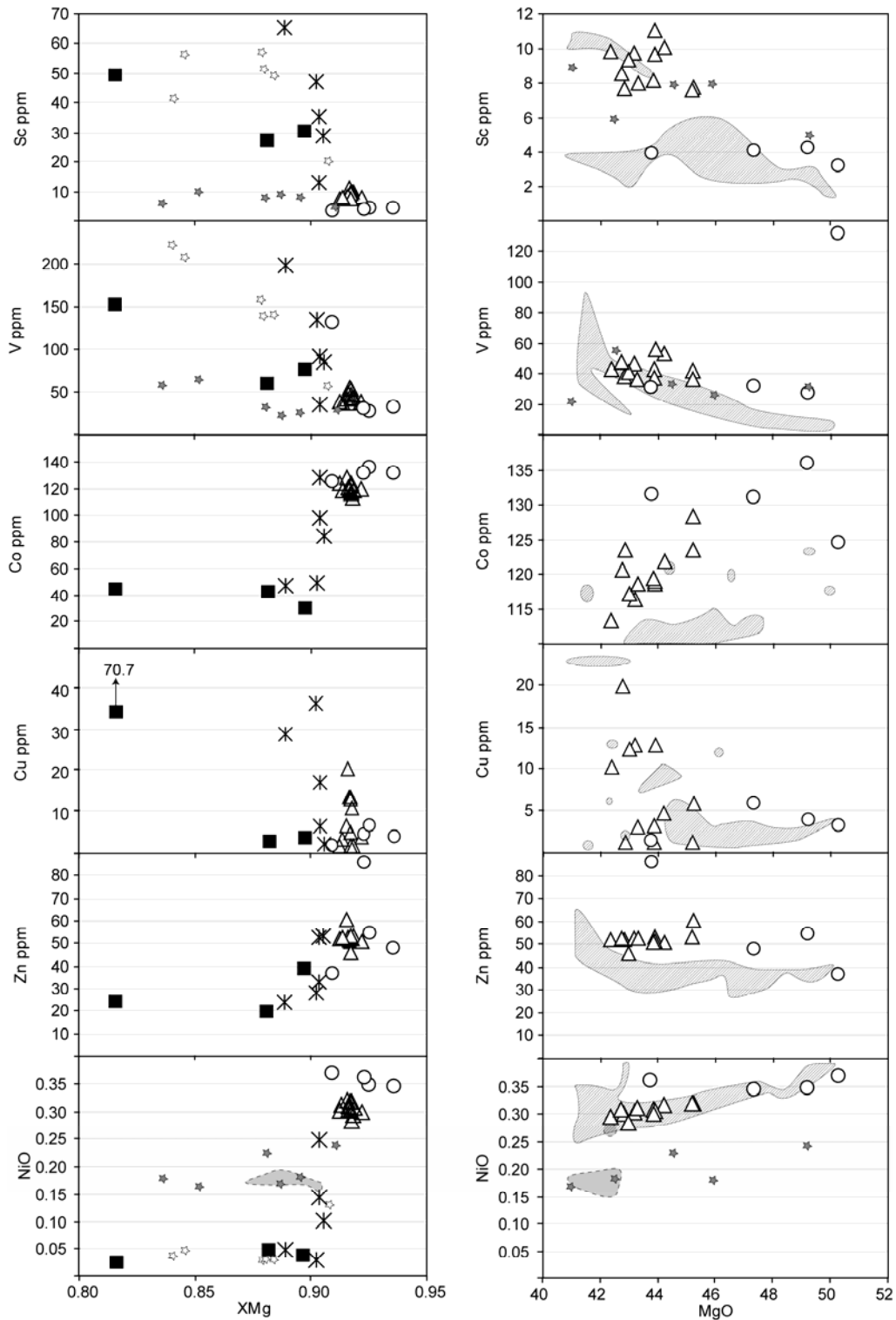
Figure II.13: Left: Bulk-rock minor transition metal compositions versus X_{Mg}. Right: Bulk-rock minor transition metal compositions versus MgO of Sapat meta-harzburgites and dunites. Same Legend as in Fig. II.12.

II.1.5.2.   REE and other trace elements

Meta-harzburgites and dunites display similar, U-shaped chondrite-normalized REE patterns (Fig. 13a), marked by a highly fractionated heavy REE (HREE) to medium REE (MREE) segment ($Lu_N/Tb_N = 4.5-38.1$) and significant enrichment of light REE (LREE) relative to middle REE (MREE) ($La_N/Sm_N = 1.2-4.5$). In spite of their more refractory (olivine-dominated) composition, the dunites are indistinguishable from the harzburgites with respect to LREE and HREE concentrations (Fig. II.14a). However, they are less depleted in MREE relative to LREE and HREE than the harzburgites; the Lu_N/Tb_N ratio is in range 5.5-6 in dunites, compared to 8-9 in the transitional sample D9 (Fig. II.2D), and 11-38 in harzburgites. When normalized to primitive mantle (Fig. II.14b), the highly incompatible elements Rb, Ba, Th and U are enriched with respect to REE and plot on an extension of the enriched LREE segment. Cs and Pb are selectively enriched, by factors of 50-100, relative to trace elements with a similar degree of incompatibility. Moderate enrichment in Sr is noticed in all samples, three meta-harzburgites excepted. Most samples are depleted in Zr relative to Hf and MREE, and in Nb relative to Ta and LREE.

With few exceptions, Zr/Hf and Nb/Ta ratios are subchondritic and Nb/Ta ranges from 3.6 to 10.4, compared to a chondritic value of 17.5, (except for 3 meta-harzburgites that have Nb/Ta = 20.4-23.5). Dunite D50 (Fig. II.2D) is anomalously enriched in HREE, Y, Nb and U whereas the chromite-rich dunite D10 (Fig. II.2D) is strongly enriched in Ti, Nb and Ta, which could be attributed to Nb-rutile associated with spinel (Bodinier et al., 1996).

Pyroxenites and meta-gabbros show similar, 'N-MORB-type' REE patterns (Fig. II.15a) marked by a flat HREE segment at 0.5-5 times chondrite abundances combined with LREE depletion ($La_N/Sm_N = 0.12-0.33$; Fig. II.14a). REE abundances roughly increase with decrasing X_{Mg} from the pyroxenite D17 ($X_{Mg} = 0.906$) to the meta-gabbro D104 ($X_{Mg} = 0.816$).

The meta-gabbros further differ from pyroxenites by subtle but significant positive anomalies of Eu, suggesting that the gabbros do not correspond to true melt compositions but are rather plagioclase cumulative. When normalized to primitive mantle (Fig. II.15b), the abundances of the highly incompatible elements Rb, Ba, Th

Figure I.14: Meta-harzburgites and dunites; a) Chondrite normalized Rare Earth Element patterns. b) Bulk-rock Primitive normalized trace element patterns. Chondritic and primitive mantle values from Sun and McDonough (1989). Grey array = dunites from Jijal (Dhuime et al., 2007)
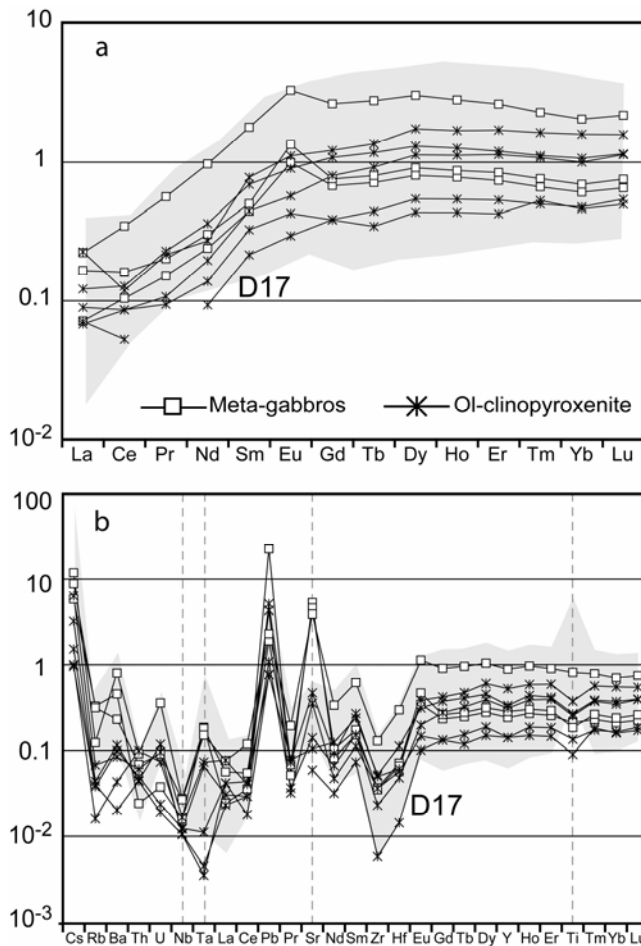
Figure II.15: Pyroxenite and meta-gabbro trace element compositions a) Chondrite normalized Rare Earth Element patterns; b) Bulk-rock primitive normalized trace element patterns. Chondritic and primitive mantle values from Sun and McDonough (1989). Grey array = wehrlites, websterite and clinopyroxenite from Jijal (Dhuime et al., 2007)

and U in pyroxenites are at about the same level as LREE, whereas the gabbros are significantly enriched, notably in Ba. Sr shows positive anomalies in most samples. Like peridotites, all pyroxenites and meta-gabbros show prominent spikes for Cs and Pb. Compared to peridotites, however, pyroxenites and meta-gabbros are more depleted in Zr and Nb relative to the other incompatible elements. They also tend to be depleted in other high field-strength elements (HFSE) such as Ti, Hf, as well as Ta in a few pyroxenites. Like most peridotites, pyroxenites and meta-gabbros are characterized by subchondritic Zr/Hf ratios and most of them have very low Nb/Ta ratios (2.2-3.9). Three pyroxenites, however, display surprachondritic Nb/Ta values (19.3-51.6).

II.1.6. Discussion

II.1.6.1. *Provenance of the harzburgites*

Structural and textural evidence indicates that the meta-harzburgites are the oldest ultramafic lithology of the Sapat massif. These rocks show high-temperature microstructures typical of mantle deformation. The most magnesian olivine ($X_{Mg} \sim 0.91$) with high Ni contents (Fig. II.7) is associated with spinel of medium to high-Cr and low-Ti contents (Fig. II.8), implying highly refractory compositions and a high degree of melt extraction, i.e. 30% within the OSMA array of Arai (1994). While melt extraction

Unit				Meta-harzburgite						Meta-harzburgite		
Sample	D87	D11'	D90	D89	D67	D88	D9	D56	D55	D83	D53	D85
SiO2	42.34	42.08	43.53	44.49	41.98	42.09	41.93	41.91	41.85	41.95	41.50	42.44
TiO2	0.009	0.008	0.009	0.009	0.010	0.011	0.009	0.010	0.010	0.010	0.009	0.008
Al2O3	0.346	0.350	0.636	0.644	0.557	0.505	0.391	0.512	0.426	0.414	0.584	0.521
Fe2O3	9.18	8.98	8.77	8.79	8.56	8.17	9.03	8.59	8.53	9.04	8.61	8.33
MnO	0.121	0.127	0.127	0.130	0.123	0.119	0.140	0.125	0.125	0.129	0.127	0.119
MgO	45.23	45.20	44.21	43.91	43.88	43.85	43.29	43.18	42.98	42.85	42.74	42.36
CaO	0.597	0.829	0.665	0.907	0.668	0.489	1.779	2.223	1.910	0.434	0.487	0.889
Na2O	0.231	0.110	0.091	0.057	0.164	0.041	0.028	0.030	0.032	0.045	0.026	0.063
K2O	0.01	0.01	0.01	0.00	0.02	0.00	0.00	0.00	0.00	0.00	0.00	0.00
P2O5	0.01	0.01	0.01	0.01	0.01	0.01	0.01	0.01	0.01	0.01	0.01	0.01
Cr2O3	0.47	0.44	0.50	0.47	0.40	0.36	0.35	0.46	0.42	0.33	0.39	0.43
NiO	0.32	0.32	0.32	0.30	0.31	0.30	0.31	0.30	0.28	0.30	0.31	0.29
L.O.I	1.58	2.33	1.81	0.82	3.54	4.17	3.45	3.55	3.92	4.82	5.57	5.14
Total	100.44	100.78	100.68	100.54	100.21	100.11	100.72	100.91	100.50	100.33	100.36	100.61
X Mg	0.916	0.917	0.917	0.917	0.919	0.922	0.913	0.917	0.917	0.913	0.916	0.918
Sc	7.79	7.61	10.10	11.03	9.68	8.16	8.03	9.75	9.32	7.68	8.58	9.84
Ti	20.55	17.12	22.42	23.77	24.39	35.78	23.72	25.89	32.35	32.72	31.84	21.38
V	41.96	36.42	53.41	55.72	43.01	37.75	36.58	47.13	41.30	38.70	47.52	43.04
Co	128.41	123.47	121.87	119.02	118.65	119.44	118.48	116.26	117.13	123.51	120.57	113.36
Ni	2653	2491	2581	2467	2538	2506	2496	2405	2281	2467	2528	2337
Cu	5.78	1.14	4.56	12.79	1.14	3.05	2.95	12.89	12.32	1.10	19.94	10.17
Zn	60.65	53.33	51.03	51.39	52.98	50.76	52.50	52.40	45.93	51.77	52.52	51.98
Cs	0.0007	0.0636	0.0412	0.0161	0.3396	0.0111	0.0072	0.0322	n-d	0.0659	0.0259	0.0128
Rb	0.015	0.042	0.057	0.031	0.409	0.032	0.023	0.034	n-d	0.016	0.027	0.019
Ba	0.282	0.130	0.169	0.246	0.198	0.178	0.291	0.301	n-d	0.226	0.200	0.114
Th	0.0029	0.0052	0.0030	0.0044	0.0018	-	0.0045	0.0034	n-d	0.0046	0.0039	0.0034
U	0.0007	0.0007	0.0004	0.0008	0.0002	0.0006	-	0.0004	n-d	0.0007	0.0007	0.0003
Nb	0.0055	0.0065	0.0056	0.0046	0.0041	0.0050	0.0055	0.0042	n-d	0.0055	0.0047	0.0065
Ta	-	0.0002	-	0.0008	0.0005	-	-	0.0005	n-d	0.0015	0.0013	0.0003
La	0.0061	0.0135	0.0064	0.0149	0.0042	0.0074	0.0124	0.0094	n-d	0.0102	0.0083	0.0097
Ce	0.012	0.025	0.012	0.031	0.008	0.014	0.022	0.016	n-d	0.019	0.016	0.014
Pb	0.024	0.049	0.013	0.032	0.049	0.041	0.071	0.070	n-d	0.170	0.050	0.076
Pr	0.0015	0.0027	0.0013	0.0033	0.0011	0.0016	0.0029	0.0023	n-d	0.0022	0.0018	0.0016
Sr	0.338	0.335	0.176	0.259	0.055	0.046	0.378	0.932	n-d	0.308	0.036	0.181
Nd	0.0048	0.0112	0.0058	0.0104	0.0042	0.0056	0.0105	0.0064	n-d	0.0075	0.0076	0.0056
Zr	0.025	0.025	0.015	0.025	0.013	0.096	0.026	0.021	n-d	0.034	0.030	0.017
Hf	0.0005	0.0008	-	0.0009	0.0005	0.0029	0.0006	0.0006	n-d	0.0014	0.0009	0.0006
Sm	0.0015	0.0023	0.0012	0.0021	0.0010	0.0021	0.0035	0.0020	n-d	0.0028	0.0019	0.0015
Eu	0.0003	0.0006	0.0005		0.0003	0.0004	0.0015	0.0008	n-d	0.0007	0.0009	0.0004
Gd	-	0.0029	-	-	-	-	0.0044	-	n-d	0.0038	-	0.0009
Tb	0.0004	0.0006	0.0002	0.0005	0.0004	0.0006	0.0010	0.0005	n-d	0.0009	0.0006	0.0002
Dy	0.0049	0.0054	0.0035	0.0065	0.0066	0.0074	0.0110	0.0073	n-d	0.0098	0.0072	0.0036
Y	0.0492	0.0465	0.0582	0.0754	0.0768	0.0816	0.0879	0.0755	n-d	0.0852	0.0834	0.0348
Ho	0.0012	0.0019	0.0014	0.0022	0.0024	0.0024	0.0032	0.0023	n-d	0.0029	0.0024	0.0012
Er	0.0055	0.0070	0.0084	0.0109	0.0128	0.0105	0.0124	0.0121	n-d	0.0116	0.0123	0.0059
Tm	0.0013	0.0017	0.0022	0.0025	0.0027	0.0022	0.0027	0.0027	n-d	0.0026	0.0028	0.0016
Yb	0.0131	0.0140	0.0229	0.0261	0.0311	0.0233	0.0246	0.0253	n-d	0.0267	0.0278	0.0177
Lu	0.0033	0.0035	0.0056	0.0063	0.0061	0.0054	0.0055	0.0059	n-d	0.0066	0.0062	0.0042

Table II.8: Bulk-rock major and trace element compositions. Total iron has been analyzed as Fe_2O_3. Meta-harzburgites and dunites are classified with decreasing MgO content, pyroxenites and meta-gabbros are classified in decreasing X_{Mg} number.

Unit	Dunite				Pyroxenite					(Meta-gabbros)		
Sample	D49	D86	D50	D10	D17	D64	LD5	D15	D18	D25	LD10	D104
SiO2	40.41	40.39	40.47	34.97	46.96	44.49	39.51	50.73	48.89	44.57	40.80	47.02
TiO2	0.010	0.008	0.008	0.030	0.03	0.06	0.03	0.06	0.09	0.05	0.05	0.19
Al2O3	0.230	0.097	0.193	1.807	0.724	1.574	2.786	1.570	2.657	18.53	19.89	16.24
Fe2O3	7.57	9.03	8.40	9.61	6.97	7.95	9.55	4.91	5.59	2.91	3.84	5.49
MnO	0.103	0.127	0.119	0.114	0.148	0.131	0.154	0.117	0.110	0.058	0.061	0.098
MgO	50.28	49.22	47.34	43.78	30.35	33.94	40.70	20.62	20.31	11.56	13.00	11.09
CaO	0.036	0.102	0.254	0.134	12.89	9.96	2.74	19.32	19.05	18.82	17.90	15.94
Na2O	0.032	0.032	0.031	0.034	0.06	0.08	0.00	0.09	0.04	1.57	0.15	1.58
K2O	0.00	0.00	0.00	0.00	0.00	0.00	0.00	0.00	0.00	0.06	0.00	0.02
P2O5	0.01	0.01	0.01	0.00	0.01	0.01	0.01	0.01	0.01	0.01	0.01	0.01
Cr2O3	1.02	0.48	0.41	7.22	0.82	0.52	0.47	0.41	0.68	0.35	0.22	0.07
NiO	0.37	0.35	0.34	0.36	0.10	0.14	0.25	0.03	0.05	0.04	0.05	0.02
L.O.I	0.51	0.37	2.84	0.51	1.56	1.33	3.83	2.48	2.51	1.81	4.19	1.87
Total	100.59	100.22	100.43	98.57	100.62	100.18	100.02	100.33	99.97	100.33	100.17	99.63
X_{Mg}	0.936	0.923	0.925	0.909	0.906	0.904	0.904	0.902	0.889	0.897	0.882	0.816
Sc	3.21	4.20	4.05	3.94	29.05	35.59	12.90	46.90	65.30	30.45	26.90	48.90
Ti	35.67	17.68	21.52	161.75	174.87	344.80	117.32	325.84	482.42	273.27	238.99	1059
V	31.55	30.60	27.36	131.16	85.13	90.87	34.56	135.74	198.50	74.40	58.96	152.47
Co	124.48	135.91	131.11	131.36	84.03	98.27	128.16	49.42	46.75	28.69	41.50	42.58
Ni	3082	2804	2878	2651	789	1122	1489	231.6	288.4	272.0	284.5	129.2
Cu	3.14	3.85	5.68	1.28	1.61	6.10	16.99	36.28	28.88	3.38	1.67	70.70
Zn	36.68	54.24	47.91	85.68	53.30	33.35	52.59	28.13	24.10	38.78	19.37	23.82
Cs	0.0084	0.0090	0.0064	0.0094	0.0076	0.0121	0.0079	0.0500	0.0257	0.0462	0.0931	0.0695
Rb	0.036	0.015	0.020	0.029	0.024	0.026	0.010	0.043	0.028	0.207	0.078	0.198
Ba	0.262	0.126	0.225	0.260	0.698	0.141	0.303	0.589	0.806	3.165	5.586	1.603
Th	0.0039	0.0029	0.0052	0.0027	0.0042	0.0037	0.0084	0.0052	0.0038	0.0021	0.0078	0.0059
U	0.0005	0.0004	0.0019	0.0003	0.0005	0.0004	0.0016	0.0020	0.0025	0.0008	0.0074	0.0019
Nb	0.0068	0.0084	0.0249	0.0643	0.0089	0.0076	0.0087	0.0077	0.0119	0.0114	0.0198	0.0192
Ta	0.0006	0.0009	0.0012	0.0073	0.0005	0.0001	0.0027	0.0002	0.0030	0.0076	0.0074	0.0062
La	0.0098	0.0063	0.0108	0.0049	0.0166	0.0287	0.0211	0.0159	0.0533	0.0168	0.0389	0.0524
Ce	0.019	0.013	0.023	0.012	0.032	0.078	0.052	0.052	0.072	0.063	0.098	0.211
Pb	0.051	0.035	0.063	0.034	0.054	0.054	0.305	0.077	0.365	1.602	0.135	0.163
Pr	0.0022	0.0014	0.0029	0.0014	-	0.0216	0.0089	0.0101	0.0203	0.0143	0.0189	0.0533
Sr	0.204	0.277	0.268	0.532	1.26	2.21	7.43	2.96	9.82	111.59	96.79	82.43
Nd	0.0099	0.0063	0.0129	0.0064	0.0432	0.1675	0.0641	0.0907	0.1260	0.1110	0.1398	0.4520
Zr	0.033	0.037	0.049	0.093	0.033	0.105	0.050	0.068	0.118	0.067	0.077	0.272
Hf	0.0015	0.0011	0.0021	0.0018	0.066	0.585	0.407	0.258	0.560	0.415	0.393	1.441
Sm	0.0026	0.0023	0.0046	0.0026	0.0045	0.0347	0.0177	0.0149	0.0190	0.0221	0.0205	0.0912
Eu	-	0.0010	0.0008	0.0007	0.017	0.052	0.025	0.033	0.064	0.057	0.078	0.191
Gd	-	0.0021	-	0.0017	0.079	0.221	0.078	0.163	0.249	0.138	0.155	0.540
Tb	0.0006	0.0006	0.0017	0.0007	0.016	0.044	0.013	0.034	0.051	0.027	0.030	0.103
Dy	0.0067	0.0041	0.0155	0.0058	0.138	0.331	0.110	0.286	0.440	0.203	0.230	0.768
Y	0.0565	0.0326	0.1175	0.0482	0.64	1.51	0.64	1.40	2.37	1.09	1.28	4.04
Ho	0.0017	0.0011	0.0045	0.0019	0.0305	0.0714	0.0244	0.0633	0.0954	0.0438	0.0490	0.1589
Er	0.0054	0.0045	0.0154	0.0062	0.0880	0.1979	0.0698	0.1873	0.2809	0.1215	0.1387	0.4331
Tm	0.0012	0.0010	0.0030	0.0015	0.0127	0.0283	0.0134	0.0274	0.0415	0.0168	0.0193	0.0581
Yb	0.0128	0.0083	0.0256	0.0129	0.0806	0.1810	0.0781	0.1695	0.2693	0.1030	0.1170	0.3465
Lu	0.0025	0.0024	0.0053	0.0027	0.0137	0.0291	0.0126	0.0287	0.0400	0.0165	0.0191	0.0552

Table II.8 continues

explains the fractionated HREE trend (low MREE/HREE), substantial influx of enriched fluid/melt during partial melting (i.e. flux melting) is necessary to account for the enrichment of LREE relative to MREE (e.g. Vernieres et al., 1997). Some meta-harzburgites are distinguished by more fertile characteristics, notably lower X_{Mg} in olivine (0.87-0.88) and, occasionally, small amounts of now metamorphosed clinopyroxene. However, low X_{Mg} olivine contains as much Ni as high-Mg olivine, which suggests that meta-harzburgites were re-fertilized and thus do not represent a pristine mantle composition. Clinopyroxene from set #2 dykes, only found in meta-harzburgites, is now entirely metamorphosed and would be inherited from the melt/fluid percolation recorded in the U-shape REE pattern of the meta-harzburgite. Whether the extensive melting and influx of an enriched fluid or melt occur concomitantly, or during two distinct events cannot be resolved in this study. Secondly, the timing of melt extraction is unconstrained, and could either be ancient and unrelated to the Kohistan arc history, or may have occurred below the Kohistan arc during its formation.

The bulk compositions of the Sapat ultramafic rocks are highly refractory compared to abyssal peridotites and Oman ophiolites (e.g. Bodinier and Godard, 2005), which have much lower MgO and higher TiO_2 content. Melt extraction and subsequent LREE enriched metasomatism yield refractory characteristics and an evolution of major elements similar to those observed in present-day forearc harzburgites and dunites (Parkinson and Pearce, 1998; Pearce et al., 2000) (Fig. II.12). The transition metals (Fig. II.13) also show characteristics of forearc ultramafic rocks. Similar REE patterns have been reported for oceanic peridotites from the Izu-Bonin-Mariana, and Sandwich island forearcs (Parkinson and Pearce, 1998; Pearce et al., 2000) and for supra-subduction ophiolites (e.g. Bodinier and Godard, 2005; Zhou et al., 2005).

Mineral compositions of dunites and pyroxenites show variation trends (e.g., decreasing Ni in olivine and increasing Ti in spinel, with decreasing X_{Mg} from dunites to pyroxenites) that differ from typical primary minerals of meta-harzburgites. Moreover, secondary olivine and spinel within meta-harzburgites is compositionally similar to the olivine and spinel of pyroxenites. This would indicate that the melt which formed the dunites and pyroxenites infiltrated also the meta-harzbugites. Similarly, olivine transition metal compositions from dunites define differentiation trends (Fig. II.8) to which the primary meta-harzburgite olivine does not pertain, pointing to the fact that the primary mineralogy of the meta-harzburgites resulting from the first stage melt extraction, is older and unrelated to the dunite formation.

II.1.6.2. *Dunite, pyroxenite, and gabbro formation*

The trace element compositions of the melts parental to the meta-gabbros and pyroxenites were calculated from the trace element composition of clinopyroxenes using Kd's of Hart and Dunn, (1993) (Fig. II.10). The calculated parental melts show identical trace element patterns, and given the spatial and textural relationships described above, we consider that both the pyroxenites and gabbros derived from the same melt. This parental melt has a MORB like REE pattern (Fig. II.10) with flat HREE to MREE segments and a depleted LREE segment. This latter characteristics clearly distinguishes the parental melt of the pyroxenites and meta-gabbros from the fluid or melt responsible for the U-shape REE patterns of the meta-harzburgites. The REE pattern of the parental melt to the pyroxenites

is significantly more depleted than for oceanic and ophiolitic gabbros (e.g., by a factor of 5 to 20 for MREE, compared to gabbros of the Oman ophiolite with similar X_{Mg} values; Koga et al., 2001). Together with the low HFSE, high Cr and Ca contents of the pyroxenite and meta-gabbro suite and of the clinopyroxene, we suggest that this parental melt represents a primitive arc melt ($X_{Mg}^{melt} = 0.74$, in equilibrium with $X_{Mg}^{olivine} = 0.9$ of sample D64, Fig. II.2B, using the Kd of Ulmer, 1989). This primitive arc melt does not correspond to primitive arc tholeite or primitive andesite (Kelemen et al., 2003) but is comparable to some high-Ca boninites (e.g. Sobolev and Danyushevsky, 1994; Smellie et al., 1995; Bedard, 1999), consistent with the high Cr and low Al contents of spinels (Barnes and Roeder, 2001). Such melts are produced from a refractory source during high temperatures affecting a previously depleted mantle region, and are usually related to back-arc or forearc environments (Crawford et al., 1989).

The scenario involving the parental melts of pyroxenites as reactant for dunite formation is consistent with the pyroxenites and metagabbros forming a single differentiation suite on major- and trace-element covariation diagrams. Pyroxenites show a compositional range between a composition that is only slightly more fertile than the peridotites (MgO = 40.7, Al_2O_3 =2.78, CaO = 2.74, X_{Mg} = 0.903) and one that resembles the composition of the less evolved gabbros. This differentiation trend is further reflected by the clinopyroxene evolution, which mirrors the Al-enrichment in the melt with progressing crystallization of Al-poor clinopyroxene and olivine. Clinopyroxenes from thin dykes (set#1) and meta-harzburgite grain boundaries equilibrated with less evolved melts, whereas the lowest X_{Mg} and highest Al_2O_3 and TiO_2 clinopyroxenes are present in the meta-gabbros. In addition, secondary olivine and spinel of dunites are compositionally comparable to olivine and spinel in pyroxenites. Therefore, we suggest that the dunites formed first at the expense of meta-harzburgites, as described by Kelemen et al. (1995), and that this melt, which lead to the replacive dunites, then formed also the pyroxenites and meta-gabbros within a single suite of protracted dissolution and crystallization events.

The difference in REE composition observed between dunites and meta-harzburgites i.e $Lu_N/Tb_{N\ dunite} \ll Lu_N/Tb_{N\ meta-harz}$ would reflect the dunite formation process. Based on REE partitioning between olivine and orthopyroxene (e.g. Bedini and Bodinier, 1999), this implies that dunites formed from melts that were significantly more enriched in MREE, and to some degree in HREE, than the melts which equilibrated with the harzburgites. As discussed by Bodinier et al. (2008), selective MREE enrichment in mantle rocks is symptomatic of reactive porous flow at decreasing melt mass, due to the superimposed effects of a chromatographic fractionation due to melt transport and fractional crystallization resulting in incompatible element enrichment. Numerical simulations of reactive porous flow indicate that this process results in a gradual evolution from preferential MREE enrichment within the reaction domain to selective LREE enrichment at reaction fronts. The olivine-forming, melt-rock reaction invoked for the formation of mantle dunites is thought to occur at increasing melt mass, due to pyroxene dissolution (Kelemen et al., 1995). Hence, dunite formation should be associated with REE depletion rather than enrichment. In fact, the Sapat peridotites show widespread evidence for precipitation of secondary olivine unrelated to pyroxene dissolution, suggesting that olivine-saturated melts percolated through these peridotites. As has been suggested by Spiegelman et al. (2001), the dunites are likely to have focused

the parental melt of the pyroxenites and gabbros in high-permeability porous-flow channels. After initially precipitating only olivine, the percolating melts then saturated also in clinopyroxene leading to the formation of the wehrlite and pyroxenite layers that are spatially related to the dunites.

To simulate this process, we used the Plate Model of Vernières et al. (1997) in a configuration where a harzburgite column is first traversed by a reaction involving orthopyroxene dissolution and olivine precipitation at increasing melt mass. At this stage, the initial porosity (arbitrarily set at 1%) increases to a value that depends on the reaction stoichiometry (2.15% for the experiment shown in Fig. II.16). Then, once orthopyroxene is consumed, continuous melt infiltration is associated with olivine precipitation until the residual porosity renders melt infiltration ineffective. The initial REE composition of peridotite for this model is that of harzburgite D85, characterized by very low MREE contents and elevated HREE/HREE ratio ($Lu_N/Tb_N = 31$). The composition of the infiltrated melt is that of the theoretical melt in equilbrium with pyroxenite D21 (Fig. 10), which is close to the average composition of pyroxenite equilibrium melts when the strongly depleted sample D17 is disregarded. The model (Fig. II.16) satisfactorily accounts for the observed flattening of REE patterns from harzburgites to dunites: for residual porosities around 0.01%, the MREE (e.g., Gd) increase by a factor of three in the dunites while both LREE and HREE remain constant.
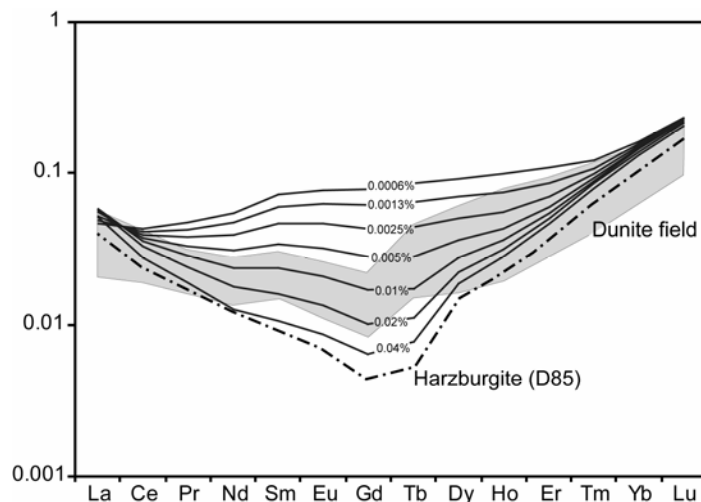
Figure II.16: Numerical simulation of REE variations in dunite formed at the expense of the harzburgite sample D85 via a melt-rock reaction involving complete opx dissolution, olivine precipitation and increasing melt fraction, followed by interstitial precipitation of olivine from percolating melt until closure of rock porosity. Calculation was performed with the 'Plate model' of Vernières et al. (1997), using a 40 reaction cells column. The 20 upper cells were affected by the olivine-forming reaction and the 20 bottom cells by further melt percolation and intersitial olivine crystallisation. Initial porosity set at 0.01%; porosity after the olivine-forming reaction = 2.15% (in cells 21 to 33 from bottom). Results shown for cells 9 to 15 from bottom (residual porosities = 0.0006 and 0.04%, respectively). Infiltrated melt composition: theoretical melt in equilbrium with pyroxenite sample D21 (see text). Mineral/melt partition coefficients as in Vernières et al. (1997). Grey array : analyzed dunites.

II.1.6.3. *Infiltration of slab derived fluids*

The Sapat chlorite+calcite+olivine+spinel paragenesis in the Ol_2-bearing veins in the dunites differs from parageneses formed during the late retrogression in e.g. alpine peridotites (Müntener et al., 2000). The concentrations of fluid mobile elements such as B in the vein olivines of the dunites (dunite-Ol_2 Fig. II.8) are much higher than in the primary olivines of the meta-harzburgites (Ol_1) and dunites (Ol, Table II.1). The Cr-clinochlore compositions found in Sapat are similar to those reported from kimberlitic pipes, where this mineral is ascribed to volatile-rich fluids reacting with mantle rocks (McGetchi et al., 1973) and to those from alpine peridotites equilibrated at 2.5 GPa and 800°C (Pfiffner, 1999) in a subduction setting.

Since Ol_2-bearing veins are only found in dunites, we consider that the fluids responsible for the Ol_2-Chl-Cal-Spl bearing veins are expelled from CO_2 and H_2O enriched small melt fractions residual after porosity closure in the dunites. As the dunite forming melts are generated within an arc context, most of the volatiles and LILE are ultimately slab derived.

II.1.6.4. *Comparison to the Jijal ultramafics*

Sapat meta-harzburgites represent a refractory mantle apparently absent in the Jijal complex, although some harzburgites have been mentioned there (Miller et al., 1991). Besides, the Jijal peridotites have major and trace element characteristics different from the Sapat peridotites. Jijal dunites have much lower X_{Mg} and MgO contents and show less refractory compositions (higher Ti, Al, Fe, Mn, lower Ni content); and enrichment in LREE is absent and the REE pattern is similar to abyssal peridotites and Oman dunites. The Jijal pyroxenites have much lower X_{Mg} and much higher Fe, Ti, Mn, and lower Ni contents than the Sapat pyroxenites. Even if Sapat and Jijal pyroxenites display comparable REE patterns, Jijal has much higher Ba and U contents (Fig. II.15). The Jijal complex does not display the most differentiated product of these reactions, the meta-gabbros present in Sapat. Finally, the pyroxenite/meta-gabbro parental melt identified at Sapat is different to the parental melt of Jijal pyroxenites (Garrido et al., 2007). All these differences suggest that Sapat and Jijal belong to different positions within an arc section, Jijal deriving most likely from a typical subarc mantle (Burg et al. 1998).

II.1.7. Conclusions

Mineral and bulk rock chemistry suggest that the Sapat meta-harzburgites represent a relict refractory mantle imprinted by an uncharacterized metasomatic event which is responsible for its U-shaped REE pattern. Whether this part of the history is linked to formation of the Kohistan arc is at present unconstrained. Dunites and pyroxenites forming the crust-mantle transition zone are the product of protracted reactions between the refractory mantle and the parental melt of pyroxenites and meta-gabbros. This parental melt was a highly-depleted primitive arc melt of supra-subduction affinity which shares similarities with other subduction related melts derived from refractory sources such as high Ca-boninites. The Sapat ultramafic sequence differs from the subarc Jijal ultramafic section and resembles fore-arc peridotites. Refractory mantle such as the Sapat ultramafics also occurs in back-arc regions, but the current position of the Sapat massif at

the front of the Kohistan arc excludes such an origin. Integrating the fact that upon cooling this mantle portion suffered extensive hydration by fluids of supra-subduction origin, and the structural occurrence of the massif in front of the Kohistan arc, we suggest that the Sapat ultramafic sequence and crust-mantle transition formed during a magmatic episode affecting the most frontal part of the Kohistan arc.

II.2.   Fluids of Subduction origin

II.2.1.   Introduction

High temperature gradients along slabs at convergent plate margins may induce carbonate destabilization and recycling (Molina and Poli, 2000), so providing carbonate in subduction-related melts and fluids. Although carbonaceous minerals, melts or fluids have been postulated to be involved in arc magma production (McInnes and Cameron, 1994; Laurora et al., 2001) they have yet to be identified in exhumed arc-mantle rocks. We examined olivine-magnetite-calcite-chlorite-serpentine bearing veins in the ultramafic rocks of Sapat (Kohistan / Pakistan, Fig. II.17) and found that they contain both a slab signature and a mantle component. Such slab-derived fluids are characterized (i) by their B isotopic composition, to the point that B concentration and isotopic ratios are used to quantify fluid flux in the mantle wedge (Morris et al., 1990) and (ii) by their Nb-Ta signature, i.e. by two high field strength elements (HFSE) whose depletion with respect to similarly incompatible elements characterizes arc magmas. Variable Nb/Ta values in arc magmas (Stolz et al., 1996; Munker, 1998) are mostly ascribed to residual slab phases that explain their variations (Tiepolo et al., 2000; Green and Adam, 2003). However, Nb and Ta, which have very similar atomic and ionic radii (~0.143 nm and 0.07 nm, respectively), are geochemically close and difficult to fractionate (Jochum et al., 1986). It was therefore suggested (Rudnick et al., 1993; Hervig et al., 2002) that Nb/Ta variations and B isotopic fractionation could be influenced by carbonated fluids.
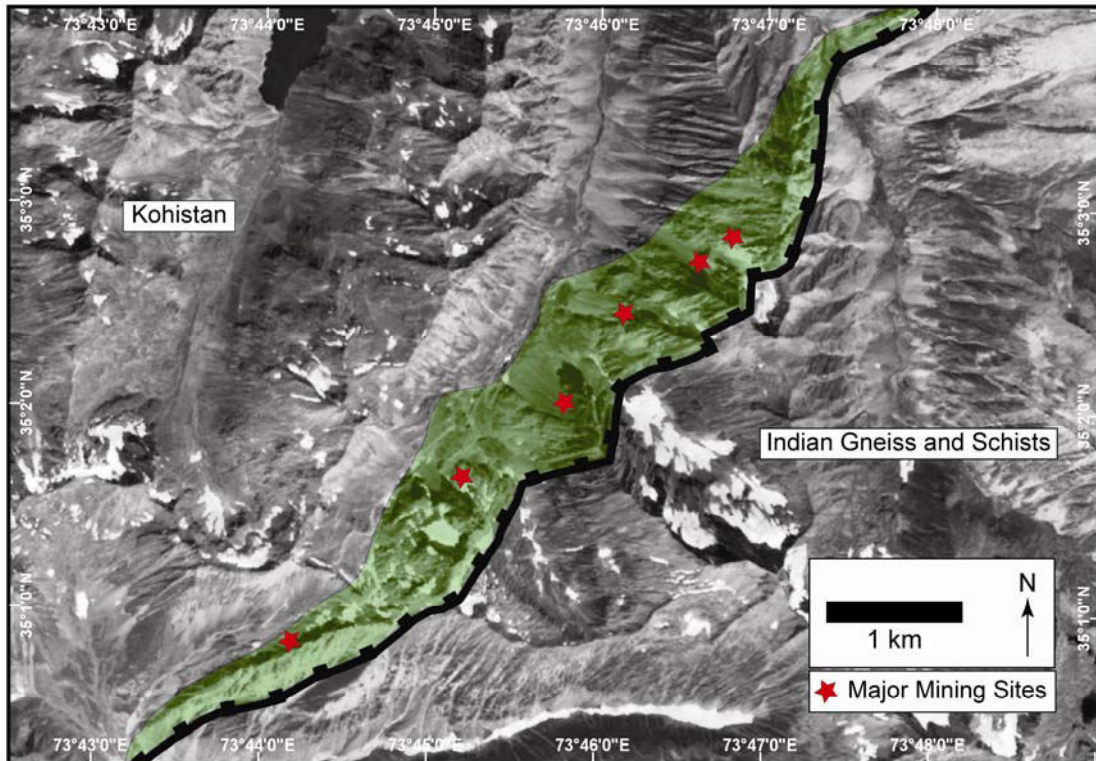
Figure II.17: Major mining sites in the ultramafic rocks (green) of Sapat. Background satellite image from SPOT.

II.2.2.   Occurrence and paragenesis

The Kohistan terrane, between the Karakoram–Kohistan Suture to the north and the Indus Suture to the south, have been an island arc active during Mesozoic times (Bard, 1983; Coward et al., 1987). The Sapat peridotites represent a part of the supra-subduction mantle on the southern boundary of this terrane (Bouilhol et al., 2008). Steeply-dipping, approximately N-S-striking tension gashes occur solely in the dunites of the subarc crust-mantle transition zone (Figs. II.2, II.3, II.17, II.18, II.19).
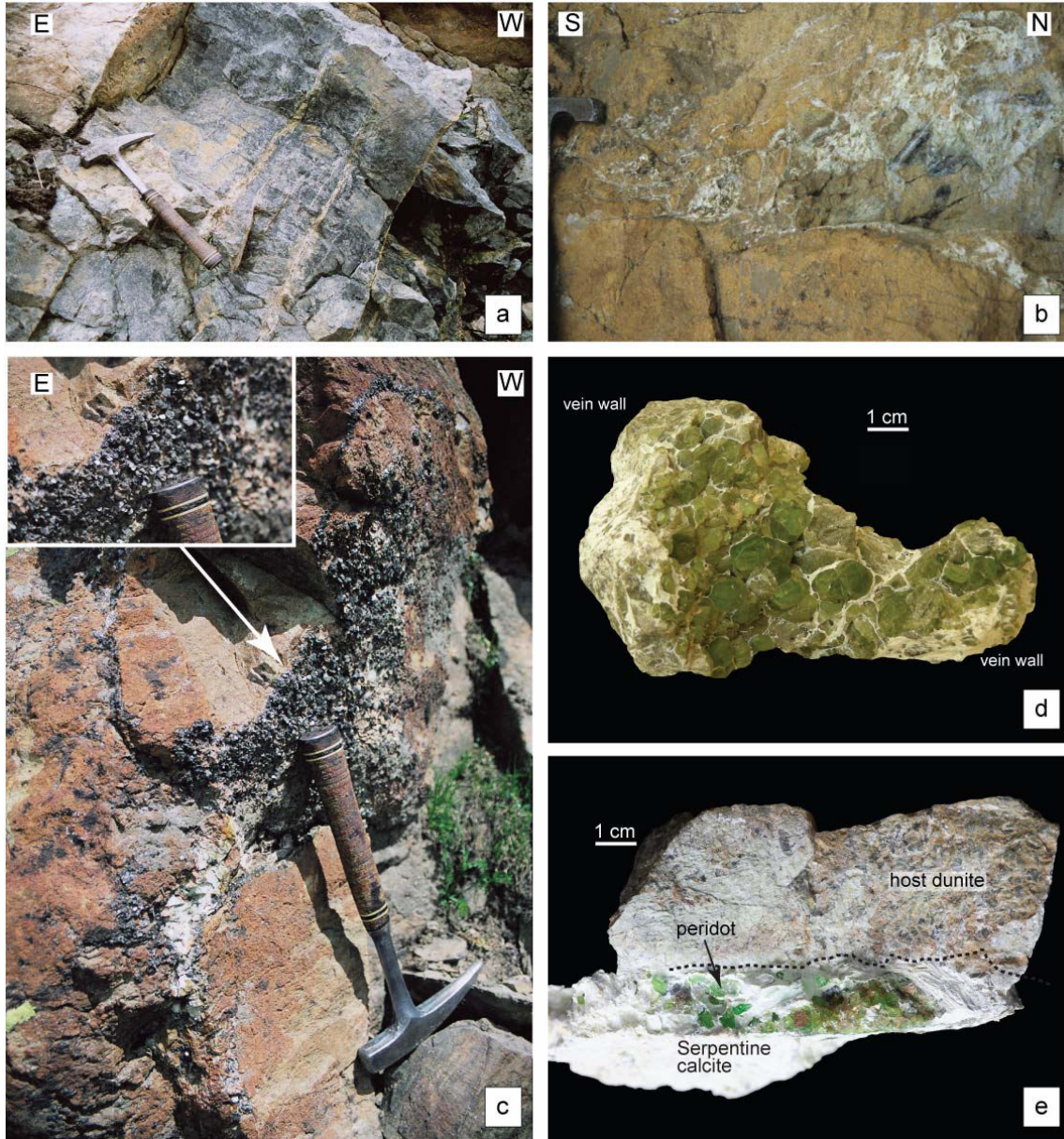
Figure II.18: a) Olivine-bearing tension gash. b) Brecciated dunite with gems in filled welding fractures. c) Vein with diffuse boundary and with antitaxial chlorite growth. d) J.M. Dautria's collection specimen, with gem olivine "bridging" the opposed vein walls. e) Hand specimen of olivine-bearing vein.

The few centimeters to several meters long and few millimeters to tenth of centimeters wide veins are associated with chromite schlieren in the dunite. The host dunite is usually fresh, most vein walls are sharp, but some diffuse vein boundaries with centimeter-wide alteration zones suggest reaction with the host dunite (Fig II.18).

Minerals of the primary vein assemblage, olivine-magnetite-calcite-chlorite-serpentine, are epitaxial; gem-quality olivine crystals (Fig. II.19a, b, c) are mostly enclosed in serpentine (Fig. II.18e) but also occur as antitaxial crystals. Brucite, lizardite and second generation calcite intergrown with serpentine or forming recrystallization rims (Fig II.19f) are remobilized products of the primary vein phases, as indicated by corrosion of primary crystals by the late lizardite-brucite matrix.
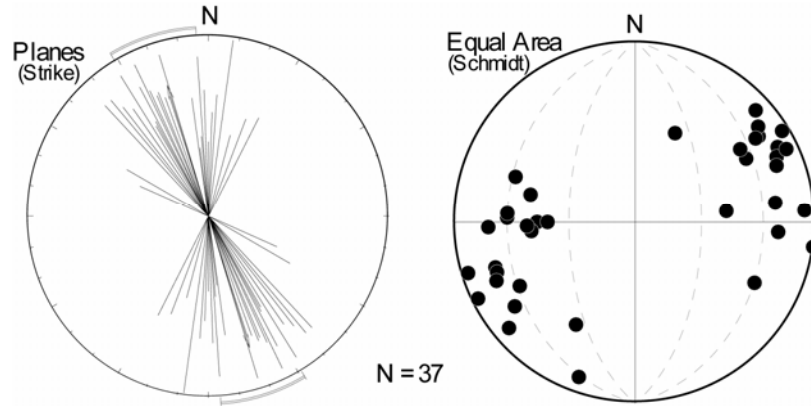
Figure II.19: Lower Hemisphere projection of 37 gem olivine-bearing veins: strike and dip measurements.

II.2.3.   Phases trace and isotopic composition

Vein-euhedral calcite grains may contain magnetite, olivine, serpentine, elemental copper and silver and fluid inclusions; they are not zoned and have a restricted range in isotopic composition: $9.44 < \delta^{18}O$ SMOW< 11.79 ‰ and $-3.98 < \delta^{13}C$ VPDB < -0.50 ‰ (Fig. II.20). These values exclude a meteoric or metamorphic origin and match a two-component mixing of a mantle ($\sim \delta^{18}O= 8$‰, $\delta^{13}C= -5$‰) and a sedimentary carbonate end-member ($\sim \delta^{18}O=15$‰, $\delta^{13}C= 0$‰) i.e. slab-related contamination of the mantle from which the calcite-forming fluids originated. Some euhedral vein calcites have an Mg-poor recrystallized rim high in $\delta^{13}C$ and $\delta^{18}O$. Calcite crystals intergrown with serpentine fibers (CAF and CAS, Fig. II.19, 20) have higher $\delta^{13}C$ (0.91-0.99 ‰) for the same $\delta^{18}O$ than euhedral vein crystals. The $\delta^{13}C$ and $\delta^{18}O$ compositions of all calcites (Fig. II.20, Table II.9) indicate a trend from euhedral calcite through serpentine intergrowth calcite to rim calcite at lower temperature (200-250 °C) crystallization. Euhedral calcite (CA2, CAZcore) and the second generation calcite (CAZrim) have similar Sr isotopic values (Fig. Fig. II.19, 20; Appendix 3). However, the most primitive calcite (CAP) has slightly lower isotopic values ($\delta^{13}C = -3.98$, $\delta^{18}O= 11.8$; $^{87}Sr/^{86}Sr = 0.77705449$ (40)) close to that of EM1 (Enriched Mantle). These Sr isotopic compositions corroborate the C and O isotopic signatures of a slab-contaminated mantle origin. They further indicate that rim calcite is a direct remobilization product of euhedral calcite.
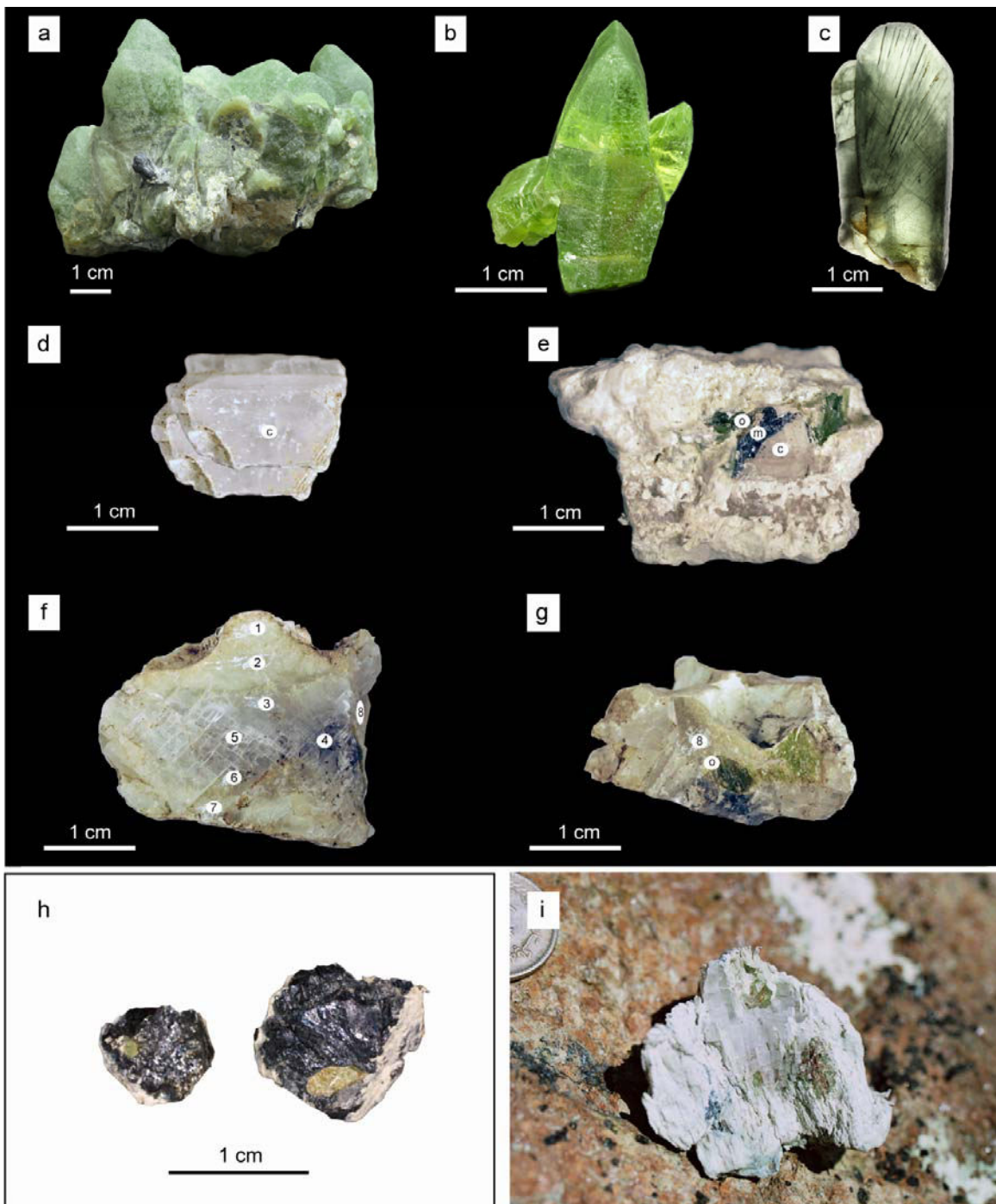
Figure II.19: Mineral specimens. a) Antitaxial group of olivine. b) gem olivine with two amalgamated crystals. c) gem olivine with borates needles (ludwigite-vonsenite). d) Euhedral calcite crystals (sample CAB). e) euhedral calcite with magnetite and olivine as inclusions (sample CAG). Crystal embedded in serpentine. f) euhedral calcite crystal with recrystallization rims (sample CAZ). g) other face of sample CAZ, with olivine as inclusion. h) euhedral magnetites with olivine inclusions. i) Fibrous calcite-serpentine intergrowth with olivine inclusions (sample CAF). All number spots on minerals represent analysis points (Table II.9)

Sample	Mineral	$\delta^{18}O_{SMOW}$ ‰	Sample	Mineral	$\delta^{18}O_{SMOW}$ ‰	$\delta^{13}C_{VPDB}$ ‰
MO1-O	olivine	5.70	CAP	calcite	12.94	-4.25
	olivine	4.25		calcite	10.65	-3.70
MO1-M	magnetite	-0.07	CAG	calcite	21.30	3.25
CAG-M	magnetite	-0.71	CAO	calcite	10.87	-1.37
OGIB	olivine	5.01	CAN1	calcite	10.68	-1.34
CAG-O	olivine	5.08	CAN2	calcite	10.71	-1.44
OG	olivine	5.22	CAB1	calcite	9.50	-1.86
OGM	olivine	6.30	CAB2	calcite	9.44	-1.94
	olivine	4.47	CAB3	calcite	9.51	-1.86
MO1-O	olivine	4.90	CAS	calcite	9.92	0.91
OG1	olivine	4.44	CAF	calcite	9.72	1.00
O1	olivine	4.63	CAZ1-rim	calcite	15.52	4.70
Ogi	olivine	5.42	CAZ2	calcite	12.02	-0.54
CAZ-O	olivine	5.04	CAZ3	calcite	10.49	-2.17
	olivine	4.66	CAZ4	calcite	10.65	-2.39
MO2-O	olivine	5.40	CAZ5	calcite	10.59	-1.99
MO2-M	magnetite	-0.16	CAZ6	calcite	10.63	-1.93
			CAZ7-rim	calcite	16.05	4.61
			CAZ8	calcite	10.61	-1.94
			CAZ9	calcite	10.45	-2.10
			CAST rim	calcite	12.35	0.65
				calcite	10.61	-1.60
				calcite	10.81	-1.39
				calcite	10.99	-1.49
				calcite	11.17	-1.28
				calcite	11.50	-1.21
				calcite	10.60	-1.84
				calcite	11.07	-1.47
				calcite	11.22	-1.60
				calcite	11.33	-1.21
			S2	calcite	9.75	-1.35
				calcite	10.12	-1.01
			S2rim	calcite	12.73	3.03
			Ca	calcite	10.18	-1.57
				calcite	10.04	-1.52
				calcite	9.91	-1.60
				calcite	9.90	-1.62
				calcite	9.92	-1.58
			Ca1	calcite	9.78	-1.63
				calcite	9.71	-1.60
				calcite	9.63	-1.63
			Ca2	calcite	9.66	-2.26
				calcite	9.24	-2.28

Table II.9: Isotopic compositions dataset. Left: O isotopic compositions of olivine and magnetite. Right O and C isotopic composition of calcites

The REE pattern of the most pristine euhedral calcite (CAP, Fig. II.21a) shows a strong enrichment in La and Ce, Pb, Cu and Zn, and an extreme Nb-Ta fractionation (Nb/Ta= 0.18, Fig.II.21b and Table 9). The enrichment in Sr and Ba and the strong depletion in Ti, Zr and Hf reflect the ability of the calcite structure to incorporate these elements.
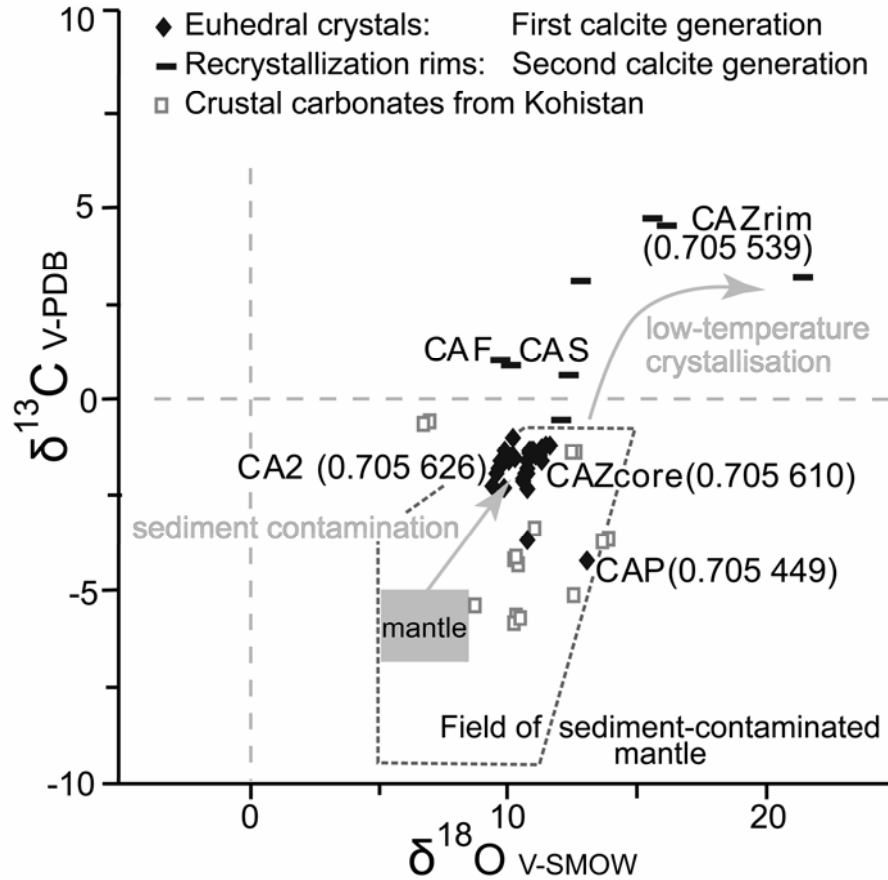
Figure II.20: $\delta^{13}C$ versus $\delta^{18}O$ of analyzed calcite. Kohistan crustal carbonates for comparison from (Yoshino and Satish-Kumar, 2001). CAS and CAF = fibrous calcite grown with serpentines; CAP, CAZ and CA2 = euhedral crystals. $^{87}Sr/^{86}Sr$ values in bracket. Field of sediment-contaminated mantle corresponds to primary carbonatitic field of (Ray and Ramesh, 1999). Reference box for mantle from (Ray and Ramesh, 1999).

The vein chlorite is a chromium-rich clinochlore (2.98-5.89 wt% Cr_2O_3) with high NiO contents (0.17-0.24 wt %). Clinochlore is included in olivine and occurs also in the vein matrix. Cr-clinochlore is extremely depleted in almost all trace elements except a notable enrichment in B, Cs, and Pb (Appendix 3). Chlorites with Cr-contents comparable to the Sapat clinochlore were found in kimberlitic pipes where chlorite results from reactions between fluids and mantle rocks, involving carbonatite genesis (McGetchi et al., 1973), and in alpine peridotites that recrystallized in a subduction setting (Pfiffner, 1999). The high chromium content of Sapat clinochlore indicates crystallization from a fluid equilibrated with a mantle.

The Sapat vein-olivine is transparent and one of the best quality worldwide. Single vein euhedral crystals, commonly several centimetres in size (Fig. II.19a, b, c), are often imbricated with euhedral magnetite and contain Fe-Mg borates (ludwigite-vonsenite solid

Mineral	gem-ol.	gem-ol.	gem-ol.	gem-ol.	gem-calcite
Sample:	OG	Ogi	OGM	OG1	CAP
Cs	0.0028	0.0027	0.0035	0.0025	0.0100
Rb	0.0027	0.0013	0.0052	0.0011	0.0093
Ba	0.0455	0.0634	0.0430	0.1077	5.5787
Th	0.0042	0.0088	0.0186	0.0008	0.0005
U	0.0007	0.0012	0.0029	0.0004	0.0003
Nb	0.00633	0.01124	0.00563	0.01314	0.00277
Ta	0.00038	0.12885	0.00100	0.11673	0.01498
La	0.00188	0.22297	0.00144	0.16641	0.17700
Ce	0.00258	0.67494	0.00182	0.48622	0.55957
Pb	0.0520	0.1701	0.0548	0.2040	0.2345
Pr	0.00030	0.00104	0.00026	0.00072	0.00737
Sr	0.01820	0.06744	0.02372	0.07204	36.585
Nd	0.00343	0.06097	0.00358	0.04512	0.11253
Sm	0.00142	0.00186	0.00090	0.00139	0.05500
Zr	0.0424	0.0686	0.0507	0.0473	0.0264
Hf	0.00131	0.00144	0.00109	0.00126	0.00023
Eu	0.00043	0.00045	0.00034	0.00047	0.03520
Gd	0.00079	0.00061	0.00096	0.00035	0.11411
Tb	0.00008	0.00027	0.00007	0.00020	0.02337
Dy	0.0028	0.0072	0.0014	0.0038	0.2293
Y	0.0467	0.1646	0.0073	0.0522	1.7595
Ho	0.0015	0.0051	0.0002	0.0018	0.0569
Er	0.0163	0.0503	0.0022	0.0180	0.1867
Ti	8.79	3.47	3.12	5.12	2.64
Tm	0.00590	0.01583	0.00099	0.00694	0.02501
Yb	0.0671	0.1380	0.0101	0.0811	0.1434
Lu	0.0147	0.0244	0.0027	0.0186	0.0199
Li	5.67	2.12	2.14	11.02	0.32
Cu	0.78	207.61	8.08	181.52	210.97
Zn	16.47	139.14	17.02	151.98	127.20
Nb/Ta	16.49	0.09	5.66	0.11	0.18
Zr/Hf	32.39	47.73	46.31	37.71	112.73

Table II.10: Trace element compositions of vein olivine and vein calcite

solution). Microprobe analyses of olivine crystals demonstrate a patchy compositional distribution with a wide range in X_{Mg} (0.89-0.97) without any correlation with NiO contents ranging from 0.22 to 0.88 wt%. For further analyses, several olivine crystals were crushed and fragments were optically examined under the binocular for the presence of inclusions. Inclusion-free fragments were hand-picked and analyzed for their oxygen isotopic composition, which ranges from $\delta^{18}O$ = 4.35‰ to 6.40‰ (Table II.9). Analyses of several fragments from the same olivine grain show that the isotopic composition is heterogeneous within each single grain. Nevertheless, the averages for single grains and for all measurements ($\delta^{18}O$ = 5.03(55) ‰) are within the mantle array (Mattey et al., 1994), hence reflect origin from fluids equilibrated in the mantle. Coexisting magnetite has isotopic compositions ranging from $\delta^{18}O$ = -0.60 to 0.20‰ (Table II.9), and O-isotope thermometry on olivine-magnetite pairs yields 450-500 °C as a temperature of vein formation.
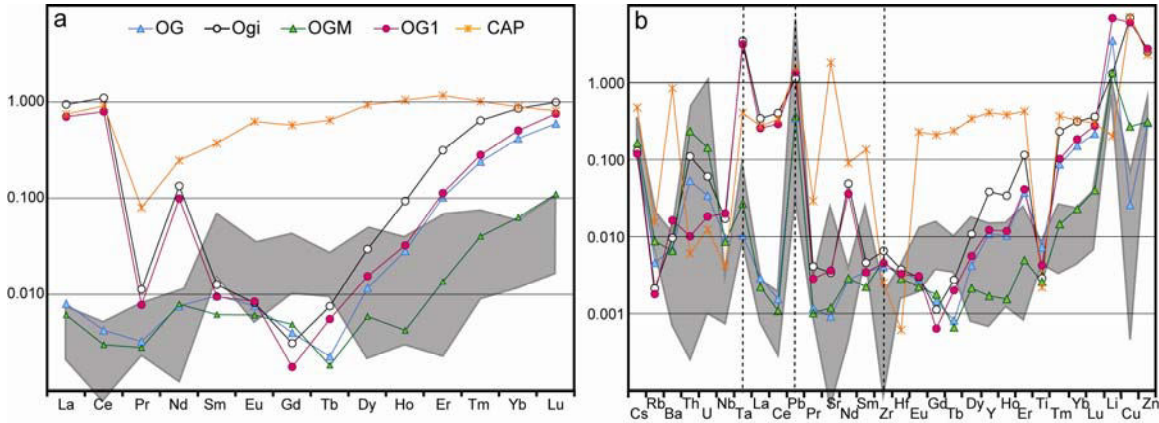
Figure II.21: a) Chondrite normalized rare earth element (McDonough and Sun, 1995) patterns for 4 gem-olivines (OG and OG1: gem quality crystals with no visible inclusions; OGM: magnetite+serpentine inclusions; OGi: euhedral crystals with ludwigite-vonsenite inclusions); and one gem calcite (CAP). b) Primitive mantle normalized diagram (McDonough and Sun, 1995) of trace elements of the same samples. Shaded areas on both diagrams correspond to the olivine compositions obtained by LA-ICPMS from dunite of the crust-mantle transition zone of Sapat (Appendix 3).

Four crystals with different inclusion populations were analyzed for trace elements with bulk solution ICP-MS (Table II.10), and olivines from the host dunite were measured by in-situ LA-ICP-MS (Fig. II.21 and Appendix 3). REE patterns of vein olivines (Fig. II.21a), compared to the dunite olivines, show a strongly fractionated HREE segment. One sample with fluid inclusions (OG1) and one with borate and fluid inclusions (OGi) have, like the euhedral calcite, a highly fractionated LREE segment, in particular for La, Ce, and Nd. Another sample with fluid inclusions (OG) and one with fluid+magnetite+serpentine inclusions (OGM) have a rather flat LREE segment. The primitive mantle normalized diagram (Fig. II.21b) highlights the Pb enrichment common to all samples. The LREE enriched olivines have extremely subchondritic Nb-Ta ratios close to 0.1, a much higher Zr/Hf than the dunite olivines, and enrichments in La, Ce, Cu and Zn (Table 1) similar to the vein calcite. These enrichments are not correlated with any visible solid inclusions and exist also in calcite, inferring that these elements were enriched in the fluid that supplied these minerals.

Gem olivines with borate inclusions have $\delta^{11}B= -7.3(2.5)$ ‰ Boric acid SRM 951 (Table II.11), which corresponds to mantle values (Chaussidon and Jambon, 1994). Fibrous inclusions of Fe-Mg borates (ludwigite-vonsenites; Fig. II.19c) contain up to 20 wt% of B_2O_3, indicating a relatively B-enriched fluid. The isotopic composition of borates has high negative values: $\delta^{11}B= -23.21(73)$ ‰ (Table II.11) reflecting an extremely light B isotopic composition of the fluid. The expected boron fractionation (Palmer et al., 1992; Sanchez-Valle et al., 2005) between olivine (coordination IV (Kent and Rossman, 2002)) and borates (coordination III (Dodony and Weiszburg, 1983)) would lead to a $\delta^{11}B_{borate} \gg \delta^{11}B_{olivine}$, but is not fulfilled. This implies that (i) either boron isotopic behavior is not only driven by the coordination of B in minerals or (ii) that borates and olivine are not in equilibrium

sample	O1		OIB	
borate	δ11B ‰	1σ	δ11B	1σ
	-23.17	0.75	-22.41	0.74
	-22.64	0.69	-23.28	0.74
	-21.81	0.70		
	-22.05	0.67		
	-24.7	0.70		
	-24.69	0.75		
	-23.4	0.72		
	-23.83	0.85		
olivine	δ11B	1σ	δ11B	1σ
	-6.85	2.55	-6.06	1.47
	-8.27	2.73	-8.66	2.42
	-6.99	2.59	-8.59	1.93
	-5.32	2.85		
	-5.81	2.78		
	-6.33	2.91		
	-8.77	2.73		
	-9.18	3.22		

Table II.11: B isotopic composition of borates inclusion and olivine host from two sample.

but kinetic fractionation causes "transient" values between the fluid and the borates or (iii) that olivine has overgrown and incorporated the borates without reequilibrating with them. Regardless of the process, crystallization of such ultra-low $\delta^{11}B$ minerals leads to a strong fractionation and the enrichment in ^{11}B of the remaining fluids. Further, crystallization of such minerals would explain the positive $\delta^{11}B$ fluid denoted in fore-arcs (Rosner et al., 2003).

II.2.4.　　　Discussion-Conclusions

The Sapat vein olivines and calcites crystallized from a carbonate-rich fluid with an isotopically light B. The Sr, O, and C-isotopic compositions of the minerals indicate a mantle-equilibrated fluid with a distinct slab signature, enriched in La, Ce, Nd, HREE, Li, Cu, and Zn. Precipitation of carbonates within the subarc mantle demonstrates that carbonate-rich fluids exist in subduction settings and that crystallization of such fluids within the mantle results in a boron-rich carbonated residue, retaining parts of the slab component. In the absence of appropriate experimental partition coefficients, we cannot quantify the composition of the fluid. However, the fluid precipitates allow deducing that Boron and Nb/Ta fractionations are not restricted to processes at the slab interface but also took place within the Sapat mantle wedge. The gabbros and melt-precipitated pyroxenites in the Sapat mantle have Nb/Ta as low as 1.5 (Bouilhol et al., 2008), similar to the vein minerals (Nb/Ta = 0.1), which indicates that the fluids and arc melts that crystallized pyroxenites could have a common source. We therefore consider that the CO_2, B, Cu, and Zn rich fluids that have precipitated the olivine-calcite-chlorite-magnetite veins were expelled from the same crystallizing magmas at larger depths, implying that the percolating magmas were degassing at near-Moho depths. Furthermore, some pyroxenites from arc settings (Jijal-Kohistan, Dhuime et al., 2007); Tonsina-Alaska (Kelemen et al., 2003), show strong Nb/Ta fractionation. Such fractionated Nb/Ta ratios might imply the involvement of carbonated fluids in the genesis of these rocks. Moreover, they highlight the role of carbonated fluids for Nb-Ta and B fractionation in subduction setting. The relative abundance of carbonated residues might explain the variability of $\delta^{11}B$ e.g. (Rose et al., 2001) and Nb/Ta (Green, 1995; Stolz et al., 1996) reported in arc-magmas. Recycling B-enriched mantle wedge material into the deep mantle could trigger low $\delta^{11}B$ observed in OIB and implies that arc-mantle could be a repository for Ta.

II.3.   Transfer of melt in the mantle – Modelling constraints

II.3.1.   Introduction

Because the migration of mantle melts is not directly observable and the time-scale of migration ($\approx 10^3$ years e.g Turner et al., 1997) complicates indirect geophysical observation, the migration process is a matter of debate. Structures attributed to migration processes in exhumed mantle rocks, usually of oceanic lithosphere origin (review by Kelemen et al., 1997) are primary evidence for the nature of mantle melt migration. Several models have been proposed on the basis of physical behavior to explain melt migration and to reconcile geochemical and field observations (e.g Spiegelman and Kelemen, 2003). Two end-member processes are thought to be responsible for melt migration: (1) pervasive/porous flow, where the melt migrates at grain boundaries in a porous media, is manifest by impregnation features in natural structures; and (2) channelized flow wherein the melt is segregated from the matrix, dykes representing one extreme. Some combination of these end-members appears essential for efficient melt extraction (reference hereafter). Physical models that are capable of partially bridging the gap between pervasive and channelized flow include porosity waves (Richter and McKenzie, 1984; Scott and Stevenson, 1984; Connolly and Podladchikov, 2007), reactive infiltration instability (Daines and Kohlstedt, 1994; Aharonov et al., 1995; Kelemen et al., 1995; Spiegelman et al., 2001; Braun and Kelemen, 2002) and shear-enhanced melt segregation (Stevenson, 1989; Holtzman et al., 2003). Observations from ophiolitic mantle rocks have validated aspects of these models for mid ocean ridge settings, but analogous observations have been lacking for other geodynamic settings, notably arcs and hot spots (Kelemen et al., 1995). In the present-day knowledge of arc mantle rocks, none of the observable mantle outcrops shows structures relating arc-melt transfer. To alleviate this deficiency, here we present observations of structures in exhumed sub-arc mantle that we interpret as evidence of both pervasive and channelized melt flow. The observations are from ultramafic rocks of the Sapat Complex, part of the lithospheric mantle of the Mesozoic Kohistan Island Arc (Bouilhol et al., 2008; Chapter II.1). The stratigraphically upper portions of the Sapat ultramafic body preserve a crust-mantle transition zone where subduction-related melts have migrated toward the crust and generated the structures discussed here (Bouilhol et al., 2008; Chapter II.1). In an island arc setting, in contrast to mid-ocean ridge settings, crystallization in the direction of flow suppresses the reactive transport mechanism and, as the rocks show no evidence suggestive of extensive shearing, we refer to the porosity wave model as an explanation for our observations.

II.3.2.   Field relationships

Within the meta-harzburgites of the Sapat Complex, ten to hundred square meter zones of coarse grained dunites host clinopyroxenites that range from homogeneous olivine-clinopyroxenite to zones referred as "trail zones" where trails of clinopyroxene evolve into gabbroic bands. These gabbroic rocks are metamorphosed but are nevertheless called gabbros for clarity. The largest "trail zone" has been mapped in detail (Fig. II.22). Within this "trail zone" clinopyroxene occurs as centimeter-scale porphyroblasts and as trails of near vertically aligned, millimeter-size crystals (Fig II.23a and b). Spatial repetition of the trails leads to a banded pattern (Fig II.23a-d). Plagioclase appears in some bands where clinopyroxene (cpx) is modally abundant (Fig II.23a, c). Where patches of plagioclase
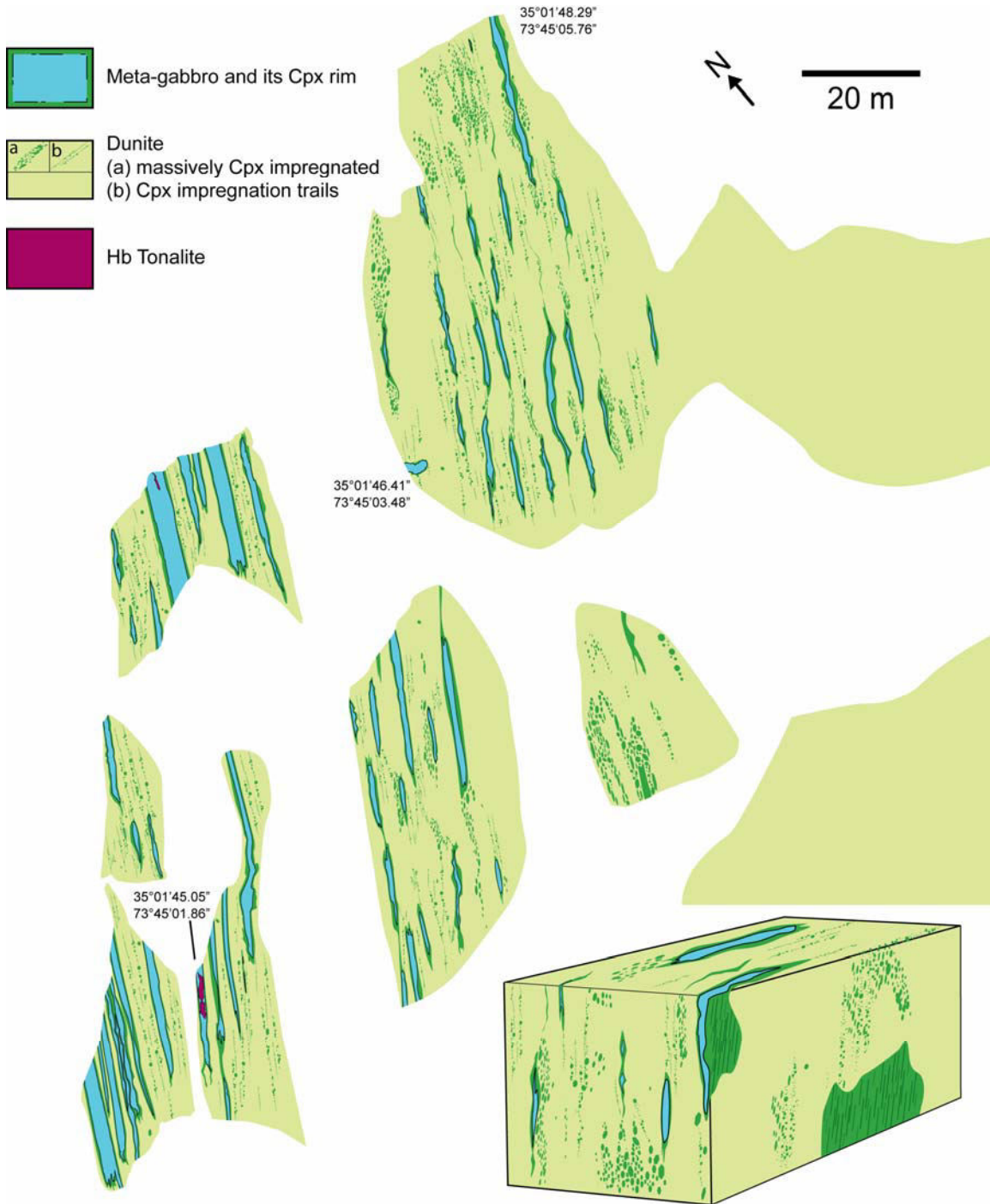
Figure II.22: Detailed map of the "trail zone" within the crust mantle transition zone of Sapat, where 3D, flattened lenses of meta-gabbros are enclosed in clinopyroxene-rich rims. White zones = snow or gravels. Lower right corner: synthetic 3D diagram illustrating the sub-vertically elongated structures along subvertical foliation and mineral lineation.
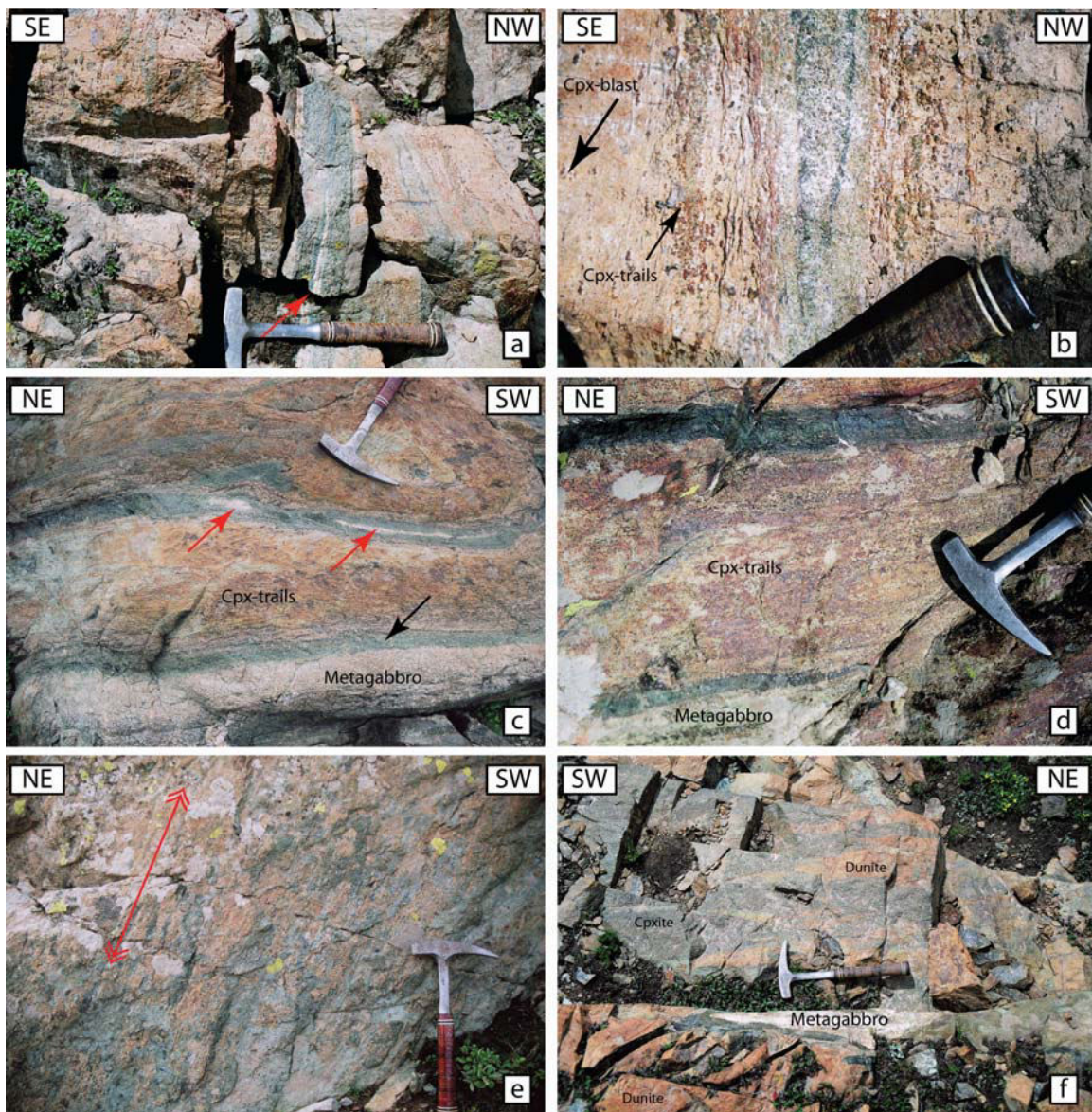
Figure II.23: structural relationships between the different lithologies in the "trail zone". a) vertical view of the outcrop with plagioclase (red arrow) appearing in a subvertical cpx-rich vein (dark) in impregnated dunite (brownish country rock). b) map view of cpx-rich vein and parallel cpx trails (zoom of the right part of a). c) map view of plagioclase "eyes" (red arrow) in a cpx-rich vein next to a gabbroic lense and its rim (black arrow). d) map view of alternating cpx veins and cpx trails and gabbroic lenses. e) vertical view of a cpx-rich gabbroic lense rim with steeply-plunging magmatic lineation (overlined by arrows). f) map view of cpx-rich (Cpxite=Clinopyroxenite) flames isolating dunite clusters and a gabbroic lense termination.

coalesce, they form gabbroic, dyke-like structures (hereafter named lenses), which range in width from 0.1 to 1 meters (Fig II.23a, d).

These dykes always show a clinopyroxene rich rim isolating them from the surrounding impregnated dunite (Fig II.23a, b, c, d, e, f). The clinopyroxene rim often has gradational boundaries and clinopyroxene defines a fabric parallel to the boundaries with the country impregnated dunite. These rims correspond to proto-lenses, i.e, they formed prior to plagioclase appearance.. The gabbroic lenses represent channelized flow, embodying the transfer of melt in an isolated conduit. These dykes have fingering, flame-shaped terminations. In three dimensions, the clinopyroxene trails, and the cpx-rich rims show a near-vertical alignment of cpx defining a near-vertical mineral lineation which, in the absence of any sign of crystalline plasticity, is considered as the direction of magmatic flow (Fig II.23e). The fingering map-view terminations of lenses are also seen in vertical planes, suggesting that the primary direction of melt percolation was sub-vertical, in the present-day reference frame, and the gabbro lenses are 3-dimensional lenses terminated horizontally and vertically in clinopyroxene proto-lenses. Hbl-tonalite is found as patchy intrusions within the core of two of the largest gabbro lenses. The boundary with the host gabbro is contorted and pieces of the host gabbro are enclosed in the Hbl-tonalite (Fig II.24 a, b, 105 Ma see chapt.III.3)
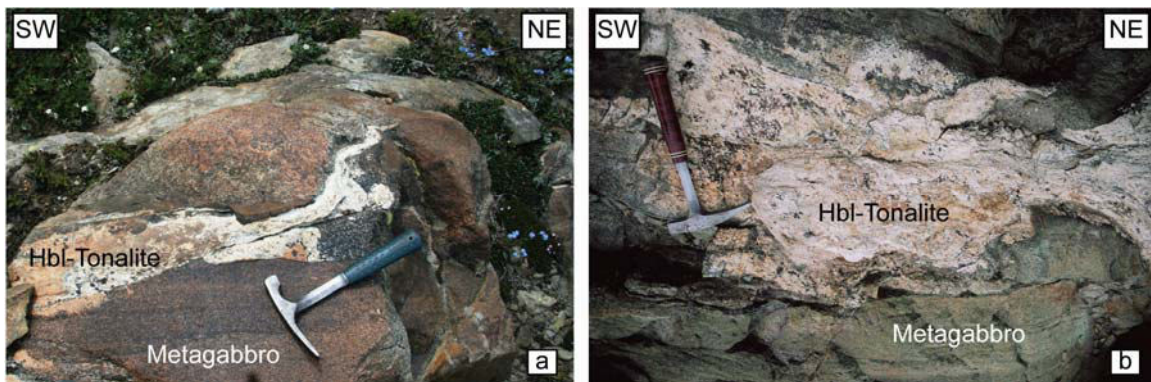
Figure II.24: a) map view of the tip of a Hbl-tonalite in a gabbroic lense. b) Hbl-tonalite patch showing the fuzzy boundary with the host gabbro.

These features are taken as evidence for melt migration in the Sapat crust-mantle transition zone where the percolation of melts has led to melt-rock reaction and crystallization leading to a "trail zone" of dunite-pyroxenite formation (Bouilhol et al., 2008; Chapter II.1). The texture of the impregnated dunite, consisting of interstitial clinopyroxene, olivine and spinels suggests melt percolation and crystallization during pervasive flow of the melt through the host dunite.

II.3.3. Structural-petrogenetical relationships.

The formation of dunite has been attributed to melt percolation in the surrounding meta-harzburgites (Bouilhol et al., 2008; Chapter II.1). Melt percolation resulted in orthopyroxene dissolution and olivine crystallization via the peritectic reaction opx + melt = ol. On the basis of the chemical compositions of olivine and clinopyroxene (Bouilhol et al., 2008), the clinopyroxene-rich parts and gabbros were recognized to have formed from the same melt as dunite (see Chapter I.2). The melt forming gabbros and cpx-rich parts were in near-equilibrium with dunite, but not with the surrounding

harzburgite. The structural relationships (i.e parallelism of gabbroic lenses and cpx-trails, and 3D evolution of trails into gabbroic lenses) within the "trail zone" strengthen the co-genetic origin of the lithologies. Isolated clinopyroxene porphyroblasts evolve into trails that turn into bands in which plagioclase pseudomorphs appear. From these observations we infer that the percolation of melt into dunite formed a succession of structures, with increasing melt flux: Isolated clinopyroxene porphyroblasts → clinopyroxene trails → clinopyroxene bands → gabbroic lenses.

From the sub-vertically oriented lens-like geometry of the gabbroic lenses and magmatic foliation and lineation we concluded that isolated lenses (from the dunite) represent a dynamic mode of melt transport, similar to a self-propagating dyke or porosity wave that has been frozen in place. The surrounding cpx trails and veins indicate high melt flux.

II.3.4. Model of percolation

It has been shown that a rheological asymmetry in compaction, referred to as "decompaction weakening", wherein the matrix yields more easily during decompaction under negative effective pressures than it does during compaction, then this generates tube-like porosity waves (Connolly & Podladchikov 2007. This mode of melt transport could explain many of the features described at Sapat. While the strength of the rheological asymmetry in natural rocks is a subject of conjecture: it would be strongest at low temperatures where the plastic component of the rheology becomes important. As Sapat represents a crust-mantle transition zone, the environment would favor such effects. To illustrate the likely petrological consequences of porosity wave transport, we have expanded the numerical model of Connolly & Podladchikov (2007) to include thermal effects (conduction, advection, and latent heat of crystallization) and transport of saturated solute with temperature dependent solubility e.g (Aharonov et al., 1995). Although the chemical model accounts for only a single solute, to emulate the melt-olivine-pyroxene peritectic, we assume that the mineral that precipitates during cooling is clinopyroxene and the mineral that dissolves during heating is orthopyroxene.

The spatial domain of the model is a 2-dimensional section. The model assumes a harzburgitic matrix with a uniform background melt-filled porosity and a steady state geothermal gradient. The model is parameterized by the viscous compaction length (δ= 500 m), the background porosity ($\phi0=10^{-3}$), the compaction time scale ($\tau=10^4$ y), the density difference between solid and melt (500 kg.m^{-3}), the ratio of the effective viscosity for decompaction to that for compaction (0.1), the thermal diffusivity (10^{-6} m^{2}s^{-1}), the solubility gradient (10^{-3}K^{-1}), the latent heat of clinopyroxene and orthopyroxene crystallization (-0.18^{e10} and -0.13^{e10} J.m^{-3}), and the specific heat capacity of the melt and matrix (4.10^6 J.kg^{-1}K^{-1}). The porosity waves are initiated in the model by introducing a Gaussian perturbation to the background porosity at the base of the model. This perturbation has a half-width of two compaction lengths and maximum amplitude equal to the background porosity.

II.3.4.1. *Model results*

Typical model results are illustrated in figures II. 25, 26, 27 and 28. In these figures, the spatial domain of the model is oriented so that the axis parallel to the gravitational field is vertical and the upward direction, i.e., the direction of melt flow, is to the top. The top three nodes of the model box simulate the Moho and are inactive. The first wave initiating from the porosity perturbation at the base of the model domain propagates

upward, decompacting the matrix at its tip and compacting the matrix over a width of roughly two compaction lengths in its wake (Fig. II.25). The center of this wake is marked by a tail of slightly less compacted porosity. The wave tip is characterized by high melt fluxes that result in strong heat advection and dissolution of pyroxene (representing the change in the volume fraction divided by the initial porosity ϕ_0) from the matrix, forming a dunite channel (Fig. II.26). In contrast, compaction in the wake of the wave causes a diffuse advective heat shadow that results in temperatures below the initial steady state geotherm and the precipitation of clinopyroxene, i.e., the formation of impregnated dunite.
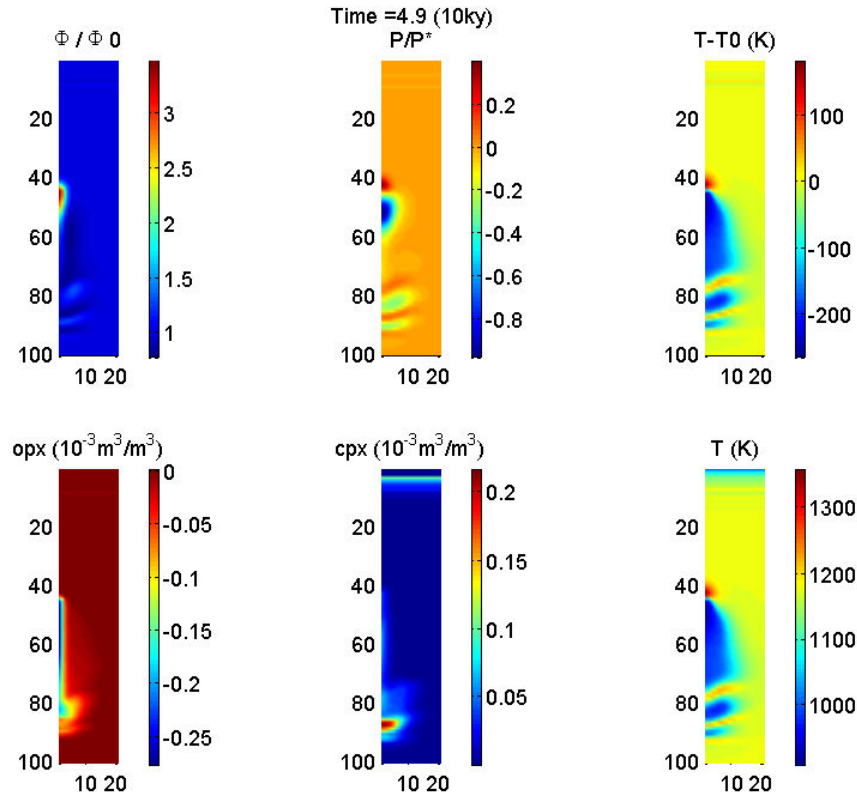
Figure II.25: Initiation and propagation of the first wave. Upper row, from left to right: porosity difference; pressure difference (P=Pfluid-Psolid; P*=δΔρg); temperature difference (T0 = initial steady state temperature). Lower row, from left to right: time integrated opx dissolution; time integrated cpx crystallization; temperature of the system

The initial wave generates perturbations from which secondary waves nucleate, so that by a model time of 20 τ four dunite channels have been formed and the thermal and porosity structure has become increasingly heterogeneous (Fig. II.27). Beyond this time, subsequent waves tend to be localized within the dunite channels formed by earlier waves (Fig. II.27). This localization is a consequence of both the relatively high porosity left in the center of the wake of waves, which corresponds to the dunite channel, and to the advective heat shadow that cools the surrounding matrix. The latter effect creates a hostile environment for melt transport in the inter-channel regions of the matrix.
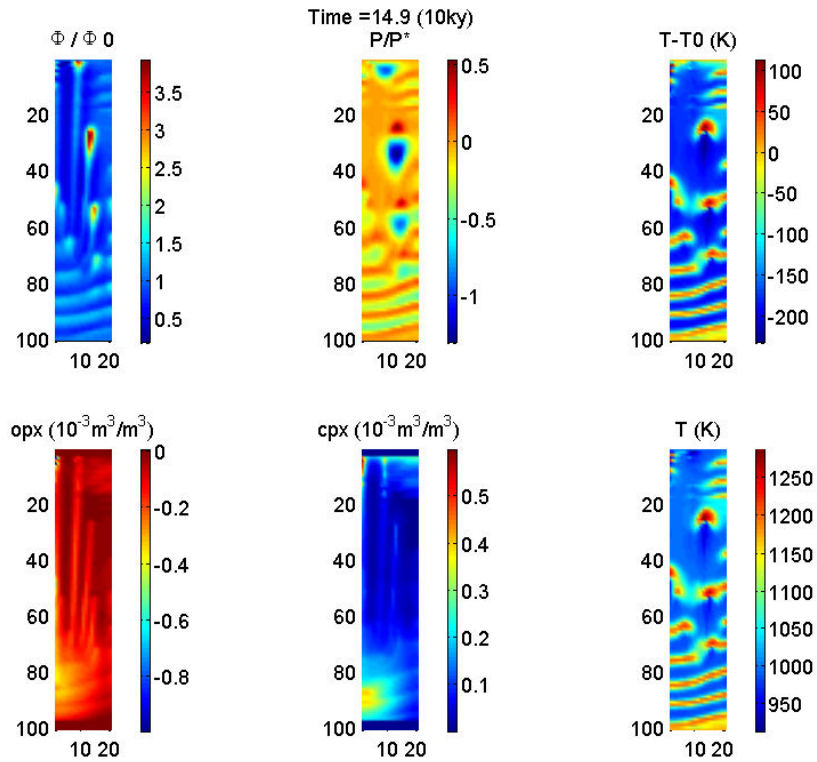
Figure II.26: The waves are initiating in the trail of each other due to porosity perturbation. It results in the formation of dunitic channels
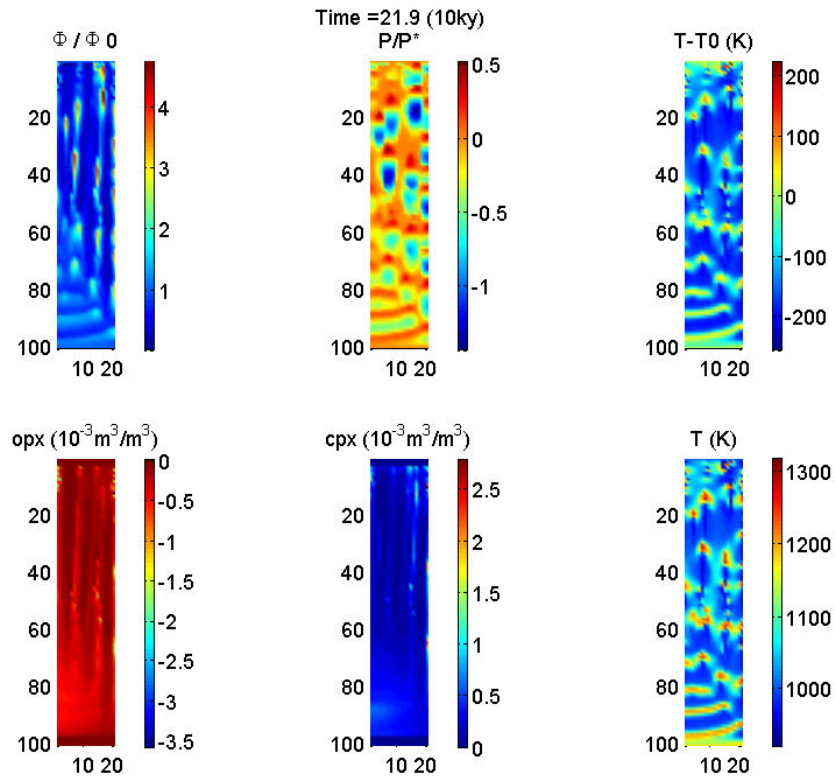
Figure II.27: The open porosity left behind waves allows further melt percolation within individualized dunitic channels.

From a petrological perspective, once melt flow becomes confined to a finite number of channels, pyroxene crystallization becomes more efficient and dissolution precipitation is competing in time and space within individual channels. Channels re-used several times show clinopyroxene crystallization whereas those used only few times show only little mineral crystallization. Thus, the final model result shows a system of two dunitic channels in which clinopyroxene has crystallized heterogeneously (Fig. II.28).

The time-scale for the model evolution is dictated by the magnitude of the initial perturbation, such that by a model time of 30 τ, the model appears to be essentially static on the compaction time scale. However, except in the waning stages of natural system, the modeled processes could be maintained indefinitely by melt input generated at depth.
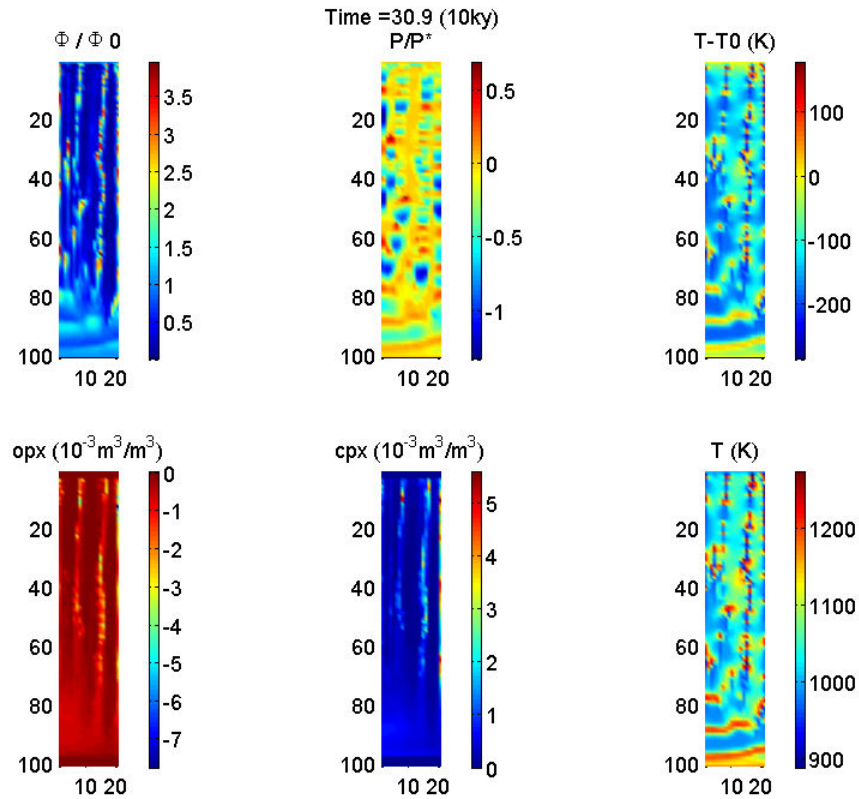
Figure II.28: Multiple wave propagation within dunitic channels allows cpx to crystallize until the system stops due to unsupplied melt input.

II.3.5.　　Discussion

Both field and petrological evidence show that the flattened tube-shaped dunites of the Sapat complex formed from the harzburgitic host rocks by Opx dissolution and olivine precipitation induced by pervasive melt percolation. The shape difference observed between the modeled, tube-shaped channels and the observed flattened tubes in the field reflects the absence of a far stress field in the model, which likely was present in nature. Under the assumption that the abundance of clinopyroxene precipitated by the melts can be taken as a measure of melt flux, the ultramafic rocks at Sapat reveal a continuous spectrum of behaviors from pervasive (cpx trails, impregnated dunite) to segregated melt flow (gabbroic "lenses") at the center of some dunite channels. These features (qualitative statement) can be explained by a hydraulic model in which the porous

harzburgitic (i.e the Sapat ultramafic main lithology) matrix yields more rapidly under negative effective pressure than it does under positive effective pressure (Connolly and Podladchikov 2007). Flow instabilities resulting from this rheology cause the pervasive melt flow through the harzburgite to be focused into tube-like porosity waves that induce strong advective heating and leave a tail of slightly elevated porosity in their wake. The high temperatures and melt fluxes at the tips of the waves result in the formation of the dunites by enrichment of olivine and depletion of pyroxene (the peritectic reaction opx+melt = ol forming dunites of the crust-mantle transition zone). Subsequent melt flow that exploits the relatively high permeability of the dunite channels at lower temperature results in the precipitation of clinopyroxene (the "trail zone" within the dunites). The simplifications in the numerical model of this process preclude the simulation of fully segregated melt flow, i.e., the formation of melt-filled lenses; however we speculate that such a mode of transport would initiate when high melt fluxes overwhelm the capacity of the porous media to accommodate melt flow. The spatial association of lens-shaped gabbroic lenses with domains of particularly high clinopyroxene abundance within the dunitic channels is the reason for this conjecture.

II.3.6. Conclusion

The structural and petro-geochemical characteristics of the crust-mantle transition zone of Sapat are indicative of melt percolation resulting in a combined porous and channelized flow process. A porosity wave melt migration model explains well the spatial relationships between the "trail zone" and the dunite on the one hand, and the concomittent of gabbroic lenses and cpx impregnated dunite in the "trail zone" on the other hand. The propagation of porosity waves into harzburgite leads to the formation of porous dunitic channels, in which further melt propagation induces the appearance of clinopyroxene. The high melt flux within the dunitic channels further explains the relationships between impregnated dunites and gabbroic lenses in the "trail zone". The change in mode of melt migration, i.e from porous to channelized flow, reflects the mechanical instability of porous flow in a deformable medium.

Inasmuch as Sapat is, to date, the only example of an exhumed sub-arc mantle crust system, we suggest the model as generic explanation for the chemical characteristics and physical nature of melt flow in the sub-arc mantle. The important feature of this model is that melts are transferred via dunitic conduits that chemically isolate the melts from the surrounding peridotite. We have concentrated on buoyancy-induced mechanical instabilities rather than shear-induced instabilities because of the absence of evidence for significant shear strain at Sapat and the sub-vertical geometry of melt segregation features, which suggest a gravitationally driven segregation process. Although our expectation was that reactive transport instability could not explain melt segregation because of the retrograde thermal regime in island arc systems, our models suggest heat advection as a consequence of strong channelization can lead to melting and reactive transport instability. Thus, while there is no doubt that channelization in the physical model is a consequence of mechanical instabilities, we cannot preclude that reactive transport accounted for in the model would be adequate to induce channelization.

III. Mafic rocks

III.1. The meta-plutonic series

III.1.1. Introduction

The crustal part of the Sapat Complex is made of a predominantly plutonic series, now metamorphosed, ranging from mafic to silicic and including kilometer-size pyroxenitic bodies (Fig. III.1, 2 and 3). The contact with the underlying ultramafic rocks is rarely exposed and where it could be observed is a meter thick, brittle fault zone. This brittle fault reworks the primary contact between the ultramafic rocks and the metaplutonics (i.e the petrological Moho), which seems to have been an intrusive relationships, as in Jijal (Burg et al., 1998). Indeed, the 200 m thick zone that makes the direct footwall of the fault zone already contains gabbroic lenses intruding the ultramafic rocks and this rock association is interpreted as a part of the crust-mantle transition zone. Just above this brittle contact, over 10 meter in thickness, the metaplutonic rocks display a steep foliation (80-90° NW) representing ductile deformation that cross cuts metaplutonic primary magmatic foliation. The upper boundary of the Sapat Complex is more complex, and displays different features in different areas. The NE tip of the Sapat Complex (Babusar section) is bounded by a north dipping tonalitic laccolith, which is mylonitic with southwestward sense of shear at the contact with the Sapat mafic rocks. Further to the east (Thoregah Shear Zone, Fig. III.1, 2), the contact between the Sapat Complex and the "Southern Amphibolites" consists of a 10-50 m thick mylonite zone whose foliation is dipping 70°NW. There, tonalites have intruded the sheared Sapat metaplutonic series (Fig. III.4a) during and after top-to-the-SE shear, according to the mylonite fabrics (Fig. III.4b). Amphibolite to greenschist facies shear zones randomly occurring in the Sapat Complex cut through all lithologies and the older mylonites. They represent sinistral ductile faults that strike mostly E-W. In this chapter, we describe the petrology and the chemistry of the metaplutonic rocks in order to constrain the processes that led to their formation. These metaplutonic rocks represent the lower crustal part of the Complex. Their trace element signature and isotopic composition allow characterization of the source of the melts that produced these rocks. The aim of this chapter is to complement the description of the Sapat Complex lithologies. The bulk rock chemistry of some of pyroxenites is given to document the petrological relationships of the pyroxenite bodies described in chapter III.2 with the surrounding metaplutonic rocks. The full dataset has not yet been investigated in all its aspects and the interpretations / conclusions presented at the end of the chapter remain preliminary.

III.1.2. Description

The metaplutonic rocks are principally composed of recrystallized and foliated greenish to blackish mafic sills (1-10m thick) comprising in some places bluish-quartz-bearing white sills. Contacts are sharp. Sills can be massive and homogeneous or display magmatic structures such as layers, mineral (amphibole) clusters and modally graded beds (Fig. III.5a, b). The rocks are variably unfoliated to strongly foliated, foliation being generally parallel to the sill boundaries and magmatic layering and defined by plastically stretch mafic minerals. This heterogeneous strain distribution and magmatic pattern together suggest protracted intrusion, late sills deforming older, possibly unconsolidated

and approximately cogenetic ones. Both layering and foliation are persistently dipping north and become steeper northward (from 30° to 70°). Up sequence, coarse silicic dykes cross cutting the earlier magmatic-tectonic foliation of the metaplutonic rocks increase in abundance.
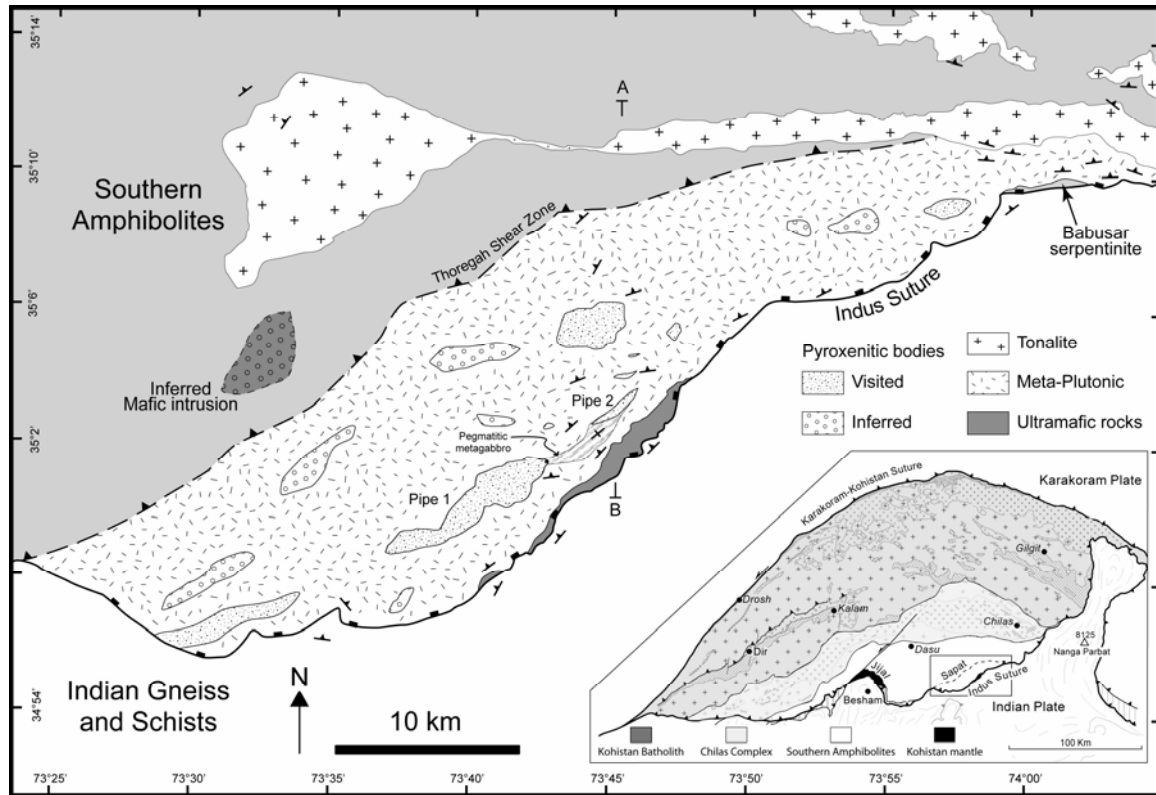
Figure III.1: Geological map of the Sapat complex. Inferred pyroxenite bodies from landscape and satellite picture observations. A-B trace of section of Figure III.2

III.1.2.1.   *Mafic metaplutonic rocks*

The greenish sills owe their color to greenish minerals in a white matrix and range from melano- to leuco-metagabbros with a wide range of mafic mineral proportions. In some places, mesoscale magmatic gravitational instabilities evolved into small-scale, diapir-like structures. They indicate, along with magmatic graded bedding, rhythmic in places, that the pile is normally oriented (up = top at magmatic time) (Fig. III.5b). Some less recrystallized sills show clusters of deep-green amphiboles in a white matrix; their protolith were gabbros, likely containing magmatic amphibole. Scarce metahornblendites (Sample G42, G48, G33) are deep-green, homogeneous sills.
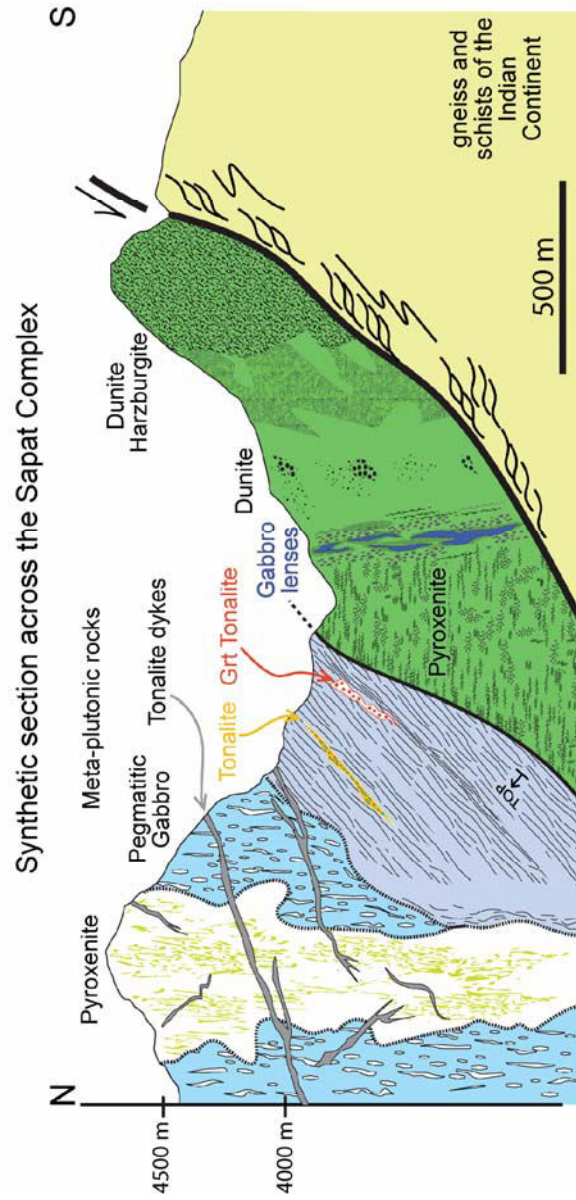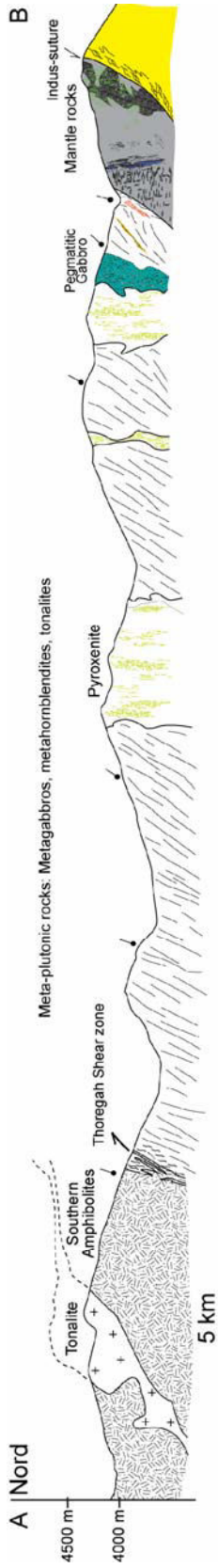
Figure III.2: Cross section of the Sapat Complex (A-B on Figure III.1) and synthetic section of the bottom part of the complex illustrating the relationships between the different rock units.
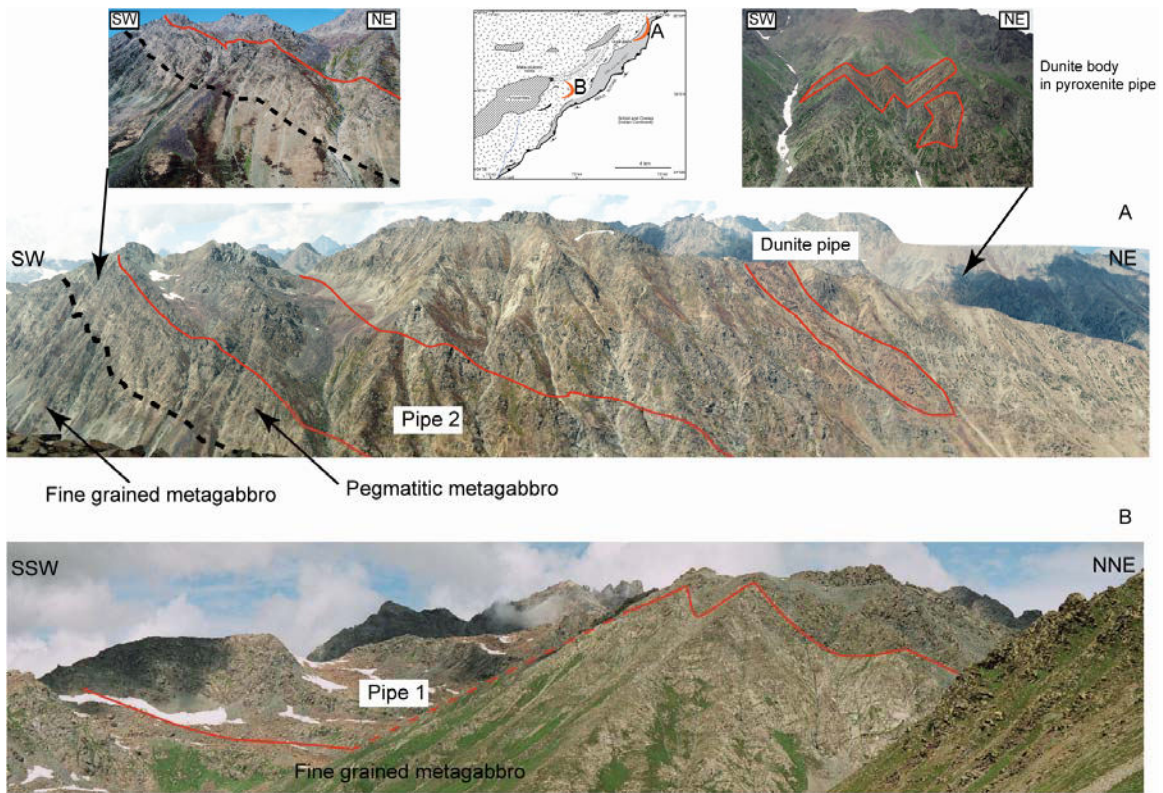
Figure III.3: Lanscape from locations A and B on map of Fig. II.1 showing the two pyroxenite pipes (Fig III.1) investigated in details in chapter III.2. Note the steep contact between the pyroxenite body and the host metagabbro.
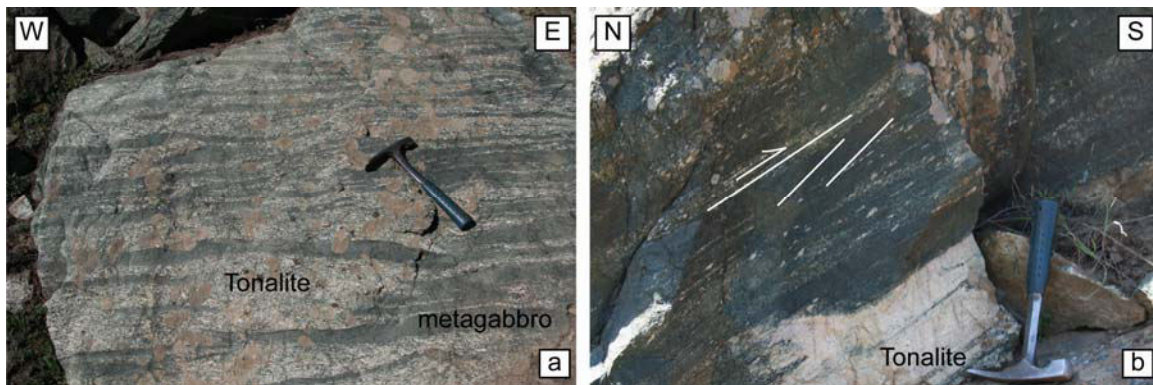
Figure III.4: Northern boundary of the Sapat Complex. a) Tonalite veins into metagabbro below the Thoregah shear zone (35°08'05.2'; 73°43'56.7"). b) Thoregah shear zone (50m above photo a) with top-to-the SE sense of shear (arrow along shear plane oblique to the underlined foliation) and syn-tectonic tonalite intrusion

The pegmatitic metagabbros are composed of centimeter long clinopyroxene pseudomorphs (amphiboles), saussuritized plagioclase and chlorite. These pegmatitic metagabbros (Sample G11, 46, 54, 56, 57) display vertical alignment of cpx pseudomorphs exempt of plastic deformation and vertical dynamic flow structures (e.g

cross bedding) synonym of a vertical magmatic foliation (Fig. III.6). This magmatic foliation, striking N060E, is parallel to the pyroxenite bodies which they "mantle". The contact between fine grained and pegmatitic metagabbro is of magmatic origin, with a continuous gradation from fine to coarse grain within *ca* 1m. All of these meta-mafic rocks contain epidote, amphibole, chlorites and locally quartz, titanium oxides, sphene, calcite, Fe-sulfides, magnetite and other opaque minerals.
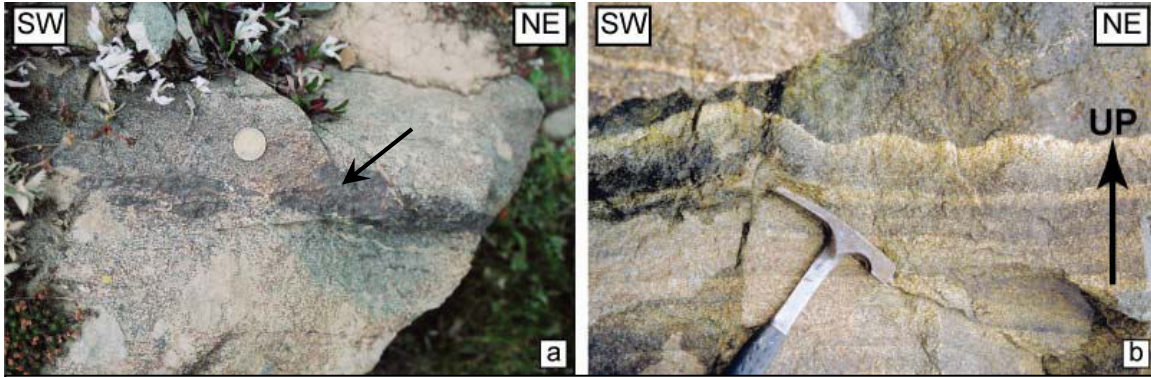
Figure III.5: Magmatic fabric in metagabbro sills. a) Aligned blackish amphibole clusters (arrow) in a clearer gabbroic matrix. GPS: 34°59.899' 73°42.085' b) way-up criteria showing modally graded layering, interpreted as gravitational instabilities. Note the wavy layer top, and crystal density segregation at the layer bottom GPS: 35°01.14.4' 73°44.21.8'

Figure III.6: Mapview of the vertical magmatic foliation in the pegmatitic metagabbro. GPS: 35°02.072'; 73°44.583'

<u>*III.1.2.2.*</u>   <u>*Silicic interlayered sills*</u>

>100 m long and meter thick sills of fine to medium grain size (ca. 0.2 to 1 cm) quartz, saussuritized plagioclase, chlorite, garnet and amphibole tonalites occur in the fine grained metagabbros. Such non-foliated leuco-tonalite sills intrude the fine grained metagabbros close to the contact with the ultramafic rocks whereas leuco-tonalite sills, similar in composition but foliated, are intruded by metagabbros in the top levels of the sequence (Fig. III.7a, b). North of Parla-Sapat (Fig. II.1), one of these sills (sample G32) contains small (0.2 cm) magmatic, euhedral garnets and deep-green hornblende. This sill intruded a garnet-bearing melano-hornblendite (G33). Some fine grained metagabbros evolve into tonalite and have increasing modal quartz upwards through the sill.
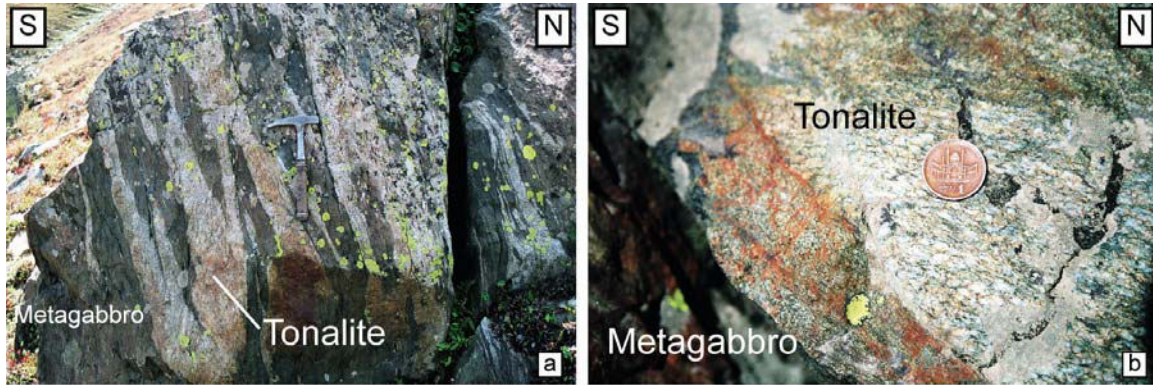
Figure III.7: relationships between silicic, tonalite sills and metagabbro. a) Tonalite veins intruding metagabbro above the contact with the ultramafic rocks GPS: 34°59.693' 73°42.741'. b) Foliated tonalite sill deformed before being intruded by a metagabbro sill. GPS: 35°00.482' 73°42.757'.

<u>*III.1.2.3.*</u>   <u>*Silicic dykes*</u>

Northward (upward) in the meta-plutonic sequence, meter thick, north-dipping (~ N070 20NW) trondhjemite-tonalite dykes cross cut the tectonic and magmatic foliations of all previously described lithologies (Fig. III.8). They have coarse grains and are mainly composed of quartz, saussuritized plagioclase and chlorite; garnet was found in one of these dykes (sample G13). This garnet-bearing dyke dips north and stops at a 2 m wide top-to-the-north ductile normal shear-zone. However, several tonalitic digitations, some foliated and some unfoliated, intrude into the shear zone and the boundary between the dyke and the shear zone shows no fabric deviation. These features indicate that the dyke was contemporaneous with late movement on the shear zone. Another of these dykes (sample G12) has a gradational contact with the pegmatitic metagabbros and seems to be a segregate from them. Within the biggest pyroxenite body (pipe 1, chapter III.2) gently north-dipping, hornblende-bearing tonalite dykes (e.g. sample P8) cross cut the magmatic structures and increase in abundance with elevation. Within the pyroxenite pipe 2, hornblende tonalites have been attributed to the ultimate melt fraction produced by reactional fractional crystallization processes within the pipe (chapter III.2). Hbl-tonalites within the core of metagabbros of the crust mantle transition zone have the same appearance as sample G12, i.e look like segregated products.
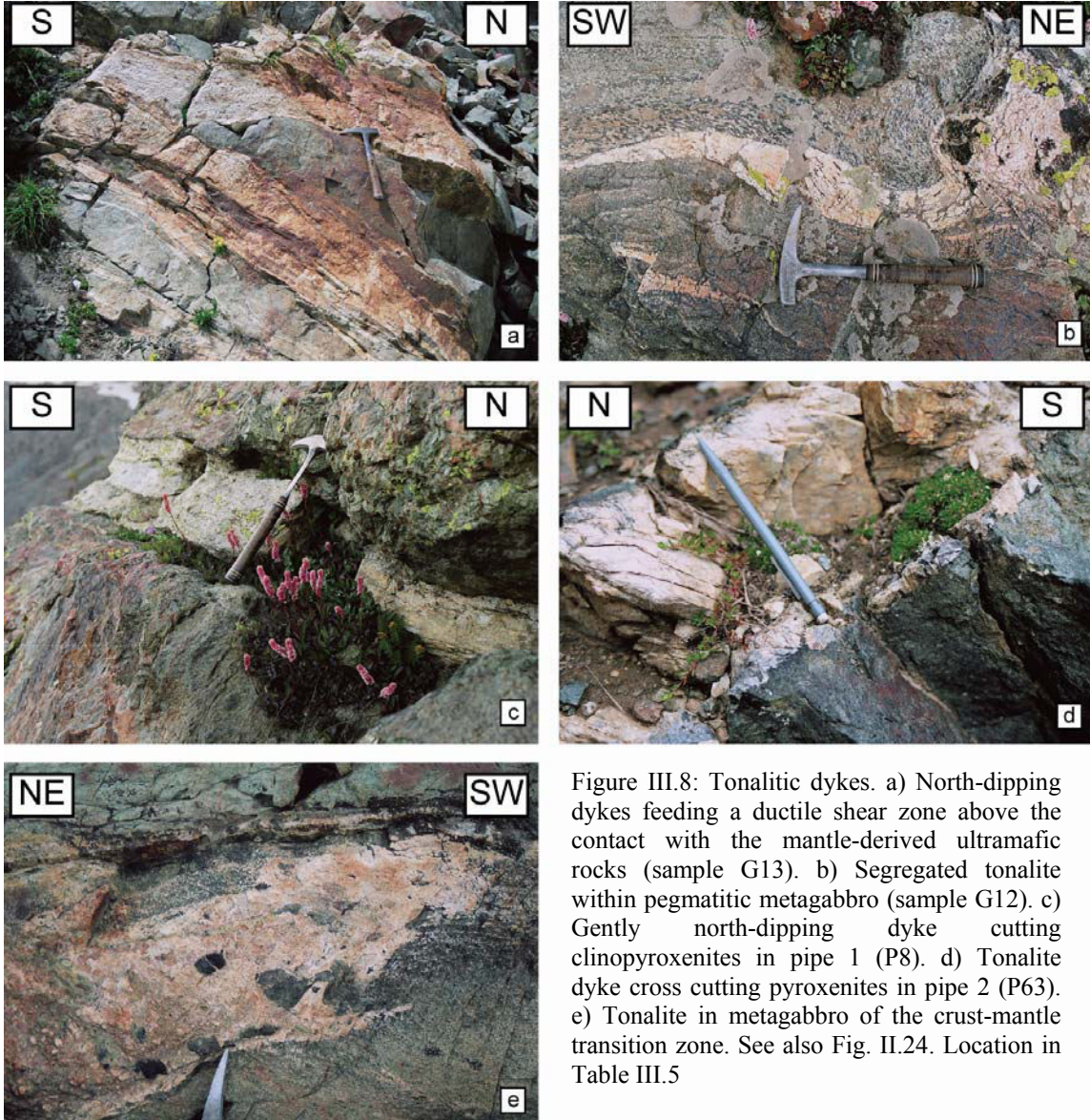
Figure III.8: Tonalitic dykes. a) North-dipping dykes feeding a ductile shear zone above the contact with the mantle-derived ultramafic rocks (sample G13). b) Segregated tonalite within pegmatitic metagabbro (sample G12). c) Gently north-dipping dyke cutting clinopyroxenites in pipe 1 (P8). d) Tonalite dyke cross cutting pyroxenites in pipe 2 (P63). e) Tonalite in metagabbro of the crust-mantle transition zone. See also Fig. II.24. Location in Table III.5

III.1.2.4. *Micro-structures*

All metagabbros display a recrystallized texture (Fig. III.9). Clinopyroxene is now exclusively replaced by tremolite, and plagioclase has rarely been found. Amphiboles are often zoned and, in some samples, hornblende crystals rim tremolite (Fig. III.9a). The fine-grained metagabbros are made of an intergrowth of tremolite, epidote and chlorite (Fig. III.9b). Titanium oxides often show a rim of titanite. Dykes of metagabbro within the ultrabasic rocks have preserved their Cpx despite recrystallization documented by Cr-rich grossular and the metamorphic paragenesis (Amph-Chl-Tr) (Bouilhol et al., 2008).
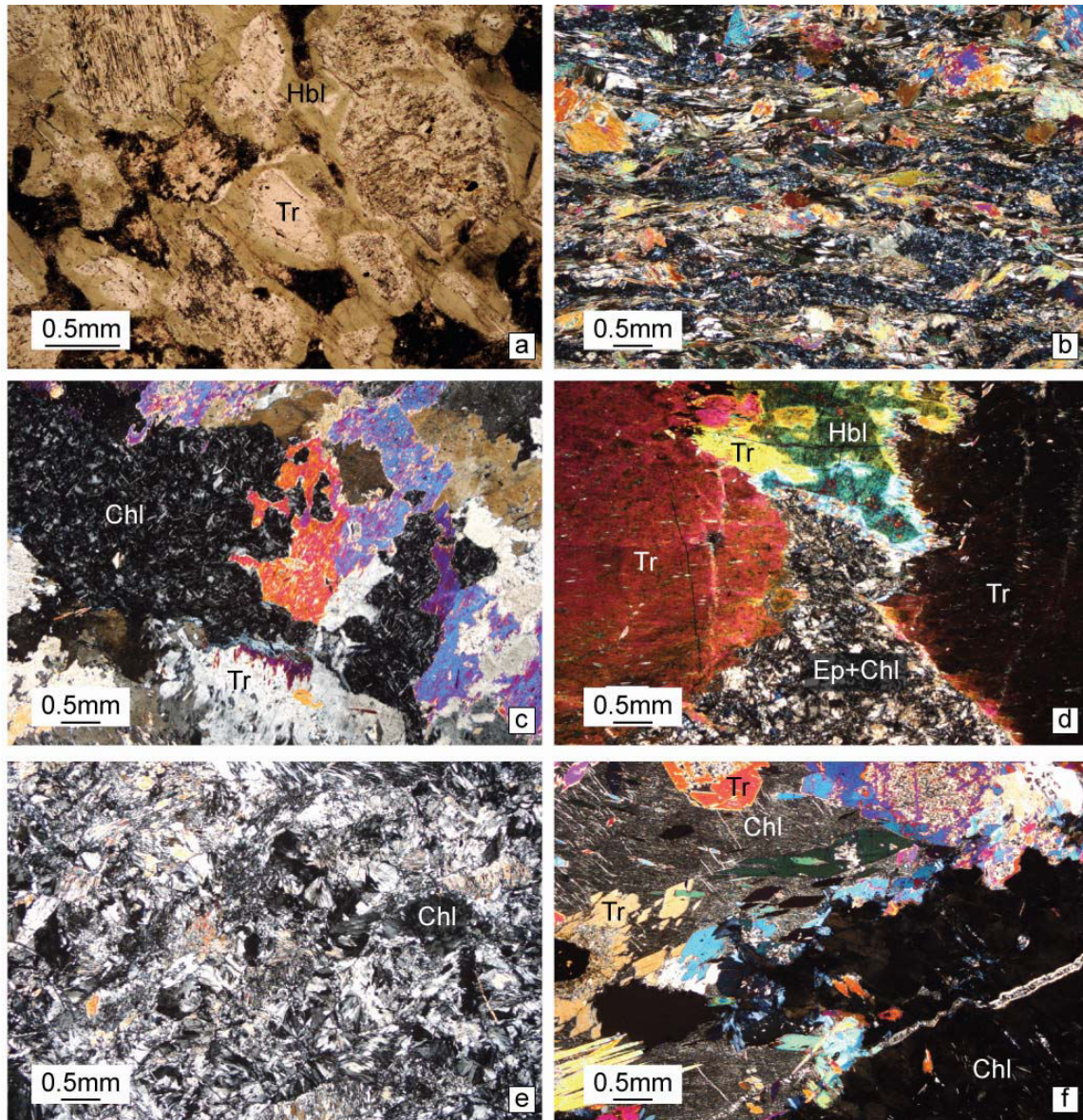
Figure III.9: Photomicrographs of metagabbros. a) Tremolite (Tr) pseudomorph after cpx rimmed by green amphibole (Hbl). All analyzed by LA-ICPMS, sample G25. Table II.1. b) Ep+Tr±Chl defining the foliation of a fine grained metagabbro. c) pegmatitic metagabbro, with lathy chlorite matrix (Chl) and tremolite pseudomorph after cpx. d) Pegmatitic metagabbro with Ep+Chl matrix, tremolite pseudomorph after cpx and relictual magmatic amphibole (Hbl). e) Fine grain metagabbro in contact with pyroxenite pipe 1. Most of the sample is chlorite. f) Pegmatitic metagabbro in contact with pyroxenite pipe 2. Multiple generations of amphiboles and chlorite.

The pegmatitic metagabbros display centimeter-big tremolite pseudomorphs after Cpx associated with, or rimmed by smaller hornblende. These pseudomorphs occur in a matrix of interlocked lathy grey chlorite and epidote (Fig. III.9c, d).

Metagabbros are extremely to entirely chloritized against the contact with pyroxenites (Fig. III.8e). Some pegmatitic metagabbros show complex structures with chloritized clinopyroxene overgrown by tremolite (Fig. III.9f).

Meta-hornblendites are almost exclusively made of millimeter-size green hornblende more or less recrystallized into tremolite (Fig. III.10a). Epidote and chlorite constitute the volumetrically minor matrix in which calcite, ilmenite and titanite are common. Euhedral garnet and quartz have been found in some samples (e.g G33, Fig. III.10b).
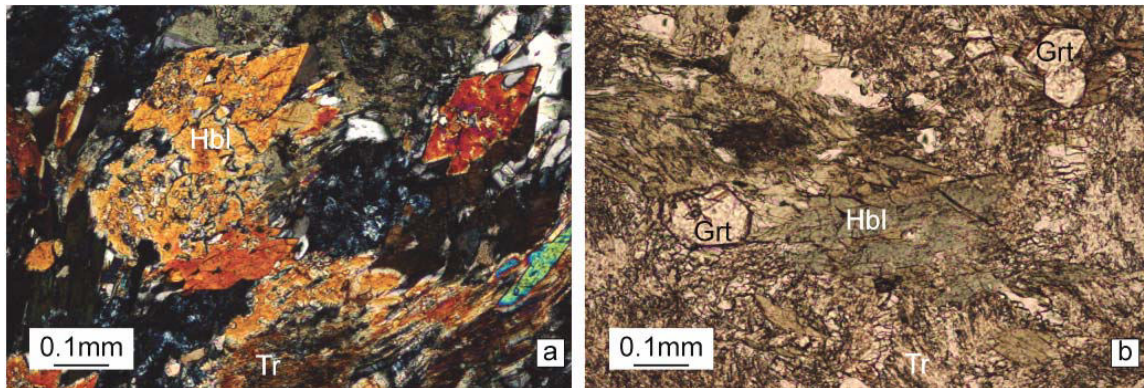
Figure III.10: Metahornblendite texture (sampleG33). a) euhedral hornblende b) euhedral garnet, hornblende and metamorphic chlorite and tremolite.

Fe, Cu and Zn sulfides are common in all lithologies.

Tonalite layers contain quartz and millimeter to centimeter big, saussuritized plagioclase (Fig. III.11a). Quartz is usually sub-millimetric and strongly undulose. Chlorite can be a pseudomorph of biotite or, where associated with epidote (Fig. III.11b), of plagioclase. Titanite is often present. Both tonalite samples G32 and G19 contain magmatic, euhedral hornblende and garnet (Fig. III.11c, d).

Tonalite dykes always show centimeter-size, saussuritized plagioclase and, locally, centimeter-size, zoned hornblende (Fig III.12a). Quartz, is very undulose and belongs to the matrix (Fig III.12b). Magmatic epidote (enclosed in plagioclase or in hornblende), euhedral garnet and biotite (Fig III.12b and c) can be present. Albite rims and replaces saussuritized plagioclase or is found in micro-veins cross-cutting plagioclase in samples G12 and P8 (Fig III.12d). Hornblende can be transformed into tremolite and calcite is occasionally present (Fig III.12e). In some samples (e.g P63), graphic textures of quartz and plagioclase indicate crystallization at the eutectic (Fig III.12f). Titanium oxides are usually transformed into titanite.

III.1.3. Mineral chemistry

III.1.3.1. *Clinopyroxenes*

Clinopyroxene has not been found in metagabbros of the crustal sequence. Clinopyroxene found in the metagabbros of the crust-mantle transition zone has been described in Chapter II.I.

III.1.3.2. *Amphiboles*

Amphibole is the most common mineral in metagabbros, occurring in all lithologies, from top to bottom: Amphibole from metagabbros of the crustal section is mainly tremolite pseudormorph after clinopyroxene.
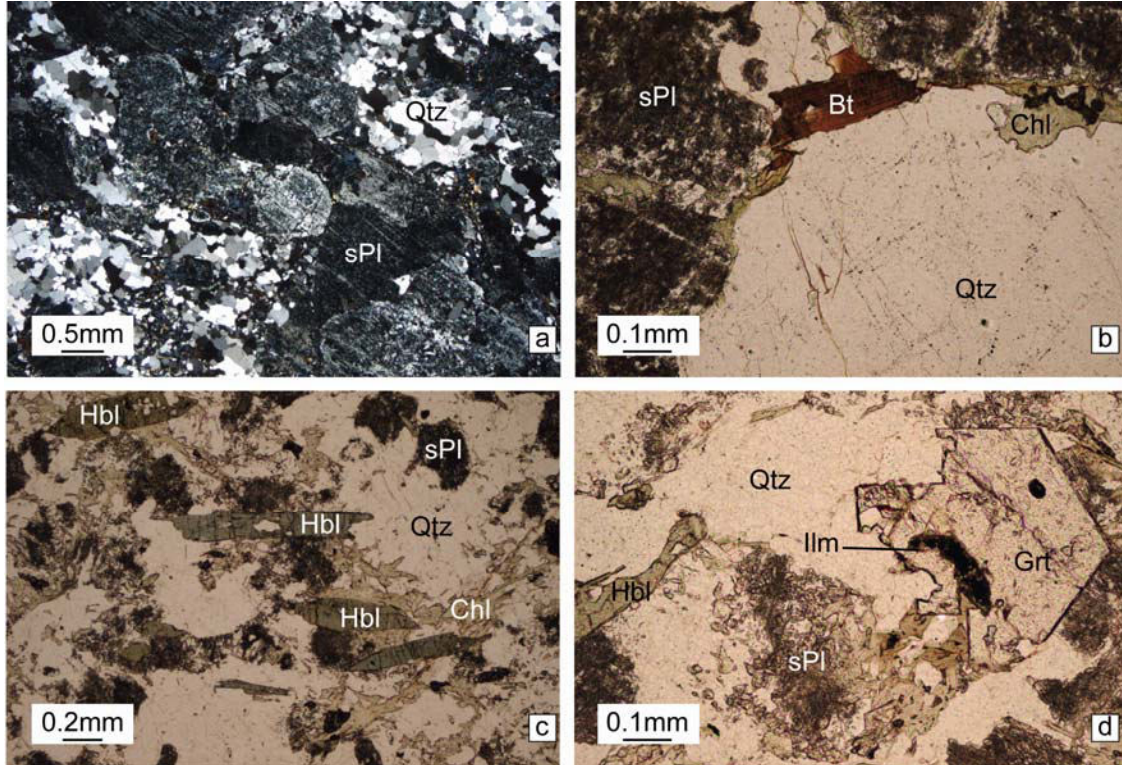
Figure III.11. Photomicrograph of tonalite interlayered with metagabbros. a) Sample G19 mainly composed of saussuritized plagioclase (sPl) and quartz (Qtz). b) Sample LG4 showing biotite (Bt) that escaped chloritization (Chl). c) euhedral Hbl and chlorite pseudomorphs after biotite in G32. d) euhedral garnet with ilmenite inclusions in G32.

Texturally, primary amphibole of likely magmatic origin is also transformed into tremolite due to greenschist facies metamorphism. In the metagabbros, amphiboles show compositions between tremolite and pargasite (Fig III.13). Magmatic amphibole from fine grained metagabbros is mainly Mg-hornblende, and that of pegmatitic metagabbros is mainly pargasitic. Magmatic amphiboles have X_{Mg} between 0.86 and 0.60 and a wide range of titanium content ($0.19 <TiO_2< 0.82$ wt%, table II.1).

Amphibole from metahornblendites is tschermakite to pargasite, with low X_{Mg} ($0.38 <X_{Mg}< 0.50$) and a narrow range of titanium content ($0.25 <TiO_2< 0.35$ wt%).

Amphiboles from one of the interlayered tonalites (sample G32) are tschermakite with low X_{Mg} (≈ 0.40) and a small range of titanium comparable to amphiboles from the meta-hornblendites ($0.22 <TiO_2< 0.37$ wt%).

Magmatic amphiboles from tonalite dykes are edenites with X_{Mg} ranging from 0.59 to 0.70, and a wide range of titanium content ($0.16 <TiO_2< 0.79$ wt%). Edenites from the

tonalite dyke in the crust mantle transition zone show the highest X_{Mg} and the lowest titanium content ($0.63 < X_{Mg} < 0.71$; $0.16 < TiO_2 < 0.29$ wt%).

Amphibole from the metagabbros in the crust-mantle transition zone is edenite to pargasite; it has a restricted X_{Mg} around 0.89, low TiO_2 (≈ 0.08 wt%) but a considerable amount of Cr_2O_3 (up to 1.45 wt%).

Trace elements of Mg-hornblendes rimming tremolite and tremolite itself have been analyzed in one fine grain metagabbro (Fig III.14, table II.2). Normalized to chondrites,
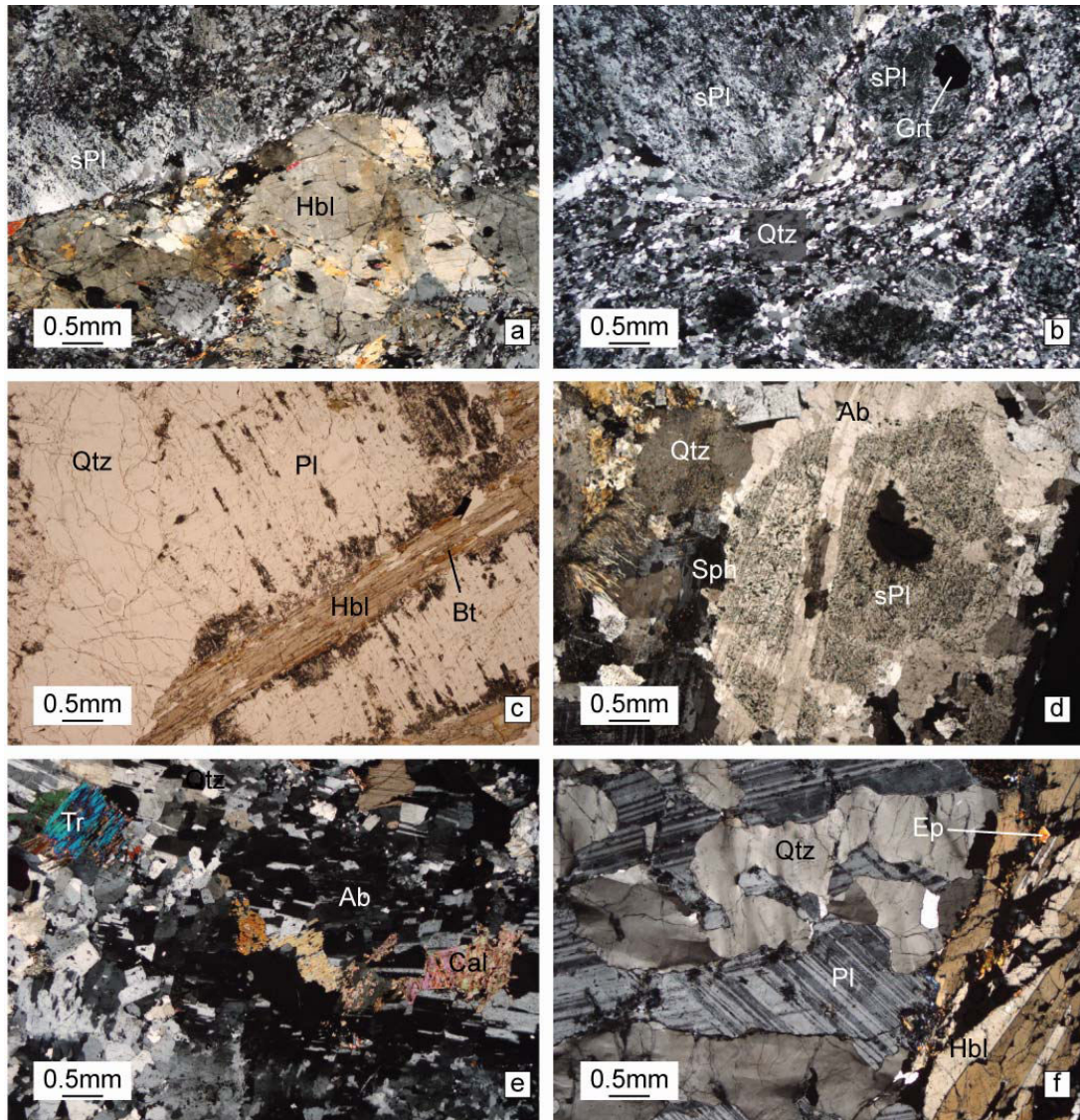
Figure III.12: Photomicrograph of tonalite dykes. a) Zoned euhedral hornblende in a matrix of saussuritized plagioclase. Sample D101. b) Sample G13 mainly composed of saussuritized plagioclase and quartz. Few subhedral garnets (Grt) are found in saussuritized plagioclase. c) Co-crystallization of hornblende and biotite in sample P63. d) Evidence for albitization in sample P8. Note the micro albite vein cross cutting saussuritized plagioclase. e) Sample G12 mainly composed of albite and tremolite overgrown by calcite. f) Graphic texture of plagioclase and quartz indicating eutectic crystallization of plagioclase and quartz in P63. Note the small magmatic epidote at the rim of hornblende.

tremolites show a flat to slightly downward HREE segment (0.9 <Dy_N/Lu_N< 2.3), a slightly fractionated MREE segment ($Sm_N/Dy_N \approx 0.4$), a strong negative Eu anomaly (Eu* =0.13-0.33), and a strongly fractionated LREE segment (La_N/Sm_N = 0.004-0.017). These trends are similar to the trends of clinopyroxene from the crust mantle transition zone (except for the negative Eu anomaly). This similarity strengthens the interpretation of tremolite as pseudomorphosed clinopyroxene.

Mg-hornblende shows a fractionated LREE segment (0.07 <La_N/Sm_N< 0.09) a slightly fractionated MREE segment ($Sm_N/Dy_N \approx 0.5$) and a rather flat HREE segment. Mg-hornblende is 6-7 times more enriched in REE than tremolite, which together with
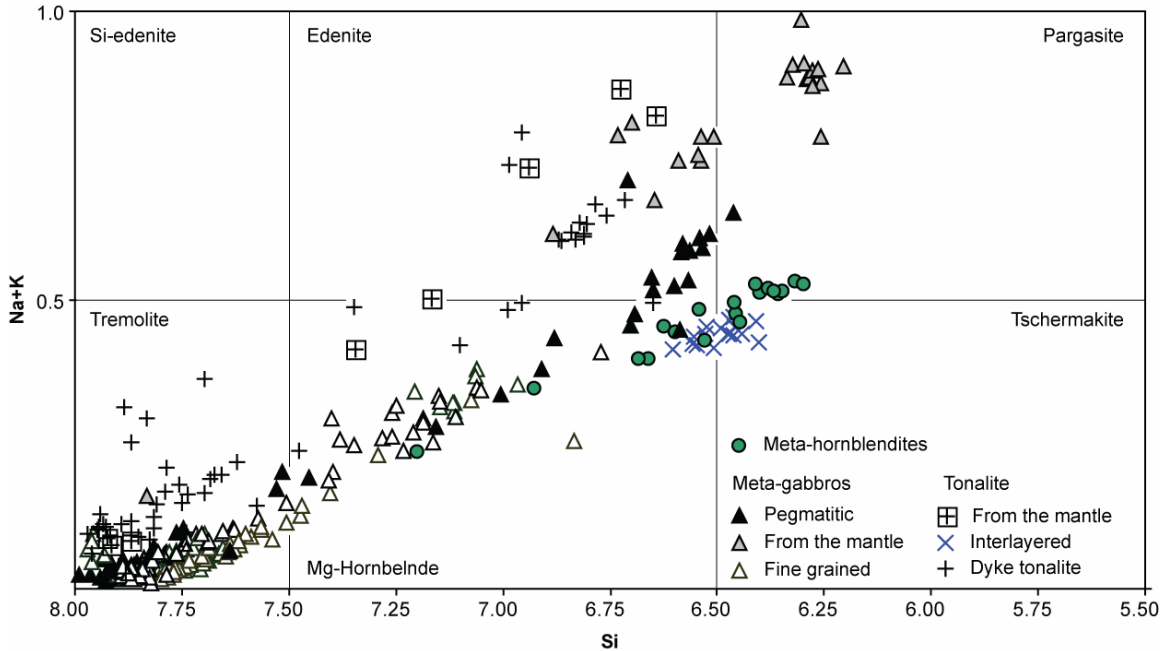
Figure III.13: Leake (1978) diagram of amphiboles from the metaplutonic rocks

the observed trends, points to a magmatic origin.

Tremolites normalized to primitive mantle show a positive Ti anomaly. Nb shows a negative anomaly and, as for the clinopyroxene of the crust mantle transition zone, Ta is decoupled from Nb. Tremolite shows a strong subchondritic Nb/Ta ratio (Nb/Ta ≈ 0.1) and shows an important Pb positive anomaly, a variably small Sr anomaly (positive or negative) and a small U positive anomaly.

Sample	Inter. Ton.		Mta.Hblite		Peg.gbro		Fine.gbro		Mantle.gbro		Tonalite dyke			
	G32		G33		G57		G25		D25		P63		D101	
	n=17	2σ	n=20	2σ	n=12	2σ	n=17	2σ	n=23	2σ	n=15	2σ	n=5	2σ
SiO2	43.00	0.57	43.52	1.83	46.00	0.59	49.51	0.85	45.72	2.85	46.99	0.84	48.54	2.73
TiO2	0.32	0.05	0.28	0.06	0.44	0.06	0.50	0.10	0.08	0.07	0.65	0.11	0.23	0.05
Cr2O3	0.02	0.05	0.01	0.01	0.14	0.03	0.01	0.01	0.57	0.44	0.01	0.01	0.01	0.01
Al2O3	15.06	0.57	14.74	3.10	12.83	0.43	5.93	0.65	13.24	3.10	9.85	0.69	8.36	2.32
FeO	18.66	0.43	17.78	3.03	8.47	0.35	11.73	0.58	4.29	0.43	14.77	0.38	13.07	1.04
MnO	0.34	0.03	0.31	0.06	0.14	0.03	0.17	0.03	0.07	0.01	0.37	0.06	0.49	0.05
MgO	6.84	0.32	7.26	2.09	15.14	0.37	15.63	0.39	17.61	1.21	12.76	0.54	14.59	1.32
CaO	11.43	0.14	12.13	2.40	12.64	0.18	11.65	0.15	12.97	0.34	11.44	0.43	11.98	0.42
Na2O	1.49	0.05	1.47	0.42	2.02	0.19	0.99	0.13	2.86	0.58	2.01	0.27	2.32	0.66
K2O	0.03	0.01	0.06	0.05	0.03	0.01	0.01	0.01	0.11	0.06	0.10	0.04	0.10	0.05
Total	97.19	0.65	97.59	0.66	97.85	0.50	96.13	0.49	97.57	0.35	98.95	0.52	99.69	0.49
XMg(Fe2)	0.40	0.01	0.40	0.10	0.76	0.01	0.72	0.02	0.71	0.19	0.61	0.02	0.67	0.04
NaK (A)	0.44	0.02	0.44	0.13	0.57	0.05	0.28	0.04	0.81	0.17	0.59	0.08	0.67	0.20
Si	6.49	0.05	6.52	0.22	6.58	0.07	7.24	0.10	6.49	0.35	6.84	0.11	6.96	0.29
Ti	0.036	0.005	0.031	0.007	0.047	0.007	0.055	0.011	0.009	0.008	0.071	0.012	0.025	0.006
Cr	0.003	0.006	0.001	0.001	0.015	0.004	0.001	0.001	0.064	0.049	0.001	0.001	0.001	0.001
Al	2.68	0.10	2.61	0.55	2.16	0.07	1.02	0.11	2.22	0.52	1.69	0.12	1.42	0.41
Fe3+	0.000	0.000	0.003	0.013	0.019	0.035	0.117	0.076	0.008	0.021	0.024	0.093	0.012	0.027
Fe2+	2.36	0.06	2.23	0.39	0.99	0.03	1.32	0.10	0.50	0.05	1.77	0.10	1.56	0.16
Mg	1.54	0.07	1.62	0.46	3.23	0.07	3.40	0.08	3.72	0.22	2.77	0.12	3.12	0.24
Ca	1.85	0.03	1.95	0.38	1.94	0.03	1.82	0.03	1.97	0.04	1.78	0.06	1.84	0.04
Al4	1.51	0.05	1.48	0.22	1.42	0.07	0.76	0.10	1.51	0.35	1.16	0.11	1.04	0.29
Al6	1.17	0.07	1.13	0.42	0.74	0.04	0.26	0.05	0.71	0.19	0.53	0.06	0.38	0.13

Table III.1: Representative magmatic amphibole analyses. Recalculation assuming no Na on M4 site

Y shows a small depletion compared to neighbor elements. Mg-hornblendes have a small negative Ti anomaly, and a strong Zr-Hf depletion. Nb and Ta do not show anomalous behavior. Sr shows a negative anomaly, and Pb shows no anomaly.

Edenites from the garnet-bearing tonalite (G32) have a peculiar chondrite normalized REE pattern with a fractionated trend ($0.01 < La_N/Lu_N < 0.06$) and a positive Eu anomaly. Such a trend suggests that edenites have been extensively re-equilibrated with other minerals, or are pseudomorphs of unknown origin. Their primitive mantle normalized pattern shows positive Ti, Zr and Hf anomalies. Nb is enriched compared to neighbor elements and Nb-Ta ratios are extremely suprachondritic ($51 < Nb/Ta < 108$). Pb and Sr show a slight positive anomaly whereas concentrations in Th, Ba, Rb and Cs are extremely low.

Edenites from the D101 tonalite dyke in the crust mantle transition zone also show unusual patterns for amphiboles. The chondrite normalized patterns show a fractionated M-HREE segment ($Sm_N/Lu_N \approx 0.2$), a strong negative Eu anomaly ($Eu^* \approx 0.02$) and a strongly fractionated LREE segment ($La_N/Sm_N \approx 0.02$). Normalized to primitive mantle, the pattern shows a strong Ti negative anomaly, a slight negative Zr anomaly but no Hf anomaly. Whereas Nb is depleted, Ta is enriched compare to Nb and La and Nb-Ta ratios are infrachondritic with values comparable to Nb-Ta ratios found in the metagabbro Cpx $Nb/Ta \approx 4$). Sr shows a negative anomaly, there is no Pb anomaly and U is enriched compared to neighbor elements. Th as extremely low values (Th = 0.0004 ppm).
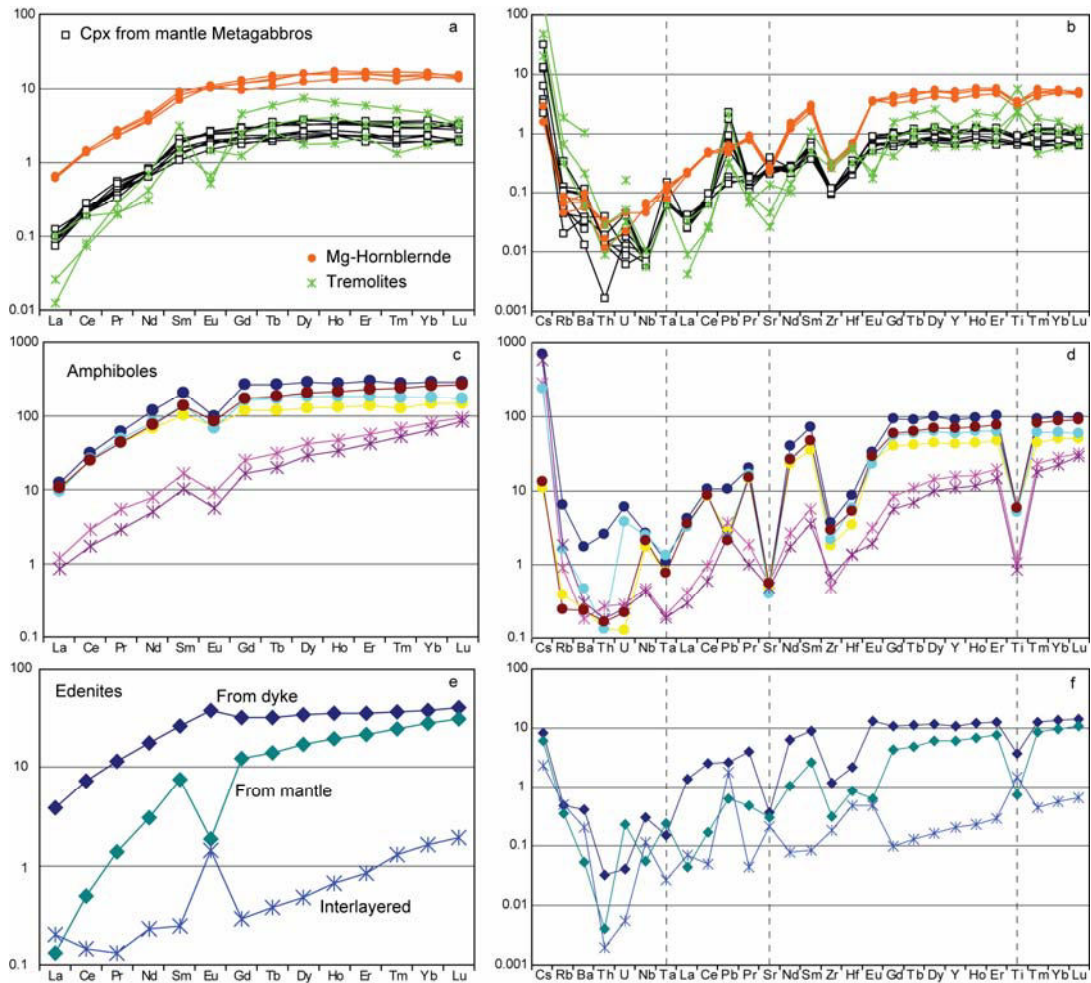
Figure III.14. Amphibole compositions normalized to chondrite (left column) and primitive mantle (right column). Normalized values from Sun and McDonough, (1989) a) and b): amphiboles from fine grain metagabbros compared to Cpx from the metagabbro of the crust mantle transition zone. c) and d) amphiboles from sample P8, tonalite dyke. e) and f) amphiboles from tonalitic samples. P63=dyke; D101=from the mantle; G32=interlayered tonalite

Amphiboles from the tonalite dyke cross cutting pipe 1 (sample P8) show two types of trace element patterns uncorrelated with major elements: (i) Two have a fractionated chondrite normalized REE pattern comparable to edenites from the tonalite dyke of the crust mantle transition zone (D101), a fractionated M-HREE segment ($Sm_N/Lu_N \approx 0.15$) a negative Eu anomaly (Eu* ≈ 0.45) and a fractionated LREE segment ($La_N/Sm_N \approx 0.07$). (ii) Four others are tenfold more enriched and show a flat HREE segment, a similar Eu negative anomaly than the previous ones, and a fractionated LREE segment ($La_N/Sm_N \approx 0.6$). Both amphibole types normalized to primitive mantle show extreme Ti, Zr and Hf negative anomalies and suprachondritic Nb-Ta ratios (32 <Nb/Ta < 46). Both have a strong negative Sr anomaly. The main difference between the two groups are Pb anomalies, positive in the less REE rich amphiboles and negative in the other amphiboles, in the primitive mantle normalized diagram.

Sample	D101		G25				P8				P63		G32	
Mineral	Hbl n=3	2σ	Tr n=3	2σ	Hbl n=4	2σ	Hbl n=4	2σ	Hbl n=2	2σ	Hbl n=2	2σ	Hbl n=4	2σ
B	6.38	1.10	1.20	1/3	<0.94		6.61	1.47	11.05	0.22	5.20	0.25	6.69	0.82
Sc	38.27	2.20	149.97	48.78	115.13	14.32	91.84	31.20	41.36	8.15	33.39	0.89	20.16	5.49
V	20.86	3.05	449.68	185.20	643.01	90.32	75.74	15.21	27.33	5.10	744.93	328.69	373.47	171.52
Cr	34.15	34.71	135.48	104.06	51.81	25.80	99.04	57.97	48.14	3.35	1.95	0.03	3.40	5.13
Mn	3385	75	8310	8585	1496	95	6502	1477	16874	4042	2824	201	2450	50
Co	45.90	3.26	421.04	493.53	87.70	4.30	35.13	2.60	40.63	6.71	58.23	0.07	48.17	1.70
Ni	58.14	27.19	483.95	584.01	118.03	7.03	41.81	3.37	47.76	2.33	78.75	6.65	8.72	4.58
Cu	0.54	1/3	427.04	512.75	2.06	1.31	1.16	0.84	0.62	0.66	1.67	0.07	1.51	1.23
Zn	114.13	5.53	631.08	730.87	86.73	4.04	231.50	61.74	228.57	15.29	90.01	1.64	199.20	8.17
Li	0.31	0.19	20.44	27.21	0.17	0.09	2.99	1.37	2.01	0.82	6.11	1.65	2.07	0.66
Cs	0.048	0.012	0.614	0.603	0.018	0.008	1.885	2.543	3.376	1.675	0.065	0.039	0.018	0.005
Rb	0.228	0.033	0.613	0.522	0.042	0.011	1.377	1.832	0.887	0.443	0.310	0.007	0.321	0.039
Ba	0.377	0.102	3.060	3.668	0.519	0.123	4.765	5.055	1.742	0.620	2.837	1.193	1.432	0.146
Th	0.00035	0.00001	0.00160	0.00118	0.00190	0.00085	0.06511	0.10540	0.01940	0.00537	0.00284	0.00026	0.00017	1/4
U	0.0048	1/3	0.0018	0.0015	0.0007	0.0004	0.0538	0.0612	0.0058	0.0006	0.0009	0.0003	0.0001	1/4
Nb	0.0409	0.0095	0.0057	0.0024	0.0423	0.0068	1.6128	0.3062	0.3250	0.0212	0.2133	0.0728	0.0825	0.0061
Ta	0.0099	0.0093	0.0025	1/3	0.0045	0.0010	0.0418	0.0110	0.0083	0.0005	0.0063	0.0021	0.0011	0.0004
La	0.031	0.004	0.011	0.011	0.152	0.006	2.481	0.282	0.246	0.057	0.925	0.110	0.048	0.050
Ce	0.303	0.062	0.069	0.039	0.859	0.028	16.073	1.721	1.412	0.491	4.510	0.707	0.089	0.120
Pb	0.045	0.025	0.066	0.074	0.039	0.005	0.317	0.292	0.218	0.067	0.184	0.003	0.126	0.050
Pr	0.132	0.054	0.021	0.004	0.234	0.019	4.570	0.737	0.393	0.167	1.100	0.225	0.012	0.018
Sr	6.51	7.79	1.49	1.26	5.51	0.47	10.46	1.41	11.20	1.06	7.74	0.33	4.57	3.50
Nd	1.418	0.373	0.222	0.096	1.860	0.183	39.193	10.061	2.982	0.888	8.430	1.937	0.108	0.114
Sm	1.15	0.29	0.35	0.18	1.23	0.13	22.07	6.81	2.04	0.65	4.01	0.97	0.04	0.04
Zr	3.50	1.03	29.46	45.29	3.31	0.23	29.89	9.57	6.65	1.48	13.24	3.28	2.05	0.15
Hf	0.270	0.104	0.150	0.044	0.194	0.016	1.797	0.660	0.425	0.018	0.674	0.117	0.148	0.036
Eu	0.106	0.092	0.050	0.029	0.604	0.018	4.605	0.730	0.430	0.143	2.186	0.395	0.082	0.065
Gd	2.54	0.48	0.57	0.34	2.35	0.29	36.64	12.90	4.22	1.18	6.54	1.24	0.06	0.06
Tb	0.523	0.073	0.147	0.065	0.483	0.064	6.835	2.232	0.947	0.296	1.197	0.220	0.014	0.010
Dy	4.403	0.453	1.105	0.726	3.730	0.419	50.775	16.583	8.825	2.298	8.745	1.803	0.120	0.067
Y	27.75	3.22	4.24	1.59	21.24	2.58	297.81	93.39	60.12	14.25	50.05	11.18	0.95	0.41
Ho	1.10	0.17	0.23	0.13	0.87	0.09	11.20	3.44	2.24	0.51	1.99	0.41	0.04	0.02
Er	3.60	0.22	0.62	0.31	2.57	0.22	34.66	11.16	8.13	1.64	5.98	1.25	0.14	0.05
Ti	964	208	4535	2507	4219	466	7213	455	1244	206	4764	591	1941	213
Tm	0.62	0.03	0.08	0.05	0.37	0.04	5.17	1.64	1.49	0.27	0.93	0.23	0.03	0.01
Yb	4.80	0.47	0.53	0.25	2.57	0.17	36.82	11.21	12.44	1.86	6.60	1.69	0.28	0.04
Lu	0.80	0.09	0.07	0.02	0.36	0.02	5.49	1.73	2.26	0.15	1.04	0.27	0.05	0.01

Table III.2: Amphiboles trace element composition measured by LA-ICPMS

III.1.3.3. Garnet

Garnets are found in the metagabbros of the crust mantle transition zones (samples D25 and D104), in one of the metahornblendites (sample G33), in one of the interlayered tonalite (sample G32) and in some of the tonalitic dykes (samples G13, P68 and P98).

Garnet from the metagabbros of the crust mantle transition zones are secondary Cr-rich grossular (up to 14 wt% Cr_2O_3) (Fig. III.15, table II.3). Garnet from the interlayered tonalite is similar in composition to garnet of the metahornblendite (G33). These garnets have ≈ 55% of almandine component, ≈ 30% grossular, 12% spessartine and 5% pyrope. Some garnets found in cm-wide tonalite dykes of pipe 2 (e,g P98) are made of 65% almandine 25% grossular and 10% spessartine component.

The fractionated pattern ($La_N/Lu_N ≈ 0.02$) of euhedral G32 garnets (table II.4) normalized to chondrite (Fig. III.15) indicates a magmatic origin. In contrast, garnet from one tonalitic dyke (P98) formed from plagioclase through metamorphic reactions as indicated by a slightly fractionated M-REE pattern ($Sm_N/Lu_N ≈ 2.3$) a strong Eu positive anomaly and a strongly fractionated LREE segment ($La_N/Sm_N ≈ 0.005$).

Below: Table III.3; representative major element composition of garnet from mantle metagabbros, interlayered and dyke tonalite

Right: Table III.4; Some of the trace element compositions of garnet from interlayered tonalite and tonalite dyke (P98).

Sample	G32		P98	
Mineral	Grt n=5	2σ	Grt n=3	2σ
B	3.15	0.28	2.39	0.28
Sc	30.40	28.24	0.29	0.09
V	172.82	107.23	1.58	2.30
Cr	4.97	3.86	0.28	0.06
Mn	46675	2551	24732	5830
Co	8.98	0.54	12.31	0.35
Ni	2.26	0.46	1.49	0.38
Cu	0.14	0.08	25.80	44.43
Zn	15.11	1.16	31.97	17.48
Li	0.49	0.22	0.26	0.09
Cs	0.006	0.004	0.049	0.025
Rb	0.011	0.002	0.037	0.005
Ba	0.180	0.242	0.107	0.076
Th	0.00130	0.00115	<0.0003	
U	0.0005	0.0005	0.0002	1/3
Nb	0.0103	0.0057	0.0015	0.0002
Ta	0.0018	0.0007	<0.0006	
La	0.153	0.237	0.002	0.001
Ce	0.577	0.956	0.010	0.006
Pb	0.069	0.056	0.125	0.174
Pr	0.127	0.214	0.006	0.003
Sr	5.61	5.97	3.37	3.24
Nd	0.924	1.597	0.162	0.118
Sm	0.40	0.71	0.25	0.26
Zr	1.93	0.27	0.026	0.003
Hf	0.027	0.014	0.001	1/3
Eu	0.141	0.181	1.780	0.928
Gd	0.86	1.08	0.321	0.269
Tb	0.168	0.170	0.045	0.033
Dy	1.425	1.324	0.263	0.194
Y	11.71	11.06	1.41	0.88
Ho	0.44	0.45	0.04	0.02
Er	1.87	2.09	0.11	0.06
Ti	928	294	42	45
Tm	0.43	0.51	0.02	0.01
Yb	4.41	5.70	0.11	0.08
Lu	0.93	1.24	0.02	0.02

	Mantle mtagbro.		Interlayered Ton.		Tonalite dyke	
Sample	D25		G32		P98	
	n=3	2σ	n=63	2σ	n=22	2σ
SiO2	38.49	0.57	38.11	0.20	38.12	0.33
TiO2	0.17	0.05	0.16	0.08	0.03	0.06
Cr2O3	10.75	3.60	0.01	0.01	0.00	0.00
Al2O3	13.60	3.07	21.23	0.13	21.24	0.20
FeO	2.26	0.96	23.91	0.78	30.76	2.17
MnO	0.55	0.27	6.58	0.71	3.56	1.33
NiO	0.01	0.02	0.00	0.00	0.01	0.01
MgO	0.24	0.17	0.95	0.08	0.38	0.31
CaO	35.29	1.61	10.27	0.34	7.95	1.59
Na2O	0.00	0.00	0.01	0.01	0.08	0.36
K2O	0.00	0.00	0.00	0.00	0.01	0.05
Total	101.38	0.23	101.23	0.38	102.15	0.74
Pyr.	0.01	0.00	0.04	0.00	0.01	0.01
Alm.	0.00	0.01	0.51	0.02	0.66	0.08
Gros.	0.58	0.14	0.28	0.01	0.22	0.04
Spes.	0.01	0.00	0.14	0.01	0.08	0.03

Fig III.15: Compositions of garnets found within the metaplutonic rocks. Left: ternary diagram of major element. Right: chondrite normalized pattern of garnet from sample G32 (interlayered tonalite) and P98 (tonalite dyke in pipe 2)

<u>*III.1.3.4.*</u>   *Plagioclase*

None of the analyzed plagioclase contains potassium, and K-feldspar has not been found. In the crustal metagabbros, apart from metamorphic albite, samples in which plagioclase could be analyzed show anorthite component around 24.5%.

The G32 interlayered tonalite contains plagioclase ranging between 18 and 27 %An. Albite is a metamorphic product.

A wide range of plagioclase compositions is found in the tonalite dykes. Cores of D101 saussuritized plagioclase have 24%An component, whereas rims are albite. Within dyke G12, plagioclase has an anorthite component <7%. In dyke P8, plagioclase hardly reaches 10%An and albitization is widespread, with albite rimming saussuritized plagioclase and occurring in micro veins cutting the saussuritized plagioclase. All of these plagioclases reflect metamorphic re-equilibration. Within dyke P63, plagioclase goes up to 40%An, without albitization. Other tonalite dykes have a wide range of An content depending on their textural relationships with other minerals, ranging from 20%An in contact with garnet to 90%An in contact with the hornblende-rich rim.

III.1.4.   Bulk rock chemistry

<u>*III.1.4.1.*</u>   *Major elements*

Some of the crustal pyroxenites and dunites described in Chapter III.2 have been analyzed (analytical technique in Appendix 1, table II.5, 6). X_{Mg} of dunites ranges from 0.84 to 0.91 with high MgO (37.85-48.90 wt %), and low silica content ($\approx$ 40 wt % SiO_2) (Fig III.16, table II.6). The Ti and Na contents are close to detection limit (DL) with 0.01-0.02 wt % oxide. Ca and Al are also very low (0.62-1.28 CaO wt %; $\approx$ 0.35 Al_2O_3 wt %). MnO increases with decreasing X_{Mg}, between 0.15 and 0.25 wt %. Likewise, pyroxenites have a wide range in X_{Mg} (0.83-0.90) with MgO content ranging from 18.0 to 26.8 wt % and SiO_2 content ranging from 45.5 to 52.6 wt %, reflecting a wide range in mineralogy. Ti contents show a slight increase with decreasing X_{Mg}, from 0.04 to 0.15 wt %, as well as Al_2O_3 and MnO contents (0.83-9.5 wt %; 0.11-0.18 wt % respectively). The CaO content slightly decreases with decreasing X_{Mg}, from 21.0 to 11.0 wt %. The Ni content is scattered between 119 and 383 ppm. Ultramafic rocks from pipe 1 show higher X_{Mg} values than ultramafic rocks from pipe 2.

Metagabbros have X_{Mg} values ranging from 0.88 to 0.61. The silica content shows a slight increase from X_{Mg} = 0.88 and SiO_2 = 40 wt% to X_{Mg} = 0.75 and SiO_2= 48 wt%. From X_{Mg} = 0.75 SiO_2 decreases at 45wt % to X_{Mg} = 0.61. Ti (0.09< TiO_2 wt% < 0.28) and Mn (0.09< MnO wt% < 0.22) contents increase with decreasing X_{Mg}. Al does not show a clear relationship with decreasing X_{Mg}. Mg and Ca decrease slightly with decreasing X_{Mg} (7.98< MgO wt% <14.91; 13.26< CaO wt% < 16.57). Ni decreases clearly with decreasing X_{Mg} (42 < Ni ppm < 207.5), and the K content of the metagabbros is at the detection limit (0.01 K_2O wt%).

Unit		Sample	Location: Deg° Min'	type	magmatic	metamorphic
MANTLE		D101	N 35°01.751' E 73°45.031	fine grained meta-leucotonalite	Hbl-Pl-Qtz?	Tr-Ep-Chl-Grt-Ab-Qtz?
CRUST	Meta-Plutonics	G8	N 35°01.718' E 73°44.840'	fine grained meta-melanogabbro	Cpx ? Pl ? TiOx	Tr-Ep-Chl
		G10	N 35°01.900' E 73°44.689'	fine grained meta-melanogabbro	Cpx ? Hbl ? Pl ?	Hbl ?-Tr-Ep-Chl-Q
		G16	N 34°59.899' E 43°42.155'	fine grained metagabbro	Cpx ? Hbl ? Pl ? TiOx	Hbl ?-Tr-Ep-Chl
		G22	N 35°00.575' E 73°42.436'	fine grained metagabbro	Cpx ? Pl ?	Tr-Ep-Chl
		G36	N 34°59.705' E 73°42.754'	pegmatitic metagabbro	Cpx ? Pl ? TiOx	Tr-Ep-Chl
		G39	N 35°01.082' E 73°42.908'	fine grained metagabbro	Cpx ? Pl ? Hbl ?	Tr-Ep-Chl-Hbl ?
		G45	N 35°01.529' E 73°42.670'	fine grained metagabbro	Cpx ? Pl ? Hbl ? TiOx	Hbl?-Tr-Ep-Chl -Sph
		G49	N 35°01.087' E 73°43.580'	fine grained metagabbro	Cpx ? Pl ? Ep ? TiOx	Tr-Ep-Chl-Sph
		G50	N 35°01.172' E 73°43.549'	fine grained meta-leucogabbro	Cpx ? Hbl ? Pl ?	Hbl ?-Tr-Ep-Chl
		G59	N 35°02.787' E 73°45.981'	fine grained metagabbro	Cpx ? Pl ? Ep ?	Tr-Ep-Chl
		G11	N 35°02.082' E 73°44.554'	pegmatitic metagabbro	Cpx ? Pl ?	Tr-Ep-Chl
		G46	N 35°01.516' E 73°42.566'	pegmatitic metagabbro	Cpx ? Pl ? TiOx	Tr-Ep-Chl
		G54	N 35°03.005' E 73°45.381'	pegmatitic metagabbro	Cpx ? Pl ? TiOx	Tr-Ep-Chl
		G56	N 35°03.450' E 73°45.471'	pegmatitic metagabbro	Cpx ? Pl ? Ep ? Qtz ?	Tr-Ep-Chl-Qtz ?
		G57	N 35°03.436' E 73°45.493'	pegmatitic metagabbro	Cpx ? Pl ? TiOx	Tr-Ep-Chl
		G33	N 35°00.899' E 73°43.983'	fine grained metahornblendite	Hbl-Grt-Qtz	Tr-Ep-Chl
		G42	N 35°01.373' E 73°42.932'	fine grained metahornblendite	Hbl-Bt-TiOx	Tr-Ep-Chl-Sph
		G48	N 35°01.087' E 73°43.580'	fine grained metahornblendite	Hbl-Bt-TiOx	Tr-Ep-Chl-Sph
		G12	N 35°02.082' E 73°44.554'	fine grained trondhjemite	Hbl-Pl-TiOx	Ab-Tr-Cal-Ep
		G13	N 35°01.206' E 73°44.335'	fine grained meta-leucotonalite	Grt-Pl-Bt-Qtz-TiOx	Ep-Chl
		G14	N 34°59.774' E 73°42.793'	fine grained meta-tonalite	Pl-Qtz-Bt ?-TiOx	Ep-Chl
		G19	N 35°00.899' E 73°43.983'	fine grained meta-tonalite	Grt-Hbl-Pl-Q-Bt ?	Ep-Chl
		G24	N 35°00.329' E 73°42.281'	fine grained meta-leucotonalite	Pl-Qtz	-
		G32	N 35°01.127' E 73°44.465'	fine grained meta-tonalite	Hbl-Grt-Pl-Bt-TiOx	Ep-Chl-Sph
		LG4	N 34°58.256' E 73°41.148'	fine grained meta-tonalite	Pl-Qtz-Bt-TiOx	-
	Pipe 1	P7	N 35°01.010' E 73°42.166'	heterograular clinopyroxenite	Cpx-Hbl-Spl	Tr
		P9	N 35°00.614' E 73°42.147'	fine grained clinopyroxenite	Cpx-Hbl-Spl	-
		P18	N 35°00.733' E 73°41.927'	fine grained clinopyroxenite	Cpx-Hbl-Spl	Tr-serp
		P22	boulder	Coarse dunite-relictual Cpx	Ol-Spl (Cpx)	-
		P8	N 35°01.021' E 73°42.154'	fine grained trondhjemite	Hbl-Pl-Grt ?	Ab-Prg-Tr-Ep-Grt ?
	Pipe 2	P42	N 35°03.349' E 73°45.728'	background pyroxenite	Ol-Cpx-Hbl±Opx	-
		P30	N 35°03.028' E 73°45.297'	background pyroxenite	Ol-Cpx-Hbl±Opx	-
		P51	N 35°03.412' E 73°45.612'	Pl bearing pyroxenite	Ol-Cpx-Hbl-Opx-Pl	-
		P64	N 35°04.154' E 73°45.633'	dunite	Ol-Cpx	-
		P45	N 35°03.396' E 73°45.711'	dunite	Ol	Serp
		P31	N 35°03.017' E 73°45.273'	fine grained metagabbro	Cpx-Hbl ?-Pl?-Ep?	Tr-Ep-Chl
		P63	N 35°04.086' E 73°45.780'	fine grained tonalite	Hbl-Bt-Pl-Ep-Qtz	Tr-Ep

Table III.5: Number, location and paragenetic description of samples analyzed for major and trace element compositions (procedure in Appendix 1). Isotopic compositions of some of them are given in table II.7. All the lithologies of the Sapat Complex are represented
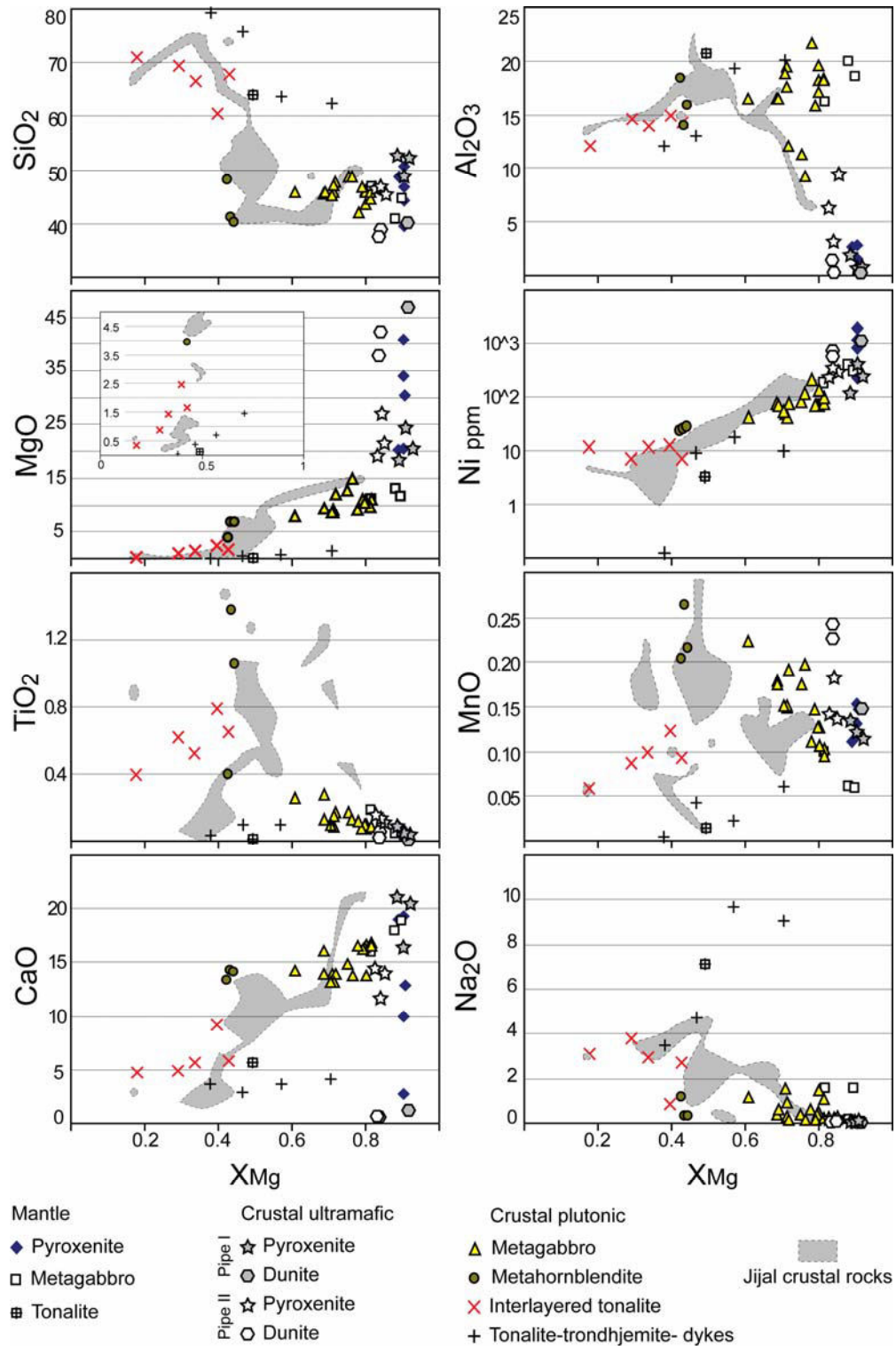
Figure III.16: Major element *vs* X_{Mg} variations of the different lithologies. The crustal rocks of Jijal (analyses from Dhuime et al., 2007; Garrido et al.,2006, and Zeilinger, 2002) are shown for comparison.

| | Pyroxenite bodies | | | | | | | | | Metaplutonic series | | | |
| | Pipe 1 | | | | Pipe 2 | | | | | Metahornblendites | | | Met.gbro |
Sample	P7	P9	P18	P22	P42	P51	P30	P64	P45	G33	G48	G42	P31
SiO2	52.29	52.64	48.82	40.34	46.93	45.50	46.61	37.61	38.93	48.09	41.01	40.09	43.33
TiO2	0.037	0.082	0.039	0.014	0.128	0.107	0.146	0.052	0.022	0.397	1.379	1.058	0.089
Al2O3	0.82	1.86	0.83	0.35	3.08	9.50	6.36	1.42	0.38	18.46	14.06	15.83	19.57
Fe2O3	3.90	5.17	5.71	9.56	11.27	8.14	8.81	16.34	17.86	11.73	19.49	18.53	5.99
MnO	0.113	0.132	0.120	0.146	0.182	0.135	0.141	0.225	0.242	0.204	0.263	0.215	0.105
MgO	20.27	18.01	24.27	46.90	26.78	21.29	19.05	37.84	42.24	3.95	6.80	6.73	10.89
CaO	20.38	21.03	16.38	1.29	11.66	13.90	14.47	0.62	0.62	13.39	14.19	14.18	16.57
Na2O	0.067	0.106	0.069	0.000	0.119	0.245	0.184	0.000	0.000	1.158	0.292	0.306	0.454
K2O	0.000	0.000	0.003	0.000	0.004	0.021	0.007	0.002	0.003	0.029	0.023	0.117	0.016
P2O5	0.007	0.006	0.006	0.006	0.009	0.011	0.007	0.009	0.008	0.102	0.007	0.010	0.018
Cr2O3	0.543	0.345	0.413	1.317	0.195	0.191	0.285	0.019	0.012	0.002	0.001	0.002	0.087
NiO	0.029	0.015	0.047	0.140	0.045	0.036	0.029	0.069	0.091	0.003	0.003	0.003	0.015
LOI	1.813	1.140	3.973	0.400	0.080	0.855	4.134	5.952	-0.476	1.487	2.447	2.899	3.053
Total	100.27	100.53	100.69	100.46	100.48	99.92	100.24	100.16	99.94	99.01	99.97	99.98	100.20
XMg	0.920	0.885	0.903	0.915	0.839	0.852	0.826	0.836	0.839	0.426	0.435	0.444	0.800
Cs	0.293	0.278	0.049	0.003	0.054	0.179	0.082	0.103	0.040	0.005	0.400	7.786	0.110
Rb	0.052	0.206	0.015	0.017	0.208	0.257	0.095	0.060	0.052	0.160	0.581	6.748	0.215
Ba	0.82	0.72	0.30	0.07	3.10	2.86	1.39	0.58	1.09	5.91	2.42	5.37	2.76
Th	0.0029	0.0048	0.0010	0.0018	0.0083	0.0286	0.0060	0.0071	0.0065	0.0126	0.0037	0.0036	0.0059
U	0.0017	0.0014	0.0006	0.0001	0.0027	0.0116	0.0020	0.0026	0.0018	0.0049	0.0008	0.0022	0.0048
Nb	0.0040	0.0055	0.0058	0.0107	0.0140	0.0515	0.0150	0.0227	0.0180	0.0688	0.0288	0.0113	0.0132
Ta	0.00022	0.00018	0.00178	0.00085	0.00058	0.00623	0.00067	0.00103	0.00059	0.00663	0.00317	0.00166	0.00321
La	0.040	0.021	0.012	0.011	0.047	0.044	0.046	0.042	0.023	0.495	0.027	0.036	0.089
Ce	0.053	0.069	0.035	0.024	0.144	0.131	0.152	0.106	0.052	1.589	0.111	0.091	0.218
Pb	0.036	0.076	0.046	0.015	0.178	1.831	0.097	0.209	0.112	0.267	0.056	0.209	0.381
Pr	0.011	0.014	0.006	0.003	0.029	0.025	0.033	0.016	0.007	0.303	0.030	0.021	0.037
Sr	2.89	3.80	2.19	0.44	10.00	28.84	6.89	4.12	2.35	119.65	45.99	51.31	95.69
Nd	0.069	0.107	0.048	0.017	0.227	0.187	0.260	0.104	0.035	2.095	0.292	0.184	0.236
Sm	0.037	0.075	0.033	0.009	0.138	0.110	0.155	0.042	0.012	0.964	0.220	0.119	0.108
Zr	0.098	0.260	0.100	0.073	0.861	0.977	0.898	0.381	0.154	2.629	0.645	0.420	0.706
Hf	0.004	0.012	0.004	0.002	0.035	0.032	0.041	0.015	0.004	0.120	0.035	0.021	0.030
Eu	0.020	0.043	0.018	0.004	0.078	0.076	0.066	0.019	0.006	0.763	0.263	0.157	0.103
Gd	0.074	0.169	0.074	0.016	0.286	0.229	0.320	0.071	0.022	1.779	0.543	0.278	0.215
Tb	0.015	0.035	0.016	0.004	0.057	0.046	0.064	0.014	0.004	0.340	0.113	0.056	0.042
Dy	0.127	0.288	0.128	0.028	0.445	0.358	0.493	0.105	0.035	2.607	0.910	0.451	0.312
Y	0.741	1.677	0.737	0.158	2.535	1.962	2.598	0.636	0.231	12.204	4.548	2.365	1.594
Ho	0.028	0.064	0.028	0.007	0.098	0.079	0.107	0.024	0.009	0.582	0.202	0.102	0.068
Er	0.080	0.185	0.079	0.021	0.277	0.223	0.306	0.075	0.030	1.711	0.589	0.302	0.184
Ti	201.5	479.9	214.2	59.7	753.2	774.2	882.1	317.0	111.1	2484.9	8290.3	6748.5	522.9
Tm	0.012	0.027	0.012	0.004	0.040	0.032	0.044	0.012	0.005	0.258	0.085	0.044	0.026
Yb	0.075	0.170	0.073	0.027	0.253	0.197	0.276	0.092	0.043	1.758	0.549	0.293	0.163
Lu	0.012	0.028	0.012	0.005	0.042	0.032	0.046	0.018	0.009	0.305	0.093	0.050	0.026

Table III.6: Major and trace element composition of analyzed samples

Metahornblendites have similar X_{Mg} ($X_{Mg} \approx 0.43$) with a wide range in TiO_2 (0.40-1.38 wt%), SiO_2 (40.09-48.09 wt %), Al_2O_3 (14.06-18.46 wt %), MnO (0.20-0.26 wt %), MgO (3.95-6.73 wt %) and K_2O (0.02-0.12 wt %); whereas CaO and Ni have a restricted range (14 wt % and 26.8 ppm respectively).

Tonalitic sills interlayered with the metagabbros have a low X_{Mg} ranging from 0.18 to 0.43. The SiO_2 (60.47-71.06 wt %) and Na_2O (0.82-3.06 wt %) contents increase with decreasing X_{Mg}. In contrast, TiO_2, Al_2O_3, MnO, CaO and MgO decrease with decreasing X_{Mg}, whereas the Ni content stays rather constant (Ni $\approx$ 10 ppm).

Dykes have a wide X_{Mg} (0.38 to 0.71) and very low MgO contents (0.05-1.45 wt%).The MgO content decreases with X_{Mg}, as well as TiO_2 (0.04-0.10 wt %), Al_2O_3 (12.13-20.11 wt %), MnO (< 0.06 wt %), Na_2O (0.38-9.66 wt %) and Ni (0.1-18.6 ppm). SiO_2 contents increase to extreme value (62.64-79.51 wt %) with decreasing X_{Mg}, and CaO stay rather constant (2.95-5.6 wt %).

| | Metaplutonic series | | | | | | | | | | | | |
| | Metagabbros | | | | | | | | | | | | |
Sample	G22	G39	G36	G59	G49	G8	G10	G16	G45	G50	G54	G56	G46
SiO2	45.95	45.19	48.88	48.67	45.84	45.54	47.80	46.00	46.39	46.84	47.13	44.65	45.87
TiO2	0.090	0.092	0.128	0.175	0.258	0.272	0.172	0.129	0.077	0.079	0.152	0.087	0.088
Al2O3	19.45	18.91	9.32	11.32	16.43	16.55	12.13	16.53	18.26	15.95	17.59	18.32	18.18
Fe2O3	7.77	8.01	10.18	9.34	11.29	9.47	10.45	9.42	5.97	6.48	8.22	5.52	4.84
MnO	0.149	0.151	0.198	0.175	0.223	0.179	0.192	0.176	0.128	0.148	0.151	0.103	0.095
MgO	8.72	8.79	14.91	12.82	7.98	9.41	12.08	9.47	10.84	11.11	9.26	11.00	9.60
CaO	13.97	13.27	13.84	14.92	14.33	16.15	13.96	14.00	13.86	16.22	13.18	16.80	16.58
Na2O	0.316	1.516	0.151	0.365	1.178	0.355	0.150	0.644	1.461	0.135	0.962	0.246	1.085
K2O	0.007	0.005	0.004	0.013	0.007	0.004	0.016	0.019	0.014	0.011	0.010	0.022	0.053
P2O5	0.008	0.007	0.007	0.007	0.008	0.009	0.007	0.008	0.008	0.007	0.008	0.008	0.008
Cr2O3	0.004	0.008	0.041	0.056	0.002	0.036	0.057	0.011	0.008	0.012	0.011	0.027	0.067
NiO	0.006	0.007	0.015	0.010	0.005	0.010	0.010	0.009	0.009	0.009	0.005	0.010	0.012
LOI	3.614	3.213	2.600	1.800	2.347	2.380	2.579	3.008	3.273	2.739	3.199	3.067	3.378
Total	100.05	99.17	100.27	99.67	99.91	100.36	99.60	99.43	100.29	99.75	99.87	99.85	99.86
XMg	0.712	0.707	0.763	0.751	0.609	0.686	0.718	0.689	0.800	0.790	0.713	0.814	0.814
Cs	0.106	0.185	0.014	0.010	0.102	0.011	0.078	0.040	0.143	0.229	0.111	0.125	0.634
Rb	0.247	0.074	0.031	0.051	0.200	0.033	0.124	0.052	0.227	0.172	0.131	0.731	2.387
Ba	1.55	1.57	0.68	0.67	1.44	0.60	0.73	1.00	2.08	0.80	6.94	1.48	1.84
Th	0.0061	0.0037	0.0052	0.0051	0.0063	0.0015	0.0047	0.0036	0.0044	0.0026	0.0047	0.0050	0.0049
U	0.0039	0.0051	0.0110	0.0032	0.0025	0.0003	0.0066	0.0028	0.0079	0.0006	0.0041	0.0112	0.0095
Nb	0.0096	0.0075	0.0098	0.0074	0.0076	0.0079	0.0177	0.0073	0.0057	0.0062	0.0112	0.0113	0.0106
Ta	0.00492	0.00378	0.00104	0.00190	0.00233	0.00570	0.00724	0.00239	0.00202	0.00291	0.00172	0.00155	0.00141
La	0.021	0.015	0.065	0.012	0.088	0.053	0.042	0.020	0.019	0.013	0.101	0.041	0.046
Ce	0.061	0.043	0.192	0.041	0.146	0.217	0.093	0.066	0.055	0.035	0.337	0.117	0.096
Pb	0.087	0.060	0.089	0.082	0.093	0.101	4.243	0.097	0.241	0.114	0.348	0.672	3.113
Pr	0.012	0.009	0.044	0.011	0.037	0.053	0.013	0.016	0.011	0.008	0.067	0.023	0.020
Sr	33.77	51.29	15.46	21.71	47.31	52.07	33.26	36.04	56.14	23.92	76.88	68.91	99.87
Nd	0.086	0.079	0.362	0.115	0.315	0.449	0.088	0.151	0.089	0.074	0.489	0.169	0.167
Sm	0.049	0.058	0.239	0.100	0.211	0.291	0.066	0.112	0.060	0.061	0.248	0.093	0.103
Zr	0.154	0.097	0.690	0.220	0.427	0.923	0.142	0.243	0.189	0.126	0.994	0.479	0.479
Hf	0.007	0.007	0.037	0.017	0.026	0.052	0.010	0.015	0.012	0.010	0.045	0.023	0.028
Eu	0.089	0.119	0.138	0.085	0.260	0.211	0.083	0.137	0.068	0.063	0.191	0.086	0.078
Gd	0.115	0.151	0.540	0.270	0.506	0.656	0.177	0.291	0.160	0.168	0.515	0.191	0.226
Tb	0.023	0.032	0.112	0.059	0.104	0.134	0.039	0.062	0.034	0.037	0.102	0.039	0.046
Dy	0.193	0.267	0.914	0.484	0.841	1.062	0.330	0.506	0.280	0.311	0.789	0.303	0.363
Y	1.107	1.417	4.900	2.534	4.293	5.588	1.742	2.591	1.470	1.670	3.998	1.505	1.922
Ho	0.044	0.061	0.207	0.109	0.188	0.237	0.076	0.116	0.064	0.072	0.175	0.067	0.080
Er	0.138	0.183	0.627	0.319	0.555	0.694	0.230	0.330	0.181	0.206	0.497	0.187	0.232
Ti	525.9	524.0	765.5	1048.5	1597.0	1665.3	1033.9	772.7	432.1	451.4	925.8	523.7	553.7
Tm	0.021	0.028	0.093	0.046	0.082	0.102	0.035	0.050	0.027	0.030	0.074	0.027	0.033
Yb	0.146	0.185	0.623	0.290	0.533	0.657	0.235	0.328	0.173	0.199	0.483	0.169	0.213
Lu	0.026	0.033	0.106	0.048	0.092	0.112	0.041	0.055	0.028	0.033	0.081	0.028	0.034

Table III.6 continues

III.1.4.2. Trace elements

Normalized to chondrite (Fig. III.17a), pyroxenites from both pipes 1 and 2 show cpx-like REE patterns with a fractionated LREE segment ($0.18 < La_N/Sm_N < 0.71$), a slightly fractionated MREE segment ($0.43 < Sm_N/Dy_N < 0.52$) and a rather flat HREE segment. pipe 1 pyroxenites show much lower REE concentrations than pipe 2 pyroxenites. Eu anomalies are nonexistent except for sample P51, in which interstitial plagioclase is responsible for the positive Eu anomaly ($Eu^*=Eu_N/(\sqrt{Sm_N*Gd_N})=1.47$). Pyroxenites from pipe 1 do not show the positive Ti anomaly that pipe 2 pyroxenites have. All pyroxenites have a Nb negative anomaly, one of pipe 1 (P18) and one of pipe 2 (Pl-Hbl websterite P51) have infrachondritic Nb/Ta (Nb/Ta = 3.25 and 8.27 respectively), whereas all the others have suprachondritic Nb/Ta ($18.69 < Nb/Ta < 29.71$).

All dunites show the same REE patterns with a gently fractionated M-HREE segment ($0.22 < Sm_N/Lu_N < 0.38$) and a slightly upward convex LREE segment. One of the pipe 1 clinopyroxenites (sample P7) shows an anomalous La value, which is attributed to the presence of chlorite and serpentine (Chapter III.2). Like for pyroxenites, pipe 1 dunites are much more depleted in REE than pipe 2 dunites. One of the pipe 2 dunites (P45)

shows a small Eu anomaly (Eu* = 1.16) that coincides with the presence of calcite inclusions in olivine. All dunite samples, normalized to primitive mantle (Fig. III.17b), show a Zr-Hf anomaly, but pipe 1 dunites contrast with the others by the absence of a positive Ti anomaly and a small positive Nb-Ta anomaly. The positive Nb-Ta anomaly witnesses the high proportion of spinel in this dunite, and suggests as for the dunite of the crust-mantle transition zone (Bouilhol et al., 2008), the presence of rutile coated spinels (Bodinier et al., 1996). All dunites show strong positive Pb and Sr anomalies. The pipe 1 dunite shows a small Th positive anomaly whereas the other dunites do not. Dunites, like pyroxenites, have a strong Zr-Hf anomaly.

Fine grained metagabbros, pegmatitic metagabbros and meta-hornblendites have the same REE chondrite normalized pattern (Fig. III.17c) as pyroxenites.

	Metaplutonic series											
	Metagabbros		Tonalite dykes					Interlayered tonalite				
Sample	G11	G57	P63	D101	G13	P8	G12	G24	G19	G14	G32	LG4
SiO2	42.06	45.87	79.51	64.01	75.80	62.64	63.63	60.48	69.42	66.60	68.02	71.06
TiO2	0.118	0.099	0.037	0.014	0.096	0.096	0.100	0.793	0.621	0.521	0.653	0.391
Al2O3	21.64	17.10	12.13	20.77	13.07	20.11	19.30	14.97	14.57	13.95	14.35	12.03
Fe2O3	5.71	6.14	0.18	0.30	0.93	1.32	1.15	8.23	4.70	6.25	4.89	3.58
MnO	0.111	0.127	0.005	0.014	0.042	0.061	0.022	0.123	0.087	0.099	0.092	0.058
MgO	9.13	10.94	0.05	0.13	0.37	1.45	0.69	2.46	0.87	1.44	1.66	0.35
CaO	16.50	16.34	3.63	5.61	2.94	4.13	3.66	9.24	4.92	5.66	5.83	4.79
Na2O	0.636	0.397	3.472	7.146	4.718	9.063	9.662	0.823	3.789	2.980	2.689	3.061
K2O	0.013	0.007	0.023	0.018	0.024	0.055	0.037	0.011	0.008	0.007	0.000	0.037
P2O5	0.009	0.007	0.009	0.012	0.018	0.019	0.015	0.148	0.086	0.108	0.169	0.064
Cr2O3	0.063	0.054	0.000	0.001	0.001	0.000	0.000	0.001	0.000	0.002	0.001	0.000
NiO	0.026	0.009	0.000	0.000	0.001	0.001	0.002	0.002	0.001	0.002	0.001	0.001
LOI	3.376	2.579	0.537	0.765	0.678	0.692	1.125	2.376	1.006	1.611	1.433	1.020
Total	99.38	99.67	99.59	98.80	98.69	99.63	99.39	99.66	100.08	99.23	99.79	96.45
XMg	0.779	0.797	0.380	0.492	0.466	0.707	0.570	0.397	0.290	0.336	0.427	0.177
Cs	0.161	0.017	0.222	0.037	0.065	2.386	0.090	0.054	0.004	0.006	0.013	0.361
Rb	0.189	0.065	0.219	0.143	0.101	2.069	0.210	0.062	0.032	0.056	0.037	1.547
Ba	2.73	2.92	10.85	17.95	15.88	72.23	9.65	2.58	7.68	6.71	2.43	5.86
Th	0.0042	0.0047	0.0190	0.0166	0.0189	0.0100	0.0037	0.0068	0.0089	0.0230	0.0044	0.0064
U	0.0013	0.0068	0.0036	0.0028	0.0040	0.0039	0.0024	0.0019	0.0046	0.0124	0.0018	0.0096
Nb	0.0434	0.0126	0.0401	0.0185	0.2904	0.3075	0.0621	0.0362	0.6733	0.3146	0.4334	0.0573
Ta	0.00241	0.00178	0.00495	0.00351	0.02148	0.01771	0.00338	0.00279	0.02987	0.01551	0.01700	0.00323
La	0.175	0.037	0.209	0.621	0.892	0.551	0.329	0.147	0.539	1.435	0.412	0.207
Ce	0.434	0.115	0.365	1.398	2.083	1.636	0.730	0.427	1.566	4.299	1.356	0.585
Pb	0.355	0.196	1.439	0.602	1.173	1.269	0.087	0.109	0.221	0.246	0.662	0.153
Pr	0.080	0.023	0.037	0.169	0.276	0.293	0.097	0.092	0.258	0.712	0.259	0.101
Sr	203.30	61.25	146.60	126.38	58.49	198.62	40.62	81.50	112.49	99.90	83.15	90.57
Nd	0.583	0.175	0.177	0.790	1.328	1.907	0.494	0.687	1.613	4.294	1.880	0.670
Sm	0.259	0.101	0.063	0.167	0.300	0.815	0.120	0.339	0.546	1.558	0.795	0.253
Zr	1.316	0.439	0.433	3.006	46.867	3.420	2.071	0.322	1.477	2.723	0.948	0.538
Hf	0.064	0.022	0.051	0.128	1.345	0.209	0.021	0.014	0.051	0.139	0.041	0.017
Eu	0.241	0.098	0.230	0.646	0.509	0.765	0.550	0.354	0.932	1.052	0.754	0.811
Gd	0.446	0.229	0.058	0.146	0.283	1.388	0.163	0.676	0.855	2.602	1.408	0.464
Tb	0.083	0.046	0.010	0.020	0.052	0.257	0.028	0.114	0.136	0.451	0.225	0.076
Dy	0.608	0.365	0.076	0.128	0.395	1.834	0.193	0.813	0.920	3.233	1.541	0.504
Y	3.197	1.827	0.465	0.718	2.951	9.739	1.140	3.867	4.629	15.928	7.091	2.511
Ho	0.130	0.081	0.017	0.028	0.095	0.391	0.042	0.172	0.196	0.693	0.325	0.109
Er	0.360	0.227	0.046	0.077	0.343	1.090	0.120	0.472	0.549	1.981	0.873	0.278
Ti	743.6	582.0	373.8	66.2	531.6	604.6	619.1	5011.5	3922.8	3269.7	4128.3	2684.5
Tm	0.050	0.033	0.010	0.013	0.063	0.162	0.019	0.064	0.079	0.287	0.114	0.038
Yb	0.315	0.208	0.048	0.082	0.536	1.036	0.127	0.401	0.515	1.870	0.704	0.237
Lu	0.051	0.034	0.008	0.013	0.101	0.174	0.021	0.064	0.088	0.315	0.118	0.038

Table III.6 continues: Zr and Hf values of tonalite dykes are from Laser ablation ICPMS on glass pills used for XRF measurement
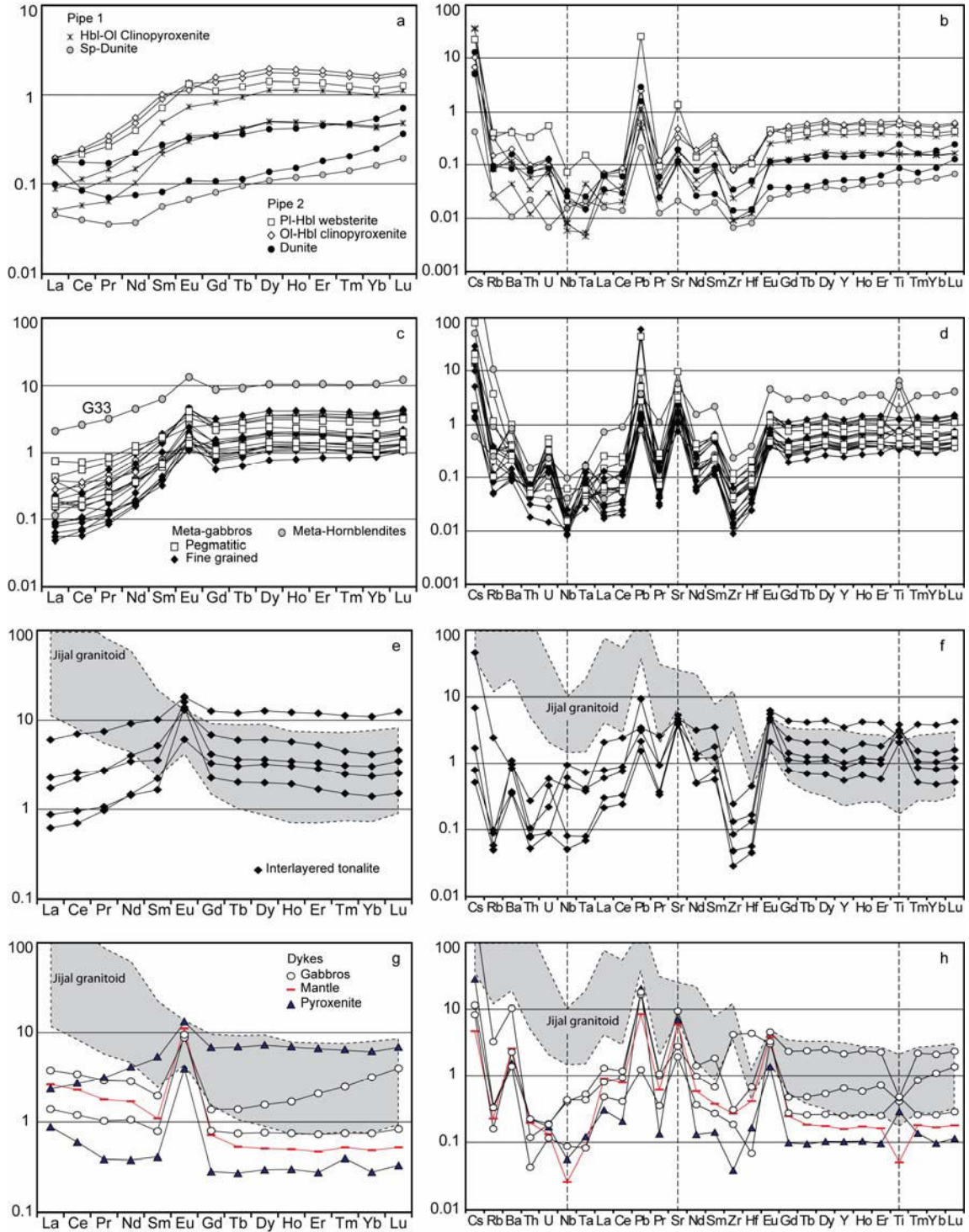
Figure III.17. Normalized concentrations of the different lithologies found in the Sapat crustal series. Left column normalized to chondrite. Right column normalized to primitive mantle. a) and b) pyroxenites, c) and d) metagabbros and metahornblendites, e) and f) interlayered tonalites, g) and h) tonalite dykes. granitoid from Jijal are plotted for comparison (same as figure III.1.16).

They have highly depleted patterns with a strongly fractionated LREE segment ($0.07 <$ $La_N/Sm_N < 0.53$), a strong Eu anomaly ($1.17 < Eu^* < 3.88$), a slightly fractionated MREE segment ($0.32 < Sm_N/Dy_N < 0.70$) and a rather flat HREE segment.

Metahornblendite G33 (which is almost unaffected by metamorphism) is much more enriched than the others. Normalized to primitive mantle (Fig. III.17d), all samples have a strong Zr-Hf anomaly and an irregular Ti anomaly (none, positive or negative). Nb is constantly depleted but Ta shows a positive anomaly with very low infrachondritic Nb/Ta. Nb/Ta ratios are higher in the metahornblendites ($6.8 < Nb/Ta < 10.37$) than in the fine grained metagabbros ($1.38 < Nb/Ta < 9.43$) and are even getting close to chondritic value in the pegmatitic metagabbros ($6.48 < Nb/Ta < 18.02$).

Fine-grain metagabbros, metahornblendites and pegmatitic metagabbros have strong positive Pb and Sr anomalies together with a strong U peak. Ba is more or less enriched compared to neighbor elements. The crustal metagabbros are identical in all trace elements to metagabbros of the crust-mantle transition zone (Bouilhol et al., 2008).

From their REE chondrite normalized patterns, silicic rocks (Fig. III.17e, f, g, h) can be divided into two groups: One has a REE pattern with a fractionated LREE segment, ($0.27 < La_N/Sm_N < 0.63$) a positive Eu anomaly ($1.59 < Eu^* < 7.23$) and slightly downward fractionated M-HREE segment ($0.99 < Gd_N/Lu_N < 1.49$). The other group has a downward fractionated LREE segment ($1.76 < La_N/Sm_N < 2.39$), an important positive Eu anomaly ($5.34 < Eu^* < 12.63$) and a rather flat M-HREE segment except for sample G13, which shows a fractionated HREE ($Gd_N/Lu_N = 0.34$) witnessing the presence of garnet. Normalized to primitive mantle, these two groups cannot be pointed anymore. All samples show a strong Zr-Hf anomaly, except G13 reflecting the considerable amount of zircons that it contains. Ti shows either a positive or a negative anomaly. Nb and Ta have different concentrations: Either Nb and Ta are depleted and show a chondritic to infrachodritic ratio ($5.26 < Nb/Ta < 18.36$); or Nb is not depleted, and Nb-Ta ratios are nearly chondritic to suprachondritic ($10.37 < Nb/Ta < 25.48$). Sr, Pb and Ba show positive anomalies.

III.1.4.3. *Isotopes*

Unleached bulk rock samples from all the lithologies have been analyzed for isotopic compositions (Table III.7, 8; procedure in Appendix 1). Plotted in a Nd-Sr initial isotopic composition (Fig. III.18), results are scattered ($0.70320 < ^{87}Sr/^{86}Sr < 0.70556$; $0.51274 < ^{143}Nd/^{144}Nd < 0.51291$). Tonalite-trondjhemite dykes show an increase in Nd with increasing Sr ($0.703723 / 0.512783$; $0.704383 / 0.512879$), except for sample P63 (in pipe 2) that has the highest Sr ($^{87}Sr/^{86}Sr = 0.705026$). Tonalite interlayered with metagabbros have a restricted Sr isotopic composition ($^{87}Sr/^{86}Sr = 0.70430$) but $^{143}Nd/^{144}Nd$ varies between 0.512814 and 0.512897. Fine grained crustal metagabbros show a restricted range in Nd and Sr isotopic compositions ($0.512840 < ^{143}Nd/^{144}Nd < 0.5128770$ and $0.704185 < ^{87}Sr/^{86}Sr < 0.704342$) whereas the pegmatitic metagabbros have a wide range. Metagabbros intrusive in the ultrabasic rocks have the lowest $^{87}Sr/^{86}Sr$ (0.7032 and 0.703373) and a scattered $^{143}Nd/^{144}Nd$ composition (0.512796 and 0.512913).

Sample	Measured 143Nd/144Nd	1σ	Age corrected 143Nd/144Nd	εNdi	Measured 87Sr/86Sr	1σ	Age corrected 87Sr/86Sr	εSri
G12	0.512879	0.000004	0.512783	5.34	0.703744	0.000003	0.703723	-9.39
G13	0.512930	0.000002	0.512842	6.48	0.704336	0.000004	0.704329	-0.78
P8	0.513047	0.000008	0.512879	7.21	0.704426	0.000004	0.704383	-0.01
D101	0.512892	0.000005	0.512809	5.84	0.704161	0.00001	0.704156	-3.23
P63	0.512923	0.000021	0.512783	5.35	0.705032	0.000003	0.705026	9.11
G32	0.513050	0.000004	0.512884	7.30	0.704306	0.000004	0.704304	-1.14
G14	0.513040	0.000004	0.512897	7.56	0.704275	0.000004	0.704273	-1.58
G24	0.513008	0.000006	0.512814	5.94	0.704326	0.000003	0.704323	-0.87
G36	0.513137	0.000002	0.512877	7.18	0.704350	0.000003	0.704342	-0.60
G49	0.513104	0.000002	0.512840	6.45	0.704222	0.000002	0.704204	-2.55
G59	0.513204	0.000005	0.512862	6.89	0.704195	0.000004	0.704185	-2.82
G54	0.513025	0.000003	0.512824	6.15	0.704445	0.000003	0.704438	0.76
G11	0.513071	0.000005	0.512896	7.55	0.703485	0.000004	0.703481	-12.82
LD10	0.513011	0.000004	0.512796	5.59	0.703376	0.000004	0.703373	-14.36
D104	0.513150	0.000003	0.512913	7.88	0.703210	0.000002	0.703200	-16.81
D64	0.513118	0.000004	0.512870	7.04	0.703804	0.000019	0.703756	-8.91
D18	0.513108	0.000009	0.512737	4.45	0.704239	0.000012	0.704227	-2.23
LD5	0.513061	0.000013	0.512756	4.82	0.703746	0.000076	0.703740	-9.14
P42	0.513049	0.000003	0.512809	5.84	0.704885	0.000005	0.704799	5.90
P51	0.513061	0.000004	0.512830	6.26	0.704548	0.000007	0.704511	1.81
P31	0.512954	0.000004	0.512774	5.16	0.704389	0.000004	0.704380	-0.06
P7	-	-	-	-	0.705646	0.000006	0.705572	16.86
P9	0.513072	0.000012	0.512796	5.59	0.705341	0.000005	0.705118	10.43
P18	0.513082	0.00003	0.512807	5.81	0.705591	0.000013	0.705563	16.74

Table III.7: Sr and Nd isotopic composition of samples representative of all lithologies found in Sapat. Description in table II.5
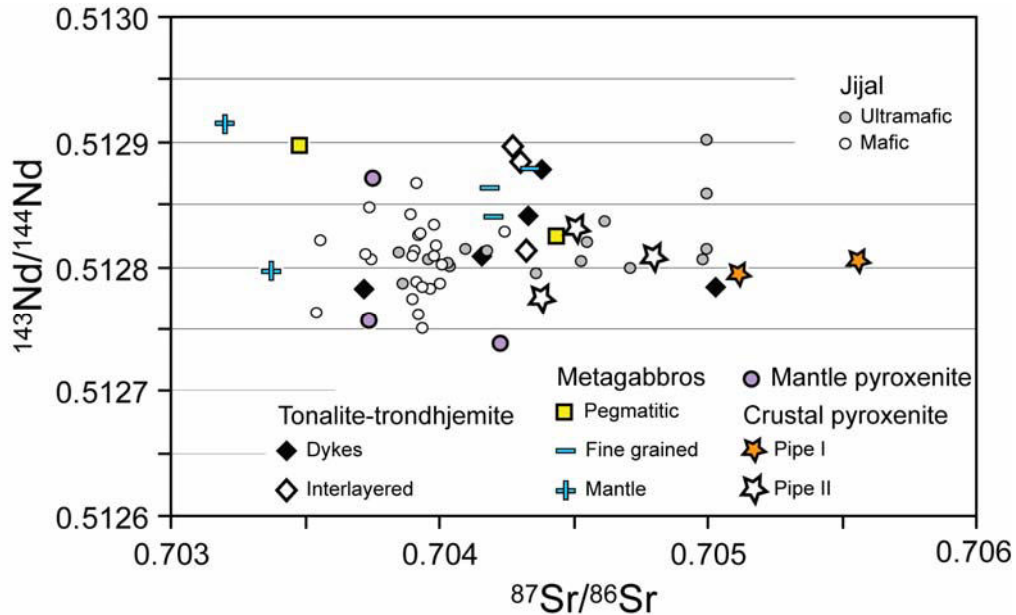
Figure III.18: Nd vs Sr initial (recalculated for t_0=100Ma) isotopic composition of some samples representing all the structural level and lithologies found in Sapat. Data from Dhuime et al. (2007) for comparison with Jijal

Mantle pyroxenites range from 0.512737 to 0.512870 in ^{143}Nd/^{144}Nd and from 0.703740 to -0.704270 in ^{87}Sr/^{86}Sr. Crustal pyroxenites show the highest ^{87}Sr/^{86}Sr values (0.704380-0.705563) and a restricted range in ^{143}Nd/^{144}Nd (≈0.51280).
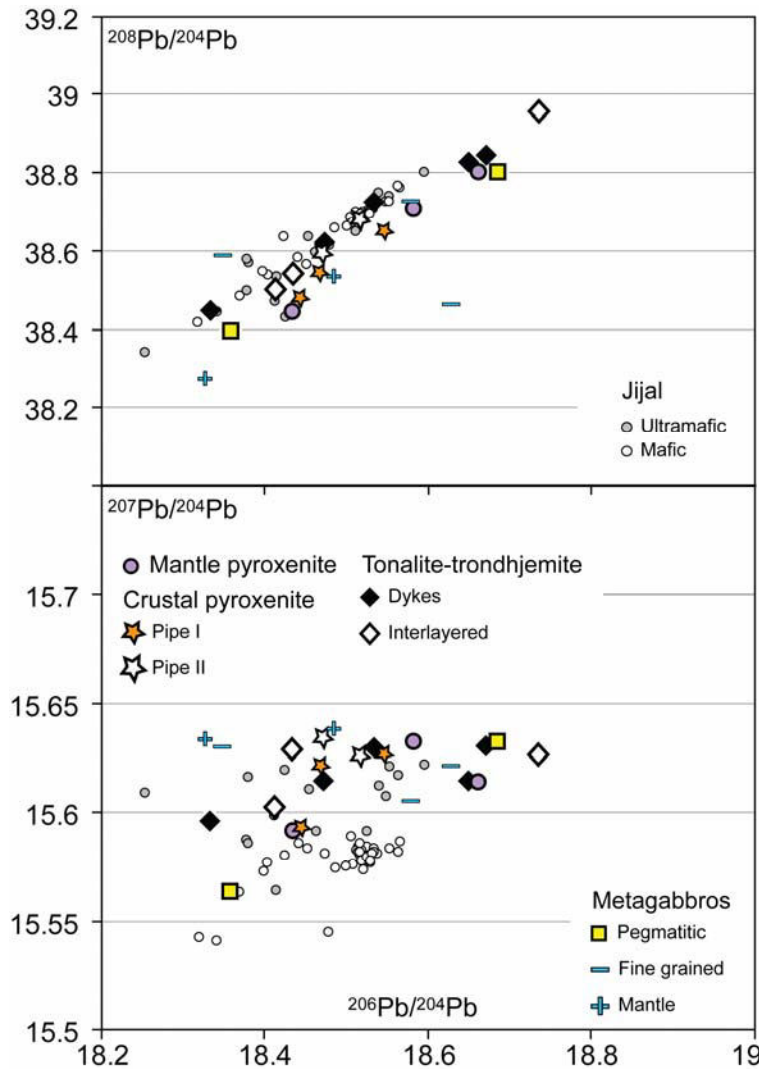
In the ^{208}Pb/^{204}Pb vs ^{206}Pb/^{204}Pb diagram (Fig. III.19), all samples show a continuous distribution from ^{208}Pb/^{204}Pb =38.271 and ^{206}Pb/^{204}Pb =18.327, to ^{208}Pb/^{204}Pb =39.139, ^{206}Pb/^{204}Pb =18.884. Two metagabbros (G36 and G49) are off that trend. Plotted against ^{206}Pb/^{204}Pb, ^{207}Pb/^{204}Pb show that most of the samples are around ^{207}Pb/^{204}Pb=15.63, with samples forming a trend toward lower values (G11: ^{207}Pb/^{204}Pb=15.563). Overall, it is impossible to attribute a range of value depending on lithology.

Fig III.19. Pb initial isotopic composition of the different Sapat lithologies. Jijal from Dhuime et al (2007) for comparison

94

Sample	Measured						Age corrected		
	206/204Pb	1σ	207/204Pb	1σ	208/204Pb	1σ	206/204	207/204	208/204
G12	18.3606	0.0058	15.5974	0.0049	38.4591	0.0122	18.333	15.596	38.445
G13	18.4761	0.0013	15.6148	0.0011	38.6256	0.0027	18.473	15.615	38.620
P8	18.5374	0.0008	15.6298	0.0007	38.7274	0.0017	18.534	15.630	38.725
D101	18.6762	0.0044	15.6306	0.0037	38.8563	0.0093	18.672	15.630	38.847
P63	18.6522	0.0013	15.6145	0.0011	38.8336	0.0028	18.650	15.614	38.829
G32	18.7381	0.0012	15.6271	0.0010	38.9599	0.0025	18.735	15.627	38.958
G14	18.4618	0.0041	15.6048	0.0033	38.5300	0.0082	18.412	15.602	38.499
G24	18.4503	0.0066	15.6294	0.0056	38.5614	0.0139	18.433	15.629	38.541
G36	18.4711	0.0153	15.6358	0.0124	38.6057	0.0318	18.348	15.630	38.587
G49	18.6544	0.0061	15.6219	0.0053	38.4827	0.0127	18.627	15.621	38.461
G59	18.6175	0.0074	15.6067	0.0062	38.7429	0.0161	18.579	15.605	38.723
G54	18.6970	0.0033	15.6326	0.0028	38.8056	0.0068	18.685	15.632	38.801
G11	18.3621	0.0033	15.5637	0.0029	38.3996	0.0071	18.358	15.563	38.396
LD10	18.3817	0.0063	15.6360	0.0053	38.2905	0.0129	18.327	15.633	38.272
D104	18.4971	0.0033	15.6383	0.0028	38.5438	0.0068	18.485	15.638	38.532
D64	18.5897	0.0029	15.6329	0.0024	38.7310	0.0062	18.582	15.633	38.708
D18	18.6684	0.0092	15.6142	0.0077	38.8047	0.0190	18.662	15.614	38.801
LD5	18.4393	0.0072	15.5918	0.0054	38.4523	0.0138	18.434	15.592	38.443
P42	18.4869	0.0058	15.6356	0.0049	38.6113	0.0121	18.472	15.635	38.596
P31	18.5285	0.0028	15.6263	0.0024	38.6828	0.0059	18.516	15.626	38.678
P7	18.4889	0.0077	15.5956	0.0060	38.5108	0.0153	18.443	15.593	38.484
P9	18.5647	0.0043	15.6288	0.0035	38.6794	0.0081	18.547	15.628	38.659
P18	18.4798	0.0037	15.6234	0.0031	38.5566	0.0074	18.467	15.623	38.550

Table III.7: Pb isotopic compositions of measured samples.

III.1.5. Preliminary interpretations

III.1.5.1. Petrogenesis

Metagabbros-pyroxenite suite

Variations in major elements between pyroxenites (from both mantle and crustal pyroxenite bodies) and metagabbros reflect a crystallization sequence best interpreted by the combination of ol, cpx and amph fractionation and accumulation. High Mg# samples (>0.8) show variable SiO_2, MgO and CaO reflecting the different proportions of ol and cpx. For the metagabbros, the high Al_2O_3 content (15-20 wt%) reflects plagioclase accumulation, absent in pyroxenites. The CaO content is nearly constant and MgO decreases between 0.6 and 0.8 X_{Mg}, while the variable silica content (42-50 wt% SiO_2) reflects different proportions of cumulus cpx and hbl before showing a discrete but steady decrease indicating greater fractionation of hbl over cpx. The wide range of Al_2O_3 content reflects the varying proportion of accumulated plagioclase. The Ti content shows a general increase from 0.9 to 0.6 X_{Mg}, but its contents is variable from sample to sample, reflecting fractionation and accumulation of Ti-oxydes.

From these lines of evidence and considering that pyroxenites and meta-gabbros have the same trace element concentrations, we conclude that metagabbros and pyroxenites form a co-genetic suite of cumulates from the same parental melt. Their major element compositions reflect different modal proportions of accumulated ol-cpx-hbl and Ti-oxydes.

Metahornblendites-tonalite suite

A gap in X_{Mg} exists between metagabbros and metahornblendites, but the latter are in line with the trends in metagabbros with $X_{Mg} < 0.8$. Metahornblendites have compositions similar to hornblende, indicating their cumulative origin. The wide range of Ti content in metahornblendites indicates different proportions of Ti oxides. The small variations in SiO_2, CaO and Al_2O_3 in these rocks point toward the MgO-richest interlayered tonalite. This indicates that hornblende accumulation would lead to the differentiated melts further crystallizing tonalites. This interpretation is supported by the accumulation of Ti oxides in hornblendites and further explains the decreasing Ti content in tonalite.

The interlayered tonalite do not show much of evolution except their decreasing MgO content with X_{Mg}.

Metahorblendites have the same trace element concentrations as the metagabbros (except for sample G33. One way to explain its higher trace element concentrations but same pattern is to assume that it contains trapped melt. In any case, these patterns show that metagabbros and methornblendites derive from the same parental melt. In addition, REE concentrations in the interlayered tonalite are the same, strengthening their attribution to fractional crystallization processes of the same parental melt as metagabbros and metahornblendites. The stronger positive Eu anomalies in tonalites reflect higher proportions of accumulated plagioclase.

Tonalite dykes

The major element concentrations of the trondhjemite tonalite dyke are scattered. This reflects extensive re-equilibration during metamorphism, the dykes draining metamorphic fluids. This interpretation is consistent with the high silica contents of some of the dykes whose high Na contents reflect albitization. Trondhjemites G12 and P8 are in that case metamorphosed tonalite and not igneous trondhjemites. These dykes reflect the latest-coolest residual melt fraction of the fractionation process forming the whole previous series. This is in accordance with the fact that these dykes are the only lithologies in which zircons are found.

The two types of REE patterns in the tonalite dykes record the magmatic and metamorphic history of these dykes, where plagioclase type REE patterns reflect albitization and bulk REE dilution due to metamorphic silicification. Sample P8 is the only tonalitic dyke in which the REE concentration has not been affected by metamorphic re-equilibration. It shows the same REE concentration as interlayered tonalite, consistent with a co-genetic origin with the previously discussed lithologies.

III.1.5.2. *Source constraints*

Due to very low concentrations, the isotopic dataset has been acquired on unleached samples (procedure on appendix 1). This implies that the isotopic ratios essentially reflect the mantle source region although fluid percolation may have affected part of these ratios for the most mobile element: Sr. Nd and Pb are considered to be unaffected by fluids and the Nd and Pb isotopic ratios should represent the source composition. Therefore, we cannot reliably constrain the source composition using Sr isotopic ratios. Nevertheless, if

we assume the Sr isotopic ratios to be unchanged, then the increase in $^{87}Sr/^{86}Sr$ combined with a decrease in $^{143}Nd/^{144}Nd$ reflects source evolution (Fig. III.20).

Figure III.20: $^{87}Sr/^{86}Sr$ *vs* $^{143}Nd/^{144}Nd$ initial composition (T=100Ma) of Sapat samples and mixing lines. DMM value from Workman and Hart, (2005). The Tethysian mantle has been calculated from 150Ma old MORB from Masirah (Mohoney et al, 1998). Indian Ocean Sediment from Ben Othman et al. (1998)
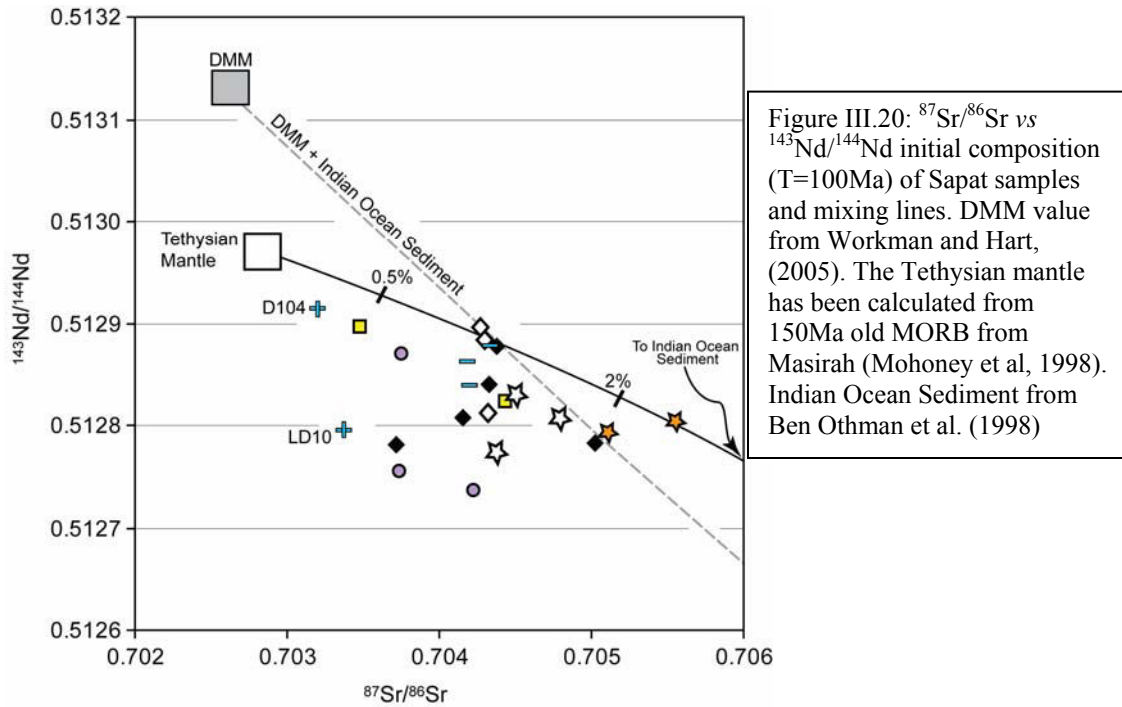
The observed range in $^{143}Nd/^{144}Nd$ at constant $^{87}Sr/^{86}Sr$ could be due to source heterogeneity. This trend is not well represented by a source composed of DMM components mixed with Indian Oceanic sediments (Ben Othman et al., 1989), but it is better fit by a two component mixture between a Tethysian mantle source and Indian Ocean sediments (Fig. III.20). The Tethysian mantle component has been constrained as follows: Since the proto-Kohistan Island arc is believed to have started at ca. 150Ma (Schaltegger et al., 2003) within the Tethys lithosphere, and since Sr and Nd isotopic values of Tethysian MORB are reflecting the isotopic composition of the mantle from which they are issued, I used the more depleted Sr and Nd isotopic values of 150Ma old, leached Tethysian MORB (Mahoney et al., 1998) as a Tethysian mantle isotopic composition. The Sr and Nd concentrations of this mantle are derived from the same samples as those from which the isotopic values were obtained by Mahoney et al. (1998). To constrain the mantle concentrations, I took the Kd between cpx and basaltic melt of Hart and Dunn (1993) (Kd^{Sr}= 0.1283, Kd^{Nd}=0.1873) to be relevant since cpx is dominating the budget of these two elements during melting. Applying these Kd's to the mean concentration of the leached samples, the Tethysian mantle component has the following characteristics: $[Sr]_{mantle}$=15.7 $[Nd]_{mantle}$=3; $^{87}Sr/^{86}Sr_{mantle}$ =0.70284 $^{143}Nd/^{144}Nd_{mantle}$=0.51297. The slope correlating the decrease in $^{87}Sr/^{86}Sr$ and $^{143}Nd/^{144}Nd$ is parallel to the above calculated mixing line (Fig. III.20).

The same reasoning is applied to the $εNdi$ *vs* $^{206}Pb/^{204}Pb$ diagram (Fig. III.21). In this, and as for the $^{87}Sr/^{86}Sr$ *vs* $^{143}Nd/^{144}Nd$ diagram, the Sapat samples with a correlation in Nd

and Pb isotopes (i.e a decrease in εNdi and $^{206}Pb/^{204}Pb$) are best explained by a mixing line between a 150Ma Tethysian mantle and up to 2% Indian sediment. Again, several samples do not plot on this trend and show variable εNdi. These samples have the same isotopic composition as the Jijal samples (Fig. III.21).

From all these line of evidence, the Sapat lithologies are: (i) All co-genetic (ii) Issued from a heterogeneous source comprising a 150Ma old Tethysian mantle plus up to 2% sediment and some part having the same isotopic composition than Jijal.
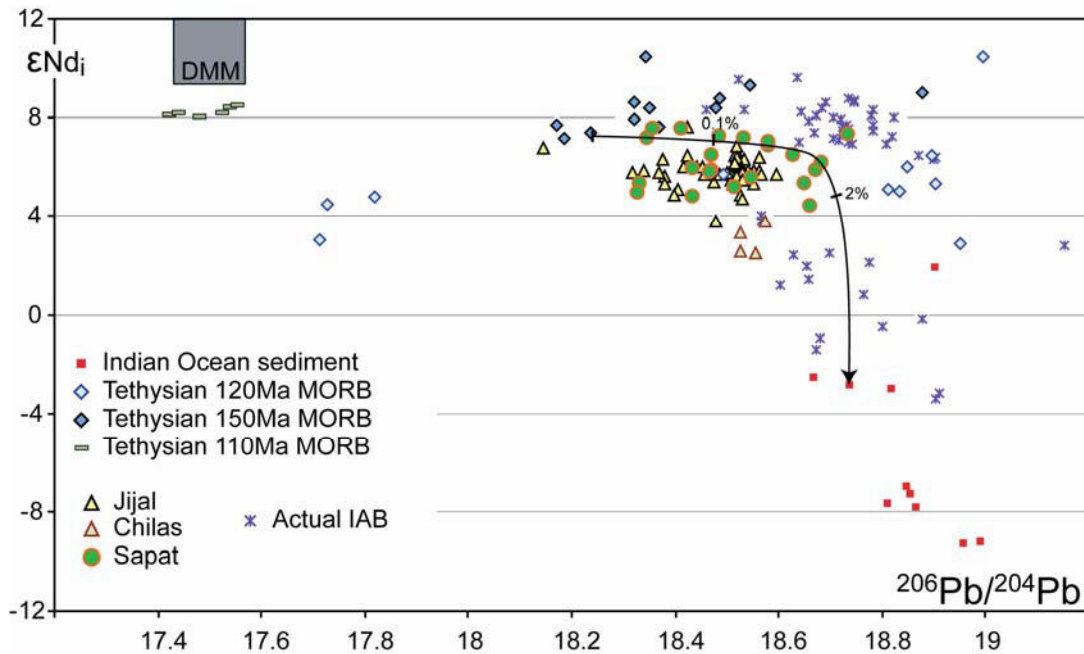
Figure III.21: εNdi *vs* $^{206}Pb/^{204}Pb$ initial isotopic composition (T=100Ma) of the Sapat, Jijal (Dhuime et al, 2007) and Chilas (Khan et al., 1997)samples. Also Tethysian MORB of 150, 120 and 100 Ma old of Mahoney et al. (1998). Indian Ocean sediment from Benothman et al. (1989). Some of the actual Island Arc Basalt from Woodhead et al. (2001).

III.1.5.3. *Comparison with the Jijal crustal rocks*

The absence of garnet in the Sapat mafic rocks is the major difference with the Jijal section. Whatever the processes leading to the formation of garnet in Jijal (igneous vs metamorphic) the Sapat crustal section neither crystallized nor evolved at the depth of Jijal i.e ≈12 kbar (Yamamoto et al. 1993). Furthermore, the Jijal section is exempt of widespread fluid-assisted amphibolite facies re-equilibration as observed in the Sapat meta-plutonic rocks. The trace element compositions of the Sapat crustal rocks are much more depleted than Jijal crustal rocks, which would indicate a more depleted source reservoir. This is somewhat consistent with the isotopic compositions showing that some Sapat samples are more depleted, whereas others have the same composition as in Jijal (Fig. III.18, 19). Nevertheless, the differentiation trends of these rocks are quite similar,

which would suggest that the Jijal and Sapat rocks are derived from the same differentiation process, but from different parental melts. This information corroborates the difference observed in the calculated melt from the mantle (Bouilhol et al., 2008). In Sapat as in Jijal, the differentiation process led to the formation of silicic rocks; the significant difference in trace element concentrations indicates the absence of garnet fractionation in the Sapat series (Fig. III.17).

Consequently, the Jijal and Sapat complex do not arise from the same parental melt and source. They formed in a different setting within the Kohistan Arc Complex.

III.1.6. Preliminary conclusions

The Sapat Complex lithologies have formed from a common parental melt that has undergone crystal fractionation. The differences in major elements reflect differences in cumulative phases: ol-cpx formed the pyroxenites and cpx-hbl-pl formed the metagabbros and the metahornblendites. The tonalites represent the more evolved silicic rocks generated from this crystal fractionation process. The tonalite dykes are the most differentiated rocks but Na-rich fluid amphibolite facies re-crystallization has obscured their primary composition.

The parental melt of the Sapat lithologies derived from a common, yet heterogeneous source. The mantle source region of the parental melts is best characterized by the involvement of a Tethysian-like mantle little affected by a slab component, and a more fertile "Jijal-like mantle".

The compositions found in the Sapat Complex are unique within Kohistan and suggest that the complex formed in a yet unrecognized geodynamical setting of the paleo-arc. The extensive fluid assisted metamorphic re-equilibration is unlikely to have been triggered by a late stage Himalayan metamorphism, but rather witnesses some metasomatic process through the entire pile during subduction. This interpretation, together with the depleted nature of the Sapat parental melt and source, strengthens the conclusion that the Sapat Complex is a remnant of the Kohistan forearc.

III.2. **The intrusive pyroxenitic bodies**

III.2.1. **Introduction**

The processes involved in the formation and transfer of arc-magmas are much less understood than magma generation and transfer at Mid-Oceanic Ridges (Kelemen et al., 1997; Nicolas et al., 2008). Melting, in the hot part of the mantle wedge enhanced by slab-derived fluids and melts (Tatsumi et al., 1983; Ulmer, 2001; Grove et al., 2006), is a prerequisite to primary arc magma formation. Nevertheless, the migration mode from the source region in the wedge toward the final emplacement site within the arc crust remains controversial. Full sections of paleo-island arcs allow (1) studying directly the influx and the type of arc-melts at Moho depth and (2) constraining the cumulate crystal proportion during early differentiation (Debari and Coleman, 1989; Debari and Sleep, 1991; Garrido et al., 2007; Kelemen et al., 2003; Bouilhol et al., 2008). The evolution of primitive arc-magmas from the mantle wedge towards evolved silicic melts in arc volcanoes (andesite, dacite and rhyolite) and plutons (tonalite, trondhjemite, granodiorite and granites) is actively debated. Petrological processes leading to silicic melt generation are: (i) slab melting (Drummond and Defant, 1990; Defant et al., 1991), (ii) mantle-slab fluid or melt interaction (review in Kelemen et al., 2003), (iii) differentiation of hydrous basalt at lower crust / Moho depth (Muntener et al., 2001; Annen et al., 2006; Ulmer, 2007), (iv) dehydration melting of amphibolitized lower crust due to basaltic underplating (Smith and Leeman, 1987; Petford and Gallagher, 2001; Jackson et al., 2005), and (v) fractional crystallization of basalt in shallow magma reservoirs (Sisson and Grove, 1993; Grove et al., 1997; Martel et al., 1999). In all of the crustal processes, amphibole plays a key role during differentiated Si-rich magma genesis, either because amphibole hosts the water necessary to lower the solidus, or because it is a stable phase during crystallization inducing SiO_2 enrichment in the residual melt (Cawthorn and Ohara, 1976; Romick et al., 1992; Grove et al., 2003; Prouteau and Scaillet, 2003; Davidson et al., 2007; Rodriguez et al., 2007; Brophy, 2008; and references therein).

High resolution tomographic images of arc-crust have revealed its heterogeneous character and depicted vertical "columns" of high velocity structures rising from the Moho into mid-crustal levels composed mainly of intermediate SiO_2 type plutons (tonalite-granodiorite) (Kodaira et al., 2007; Takahashi et al., 2008). The location of these "columns" is associated with that of the more silicic volcanoes at the surface. Hitherto, a natural equivalent to these "columns" has not been recognized, which raises the question of melt transport and enrichment.

Indeed, little is known about magma transfer, storage and evolution from the Moho toward upper-crustal levels. In order to elucidate magma transfer and evolution, we investigated a lower crustal section of the Kohistan Paleo-Island arc. We identified magmatic bodies that could correspond to the "high velocity columns" imaged in active subduction margins. Structural and geochemical analyses have been carried out on two of these mafic-ultramafic bodies. Results show that they are magmatic feeder pipes playing a key role in magma transfer; they further document the differentiation of Kohistan arc-melts and the role of amphiboles and peritectic reactions in the deep crust differentiation processes.

III.2.2.   Geological setting

The Kohistan Complex (North Pakistan) represents an intra-oceanic island arc formed during northward subduction of the Tethys ocean in Mesozoic times (Tahirkheli et al., 1979; Bard, 1983; Coward et al., 1987) and now tectonically pinched between the Karakoram (part of Asia) and Indian continents (Fig.1). Kohistan is one of the rare places that offer the opportunity to explore an arc-section, from the mantle-crust transition to the sedimentary basins. The Kohistan Arc actually displays three lithospheric sections. Two of them (Jijal and Chilas sections) document the generation of silicic melts: In the south, the Jijal section shows a succession of arc-mantle lithologies (Jan and Howie, 1981; Jan and Windley, 1990; Burg et al., 1998; Dhuime et al., 2007; Garrido et al., 2007) intruded by garnet-gabbros (Bard, 1983; Burg et al., 1998; Yamamoto and Yoshino, 1998; Ringuette et al., 1999; Garrido et al., 2006) overlain by the Southern Amphibolite sequence (Treloar et al., 1996; Zeilinger et al., 2000) (for the complete Jijal section see (Burg et al., 2005)). Based on geochemical arguments, Garrido et al. (2008) interpreted part of the Jijal crustal section as being restitic from granulite facies dehydration melting of a crustal protolith. The generated silicic melt would have supplied the arc crust in evolved melt. This interpretation favours a model of silicic melt generation by crustal melting, but other authors suggest that the crustal part of Kohistan has a cumulative origin (Bard, 1983; Burg et al., 1998; Ringuette et al., 1999; Muntener and Ulmer, 2006; Dessimoz et al., 2008; Muntener et al., 2008), thus silicic melts would be produced during intracrustal fractionation.

The second section, the Chilas Complex, intruded the Kohistan arc during intra-arc extension (Burg et al., 2006). Several ultramafic bodies represent apices of intra-arc mantle diapirs that served as porous flow conduits to feed the Chilas gabbronorite, about 85 My ago (Burg et al., 1998; Schaltegger et al., 2002). Differentiation within these conduits, led to the more evolved gabbronorite sequence (Jagoutz et al., 2006; Jagoutz et al., 2007), suggesting that near Moho-lower crustal processes generated evolved magmatic rocks.

The third section, the Sapat Complex (Fig. III.1, 2), is much less documented. Two main lithological units were identified: (1) Ultramafic rocks (dunites, meta-harzburgites and pyroxenites) at the base of the section represent an exhumed piece of arc to fore-arc mantle (Bouilhol et al., 2008). (2) Fine-grained metagabbros interlayered with tonalites represent the overlying lower crustal sequence generally affected by amphibolite to greenschist facies recrystallization. The lower crustal rocks enclose the pyroxenite bodies which are the subject of this study. Several bodies have been visited and some more have been spotted from distance in the landscape and were more precisely located and mapped on satellite images (Fig. III.1). Two of them have been investigated in detail, and quick surveys show that others have the same rock types and relationships, which allows extension of our results to all bodies. Rock types range from olivine-clinopyroxenite to plagioclase-hornblende-bearing olivine-websterite with dunite bodies. The largest of these bodies (pipe1) exclusively consists of wehrlite and ol-clinopyroxenite containing only minor reminders of more evolved interstitial melts. The smaller body (pipe2) was more interesting as it offers a wider suite of rock types ranging from ol-websterite to tonalite. These two bodies are "connected" by pegmatitic metagabbros (Fig III.1 and Fig. II.2) which show a subvertical magmatic foliation parallel to their trend. This work describes the structures and petrology of the two pyroxenite bodies and concludes that

they represent magmatic conduits in which melt has been transferred from the crust mantle transition zone towards higher crustal levels, and that during transfer in these conduits the melt has acquired part of its chemistry.

III.2.3. Structures of the bodies

III.2.3.1. *Olivine Clinopyroxenite body (Pipe 1)*

Pipe 1 has an ellipsoidal shape of about 10 * 2.5 km with the long axis striking ca. N035. The southwest contact with the surrounding fine grained metagabbros is sharp and subvertical, parallel to the foliation within the fine grained metagabbros in the ≈ 5 m closest to the contact with the pyroxenite body. This foliation wraps around the pyroxenite body and overprints fine grained metagabbros within the near proximity (ca 5m) of the contact. The metagabbros are not deformed beyond this strain fringe. Rare dykelets of fine grained clinopyroxenites intrude the metagabbros. The contact consists in a *ca.* 50 cm wide, blurry, sub-vertical zone where fine-grained clinopyroxenite tends to invade and replace the fine grained metagabbros (Fig. III.22a). At the contact, small aggregates of white secondary minerals are found in small, cm-large pockets within the body.
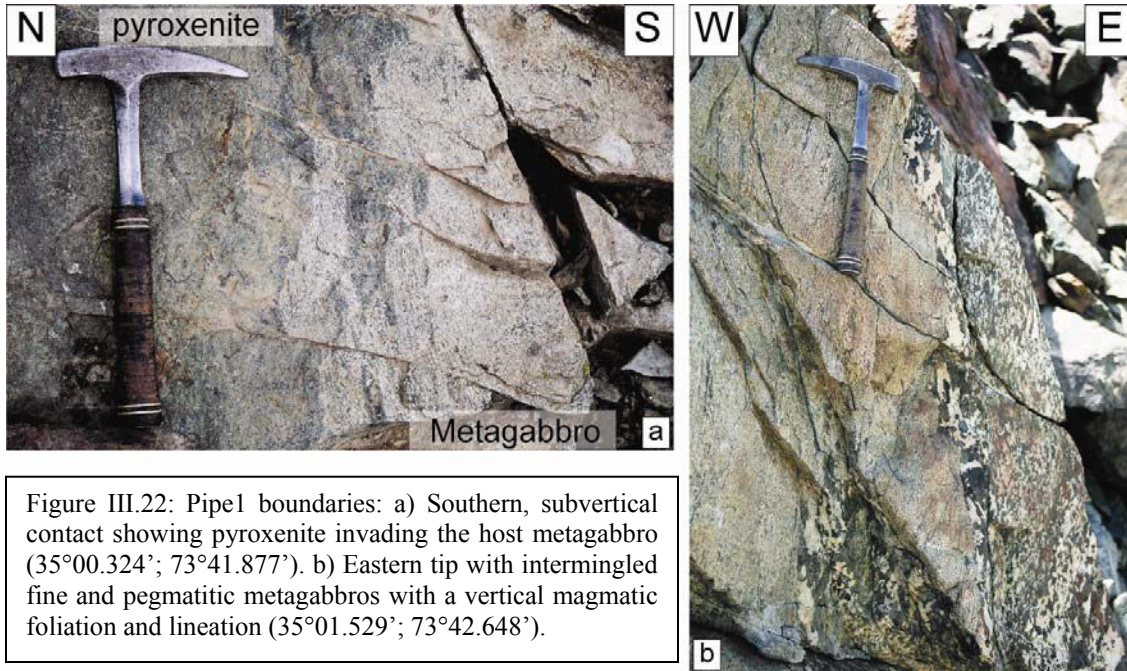
Figure III.22: Pipe1 boundaries: a) Southern, subvertical contact showing pyroxenite invading the host metagabbro (35°00.324'; 73°41.877'). b) Eastern tip with intermingled fine and pegmatitic metagabbros with a vertical magmatic foliation and lineation (35°01.529'; 73°42.648').

These pockets probably represent remnants of pieces of the host rocks. Nowhere traces of melting of the host have been observed. On its eastern tip, this body ends in a zone of *ca* 50*100 m of pyroxenite interfingered with pegmatitic metagabbro. The contact pyroxenite-pegmatitic metagabbro is sharp, subvertical and displays a strong, subvertical lineation marked by the ellipsoidal shape of clinopyroxene (pseudomorphosed in

tremolite) aggregates (Fig. III.22b). Clinopyroxene aggregates showing plastic deformation, may be aligned into trails or form flames defining the foliation. Pseudomorphosed plagioclase is plastically deformed, surrounds cpx aggregates and shows extensive fluidal texture. These characteristics indicate a magmatic foliation and lineation of the pegmatitic metagabbro. Layers or alignments of crystals within the pyroxenite are parallel to the magmatic foliation of the metagabbro, the contact between the two attesting a comagmatic origin.

The volumetrically most important lithologies are wehrlites to clinopyroxenites with fine (mm-cm) to "extremely-coarse" (up to m long) clinopyroxene grains. Within the pyroxenites, pluri-dm in diameter geodes with radial antitaxial clinopyroxene are common (Fig. III.23a).
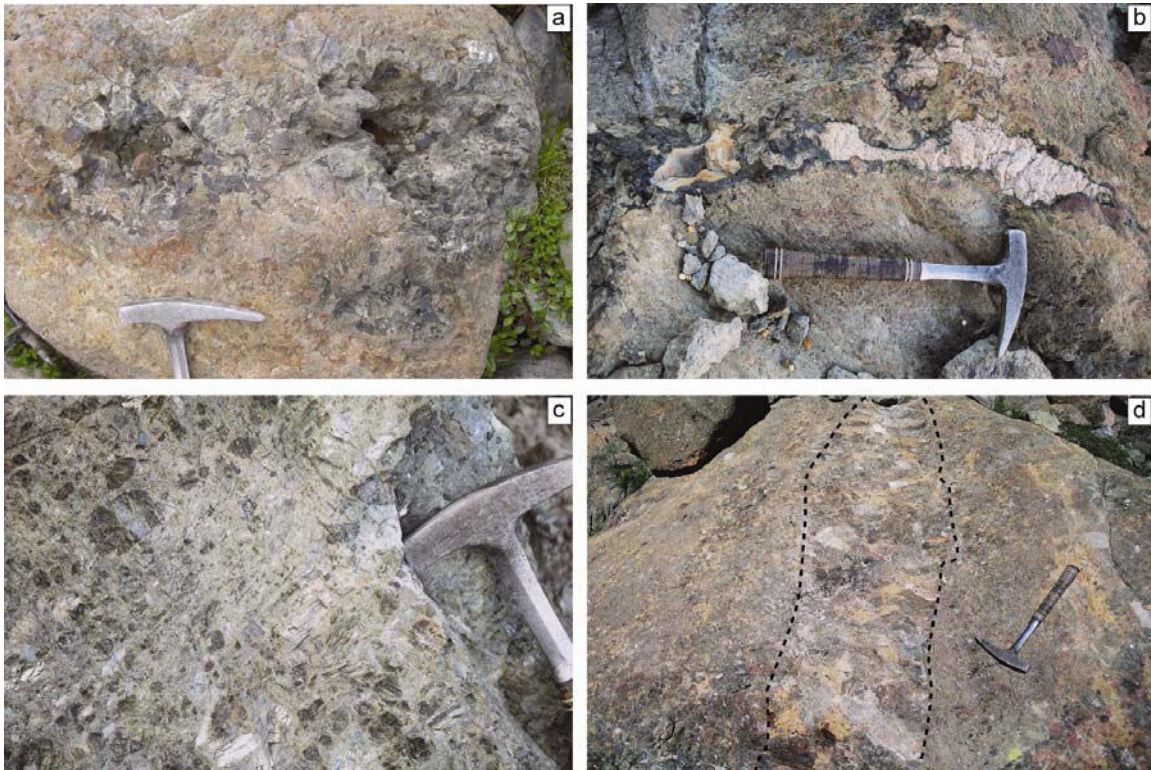
Figure III.23: Rock associations in pipe1: a) Geodes in pyroxenites. Note the antitaxial magmatic clinopyroxene (boulder in moraine). b) Leucocratic patch with amphibole rim (35°00.339'; 73°41.805'). c) Magmatic inequigranular texture in hornblende-bearing clinopyroxenite (35°01.010'; 73°42.166'). d) Vertical pegmatitic clinopyroxenite dyke with antitaxial coarse clinopyroxene. Note the blurred contact with the host clinopyroxenite (35°00.666'; 73°42.088').

A clinopyroxene + epidote + chlorite + sphene assemblage has been observed filling the inner space of one geode. Dunite occurs in *ca.* 100 m^2 bodies within the pyroxenites or as dykes and patches. Rare pegmatitic, hornblende-bearing leucocratic dykes or patches (10 to 100 cm wide and 50 cm to 20 m long) exhibit a hornblende rim at the border to the surrounding pyroxenite (Fig. III.23b). One pegmatitic gabbro dyke (10 * 1.5 m) cuts across both the pyroxenite and the host, fine-grained metagabbros. Shallowly north-

dipping, dm-wide hornblende-bearing tonalite dykes cut all the pyroxenite structures and become more abundant up-section.

Wehrlite to clinopyroxenite show a wide range of textures, from equant, fine-grained to pegmatitic, inequigranular (Fig. III.23c), with subhedral to anhedral clinopyroxene. Crystallization of olivine before clinopyroxene (documented by subhedral cpx in olivine matrix), of clinopyroxene before olivine (interstitial anhedral cpx with subhedral olivine) and co-crystallization of both (equant texture) are randomly distributed over the bodies. Layering marked by different modal proportions of olivine and clinopyroxene, magmatic slumps and cross bedding attest for magma dynamics. Subvertical, cm to dm wide dykes of fine grained ol-clinopyroxenite intrude the ol-clinopyroxenite groundmass with sharp boundaries. Subvertical dykes of pegmatitic ol-clinopyroxenite with m long clinopyroxenes have diffuse boundaries with the host rock (Fig. III.23d). The m long clinopyroxenes are antitaxial.

Equigranular ol-clinopyroxenite often exhibits a "spider" texture consisting of star-shaped cm to dm size pockets of olivine. In 3-D, these pockets represent vertical tubules tending to invade horizontally the host ol-clinopyroxenite.
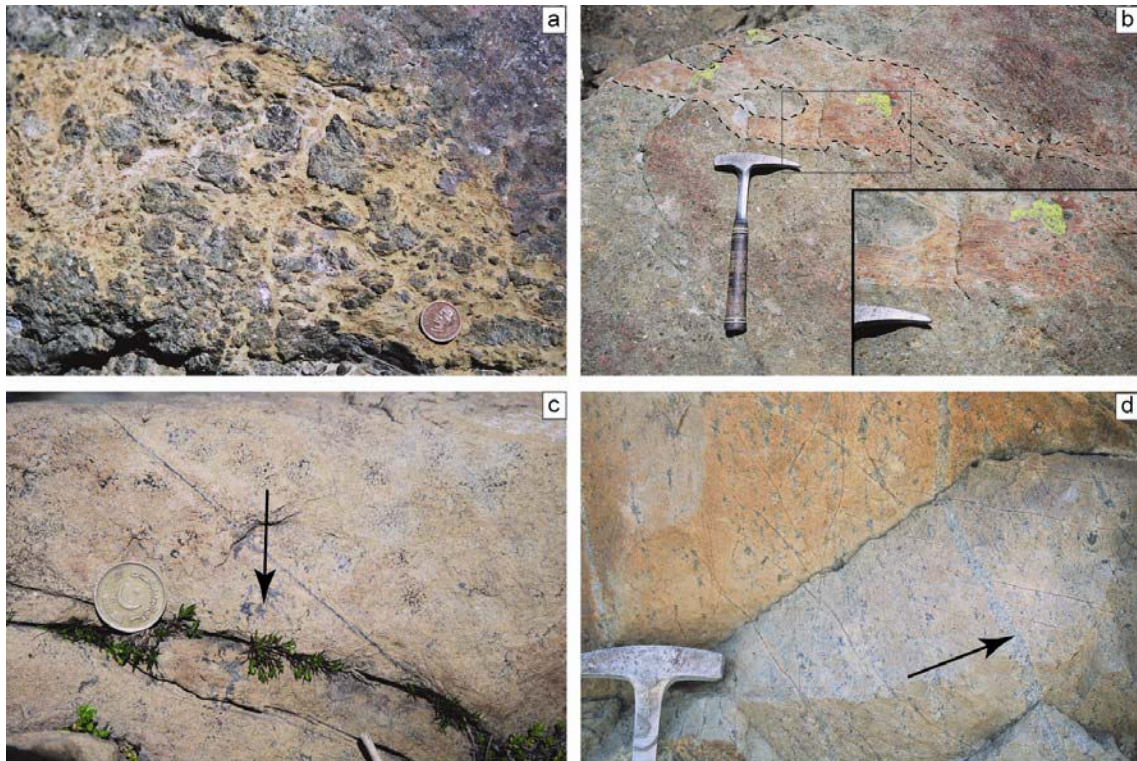
Figure III.24: Textures in pipe 1: a) Reacted (corroded) clinopyroxene in a vertical tubule of olivine (near 35°00.666'; 73°42.088'). b) Diffuse dunite dyke showing assimilated clinopyroxenite pieces. Note clinopyroxene grains teared from the host (near 35°00.666'; 73°42.088'). c) Clinopyroxene at grain boundaries (arrow) in massive dunite, indicating magma percolation (35°00.936; 73°42.252'). d) Vertically aligned clinopyroxene forming trails (arrow) in impregnated dunite (35°00.733'; 73°41.927').

Where these tubules are big enough and coalesce, olivine surrounds, isolates and corrodes the host clinopyroxene (Fig. III.24a). This type of "spider" texture is always spatially close to diffuse, subvertical dunite dykes and patches. These dunite dykes have diffuse boundaries with the host ol-clinopyroxenite and isolate and cut clinopyroxene crystals and aggregates from the host ol-clinopyroxenite groundmass (Fig. III.24b). The isolated clinopyroxene crystals often show dissolved boundaries and incorporated aggregates of clinopyroxene show a light-colored rim of serpentines. Dunite dykes include thin flames of serpentines organized into a network parallel to the dyke walls. Dunites forming massive masses have diffuse and gradual boundaries with the ol-clinopyroxenites. Within these dunite masses, clinopyroxenes may be organized in cockades at grain boundaries of olivine (Fig. III.24c), or may be aligned into trails (Fig. III.24d). Clinopyroxene may also form flames or may occur in dykes with fuzzy boundaries. Some dunites contain euhedral, mm-size spinels and relict, corroded clinopyroxenes.

III.2.3.2.   *Amphibole-plagioclase olivine-websterite body (Pipe2)*

Pipe 2 has an approximately 3.5 km long and 300 m wide ellipsoidal shape. Its long axis strikes nearly N090. The south contact with metagabbros is similar to contacts of pipe1: The contact between ol-websterite and the fine grained metagabbros shows an 80 cm wide, subvertical zone where pyroxenite infiltrates and tears apart pieces of the host rock (Fig. III.25a). Next to the contact the north-dipping foliation is not seen anymore. Where pyroxenite is in contact with pegmatitic metagabbro, the contact is sharp and subvertical, with the magmatic foliation of the pegmatitic metagabbros being vertical (Fig. III.25b). The tips of pipe 2 are not exposed or could not be reached.
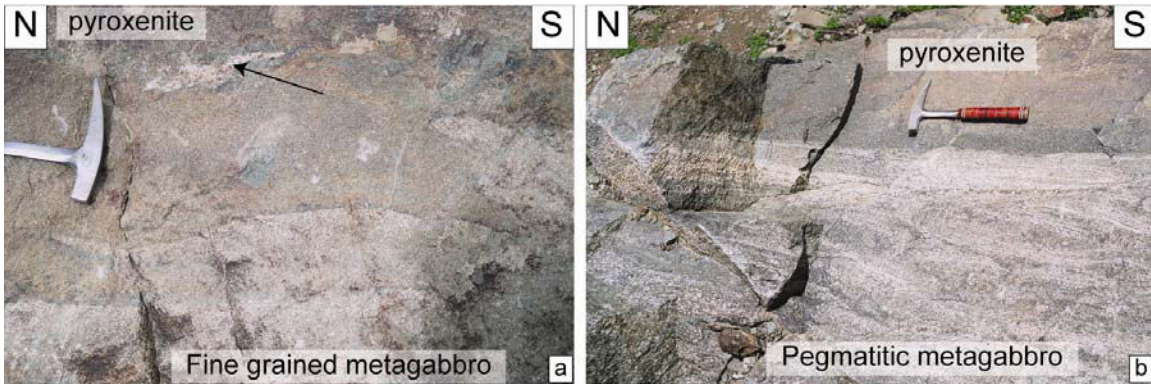
Figure III.25: Pipe2 boundaries: a) Contact between fine grained metagabbro and pyroxenite. Note the assimilated metagabbro pieces (arrow) (35°03.569'; 73°45.850'). b) Magmatic vertical fabric in pegmatitic metagabbros with reduced grain sized at the contact with pyroxenite (35°03.765'; 73°45.862').

The body is almost exclusively composed of massive ol-websterite to ol-clinopyroxenite. Varying modal proportions of clinopyroxene and olivine define a near vertical compositional banding. Elongated dunite bodies of *ca.* 10 m^2 are intruded by ol-clinopyroxenite and show diffuse boundaries with clinopyroxene content increasing toward the contact with the ol-clinopyroxenite. Within pipe 2, and mostly in its core, subvertical, tubular zones of plagioclase-hornblende-bearing ol-websterite (Fig. III.26a)

Figure III.26: Rock associations in pipe 2: a) Vertical impregnation feature with plagioclase and hornblende at grain boundaries in the host pyroxenite (35°03.000'; 73°45.307'). b) Horizontal plane view of Eye-shaped vertical and parallel impregnation zones (35°03.341'; 73°45.565'). c) reacted-dissolved pyroxenite, where remnants of pyroxenite are getting dissolved by the percolating melt crystallizing plagioclase (35°03.317'; 73°45.273'). d) Vertical dyke of Hbl-gabbro with hornblende reactional rim (black arrow) in pyroxenite with Hbl at grain boundaries (white arrow) (35°04.086'; 73°45.780'). e) Vertical dyke of Hbl-gabbronorite with fuzzy contact (next to previous). f) tonalitic dyke with Hbl reactional rim (arrow) and antitaxial Hbl, cross-cutting vertical clinopyroxene-olivine rich alternating layers (35°04.022'; 73°45.059').

have an ellipsoidal shape (horizontal section) with the long axis perpendicular to the long axis of the body (Fig. III.26b). Hornblende and plagioclase grow at grain boundaries within these zones (Fig. III.26a). In some places, plagioclase totally replaces the host pyroxenite (Fig. III.26c). Volumetrically minor hornblende gabbros (Fig. III.26d), hornblende gabbronorites (Fig. III.26e) and troctolite form subvertical, 10 cm to 1 m

wide dykes. The contact may be diffuse (hornblende gabbronorite, Fig. III.26e) or sharp, always with a hornblende rim (troctolite, hornblende gabbros, Fig. d). North-dipping, cm to dm wide tonalite dykes, locally in conjugate sets, cut across all structures (Fig. III.26f). These tonalites show a wide range of textures and modal compositions.

Amphibole crystals, minor or up to 60 % of the rock, are usually antitaxial; euhedral crystals can reach tens of cm in length. Fine grained amphibole is always present at the edges of the dykes, isolating the tonalite from the host pyroxenite. Millimeter to pluri-centimeter sized garnets have been found within these tonalitic dykes.

III.2.3.3.   *Dunitic bodies*

Several dunite bodies hundreds meters in diameter were recognized in the landscape. One of them has been investigated in detail. The body is composed of massive dunite with serpentine at grain boundaries. No contact with the surrounding metagabbros was exposed, but from the map shape of this body and the strong relief around we infer it to be subvertical. We will not discuss further such homogeneous dunite bodies, but contend that they formed through the same processes as the other ultramafic bodies hosted in the metagabbros.

III.2.4.   **Petrography**

III.2.4.1.   *Olivine-Clinopyroxenite body (Pipe1)*

Clinopyroxenites show a typical adcumulate texture with xenomorphic, strongly lobate and imbricated clinopyroxene (Fig. III.27a). Intercumulus phases comprise amphiboles, chlorite, spinel and serpentines.

Adcumulus clinopyroxene crystals range from few mm to cm in size, from what can be observed in thin section (meter long clinopyroxenes exist). They sometimes show a grayish color and clear cleavage often underlined by amphibole and, sometimes, magnetite (Fig. III.27b). In most cases, these clinopyroxenes (cpx_1) form a comb texture with smaller clinopyroxene (cpx_2) exempt of cleavage. This comb texture is always associated with amphiboles, either at the contact between the two clinopyroxenes, or as patches and exsolutions in cpx_1 (Fig. III.27c). Cpx_1 often shows a recrystallized rim of cpx_2, the latter showing no cleavage. Cpx_2 can also be present as fine grained crystals at grain boundaries of cpx_1 (Fig. III.27b). Millimeter-size secondary clinopyroxenes invade olivine grain boundaries in dunites. Subhedral to anhedral spinels are common inclusions in clinopyroxene.

Olivine in the ol-clinopyroxenite is rarely preserved, often recrystallized to serpentine with olivine ghost crystals marked by magnetite; serpentine is often associated with calcite and magnetite. Olivine in diffuse dunite dykes is also rarely preserved and magnetite and calcite grow into a network with a strong preferred orientation defining fluids pathways. Two olivine generations are recognized in some places. The first generation is serpentinized whereas the second replaces serpentine in net-like features or as large grains. New olivine often contains magnetite and/or calcite as inclusions (Fig. III.27d). Fresh, coarse dunite shows a heterogeneous grain size with strongly undulose, pluri-millimeter big, flattened grains that contain euhedral chromite grains (Fig. III.27e). These crystals are within a matrix of finer grains that show 120° triple junctions (Fig. III.27e). Few small micrometer-size corroded clinopyroxene grains are present in some
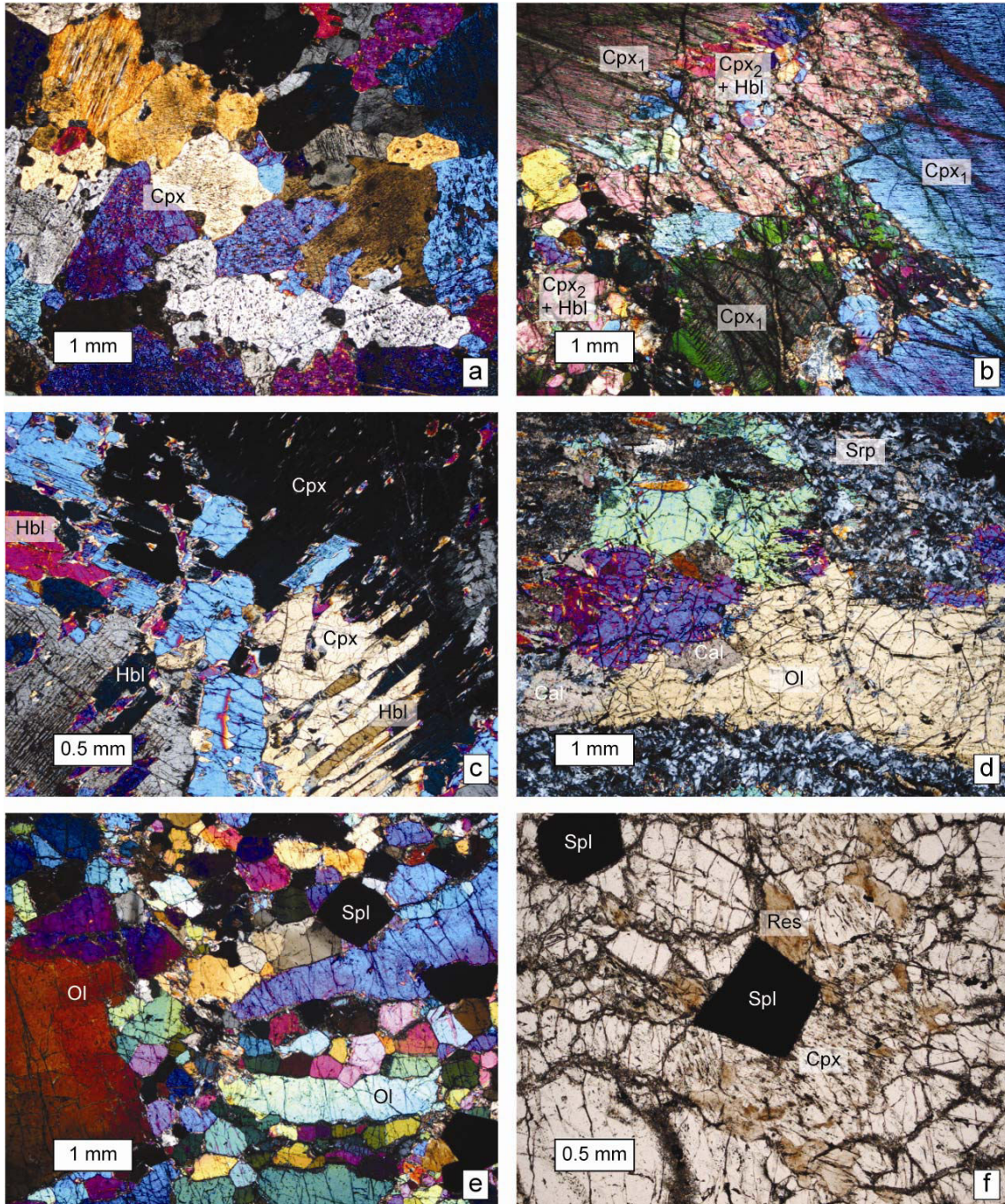
Figure III.27: Petrographical observations in pipe 1: a) Typical adcumulate texture in clinopyroxenite. b) Two generations of clinopyroxene in a Hbl-pyroxenite (Fig. III.23c). Large cpx_1 with tremolite marking cleavage and cpx_2 + hbl forming the matrix. c) Intergrown hbl and cpx in a comb texture. d) Second olivine generation overgrowing serpentine and including calcite. e) Typical porphyroclastic texture in dunite with euhedral chromite spinels. f) Residual cpx after ol formation. Res = residual after cpx breakdown.

places together with a brownish, unidentified mineral phase (Fig. III.27f). Orthopyroxene has only been found once during microprobe analysis and is otherwise absent

Large epidote grains form massive aggregates in the leucocratic patches and constitute the matrix in which mm-size amphiboles, chlorite and minor nests of 10th of micrometer large clinopyroxenes are present. In these pockets, chlorite is observed as large aggregates included in epidote, or as fine grains replacing amphibole and epidote. Amphiboles show recrystallization rims, and new mm size euhedral amphiboles overgrow chlorites. These leucocratic patches have little of their magmatic mineralogy left.

III.2.4.2. *Amphibole-plagioclase olivine-websterite body (Pipe2)*

The clinopyroxene-olivine-rich parts often show an adcumulate texture. The transition between olivine- and clinopyroxene-rich horizons is defined by a heteradcumulate texture (Fig. III.28a).
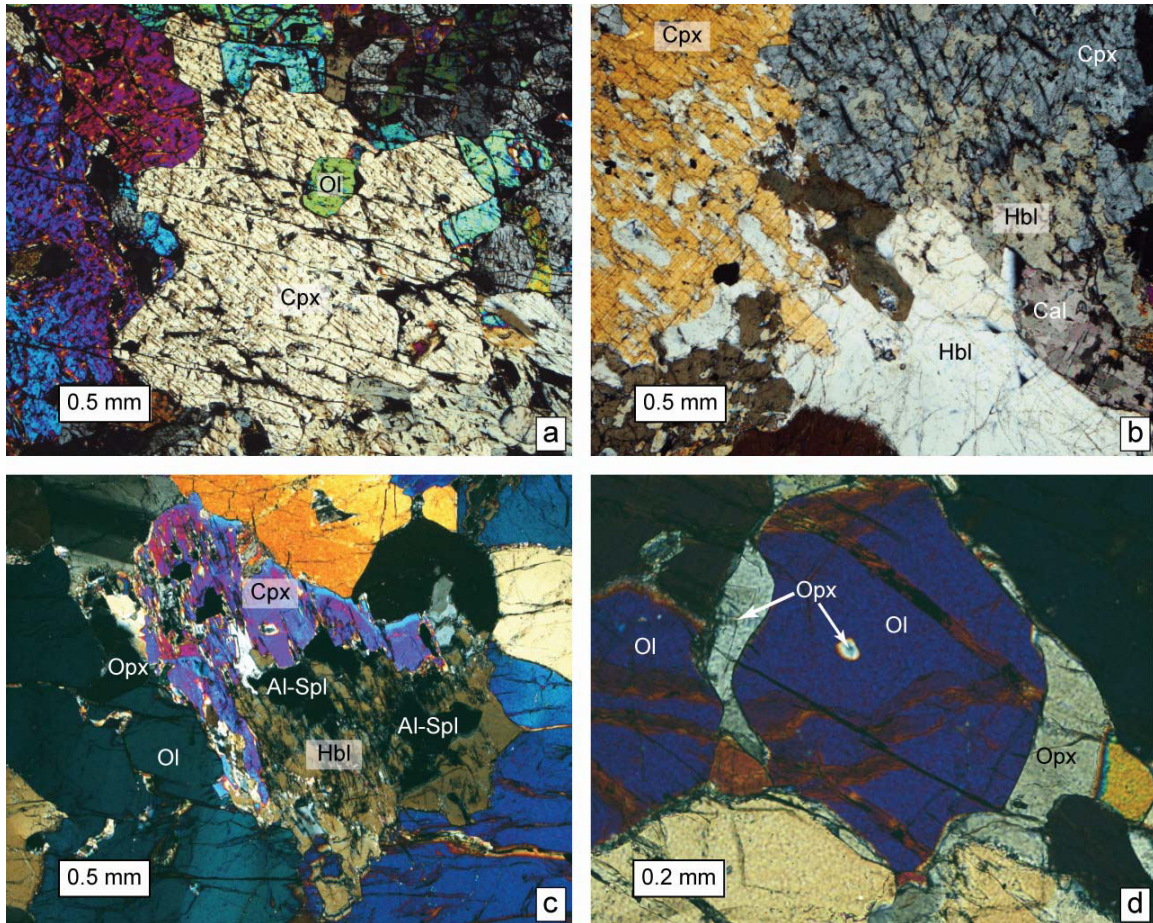

Figure III.28: Petrographical observations in pipe 2: a) Heteradcumulate texture at the interface between cpx and ol rich horizon. b) Typical hbl replacing cpx texture. c) cpx being replaced by hbl + deep green spinel. Note orthopyroxene at grain boundaries. d) orthopyroxene growing at grain boundaries and replacing ol.

In the bulk ol-websterite, only few orthopyroxene grains have the same texture as clinopyroxene. Amphibole replaces almost everywhere clinopyroxene (Fig. III.28b). Amphiboles are also present at grain boundaries or build a heteradcumulate texture with olivine and clinopyroxene. Some amphiboles, calcite and Cr-clinochlore are found at grain boundaries and as inclusions in olivine. Calcite is commonly associated with amphibole (Fig. III.28a). Anhedral Cr-spinels form inclusions in olivine.

Within dunite pods, olivine is present as adcumulate crystals. Magnetite, titanomagnetite and FeNi sulfides are present as inclusions and at grain boundaries.

Next to the pl-hbl-bearing ol-websterite zones, the replacement of clinopyroxene by amphiboles becomes more important and is associated with the presence of green spinel and orthopyroxene (Fig. III.28c). Orthopyroxene is also found at grain boundaries and often overgrows olivine (Fig. III.28d). Garnet-hornblende-spinel intergrowth can also be present as interstitial paragenesis. Rarely, interstitial amphiboles host clinopyroxene + green spinel symplectites of unknown origin.

Within pl-hbl-bearing ol-websterite zones, plagioclase systematically invades and crystallizes at grain boundaries and often includes amphiboles. Olivine and plagioclase are never in direct contact but show different types of mineral association at the olivine-plagioclase interface. These reaction rims may be made of orthopyroxene or amphibole only. More commonly symplectites of amphiboles + green spinel (Fig. III.29a) ± orthopyroxene are observed. Symplectite growth can begin at olivine surface but is observed on amphiboles coating olivine (Fig. III.29b). In fact these zones represent fully reacted pyroxenite with a percolating melt. Also, clinopyroxene is almost absent from these rocks, which mineralogy comprises plagioclase + hornblende + orthopyroxene + green spinel + relictual olivine enclose in symplectites (i.e. olivine never in contact with plagioclase).

Hornblende-gabbronorite dykes show magmatic textures with anhedral orthopyroxene, clinopyroxene and amphiboles whereas xenomorphic plagioclase constitutes the matrix (Fig. III.29d). Granophyric textures with orthopyroxene + clinopyroxene + amphiboles intergrowth are present.

Hornblende-gabbros show subhedral amphibole grains in a matrix of subhedral plagioclase. The dyke walls show syn-crystallization of plagioclase and antitaxial amphibole needles on the dyke side (Fig. III.29c), whereas subhedral amphibole and ilmenite constitute the host side. These subhedral amphibole grains gradually become interstitial away from the dyke wall, into the pyroxenitic host.

Hornblende tonalites show euhedral to subhedral amphiboles with plagioclase and quartz as matrix phases. Plagioclase and quartz are graphically intergrown, indicating eutectic crystallization. Large texturally magmatic epidote grains are present together with plagioclase. Very few microscospic biotite grains are found in contact with amphiboles. Titanium oxides and ilmenite are inclusions in amphiboles and plagioclase. Zircon and apatite are common minor phases.
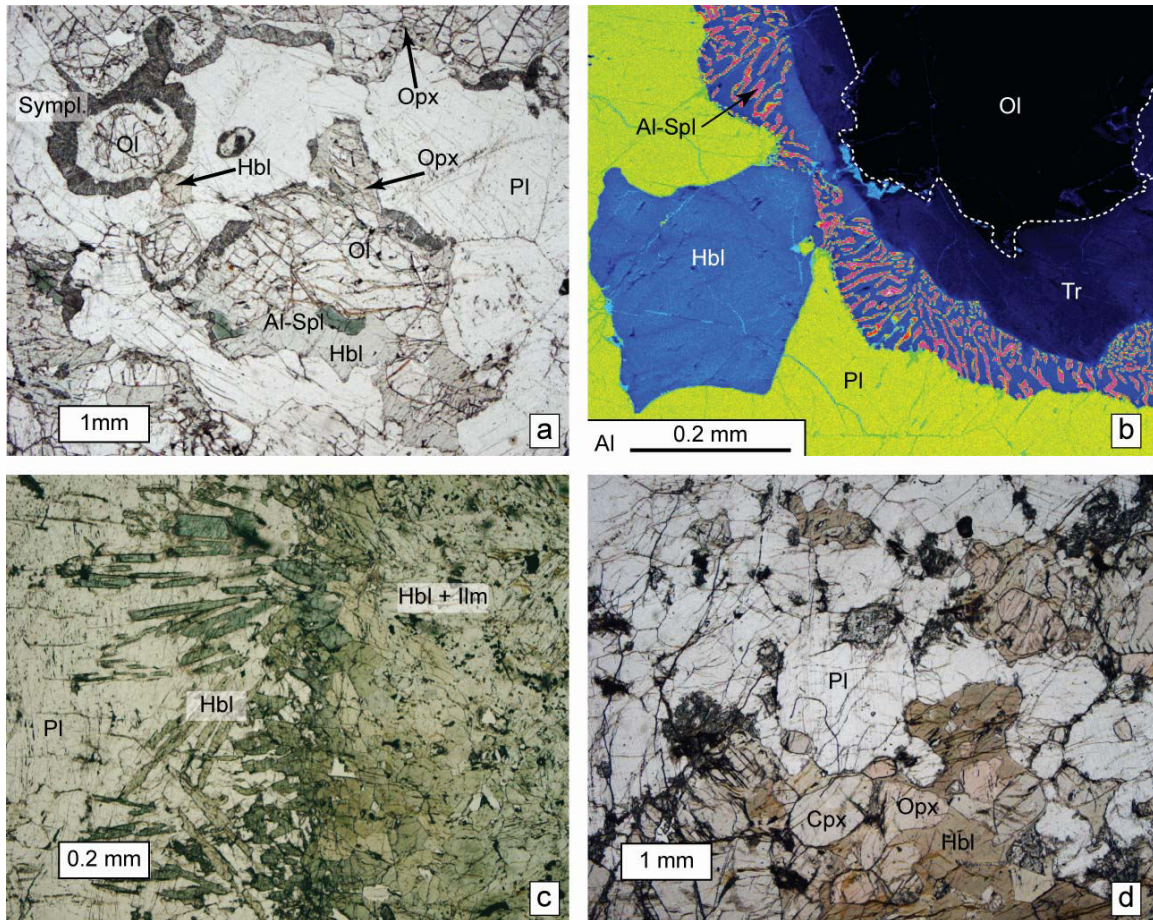
Figure III.29: Microtexture of pl-bearing rocks of pipe 2: a) Fully reacted pyroxenite with pl at grain boundaries and opx or hbl or opx + hbl + green spinels coating olivine. Green spinels + hbl symplectite are also present either coating olivine or opx or hbl. b) Aluminium WDS microprobe map of a symplectite coating hbl rimmed ol. Symplectite rooted in tremolite, pseudomorph of hbl due to late retrogression chemical exchange. c) hbl reactional rim of an hbl gabbro dyke. Note the antitaxial growth on the dyke side and the co-crystallization of hbl and ilm on the host side. d) Magmatic texture in hbl-gabbronorite.

Within hornblende-gabbro dykes, mm-size, euhedral garnets are found in plagioclase. Within tonalitic dykes, garnet is associated with green amphibole and ilmenite in plagioclase. Plagioclase in thick leuco-tonalite dykes is saussuritized and shows albitization.

The above-listed primary parageneses are often overprinted by fluid-assisted recrystallization. Within the pyroxenites, clinpyroxene and amphiboles are replaced by secondary tremolite whereas chlorite is omnipresent at grain boundaries. Plagioclase is often enclosing and replaced by secondary bluish-green amphibole and epidote, locally together with corundum or garnet. The bluish-green amphibole may rim pre-existing magmatic amphibole, or be at the interface between epidote+chlorite and plagioclase, or crystallize in cracks and twin boundaries of plagioclase. Cu and Zn sulfides are frequent in this paragenesis.

III.2.5. Interpretation of structures and textures

Contacts between the pyroxenite bodies and the host fine grained metagabbros are subvertical, locally sharp and pyroxenites assimilate, directly at the contact, the host fine grained metagabbro. The regionally northwest-dipping fine grained metagabbros show a narrow zone of subvertical foliation within 20m of the contact, whereas elsewhere they lack foliation. The pegmatitic metagabbros connecting pipe 1 and pipe 2 show subvertical magmatic foliation and lineation at the contact with the pyroxenites. These features indicate (i) the intrusive character of the pyroxenite bodies into the fine grained metagabbros (ii) that pyroxenites formed at the expense of fine grained metagabbros by thermal erosion and assimilation and (iii) the cogenetic character of the pegmatitic metagabbros and the pyroxenite bodies.

Within pipe 1, numerous individual magma conduits are represented by dunites that cut, impregnate and react with pyroxenites and *vice versa* (Figure III.30). The direction of magma flow was subvertical, parallel to the internal magmatic structures as given by tubules and dykes.
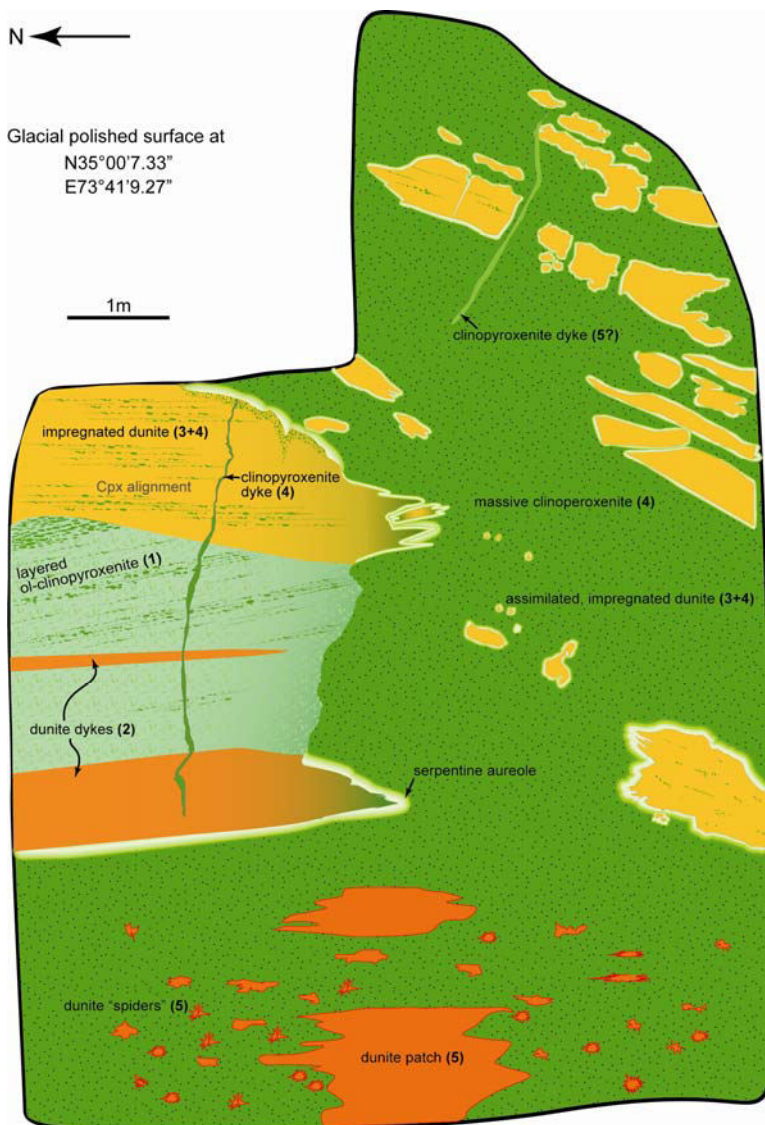

Figure III.30: Small scale map of a glacial polished surface showing the multiple relationships between clinopyroxenites and dunites. Several generations of dunites and clinopyroxenites are interact with each other via intrusive or impregnation relationships. Numbers in brackets represent the relative time between lithologies

Crystallization processes include a combination of crystallization, melt evolution and peritectic reaction with previous cumulates. A primitive, olivine-saturated melt would crystallize olivine first, generating dunites and leading to the appearance of cpx together with olivine on a cotectic. Crystallization of ol and cpx generates ol-clinopyroxenites. Small variations in melt composition, pressure, temperature or the nature and amount of assimilated material might move the liquid comnposition of the ol-cpx cotectic, leading to saturation in ol or cpx only. The remaining cooling melts further crystallize mainly cpx and amphiboles, generating clinopyroxenites. There are many other variants to this crystallization scenario. Ol-saturated melt may also percolate through cpx-rich lithologies, dissolving cpx and crystallizing ol to generate dunite with relictual, corroded cpx. Percolation of a cpx-saturated melt into dunite may result in a modal ol-clinopyroxenite. Intermediate combinations of crystallization and percolation lead to the variety of textures between ol-cpx and amphiboles. The ultimate melt fraction represented by the leucocratic patches would correspond to the end of the crystallization-reaction process, these leucocratic patches could possibly represent (the only) true liquid composition of pipe 1 that have been trapped.

 Evidence for fluid circulation is omnipresent in pipe 1: (i) syn-magmatic veins and geodes filled with hydrous phases, (ii) calcite with serpentines indicating a CO_2 bearing fluid, (iii) serpentine rimming fragment of assimilated material and (iv) cpx_1 cleavage containing amphiboles and chlorites absent in cpx_2. These features represent low temperature fluid percolation, but observations (i) and (iv) support fluid percolation between the magma batches that crystallized the pipe material. We therefore interpret the percolating fluid as being derived from unmixed fluids upon partial magma crystallization. Olivine overgrowing serpentines indicates that low temperature fluid percolation is a transient feature unrelated to the greenschist facies metamorphism unevenly affecting the body.

Within pipe 2, magmatic structures are also subvertical and the variety of textures and lithologies formed by crystallization and melt reactions is much wider. There are only a few dunite pods, always impregnated by clinopyroxene, suggesting that most of the melt reaching the outcrop level of pipe 2 was ol + cpx ± opx saturated, in accordance with the volumetrically important ol-websterite and ol-clinopyroxenite host rocks. Amphibole replacing clinopyroxene suggests a peritectic reaction between the crystallized cpx and a hydrous melt leading to amphibole stability upon crystallization. Also the appearance of orthopyroxene at the expense of olivine suggests peritectic reaction between melt and olivine. The impregnation process leading to the crystallization of orthopyroxene, plagioclase and hornblende at grain boundaries within vertical channels results from magma percolation and led to the disappearance of cpx in the fully reacted pyroxenites, in which plagioclase is present for the first time. The dissolution-reaction-precipitation showed by the fully reacted pyroxenites demonstrates disequilibrium between the host pyroxenite and percolating magmas (Fig. III.26c). Within the vertical dykes of the most differentiated rocks, mineral phases become proper cumulate phases following a classical crystallization sequence (ol + cpx + opx + amph, pl ± ep + qtz).

The destabilization products of plagioclase result from fluid-assisted, sub-solidus reactions. The bluish-green amphibole-garnet-epidote paragenesis results from post magmatic fluid re-equilibration rather than from the greenschist facies retromorphic paragenesis denoted by the presence of tremolites and chlorites. The presence of sulfides

associated with plagioclase destabilization products supports this hypothesis. Garnet present as symplectite with amphibole and green spinel is believed to be of magmatic origin, by analogy with the other symplectites.

In summary, the investigated pyroxenite bodies represent magmatic conduits in which melts migrated upward, crystallizing and reacting with their own previous cumulate products.

III.2.6. Mineral chemistry

III.2.6.1. Pipe 1

III.2.6.1.1. Olivine

Olivines (Table III.9) show a wide range of X_{Mg} (0.855 < X_{Mg} < 0.962) (Fig. III.31a) NiO (0.027< NiO <0.188 wt %) and MnO (0.108< MnO < 2.110 wt %; Fig. III.31b). The olivines with the highest X_{Mg}, MnO and lowest NiO (X_{Mg} ≈ 0.96, NiO ≈ 0.05 and MnO up to 2.1) are secondary grains overgrowing serpentine. Olivine from massive dunite with corroded relictual clinopyroxene has high X_{Mg} and high NiO content (X_{Mg} ≈ 0.915, NiO ≈ 0.15), whereas olivine from dunite dykes and from ol-clinopyroxenite has lower X_{Mg} and NiO content (0.85< X_{Mg} < 0.90; 0.07< NiO < 0.17 wt %).

	Pipe 1						Pipe 2	
	Dunite		overgrowing serp		Ol-Cpxite		Backgr. pyxite.	
	n=29	2σ	n=15	2σ	n=26	2σ	n=33	2σ
SiO2	39.52	0.46	41.03	0.22	40.11	0.22	37.46	0.84
FeO	8.75	0.27	4.08	0.15	11.27	0.67	18.52	1.22
MnO	0.16	0.02	0.76	0.46	0.19	0.02	0.27	0.03
NiO	0.15	0.01	0.05	0.01	0.14	0.02	0.09	0.02
MgO	50.54	0.45	53.01	0.51	48.66	0.49	43.00	1.03
CaO	0.01	0.01	0.03	0.01	0.01	0.01	0.01	0.01
Total	99.15	0.68	98.97	0.45	100.42	0.32	99.37	1.14
XMg	0.91	0.00	0.96	0.00	0.88	0.01	0.81	0.01

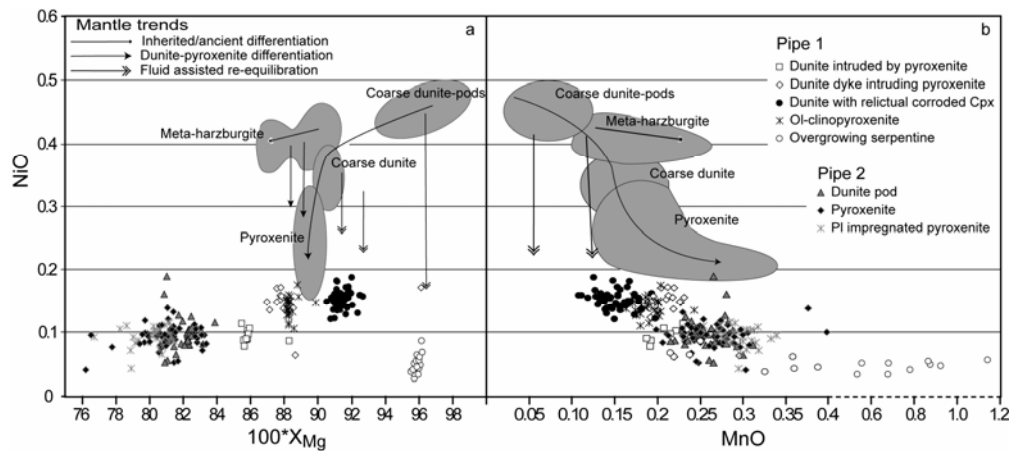Table III.9: representative olivine analyses of pipe 1 and 2

Figure III.31: Pipe1 and pipe 2 olivine compositions. Grey fields = mantle differentiation trends of the Sapat mantle rocks from (Bouilhol, et al., 2008). a) X_{Mg} versus NiO content in olivine. b) MnO versus NiO content of the same grains.

III.2.6.1.2. *Clinopyroxene*

Clinopyroxene (Table III.10) does not show systematic zoning and there is almost no systematic chemical variation between cpx_1 and cpx_2. Clinopyroxenes have a wide range in Al_2O_3 content and X_{Mg} forming a trend from high X_{Mg} and low Al_2O_3 (X_{Mg}=0.93, Al_2O_3=0.3 wt %) to low X_{Mg} and high Al_2O_3 (X_{Mg}=0.85 Al_2O_3=3 Wt %) (Fig. III.32a). Clinopyroxenes also show variation in TiO_2, typically Ti content increases with decreasing X_{Mg} (TiO_2 up to 0.2 wt %). Corroded, decomposed clinopyroxene from dunite has the highest X_{Mg} (0.98-0.94) and the lowest Al_2O_3 (0.11-1.3 wt %) and TiO_2 (up to 0.95 wt %) contents. Chromium contents range up to 0.8 wt % uncorrelated with X_{Mg}.
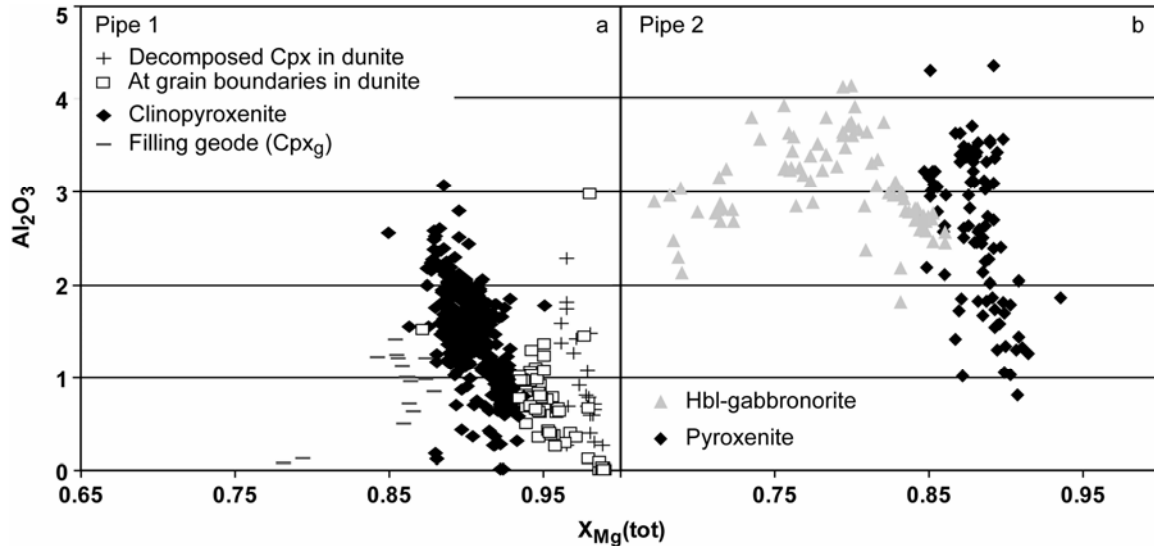

Figure III.32: X_{Mg} versus Al_2O_3 cpx composition in a) Pipe1; and b) Pipe2.

All pyroxenite clinopyroxenes have the same REE pattern, with flat HREE segments ($0.89 < Dy_N/Lu_N < 1.20$), slightly fractionated MREE ($0.35 < Sm_N/Dy_N < 0.68$) and strongly fractionated LREE ($0.06 < La_N/Sm_N < 0.34$) in chondrite normalized patterns (Fig. III.33a). None of the analyzed clinopyroxenes show any Eu anomaly. One noticeable difference comes from cpx_1 that shows La enrichment due to minute serpentines or chlorite (see appendix X) within the cleavage of the analyzed grains. The more primitive the clinopyroxenes are (high X_{Mg}, low Al_2O_3, TiO_2) the less enriched is their REE pattern. Normalized to primitive mantle (Fig. III.33b), clinopyroxenes show positive anomalies in Cs, Pb, and Sr. HFSE are depleted compared to neighboring elements, except for Ti not showing any anomaly and to some extent for Ta, which is slightly decoupled from Nb and is not depleted compared to La. U and Th are decoupled, with variable U contents and almost constant negative Th anomaly ($Th_N \approx 0.01$) compared to Ba and U.

Clinopyroxene from geodes (cpx_g on Fig. III.32 and 12a, b) is distinct, having the lowest X_{Mg} (0.84-0.88), an average of 1 wt% Al_2O_3 content, a low TiO_2 content (0.03 wt %) and nearly no chromium. The chondrite normalized patterns show a strongly fractionated HREE segment ($Dy_N/Lu_N \approx 0.04$) and a rather flat, but disturbed M-LREE. Normalized

to primitive mantle, geode clinopyroxenes show that LILE and Ta have the same distribution than the other cpx, but Hf, Zr and Ti show a strong positive anomaly.

Sample	P10 Clinopyroxenite		P13 Clinopyroxenite		P25 Clinopyroxenite		P7 Cpx1 Clinopyroxenite		cpx2	
	Avrg	2σ	Avrg	2σ	Avrg	2σ	Avrg	2σ	Avrg	2σ
Majors	n=11		n=41		n=48		n=60		n=34	
SiO2	52.95	0.68	52.52	0.53	53.07	0.48	54.03	0.58	53.76	0.49
TiO2	0.11	0.05	0.09	0.03	0.07	0.01	0.04	0.01	0.05	0.01
Cr2O3	0.24	0.14	0.46	0.08	0.45	0.11	0.54	0.09	0.55	0.08
Al2O3	1.72	0.75	1.94	0.37	1.34	0.23	0.89	0.34	1.22	0.39
FeO	3.43	0.27	3.78	0.29	3.57	0.21	2.70	0.19	2.79	0.25
MnO	0.12	0.02	0.13	0.03	0.13	0.02	0.10	0.02	0.09	0.01
NiO	0.01	0.01	0.02	0.01	0.02	0.01	0.02	0.01	0.02	0.01
MgO	16.52	0.27	16.54	0.52	16.78	0.38	17.92	0.39	17.65	0.36
CaO	24.42	0.54	23.42	0.88	23.65	0.56	24.76	0.56	24.82	0.36
Na2O	0.04	0.03	0.09	0.02	0.07	0.02	0.08	0.02	0.08	0.02
Total	99.58	0.23	99.00	0.54	99.14	0.51	101.08	0.52	101.03	0.44
XMg(Fetot)	0.90	0.01	0.89	0.01	0.89	0.00	0.92	0.01	0.92	0.01
traces	n=4		n=3		n=9		n=14		n=5	
Cs	0.27	0.28	0.26	0.36	0.07	0.06	0.44	0.27	0.03	0.02
Rb	0.89	1.32	0.06	0.03	0.02	0.00	0.07	0.03	0.02	0.01
Ba	2.50	3.13	0.27	0.36	0.19	0.18	0.84	0.61	0.17	0.08
Th	0.0076	0.0023	0.0004	0.0004	0.0009	0.0008	0.0003	0.0001	0.0013	0.0016
U	0.0483	0.0631	0.0001	0.0001	0.1071	0.3014	0.0016	0.0015	0.0004	0.0003
Nb	0.0144	0.0104	0.0027	0.0001	0.0026	0.0007	0.0050	0.0018	0.0057	0.0031
Ta	0.0043	0.0019	0.0010	1/3	0.0015	0.0007	0.0031	0.0016	0.0020	1/5
La	0.063	0.006	0.031	0.011	0.011	0.002	0.025	0.013	0.010	0.004
Ce	0.213	0.022	0.098	0.033	0.048	0.008	0.037	0.007	0.033	0.005
Pb	0.138	0.070	0.076	0.046	0.029	0.010	0.017	0.004	0.024	0.003
Pr	0.042	0.009	0.023	0.011	0.011	0.002	0.008	0.002	0.007	0.001
Sr	7.79	1.76	3.63	0.22	3.15	0.16	3.32	0.30	3.09	0.07
Nd	0.263	0.063	0.150	0.051	0.091	0.023	0.064	0.015	0.061	0.004
Sm	0.162	0.037	0.114	0.040	0.067	0.019	0.047	0.015	0.034	0.003
Zr	1.066	0.233	0.313	0.143	0.200	0.163	0.054	0.008	0.049	0.005
Hf	0.058	0.017	0.023	0.011	0.012	0.006	0.003	0.001	0.005	0.003
Eu	0.084	0.019	0.055	0.013	0.036	0.006	0.023	0.005	0.017	0.006
Gd	0.317	0.087	0.208	0.073	0.151	0.036	0.093	0.014	0.086	0.014
Tb	0.065	0.020	0.044	0.014	0.033	0.008	0.018	0.003	0.019	0.002
Dy	0.481	0.162	0.351	0.125	0.263	0.065	0.149	0.019	0.132	0.011
Y	2.68	0.84	1.92	0.59	1.44	0.34	0.84	0.10	0.75	0.04
Ho	0.105	0.035	0.079	0.027	0.060	0.016	0.032	0.006	0.027	0.002
Er	0.322	0.109	0.250	0.099	69.668	0.038	0.094	0.013	0.091	0.009
Ti	937.1	315.2	649.7	246.9	395.0	73.5	271.0	23.3	257.2	12.2
Tm	0.048	0.016	0.037	0.012	0.027	0.006	0.015	0.002	0.012	0.003
Yb	0.329	0.104	0.237	0.078	0.173	0.040	0.105	0.019	0.088	0.015
Lu	0.049	0.014	0.032	0.010	0.025	0.004	0.014	0.003	0.013	0.002

Table III.10: Pipe 1 representative major element analyses of clinopyroxene, and trace elements concentration of clinopyroxene from the same sample.

Table III.10 continues

Sample	P18 Clinopyroxenite		P1 cpx2 Clinopyroxenite		P2 Cpxg Filling geodes	
Majors	Avrg n=28	2σ	Avrg n=45	2σ	Avrg n=16	2σ
SiO2	53.15	1.16	53.26	0.69	53.38	0.28
TiO2	0.04	0.01	0.07	0.01	0.03	0.04
Cr2O3	0.40	0.18	0.33	0.06	0.03	0.02
Al2O3	1.07	0.41	1.39	0.18	0.88	0.39
FeO	2.04	0.67	3.09	0.18	4.59	0.84
MnO	0.11	0.03	0.11	0.02	0.28	0.12
NiO	0.02	0.01	0.02	0.01	0.01	0.01
MgO	18.42	1.53	16.73	0.78	14.88	0.52
CaO	23.69	1.41	23.84	0.47	24.51	0.30
Na2O	0.05	0.03	0.08	0.01	0.37	0.15
Total	99.00	1.16	98.92	1.10	98.98	0.28
$X_{Mg(Fetot)}$	0.92	0.02	0.91	0.01	0.85	0.03
traces	n=5		n=6		n=8	
Cs	0.04	0.06	0.30	0.25	1.62	3.57
Rb	0.02	0.02	0.18	0.27	1.59	3.47
Ba	0.10	0.09	1.33	1.01	0.63	1.16
Th	0.0011	0.0012	0.0008	0.0002	0.0005	0.0003
U	0.0002	0.0001	0.0009	0.0004	0.0197	0.0380
Nb	0.0026	0.0008	0.0042	0.0017	0.0207	0.0281
Ta	0.0010	1/5	0.0020	0.0008	0.0025	0.0016
La	0.010	0.001	0.071	0.023	0.008	0.007
Ce	0.040	0.008	0.103	0.012	0.131	0.324
Pb	0.022	0.004	0.069	0.019	0.044	0.056
Pr	0.010	0.003	0.027	0.004	0.009	0.014
Sr	3.06	0.44	4.24	0.19	5.79	0.37
Nd	0.072	0.011	0.163	0.025	0.018	0.032
Sm	0.051	0.008	0.080	0.017	0.011	0.010
Zr	0.118	0.050	0.178	0.019	1.371	2.192
Hf	0.007	0.005	0.009	0.006	0.041	0.064
Eu	0.026	0.002	0.038	0.007	0.007	0.014
Gd	0.105	0.012	0.165	0.021	0.013	0.014
Tb	0.024	0.003	0.034	0.004	0.002	0.002
Dy	0.189	0.021	0.270	0.038	0.013	0.017
Y	1.04	0.11	1.64	0.22	0.09	0.09
Ho	0.043	0.004	0.061	0.006	0.004	0.004
Er	0.125	0.013	0.185	0.027	0.015	0.014
Ti	329.4	35.9	539.4	36.6	205.2	124.4
Tm	0.019	0.003	0.028	0.006	0.005	0.003
Yb	0.131	0.017	0.181	0.024	0.046	0.046
Lu	0.019	0.001	0.027	0.004	0.021	0.026
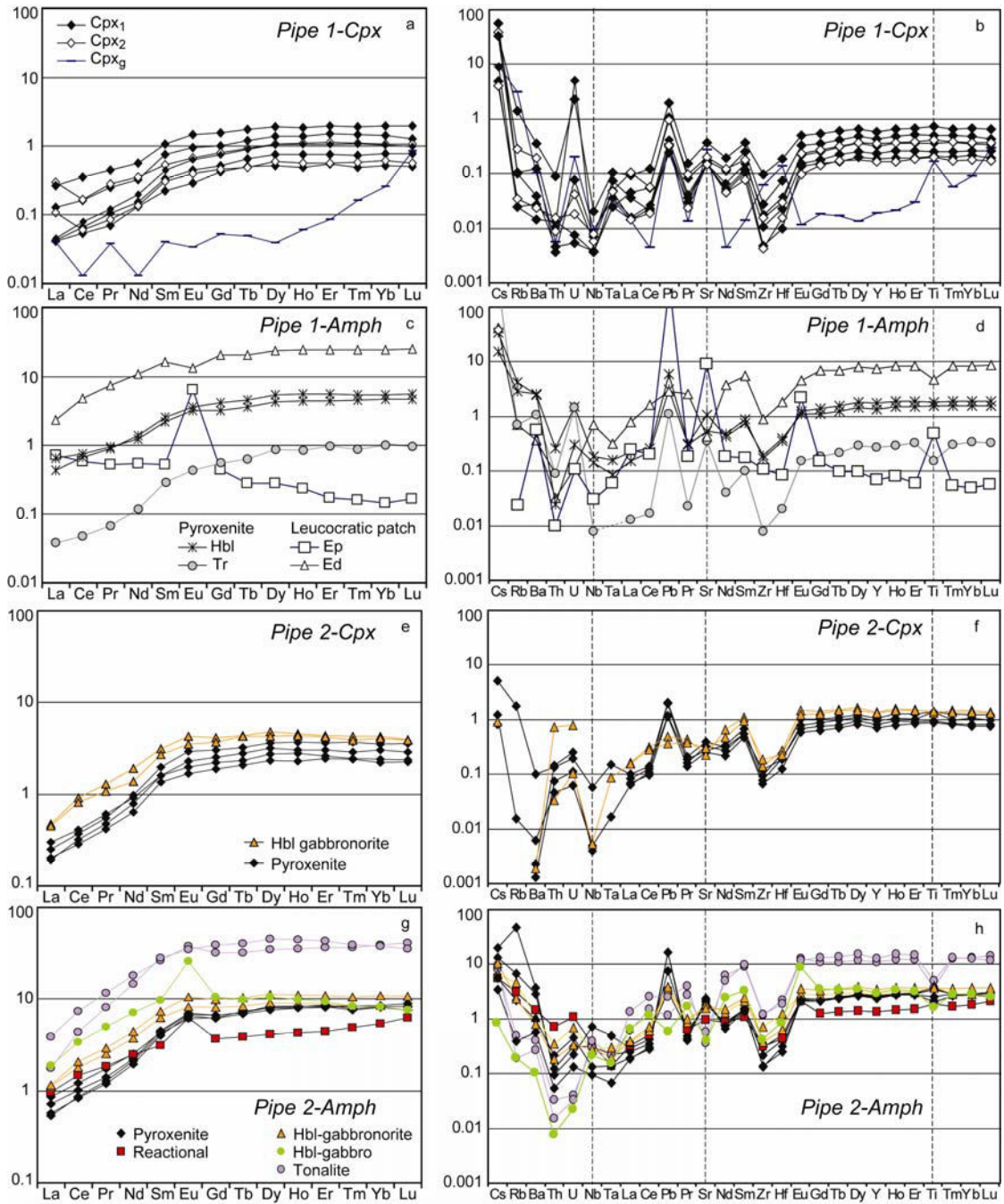
Figure III.33: Trace element composition of cpx, amphiboles and ep; a) REE chondrite normalized diagram of cpx in pipe1. b) Primitive mantle normalized diagram of cpx in pipe 1. c) Chondrite normalized diagram of amphiboles and epidote in pipe 1. d) Primitive mantle normalized diagram of amphiboles and epidote in pipe 1 e) Chondrite normalized cpx REE composition in pipe2. f) Primitive mantle normalized composition of cpx in pipe 2. g) REE chondrite normalized composition of amph in pipe 2. h) Primitive mantle normalized composition of amph in pipe 2..Normalization values are from (Sun and McDonough, 1989), also for all following normalized diagrams.

III.2.6.1.3.   *Amphiboles*

Pyroxenite amphiboles (Table 3Table III.11) are dominantly Mg-hornblende and tremolite (Fig. III.34a). Tremolite sometimes rims clinopyroxene and Mg-hornblende. The evolution of Mg-hornblende towards tremolitic compositions is mostly sharp but occasionally continuous with Si increasing from 6.85 to 8 apfu while Na(A) decreases from 0.54 to 0 apfu. These tremolitic compositions reflect re-equilibration during regional greenschist facies overprint and will not be discussed further. The Mg-hornblende (Si < 7.5 apfu.) shows an increase of Na_2O and TiO_2 with decreasing X_{Mg}, reflecting magmatic processes (Fig. III.34b and c). The magmatic character of the Mg-hornblende is further indicated by high Cr_2O_3 content ($0.25 < Cr_2O_3 < 1.6$ wt %), which decrease with increasing Si content.
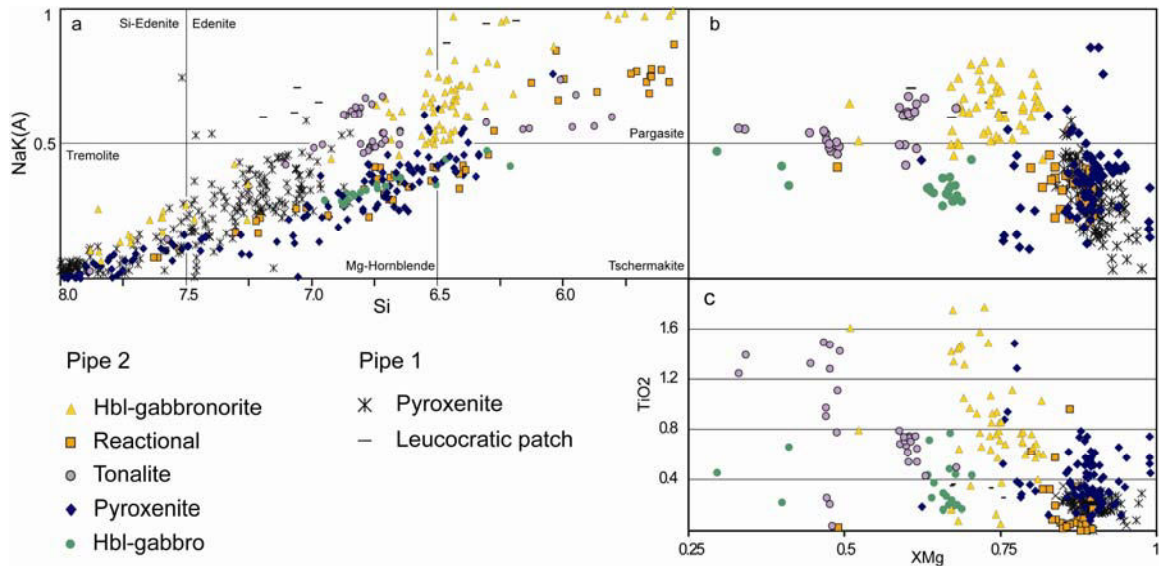
Figure III.34: a) Leake (1978) diagram of all amphiboles found in both Pipes. b) X_{Mg} versus Na + K in A site for magmatique hbl. Magmatic discrimination made on textural observation. c) X_{Mg} versus TiO2 content of magmatic hbl.

The chondrite normalized REE pattern of Mg-hornblende are similar to clinopyroxene patterns, with a rather flat HREE segment ($0.77 < Dy_N/Lu_N < 1.05$), a slightly fractionated MREE ($0.39 < Sm_N/Dy_N < 0.58$) and a strongly fractionated LREE ($0.10 < La_N/Sm_N < 0.30$) segment (Fig. III.33c). However, REE concentrations of hornblende are up to 10 fold those of clinopyroxene. Normalized to primitive mantle, Mg-hornblende shows enrichment in Cs, Pb and Sr with a significant negative Th anomaly (Fig. III.33d). Zr and Hf of the HFSE show depletion compared to neighbor elements.

Trace element content of tremolite pseudomorphs after clinopyroxenes has been analysed. Secondary tremolite shows the same general REE pattern than precursor clinopyroxene, but Cs, Rb, Ba, Th and Pb are more enriched and Ti shows a negative anomaly (Fig. III.33d). The composition of metamorphic tremolite is distinct from Mg-hornblende, supporting the interpretation that the latter is magmatic and not a subsolidus clinopyroxene destabilization product.

The leucocratic patches contain two types of amphiboles: (i) edenite with high TiO_2 content (0.25-0.36 wt %), which in part recrystallizes to (ii) pargasite with low TiO_2 (0.15 wt %), which overgrows chlorite. These amphiboles are much more enriched in K_2O (0.14-0.46 wt %) than any of those found in pipe1. Edenitic amphiboles of the leucocratic patches show similar but 20 times more enriched chondrite-normalized pattern shapes as Mg-hornblende (Fig. III.33c). In addition, edenite shows a pronounced negative Eu anomaly (Eu* = Eu_N / $\sqrt{(Gd_N*Sm_N)} \approx 0.7$). Normalized to primitive mantle, edenite shows enrichment in Cs, but not in Pb, and a strong negative Sr and Th anomaly (Fig. III.33d). Ti, Zr, and Hf show a negative anomaly whereas Nb shows a slight positive anomaly compared to Ta and especially Th. Whereas edenites are of magmatic origin, pargasites represent sub-solidus high temperature crystallization products.

Sample	P10 Clinopyroxenite		P13 Clinopyroxenite		P25 Clinopyroxenite		P14 Leucocratic patch	
Majors	Avrg n=11	2σ	Avrg n=36	2σ	Avrg n=23	2σ	Avrg n=14	2σ
SiO2	50.52	1.45	50.01	1.58	56.61	1.21	47.28	0.95
TiO2	0.23	0.07	0.23	0.07	0.03	0.04	0.32	0.05
Cr2O3	0.43	0.17	0.94	0.46	0.15	0.12	0.08	0.02
Al2O3	6.81	1.57	6.79	1.86	0.65	1.06	6.94	0.88
FeO	5.37	0.47	5.45	1.17	3.57	0.57	11.30	1.56
MnO	0.09	0.02	0.10	0.04	0.13	0.03	0.29	0.07
NiO	0.02	0.02	0.03	0.01	0.03	0.01	0.01	0.01
MgO	19.01	0.75	18.95	0.73	22.26	0.77	15.27	1.13
CaO	12.60	0.18	12.38	0.24	12.84	0.66	11.26	0.60
Na2O	1.28	0.32	1.33	0.38	0.17	0.15	2.09	0.14
K2O	0.10	0.08	0.01	0.01	0.01	0.01	0.19	0.05
Total	96.46	0.20	96.22	0.45	98.65	0.40	97.01	0.86
XMg	0.87	0.02	0.88	0.02	0.93	0.02	0.71	0.04
NaK (A)	0.37	0.10	0.37	0.11	0.05	0.04	0.64	0.05
Traces	n=4		n=6		n=1		n=2	
Cs	0.277	0.301	2.823	6.041	2.020		0.327	0.002
Rb	2.66	0.56	1.86	0.36	0.45		0.45	0.13
Ba	17.63	7.61	18.17	9.53	7.48		2.60	0.68
Th	0.0223	0.0150	0.0021	0.0016	0.0076		0.0027	0.0010
U	0.0320	0.0375	0.0064	0.0116	0.0300		0.0024	0.0009
Nb	0.1308	0.0289	0.1025	0.0573	0.0056		0.5055	0.0431
Ta	0.0065	0.0029	0.0036	0.0015	<0.0010		0.0128	0.0035
La	0.15	0.02	0.10	0.04	0.01		0.55	0.04
Ce	0.46	0.09	0.40	0.17	0.03		2.94	0.00
Pb	0.43	0.04	0.22	0.06	0.08		0.21	0.00
Pr	0.09	0.02	0.08	0.04	0.01		0.71	0.07
Sr	22.7	4.9	11.6	2.0	7.5		9.0	1.9
Nd	0.572	0.051	0.643	0.267	0.054		5.030	0.990
Sm	0.338	0.036	0.388	0.155	0.044		2.468	0.809
Zr	2.17	0.66	1.92	0.62	0.09		10.06	0.74
Hf	0.121	0.014	0.108	0.038	0.006		0.568	0.021
Eu	0.187	0.004	0.208	0.075	0.025		0.762	0.158
Gd	0.663	0.026	0.844	0.327	0.112		4.143	1.694
Tb	0.135	0.007	0.167	0.059	0.024		0.763	0.328
Dy	1.076	0.064	1.344	0.480	0.220		5.980	2.376
Y	6.238	0.151	7.914	2.624	1.217		34.575	12.919
Ho	0.250	0.006	0.308	0.106	0.048		1.352	0.540
Er	0.735	0.056	0.923	0.351	0.159		4.040	1.471
Ti	2073	108	2415	1150	196		6065	3254
Tm	0.11	0.01	0.14	0.05	0.02		0.61	0.20
Yb	0.78	0.03	0.92	0.29	0.17		4.12	1.15
Lu	0.12	0.01	0.14	0.04	0.02		0.64	0.14

Table III.11: Pipe 1 representative major element analyses of magmatic amphiboles and tremolite (P25) and trace elements concentration from the same sample.

III.2.6.1.4.   Spinel

Euhedral spinels from dunites have cores defining a trend with X_{Mg} decreasing with increasing TiO_2 and Cr # (0.24 < X_{Mg} < 0.52; 0.06 < TiO_2 < 0.36 wt %; 0.45< Cr # = (Cr/Cr+Al) < 0.90). Anhedral spinel from pyroxenites have cores with lower X_{Mg} and Cr #, but higher TiO_2 content (0.05 < X_{Mg} < 0.21; 0.22 < TiO_2 < 0.78 wt %). The rims of anhedral spinel are usually ferri-chromite, with high Cr # (0.9-1) and low TiO_2 content ($TiO_2 \approx 0.1$ wt %).

Magnetite is found at grain boundaries, along the clinopyroxene cleavages and associated with serpentines.

III.2.6.1.5.   Epidote

The big epidotes (Appendix 4) of the leucocratic patches show a strong zoning in FeO (3.1 -6.6 wt %) and in MnO (0.03-0.32 wt %) contents. $X_{Epidote}$ (Fe^{3+}/ ($Fe^{3+}+Al^{3+}+Cr^{3+}$)) varies from 0.20 to 0.44, with Mn-poor epidote having the lowest X_{Ep}. Mn-Fe-rich epidotes have a REE chondrite normalized pattern typical of plagioclase, with a slightly fractionated M-HREE segment ($Gd_N/Lu_N \approx 2.5$) an important positive Eu anomaly (Eu* ≈ 13.5) and a rather flat LREE segment (Fig. III.33a). Mn-poor epidote is much poorer in REE, and its patterns differ from Mn-rich epidote by a negatively fractionated M-HREE segment ($Gd_N/Lu_N \approx 0.1$) and a smaller Eu anomaly. Normalized to primitive mantle, both epidotes show a strong enrichment in Ba, Pb and Sr (Fig. III.33d). Only Nb and Ta of the HFSE are depleted, Ti showing an important positive anomaly, whereas Zr and Hf are not depleted. The textural and chemical aspects of high Mn-X_{Ep} epidotes point to a primitive magmatic origin.

III.2.6.2.   Pipe 2

III.2.6.2.1.   Olivine

Olivine compositions range from $X_{Mg} = 0.76$ to 0.84 and NiO contents from 0.04 to 0.20 wt % (Fig. III.31a, b; Table III.9). The MnO content is high (0.21 < MnO < 0.40 wt %).

III.2.6.2.2.   Clinopyroxene

Pyroxenite clinopyroxenes (Table III.12) have X_{Mg} values between 0.85 and 0.91 with a wide range in Al_2O_3 (0.8-4.3 wt %), TiO_2 (up to 0.38 wt %) and Cr_2O_3 (up to 0.5 wt %) (Fig. III.32b). Al and Ti contents increase with decreasing X_{Mg} whereas the Cr content is uncorrelated. Clinopyroxenes from more differentiated rocks (i.e. hbl-gabbronorite) show different variations. The Al_2O_3 content increases from 2.5 to 4.1 wt % with X_{Mg} decreasing from 0.86 to 0.79, but then decreases to 2.1 wt % with further decreasing X_{Mg} (to 0.67). Whereas Al_2O_3 starts decreasing at X_{Mg}=0.79, TiO_2 increases from 0.2 to 0.5 wt % with X_{Mg} decreasing to 0.74 and then drops drastically to $TiO_2 \approx 0.1$ wt % at X_{Mg} 0.7. The Cr_2O_3 content decreases from 0.3 wt % at $X_{Mg} = 0.86$ to the detection limit at $X_{Mg} = 0.7$.

Chondrite normalized patterns of clinopyroxenes have a flat HREE segment (0.93 < Dy_N/Lu_N <1.32), a slightly fractionated MREE (0.43 < Sm_N/Dy_N < 0.69) and a strongly fractionated LREE (0.11< La_N/Sm_N < 0.28) (Fig. III.33e). None of the analyzed clinopyroxenes shows Eu anomaly. Clinopyroxene REE concentrations increase with

decreasing X_{Mg}. Normalized to primitive mantle, clinopyroxenes show a strong Zr and Hf anomaly (Fig. III.33f). For the clinopyroxene in which Nb and Ta are not below the detection limit, Nb has a strong negative anomaly and Ta is decoupled from Nb with infra-chondritic Nb/Ta ratios. Clinopyroxenes from pyroxenite have positive Pb and Sr anomalies. Clinopyroxene from hbl-gabbronorite has no Pb anomaly but a small Sr negative anomaly. All clinopyroxenes have a pronounced Ba negative anomaly.

III.2.6.2.3. *Amphiboles*

Amphiboles have pargasite to tremolite compositions (Fig. III.34a; Table III.13). Amphibole replacing clinopyroxene in pyroxenites in reaction rims around olivine and in the hornblende-gabbros are Mg-hornblende to tschermakite. Amphiboles in the hbl-gabbronorite and in the late tonalitic dykes are edenites to pargasites.

Sample	P42 pyroxenite		P47 pyroxenite		P68 pyroxenite		P62 pyroxenite		P39 Impeg.pxt	P67 Hbl-Gabbronorite	
Majors	Avrg n=26	2σ	Avrg n=23	2σ	Avrg n=7	2σ	Avrg n=22	2σ	Avrg n=1	Avrg n=45	2σ
SiO2	52.26	0.62	52.27	0.76	51.98	0.72	52.68	0.90	51.45	51.28	0.27
TiO2	0.18	0.06	0.19	0.05	0.14	0.02	0.19	0.07	0.43	0.44	0.04
Cr2O3	0.30	0.12	0.23	0.12	0.28	0.17	0.18	0.14	0.07	0.07	0.03
Al2O3	2.49	0.68	2.37	0.92	2.78	0.70	2.28	0.81	3.41	3.36	0.29
FeO	4.19	0.69	3.73	0.27	3.74	0.32	3.62	0.47	7.09	7.81	0.54
MnO	0.13	0.03	0.12	0.01	0.13	0.02	0.13	0.03	0.21	0.23	0.02
NiO	0.00	0.01	0.01	0.01	0.01	0.02	0.02	0.01	0.00	0.00	0.00
MgO	16.34	0.72	16.33	0.58	16.23	0.23	16.23	0.49	14.39	14.01	0.40
CaO	24.15	1.20	24.28	0.63	24.15	0.56	24.49	0.66	22.59	22.43	1.18
Na2O	0.08	0.03	0.05	0.02	0.12	0.09	0.04	0.03	0.24	0.26	0.06
Total	100.13	0.58	99.59	0.39	99.58	0.48	99.87	0.73	99.88	99.91	0.40
XMg(Fetot)	0.87	0.02	0.89	0.01	0.89	0.01	0.89	0.02	0.78	0.76	0.01
traces	n=3		n=7		n=3		n=3		n=1	n=2	
Cs	bd		0.040	0.001	0.010	0.004	0.007	1/3	<0.0071	0.0072	1/2
Rb	bd		1.108	1.872	0.010	0.000	bd		<0.0138	bd	
Ba	0.009	0.002	0.714	1.360	0.044	1/3	0.016	1/3	0.014	bd	
Th	0.0065	0.0024	0.0116	0.0086	0.0039	0.0035	0.0125	0.0043	0.0615	0.0029	0.0000
U	0.0023	0.0007	0.0041	0.0022	0.0013	0.0010	0.0052	0.0029	0.0166	0.0022	0.0001
Nb	0.0028	0.0013	0.0424	0.0573	0.0036	1/3	bd		<0.0039	0.0038	1/2
Ta	bd		0.0062	0.0039	0.0007	1/3	bd		0.0036	bd	
La	0.048	0.014	0.071	0.022	0.046	0.002	0.059	0.005	0.108	0.112	0.013
Ce	0.175	0.057	0.251	0.058	0.197	0.005	0.227	0.010	0.498	0.559	0.079
Pb	0.081	0.038	0.147	0.044	0.143	0.010	0.083	0.019	0.026	0.034	0.002
Pr	0.039	0.012	0.058	0.013	0.045	0.005	0.053	0.002	0.103	0.123	0.022
Sr	5.35	1.77	8.42	3.39	6.95	0.13	5.78	0.40	6.43	4.76	0.27
Nd	0.298	0.074	0.426	0.084	0.370	0.048	0.456	0.032	0.642	0.890	0.160
Sm	0.207	0.072	0.244	0.083	0.244	0.012	0.305	0.002	0.416	0.482	0.021
Zr	0.75	0.20	1.37	0.36	0.87	0.04	1.07	0.04	2.12	1.58	0.37
Hf	0.039	0.007	0.059	0.027	0.060	0.003	0.076	0.004	0.070	0.085	0.021
Eu	0.098	0.033	0.134	0.027	0.115	0.006	0.170	0.005	0.203	0.249	0.044
Gd	0.385	0.111	0.521	0.194	0.456	0.038	0.620	0.054	0.762	0.847	0.126
Tb	0.078	0.026	0.105	0.036	0.087	0.004	0.121	0.001	0.159	0.163	0.025
Dy	0.594	0.183	0.808	0.208	0.701	0.011	0.916	0.008	1.096	1.230	0.144
Y	3.20	1.02	4.31	1.17	3.73	0.13	4.90	0.21	5.94	6.35	1.05
Ho	0.130	0.044	0.172	0.044	0.157	0.008	0.210	0.008	0.246	0.259	0.040
Er	0.404	0.115	0.498	0.113	0.437	0.034	0.600	0.047	0.703	0.725	0.141
Ti	1156	261	1773	283	1238	31	1811	10	1862	1715	179
Tm	0.061	0.018	0.074	0.022	0.062	0.004	0.094	0.006	0.100	0.110	0.022
Yb	0.379	0.119	0.516	0.163	0.411	0.012	0.599	0.028	0.688	0.729	0.099
Lu	0.057	0.018	0.073	0.024	0.061	0.002	0.091	0.003	0.099	0.100	0.017

Table III.12: Pipe 2 representative major element analyses of clinopyroxenes and trace elements concentration from the same samples.

Sample	P42 pyroxenite		P47 pyroxenite		P62 pyroxenite		P39 Impeg.pxt		P52 Impeg.pxt	
Majors	Avrg n=20	2σ	Avrg n=13	2σ	Avrg n=23	2σ	Avrg n=23	2σ	Avrg n=6	2σ
SiO2	45.25	1.60	47.83	2.09	47.93	1.44	47.45	1.90	47.72	2.96
TiO2	0.35	0.19	0.52	0.12	0.38	0.19	0.18	0.24	0.12	0.14
Cr2O3	0.26	0.25	0.67	0.18	0.39	0.28	0.01	0.02	0.04	0.06
Al2O3	12.34	0.90	9.89	1.90	10.84	1.43	12.16	1.80	12.21	2.90
FeO	6.87	2.37	5.85	0.55	5.90	0.43	7.37	2.65	5.68	0.36
MnO	0.09	0.02	0.09	0.02	0.09	0.02	0.11	0.02	0.08	0.02
NiO	0.02	0.02	0.02	0.01	0.03	0.02	0.01	0.01	0.02	0.02
MgO	16.77	1.52	17.98	1.01	17.41	0.62	16.75	1.85	17.47	1.18
CaO	12.70	0.17	12.66	0.14	12.82	0.15	12.37	0.25	12.68	0.18
Na2O	1.48	0.13	1.09	0.23	1.00	0.23	1.25	0.26	1.09	0.25
K2O	0.12	0.27	0.02	0.02	0.01	0.02	0.04	0.05	0.05	0.05
Total	96.25	0.52	96.61	1.13	96.81	0.42	97.72	0.36	97.18	0.56
XMg	0.90	0.07	0.90	0.02	0.89	0.01	0.84	0.08	0.89	0.01
NaK (A)	0.44	0.08	0.30	0.07	0.28	0.07	0.35	0.08	0.31	0.08
Traces	n=3		n=4		n=5		n=6		n=4	
Cs	0.104	0.008	0.156	0.160	0.044	0.006	0.052	0.014	0.045	0.015
Rb	4.39	1.57	29.54	44.48	1.40	0.35	2.98	1.27	1.94	0.75
Ba	19.94	3.36	26.38	24.32	6.88	1.36	7.73	3.13	10.30	0.54
Th	0.0107	0.0026	0.0082	0.0022	0.0184	0.0011	0.0305	0.0091	0.0617	0.0116
U	0.0067	0.0015	0.0047	0.0014	0.0098	0.0062	0.0145	0.0019	0.0226	0.0034
Nb	0.2230	0.0726	0.5105	0.5263	0.0959	0.0102	0.1911	0.0563	0.2510	0.0961
Ta	0.0094	0.0018	0.0200	0.0177	0.0057	0.0031	0.0127	0.0058	0.0056	0.0017
La	0.171	0.004	0.203	0.041	0.135	0.007	0.264	0.037	0.228	0.015
Ce	0.627	0.024	0.750	0.117	0.508	0.029	1.108	0.103	0.912	0.075
Pb	1.166	0.192	0.532	0.226	1.169	0.116	0.257	0.051	0.225	0.093
Pr	0.134	0.006	0.166	0.025	0.114	0.003	0.239	0.027	0.178	0.016
Sr	47.12	1.04	37.95	11.51	49.71	6.38	40.54	11.24	20.11	0.75
Nd	1.04	0.01	1.18	0.16	0.92	0.03	1.74	0.31	1.16	0.17
Sm	0.688	0.008	0.668	0.045	0.611	0.062	0.957	0.220	0.482	0.083
Zr	2.45	0.28	3.39	0.76	1.56	0.07	8.04	1.16	3.55	0.87
Hf	0.128	0.023	0.162	0.028	0.078	0.018	0.384	0.132	0.138	0.044
Eu	0.402	0.020	0.391	0.052	0.377	0.025	0.475	0.114	0.360	0.027
Gd	1.37	0.10	1.36	0.17	1.26	0.08	1.67	0.40	0.76	0.16
Tb	0.266	0.016	0.266	0.026	0.257	0.020	0.315	0.071	0.144	0.031
Dy	2.13	0.15	2.04	0.21	1.93	0.12	2.31	0.50	1.04	0.23
Y	12.04	1.10	11.78	1.52	10.97	0.75	12.59	2.61	6.12	1.53
Ho	0.477	0.056	0.467	0.043	0.453	0.011	0.504	0.100	0.244	0.058
Er	1.39	0.09	1.44	0.20	1.33	0.07	1.47	0.27	0.74	0.19
Ti	4561	1214	4862	1249	3342	328	5271	1674	2436	366
Tm	0.212	0.019	0.201	0.027	0.212	0.016	0.213	0.042	0.124	0.031
Yb	1.40	0.15	1.41	0.23	1.43	0.12	1.44	0.24	0.92	0.19
Lu	0.212	0.025	0.211	0.027	0.226	0.010	0.225	0.035	0.159	0.029

Table III.13: Pipe 2 representative major element analyses of magmatic amphiboles and trace elements concentration from the same samples.

Sample	P68host pyroxenite		P68veine Hbl-gabbro		P98 Hbl tonalite		P63 Hbl tonalite		P67 Hbl-Gabbronorite	
Majors	Avrg n=10	2σ	Avrg n=20	2σ	Avrg n=15	2σ	Avrg n=15	2σ	Avrg n=24	2σ
SiO2	46.92	1.21	44.70	2.25	44.01	2.11	46.99	0.84	44.62	0.98
TiO2	0.59	0.47	0.51	0.19	0.96	0.49	0.65	0.11	0.70	0.18
Cr2O3	0.45	0.27	0.00	0.00	0.00	0.01	0.01	0.01	0.35	0.22
Al2O3	10.79	0.96	11.94	1.96	12.08	3.17	9.85	0.69	12.23	1.30
FeO	7.56	2.14	17.19	4.51	19.22	1.23	14.77	0.38	9.16	0.99
MnO	0.15	0.08	0.23	0.12	0.41	0.04	0.37	0.06	0.12	0.02
NiO	0.03	0.02	0.01	0.01	0.01	0.01	0.00	0.00	0.02	0.02
MgO	17.04	1.33	10.50	3.30	8.60	2.10	12.76	0.54	15.14	0.83
CaO	12.42	0.40	11.60	0.64	10.93	0.41	11.44	0.43	12.32	0.69
Na2O	1.54	0.20	1.27	0.15	1.78	0.15	2.01	0.27	2.32	0.28
K2O	0.01	0.01	0.03	0.01	0.05	0.10	0.10	0.04	0.04	0.05
Total	97.49	0.34	97.98	0.52	98.05	0.40	98.95	0.52	97.03	0.41
XMg	0.85	0.06	0.55	0.15	0.44	0.08	0.61	0.02	0.77	0.04
NaK (A)	0.42	0.05	0.37	0.05	0.53	0.06	0.59	0.08	0.66	0.08
Traces	n=1		n=2		n=2		n=2		n=4	
Cs	0.028		0.007	1/2	0.076	0.064	0.065	0.039	0.083	0.095
Rb	0.26		0.13	0.03	0.12	0.08	0.31	0.01	1.49	0.21
Ba	4.06		0.74	0.22	1.89	0.79	2.84	1.19	5.70	0.54
Th	0.0047		0.0007	0.0002	0.0013	0.0002	0.0028	0.0003	0.0157	0.0019
U	0.0028		0.0005	1/2	0.0007	1/2	0.0009	0.0003	0.0070	0.0019
Nb	0.0679		0.1544	0.0270	0.2828	0.0555	0.2133	0.0728	0.1995	0.0461
Ta	0.0028		0.0064	0.0044	0.0088	0.0032	0.0063	0.0021	0.0083	0.0028
La	0.128		0.446	0.092	0.422	0.008	0.925	0.110	0.275	0.019
Ce	0.532		2.072	0.446	2.675	0.158	4.510	0.707	1.274	0.070
Pb	1.161		0.043	0.004	0.082	0.002	0.184	0.003	0.272	0.125
Pr	0.122		0.469	0.107	0.771	0.054	1.100	0.225	0.279	0.016
Sr	43.71		8.62	0.02	12.23	0.21	7.74	0.33	33.84	4.80
Nd	1.00		3.31	0.91	6.80	0.49	8.43	1.94	2.05	0.08
Sm	0.639		1.483	0.550	4.310	0.339	4.005	0.969	1.116	0.070
Zr	1.52		4.79	2.04	13.48	0.28	13.24	3.28	4.31	0.12
Hf	0.099		0.265	0.230	0.581	0.045	0.674	0.117	0.201	0.022
Eu	0.356		1.484	0.452	2.006	0.073	2.186	0.395	0.610	0.045
Gd	1.29		2.14	0.71	7.95	0.57	6.54	1.24	2.01	0.19
Tb	0.272		0.369	0.094	1.508	0.095	1.197	0.220	0.385	0.049
Dy	2.01		2.67	0.78	11.41	0.81	8.75	1.80	2.83	0.36
Y	11.19		13.44	3.19	58.68	3.97	50.05	11.18	15.72	1.94
Ho	0.452		0.558	0.136	2.485	0.154	1.989	0.412	0.620	0.084
Er	1.37		1.54	0.32	7.06	0.46	5.98	1.25	1.80	0.22
Ti	2656		2114	325	6420	237	4764	591	4762	940
Tm	0.194		0.213	0.038	0.986	0.037	0.932	0.227	0.269	0.041
Yb	1.37		1.41	0.05	6.33	0.18	6.60	1.69	1.84	0.28
Lu	0.191		0.192	0.004	0.894	0.028	1.042	0.272	0.271	0.042

Table III.13 continues

From pyroxenites to hbl-gabbronorite, Ti and Na contents in magmatic amphiboles increase (0.1< Na(A)< 0.8; 0< Ti p.f.u< 0.2) with decreasing X_{Mg} (from 0.98 to 0.70) (Fig. III.34b, c); but from hbl-gabbronorite to tonalitic dykes the Na-content decreases (0.55 < Na(A)< 0.8) and Ti stays constant whith decreasing X_{Mg} (0.33< X_{Mg}< 0.68). This chemical evolution is expected from amphiboles crystallizing from evolving magmas: Amphibole takes up Na and Ti until temperature drops sufficiently for plagioclase to

appear, which diminishes Na contents in cotectic amphiboles but leaves Ti at a constant level. Bluish-green amphiboles belonging to the plagioclase replacement paragenesis are pargasitic, with low Si and high Na(A) content and no titanium. These amphiboles are related to in-situ fluid re-equilibration, contrasting secondary tremolite from the interface between olivine and/or olivine and hornblende or between magmatic amphiboles and clinopyroxene which is related to low temperature greenschist facies re-equilibration.

Normalized to chondrites, magmatic amphiboles from pyroxenite have flat HREE segments ($0.82 < Dy_N/Lu_N < 1.17$), slightly fractionated MREE ($0.46 < Sm_N/Dy_N < 0.71$) and strongly fractionated LREE ($0.12 < La_N/Sm_N < 0.30$) segments (Fig. III.33g). Reactional hornblende at the interface between olivine and plagioclase in the impregnated zones has a slightly fractionated M-HREE segment ($0.44 < Dy_N/Sm_N < 0.56$) a positive Eu anomaly (Eu*=1.6-2), and a fractionated LREE segment ($0.13 < La_N/Sm_N < 0.16$).

Edenite from the hbl-gabbronorite shows the same pattern as hornblendes from the pyroxenites, but has higher REE values. Hornblende from hbl-gabbro dyke rims and hornblende inclusions in plagioclase of these dykes have a rather flat M-HREE segment and a strong Eu anomaly (Eu* $\approx$ 2.5), and a fractionated LREE segment. LREE concentrations of these hornblendes are the most enriched of all hornblendes in the mafic lithologies of pipe 2. Yet, magmatic edenite from the tonalites shows the highest REE concentration, a flat M-HREE segment up to 45 fold chondrite, and a steep fractionated LREE segment. Normalized to primitive mantle, all amphiboles have a pronounced negative Zr-Hf anomaly (Fig. III.33g). Ti in pyroxenite hornblende has either a slight positive or negative anomaly, whereas hornblende from hbl-gabbbronorite dykes and dyke rims have a negative Ti anomaly, as well as edenite from the tonalite. Nb and Ta are not significantly depleted compared to neighbor elements, and Nb-Ta ratios evolve from nearly chondritic in pyroxenite hornblende to suprachondritic in the tonalite edenites ($10.67 < Nb/Ta < 56.5$). Pb and Sr show a strong positive anomaly for hornblendes from pyroxenite, Sr shows a small positive anomaly in hornblende from impregnated pyroxenites and in the hbl-gabbronorites. In the most differentiated rocks (hbl-gabbronorite and tonalite) Pb is slightly depleted whereas Sr shows a strong negative anomaly. Rb, Ba and Th and U are more enriched in hornblende from the pyroxenites than from differentiated rocks. Th shows a constant negative anomaly.

III.2.6.2.4.   *Orthopyroxene*

The few orthopyroxenes from the ol-clinopyroxenite have high X_{Mg} (0.88 to 0.82) and constant Al_2O_3 content (2.5-3 wt %, Fig. III.35a, Table III.14), low titanium (close to detection limit) and Cr_2O_3 up to 0.27 wt %. Reactional orthopyroxene from symplectite and rimming olivine against plagioclase has a restricted range in X_{Mg} (0.80-0.84) and a wide range in Al content ($0.78 < Al_2O_3 < 3.8$ wt%). The latter opx does not contain significant chromium and titanium contents are close to the detection limit. Orthopyroxene from the hbl-gabbronorite shows a wide range of X_{Mg} (0.63-0.79), a decrease in Al_2O_3 (from 3.1 to 1.9 wt%) and Cr ($0.01 < Cr_2O_3 < 0.24$ wt%) contents with decreasing X_{Mg} while titanium increases significantly (0.05 to 0.21 wt % TiO_2).

Normalized to chondrite, othopyroxene has a regular fractionated REE pattern, with La_N/Lu_N varying from 0.002 to 0.024 (Fig. III.35b). Orthopyroxene rimming olivine against plagioclase in impregnated pyroxenite has a different pattern, with a fractionated

HREE segment ($0.03 < Dy_N/Lu_N < 0.71$), and a rather flat M-LREE segment ($0.34 < La_N/Dy_N < 8.61$). Orthopyroxenes from the hbl-gabbronorites have the highest REE concentration, with Lu_N up to 10.8 fold chondrite. Normalized to primitive mantle, all orthopyroxenes show positive Ti and Pb anomalies (Fig. III.35c). Zr shows a slight negative anomaly compared to Sm and Hf, whereas Nb is systematically depleted and Ta somewhat enriched compared to neighbor elements. Sr shows a positive anomaly in orthopyroxenes from the hbl-gabbronorite and in orthopyroxene rimming olivine in impregnated zones, but not in those from the pyroxenites. U shows a positive anomaly in all orthopyroxenes.
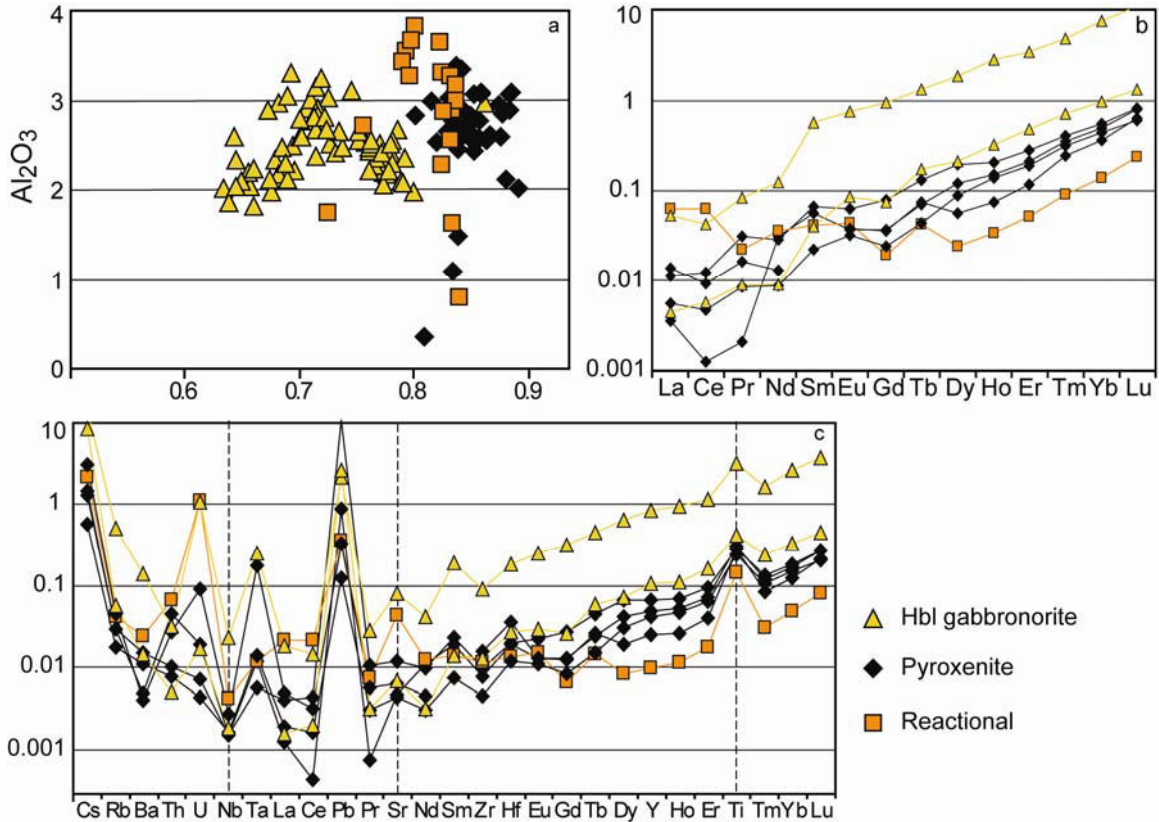
Figure III.35: Opx composition. a) X_{Mg} versus Al_2O_3 b) Chondrite normalized REE content. c) Primitive mantle normalized values.

III.2.6.2.5. Oxides

Spinels included in olivine and spinels in pyroxenite are chromite with a wide range of X_{Mg} and Cr contents. Cr#¦ increases from 0.02 to 0.8 (ferrichromite) and TiO_2 contents increases from 0.1 to 0.9 wt% with X_{Mg} decreasing from 0.62 to 0.23. Green spinel associated with hornblende and orthopyroxene and occurring in symplectite is hercynite. Ilmenite is the opaque phase in the most differentiated rocks.

Sample	P42 backgr. pyroxenite		P47 backgr. pyroxenite		P52 Impeg.pxt		P68host backgr. pyroxenite		P39 Impeg.pxt	
Majors	Avrg n=25	2σ	Avrg n=10	2σ	Avrg n=4	2σ	Avrg n=3	2σ	Avrg n=18	2σ
SiO2	54.15	0.96	53.80	1.08	55.07	0.13	53.56	0.16	54.31	0.66
TiO2	0.06	0.02	0.08	0.06	0.11	0.01	0.05	0.00	0.04	0.02
Cr2O3	0.14	0.06	0.21	0.08	0.15	0.01	0.18	0.04	0.01	0.02
Al2O3	2.67	0.21	2.83	0.55	2.51	0.09	3.37	0.01	2.87	0.81
FeO	11.91	0.44	11.29	2.51	10.88	0.08	12.58	0.11	13.95	1.58
MnO	0.27	0.02	0.27	0.05	0.26	0.02	0.30	0.02	0.33	0.05
NiO	0.00	0.01	0.02	0.02	0.02	0.02	0.03	0.01	0.02	0.01
MgO	30.43	0.38	28.59	4.63	31.16	0.02	29.66	0.01	29.21	1.34
CaO	0.49	0.11	2.81	7.47	0.54	0.04	0.60	0.01	0.38	0.12
Na2O	0.01	0.01	0.01	0.02	0.00	0.00	0.00	0.00	0.00	0.01
Total	100.15	0.97	99.92	0.58	100.69	0.05	100.31	0.22	101.12	0.31
XMg	0.85	0.02	0.85	0.03	0.85	0.56	0.83	0.00	0.81	0.03
traces	n=3		n=2		n=4		n=3		n=2	
Cs	0.010	0.002	0.011	0.012	0.017	0.008	0.004	0.001	0.024	0.014
Rb	0.019	0.005	0.019	0.000	0.027	0.009	0.011	0.012	0.029	0.002
Ba	0.034	0.006	0.106	0.031	0.170	0.077	0.077	0.102	0.028	0.015
Th	0.0038	0.0053	0.0009	0.0011	0.0056	0.0018	0.0007	0.0005	0.0023	0.0011
U	0.0004	0.0001	0.0002	0.0001	0.0232	0.0412	0.0001	0.0001	0.0019	0.0020
Nb	0.0011	0.0007	0.0011	0.0002	0.0029	0.0022	0.0012	0.0000	0.0019	1/2
Ta	0.0005	1/3	0.0002	1/2	0.0005	0.0001	0.0006	1/3	0.0073	0.0016
La	0.0152	0.0203	0.0027	0.0026	0.0148	0.0160	0.0013	0.0014	0.0033	1/2
Ce	0.0008	0.0003	0.0076	0.0080	0.0380	0.0700	0.0029	0.0024	0.0056	0.0058
Pb	0.0626	0.0676	0.7812	0.9261	0.0257	0.0146	0.0089	0.0055	0.0233	0.0064
Pr	0.0640	0.0902	0.0029	0.0036	0.0021	0.0017	0.0008	0.0006	0.0016	0.0016
Sr	0.098	0.014	0.246	0.177	0.906	1.388	0.092	0.133	0.133	0.082
Nd	0.0147	0.0180	0.0135	0.0108	0.0169	0.0269	0.0041	0.0041	0.0061	1/2
Sm	0.0085	0.0062	0.0103	0.0100	0.0063	0.0055	0.0034	0.0013	bd	
Zr	0.0854	0.0193	0.1076	0.0646	0.1267	0.0580	0.0491	0.0049	0.1731	0.0967
Hf	0.0059	0.0012	0.0062	0.0021	0.0041	0.0020	0.0036	0.0018	0.0111	0.0011
Eu	0.0022	0.0003	0.0037	0.0022	0.0025	0.0029	0.0019	0.0014	0.0022	0.0007
Gd	0.0076	0.0025	0.0164	0.0109	0.0040	0.0034	0.0050	0.0002	0.0073	0.0016
Tb	0.0026	0.0010	0.0049	0.0021	0.0016	0.0019	0.0016	0.0002	0.0028	1/2
Dy	0.0309	0.0149	0.0493	0.0181	0.0061	0.0035	0.0221	0.0031	0.0143	0.0103
Y	0.22	0.07	0.30	0.02	0.05	0.02	0.19	0.03	0.11	0.04
Ho	0.0085	0.0040	0.0116	0.0016	0.0019	0.0009	0.0078	0.0016	0.0042	0.0010
Er	0.0347	0.0111	0.0461	0.0081	0.0086	0.0031	0.0312	0.0052	0.0193	0.0110
Ti	394.7	78.2	367.2	86.3	188.4	12.9	310.8	48.7	373.6	4.3
Tm	0.009	0.002	0.010	0.001	0.002	0.001	0.008	0.000	0.006	0.002
Yb	0.083	0.017	0.092	0.012	0.024	0.010	0.074	0.009	0.062	0.007
Lu	0.020	0.004	0.021	0.000	0.006	0.002	0.015	0.001	0.016	0.001

Table III.14: Pipe 2 representative major element analyses of orthopyroxene and trace element concentrations from the same samples.

| Sample	P62 Hbl-Gabbronorite		P67 Hbl-Gabbronorite	
	Avrg	2σ	Avrg	2σ
Majors	n=3		n=39	
SiO2	54.95	1.64	53.52	0.80
TiO2	0.05	0.01	0.07	0.02
Cr2O3	0.16	0.16	0.16	0.04
Al2O3	1.97	1.24	2.49	0.29
FeO	12.72	1.62	16.33	1.60
MnO	0.32	0.03	0.37	0.03
NiO	0.03	0.01	0.02	0.01
MgO	29.77	1.84	26.61	1.47
CaO	0.35	0.14	0.57	0.17
Na2O	0.00	0.00	0.00	0.01
Total	100.32	0.26	100.14	0.57
XMg	0.82	0.02	0.75	0.03
traces	n=3		n=3	
Cs	0.118	0.045	0.068	0.056
Rb	0.330	0.158	0.037	0.039
Ba	0.983	0.781	0.103	0.060
Th	0.0026	0.0022	0.0004	0.0002
U	0.0228	0.0183	0.0004	0.0003
Nb	0.0167	0.0061	0.0013	1/3
Ta	0.0102	1/3	bd	
La	0.0125	0.0067	0.0011	0.0003
Ce	0.0257	0.0080	0.0035	0.0014
Pb	0.1570	0.0942	0.1854	0.1744
Pr	0.0079	0.0022	0.0009	0.0007
Sr	1.705	0.790	0.146	0.084
Nd	0.0570	0.0170	0.0042	0.0014
Sm	0.0863	0.0471	0.0061	1/3
Zr	1.0350	0.0942	0.1447	0.0128
Hf	0.0570	0.0106	0.0083	0.0027
Eu	0.0430	0.0076	0.0050	0.0016
Gd	0.1903	0.0784	0.0154	0.0046
Tb	0.0490	0.0063	0.0065	0.0021
Dy	0.4723	0.0447	0.0535	0.0132
Y	3.87	0.13	0.48	0.14
Ho	0.1593	0.0115	0.0185	0.0064
Er	0.5657	0.0372	0.0789	0.0215
Ti	4103.4	218.7	555.7	142.0
Tm	0.122	0.015	0.018	0.006
Yb	1.283	0.132	0.165	0.050
Lu	0.274	0.036	0.034	0.009

Table III.14 continues

III.2.6.2.6.   Plagioclase

Plagioclases invading grain boundaries within the impregnated pyroxenites shows the highest An content (0.96 < An < 0.99). With increasing degree of fractionation, X_{An} decreases steadily from the hbl-gabbronorite (0.89 < An <0.97) to hbl-gabbro dyke rims (0.76 < An < 0.94) and to the inner part of the hbl-gabbro dykes, (0.40 < An < 0.60) to the tonalites (0.15 < 0.An < 0.77). K_2O is always below detection limit (Table III.15). Plagioclase normalized to chondrite shows a slightly fractionated HREE segment, a positive Eu anomaly and a fractionated LREE segment (Fig. III.36). The concentrations of REE and the Eu anomaly increase with decreasing An content. Normalized to primitive mantle, plagioclase shows a positive Ba, U, Pb and Sr anomaly .
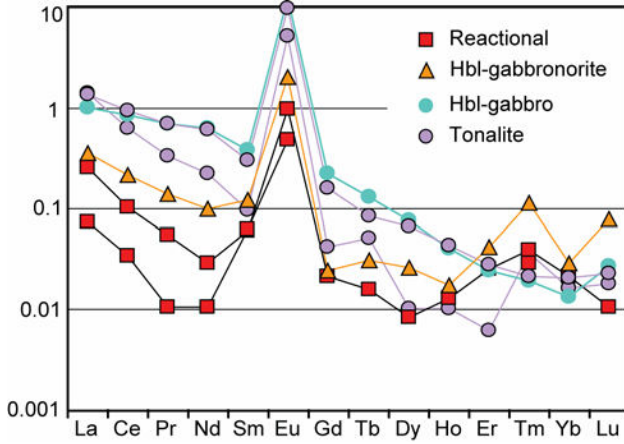
Left: Figure III.36; REE Chondrite normalized values of plagioclase in pipe 2.
Below: Table III.15; Pipe 2 representative major element composition of plagioclase and trace element compositions from the same samples

Sample	P52 Impregn. Pyxite		P39 Impregn. Pyxite		P67 Hbl-Gabbronorite		P63 Tonalite		P68 Hbl gabbro		P98 Tonalite	
Majors	Avrg n=34	2σ	Avrg n=12	2σ	Avrg n=12	2σ	Avrg n=17	2σ	Avrg n=49	2σ	Avrg n=59	2σ
SiO2	43.36	0.42	43.39	0.27	44.45	0.39	63.20	3.96	53.21	6.03	53.63	2.88
Al2O3	35.48	0.41	35.68	0.36	34.51	0.41	23.61	2.31	30.96	3.56	28.77	1.71
FeO	0.11	0.04	0.19	0.16	0.14	0.04	0.08	0.06	0.15	0.11	0.11	0.15
MgO	0.02	0.01	0.00	0.00	0.00	0.00	0.00	0.00	0.03	0.14	0.01	0.03
CaO	19.69	0.26	20.01	0.24	19.10	0.28	4.58	3.02	11.70	4.50	12.69	2.26
Na2O	0.29	0.12	0.18	0.13	0.74	0.10	8.57	1.56	4.41	2.29	4.36	1.18
K2O	0.02	0.01	0.00	0.00	0.00	0.00	0.02	0.01	0.02	0.03	0.01	0.01
Total	99.02	0.76	99.49	0.33	98.97	0.57	100.07	0.49	100.52	1.22	99.59	0.82
An	0.97	0.01	0.98	0.01	0.93	0.01	0.23	0.15	0.59	0.22	0.62	0.11
Ab	0.03	0.01	0.02	0.01	0.07	0.01	0.77	0.15	0.41	0.22	0.38	0.11
Or	0.00	0.00	0.00	0.00	0.00	0.00	0.00	0.00	0.00	0.00	0.00	0.00
Traces	n=11		n=3		n=3		n=3		n=3		n=4	
Cs	0.029	0.015	0.007	0.003	0.091	0.140	0.029	0.029	0.023	0.012	0.027	0.023
Rb	0.053	0.051	0.011	0.002	0.130	0.193	0.079	0.068	0.102	0.041	0.105	0.169
Ba	3.95	0.78	0.94	0.39	5.48	7.24	32.72	6.74	4.08	0.68	6.37	1.99
Th	0.0156	0.0224	0.0001	0.0000	0.0007	1/3	0.0002	0.0001	0.0002	1/3	0.0001	1/4
U	0.0067	0.0076	bd	bd	0.0027	0.0036	0.0133	0.0230	0.0051	0.0043	0.0000	1/4
Nb	0.0024	0.0004	bd	bd	bd	bd	0.0010	bd	0.0016	bd	0.0009	1/4
Ta	0.0021	0.0001	0.0015	0.0008	bd	bd	bd	bd	bd	bd	0.0010	1/4
La	0.061	0.018	0.017	0.005	0.083	0.011	0.334	0.126	0.240	0.026	0.318	0.017
Ce	0.063	0.041	0.021	0.009	0.131	0.031	0.379	0.161	0.516	0.077	0.578	0.028
Pb	0.553	0.141	0.097	0.009	0.791	1.021	2.573	0.304	0.470	0.091	0.656	0.060
Pr	0.005	0.005	0.001	0.001	0.013	0.004	0.032	0.015	0.066	0.011	0.066	0.005
Sr	162.9	7.6	60.3	2.8	142.3	15.2	427.5	45.4	253.8	3.5	284.4	16.9
Nd	0.0138	0.0178	0.0038	0.0017	0.0470	0.0184	0.1044	0.0640	0.2968	0.0711	0.2855	0.0200
Sm	0.0093	0.0057	0.0097	1/3	0.0187	1/3	0.0149	0.0048	0.0589	0.0155	0.0459	0.0036
Zr	0.0745	0.1293	bd	bd	bd	bd	0.0017	0.0002	bd	bd	0.0012	1/4
Hf	0.0043	0.0062	bd	bd	bd	bd	bd	bd	bd	bd	bd	bd
Eu	0.0570	0.0078	0.0278	0.0037	0.1187	0.0253	0.3006	0.0829	0.7143	0.0709	0.5620	0.0660
Gd	0.0045	0.0012	bd	bd	0.0051	bd	0.0087	0.0063	0.0459	0.0172	0.0331	0.0031
Tb	0.0006	0.0002	bd	bd	0.0012	0.0002	0.0019	bd	0.0049	0.0022	0.0032	0.0005
Dy	0.0022	0.0008	bd	bd	0.0066	0.0061	0.0026	0.0027	0.0192	0.0082	0.0169	0.0021
Y	0.0056	0.0038	bd	bd	0.0185	0.0252	0.0231	0.0113	0.0644	0.0319	0.0627	0.0027
Ho	0.0007	0.0004	bd	bd	0.0010	0.0003	0.0006	0.0003	0.0023	0.0017	0.0024	0.0005
Er	0.0042	0.0051	bd	bd	0.0069	bd	0.0010	0.0002	0.0041	0.0019	0.0047	0.0028
Ti	6.17	4.53	0.83	0.70	5.12	4.29	10.42	3.50	27.68	9.55	16.23	6.40
Tm	0.0010	0.0004	0.0007	1/3	0.0029	0.0004	0.0009	0.0002	0.0005	bd	0.0006	0.0002
Yb	0.0037	0.0018	bd	bd	0.0050	0.0045	0.0028	bd	0.0023	0.0020	0.0036	0.0029
Lu	0.0003	bd	bd	bd	0.0020	bd	0.0005	0.0003	0.0007	0.0001	0.0006	0.0003

III.2.7. Melt evolution

Minerals show composition trends indicating that they become more evolved with differentiation. First we correlate calculated trace element compositions of the melt coexisting with the mineral phases with major element evolution. From this we reconstruct the mechanism of melt evolution. All of the REE melt concentrations in equilibrium with clinopyroxene (Fig. III.37c) have been calculated using Kd's of Hart and Dunn (1993). Trace element concentrations of melts in equilibrium with hornblendes in pyroxenites have been calculated with the Kd's from sample "23" of Dalpe and Baker (2000), from Dalpe's sample "25" for the hbl-gabbronorite of pipe 2, and with the Kd's of Klein et al.(1997) for the edenites from both the tonalitic rocks of pipe 2 and the leucocratic patches of pipe 1. Since hornblendes have flat HREE patterns, we re-adjusted HREE Kd's to calculate the melts, and use the Kd value of Dy for all HREE, except for sample P98 (tonalite of pipe 2) whose amphiboles show a slightly concave HREE pattern.

III.2.7.1. Pipe1

III.2.7.1.1. Trace element evolution

The most primitive clinopyroxenes (highest X_{Mg} and Cr_2O_3, lowest Al_2O_3 and TiO_2) are in equilibrium with the most primitive olivines (highest X_{Mg} and NiO, lowest MnO) and occur in dunites. In ol-clinopyroxenite, the clinopyroxene X_{Mg} decreases with olivine X_{Mg}, whereas Al_2O_3, TiO_2, NiO and MnO contents increase. These differentiation trends reflect magma evolution and differentiation with decreasing X_{Mg}. All calculated melts in equilibrium with clinopyroxene show a rather flat M-HREE segment ($0.62 < Sm_N/Lu_N < 1.19$) (Fig. III.37a). The LREE segment is either flat or positively fractionated ($0.95 < La_N/Sm_N < 3.09$) for the melts in equilibrium with the more primitive clinopyroxene (highest X_{Mg}, lowest Al_2O_3) and become slightly negatively fractionated ($0.44 < La_N/Sm_N < 1.88$) for melts in equilibrium with the least primitive clinopyroxene (lowest X_{Mg}, higher Al_2O_3). Together with the trends observed in major elements, i.e. increase of TiO_2 and Al_2O_3 with decreasing X_{Mg}, the calculated REE concentrations increase with melt differentiation, implying melt enrichment. The melt evolution is best seen in the LREE, which, due to the lower Kd, show the stronger enrichment during progressive differentiation. Crystallization of olivine and the most primitive low Al-Ti and LREE clinopyroxene leads to enrichment in these elements in the residual melt, which then crystallizes lower X_{Mg} clinopyroxenes with higher Ti, Al and REE contents.

In the most differentiated ol-clinopyroxenite (low X_{Mg} cpx-ol), X_{Mg} values indicate that hornblende is in equilibrium with the most enriched clinopyroxene ($X_{Mg}^{cpx} \approx X_{Mg}^{Hbl}$) (Gaetani and Grove, 1998; Niida and Green, 1999), which is confirmed by almost congruent REE patterns of melts calculated from hornblende and from cpx. Thus, both minerals derived from the same evolved melt, and crystallized together. Yet, in samples where hornblende is not in equilibrium with clinopyroxene ($X_{Mg-Cpx} > X_{Mg-Hbl}$) melt compositions calculated from hbl are more enriched in REE than melt composition calculated from cpx. This finding is consistent with a peritectic reaction in which clinopyroxene reacted with a more evolved melt to produce hornblende (cpx+melt=hbl). Edenites from leucocratic patches have the lowest X_{Mg} and Cr_2O_3 contents, the highest Na and TiO_2 contents, and are therefore the most differentiated amphiboles of all lithologies within pipe 1. The chondrite normalized pattern of the calculated melt in equilibrium with

this edenite shows a positively fractionated LREE segment and a rather flat MREE segment with a slightly fractionated HREE segment. Edenite equilibrated melts have a similar pattern as those calculated from hornblende in the pyroxenites, but are 3 fold enriched. This indicates that the leucocratic patches are derived from a melt forming one cogenetic suite with those forming the pyroxenites, but more evolved.
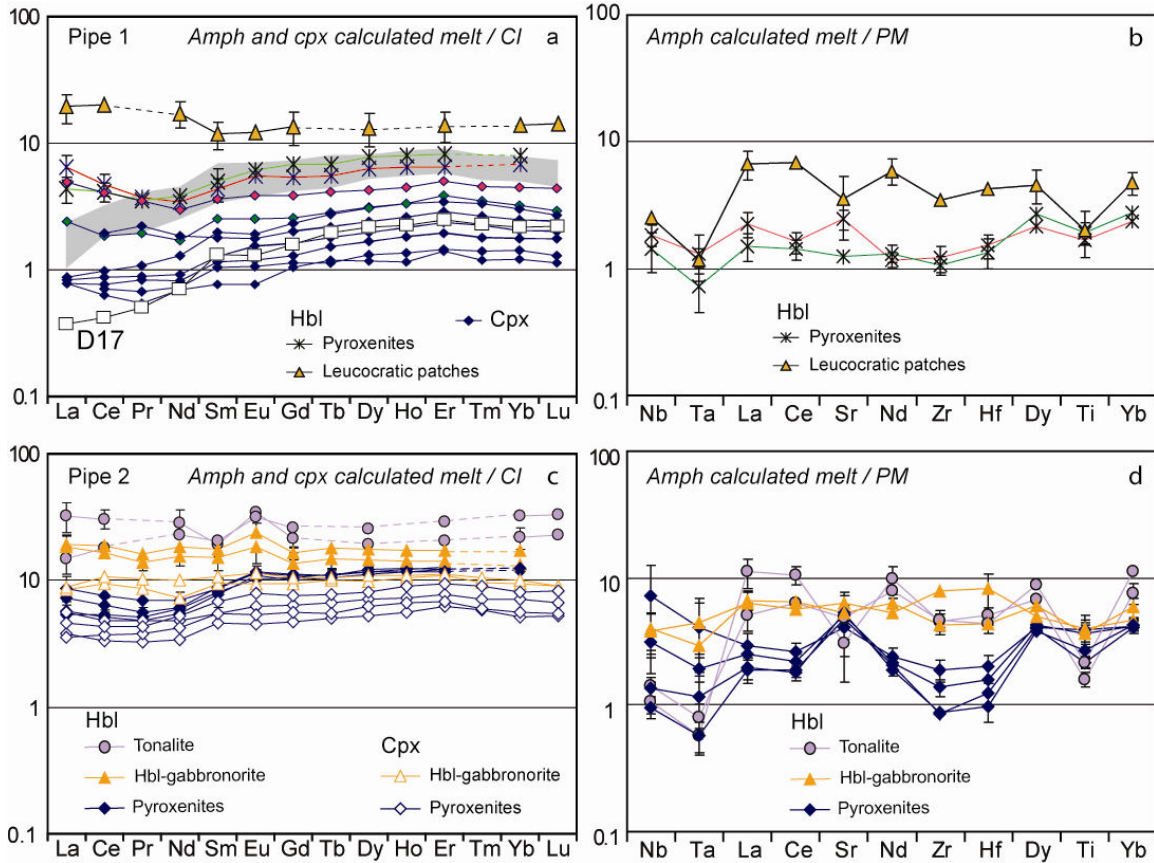

Figure III.37: a) REE chondrite normalized diagram of calculated melt in equilibrium with cpx and hbl in pipe1. See text for details. Grey field and sample D17 from (Bouilhol et al., 2008) representing melt in equilibrium with cpx in the Sapat mantle rocks. b) HFSE, Sr and La-Ce-Nd-Dy and Yb Primitive mantle normalized calculated melts in equilibrium with hbl in pipe1. c) REE chondrite normalized calculated melt in equilibrium with cpx and hbl in pipe2. d) HFSE, Sr and La-Ce-Nd-Dy and Yb Primitive mantle normalized calculated melts in equilibrium with hbl in pipe2. Error bars combine the 2σ mean of measurements and the 2σ errors on Kd's

Sr and HFSE (primitive normalized diagram, Fig. III.37b), compared to the REE enrichment in the calculated melt between the pyroxenite and the leucocratic patches, show different behavior. Sr exhibits a strong negative anomaly in the melt calculated from edenites of the leucocratic patch, while melts calculated from hbl in the pyroxenites show none or positive Sr anomalies. This indicates that crystallization of plagioclase (or alternatively magmatic epidote are at the origin of the Sr anomaly). The negative Pb and Sr anomalies in edenite of the leucocratic patch show that melts were plagioclase saturated before hornblende crystallization. The negative Nb-Ta and Ti anomaly in calculated melts from edenite of the leucocratic patches is more important than the HFSE

anomaly from hbl of the pyroxenites (i.e: $La_N/Nb_N{}^{Ed} \gg La_N/Ta_N{}^{Hbl}\ Dy_N/Ti_N{}^{Ed} \gg Dy_N/Ti_N{}^{Hbl}$). The negative titanium anomaly indicates that a titanium oxide phase became stable in the melt before the crystallization of the leucocratic patches. For Nb and Ta, it also suggests that a phase in which these two elements are compatible control the budget of these two elements in the melt.

III.2.7.1.2. *Differentiation process*

The trace element evolution of the melt is consistent with the observed texture and major element evolution of rocks and minerals. The primitive melts first crystallize olivine and clinopyroxene. Hornblende becomes stable and crystallizes together with clinopyroxene in more evolved rocks because early fractionation of ol+cpx leads to an enrichment of H_2O and incompatible elements (Al_2O_3, TiO_2, Na_2O, LREE) in the residual liquid. The appearance of low SiO_2 hornblende drives the residual liquids towards more Si, Ti, Na and REE rich compositions to form the leucocratic melt. Magmas that ascended in pipe 1 reacted with their own cumulative products. The late leucocratic patches represent the most evolved residual melt fraction issued from crystal fractionation of the pyroxenites. These leucocratic patches thus represent the latest melt that formed by crystal fractionation which could have supplied higher crustal levels. Olivine overgrowing serpentine, together with cpx_1 containing microscopic chlorites and serpentines contributing to La enrichment absent from cpx_2, indicates that fluid circulation took place during magmatic processes. Together with the presence of serpentinite rims around assimilated rock fragments, the hydrated destabilization products of clinopyroxenes in dunite and the presence of geodes filled with fluid-derived minerals indicate that the percolating melt saturated in fluids in the final stage of crystallization. The major and trace element content of geode clinopyroxene (cpx_g) indicates its origin from magmatic fluid. From these lines of evidence, the melt present in pipe 1 had a significant amount of dissolved H_2O, leading to a retarded plagioclase crystallization, extremely coarse grained textures (m sized cpx), geodes, serpentine the cpx_1 signature (La enrichment) and the stability of hornblende and probably epidote in the most differentiated products.

III.2.7.2. Pipe 2

Pipe 2 shows a continuous reactional-fractional crystallization process (RFCp) leading to an evolution from pyroxenite cumulates derived from almost primitive melts, to tonalites (Fig. III.38).

III.2.7.2.1. *Trace element evolution*

Trace element concentrations gradually increase throughout the whole RFCp. REE patterns of each mineral are preserved during this process but minerals become enriched towards tonalitic rocks. This observation implies that the described textures and inferred processes result from a common parental melt. The equilibrium state between opx, hbl and pl in the most reacted rocks, (i.e the fully reacted pyroxenite of the impregnated zone exhibiting plagioclase) is denoted by the flat M-LREE pattern of orthopyroxene, the small positive Eu anomaly in hbl and their similar X_{Mg} (X_{Mg} opx $\approx X_{Mg}$ hbl ≈ 0.8). It demonstrates (e.g de Haas et al., 2002) the magmatic origin of the symplectites.
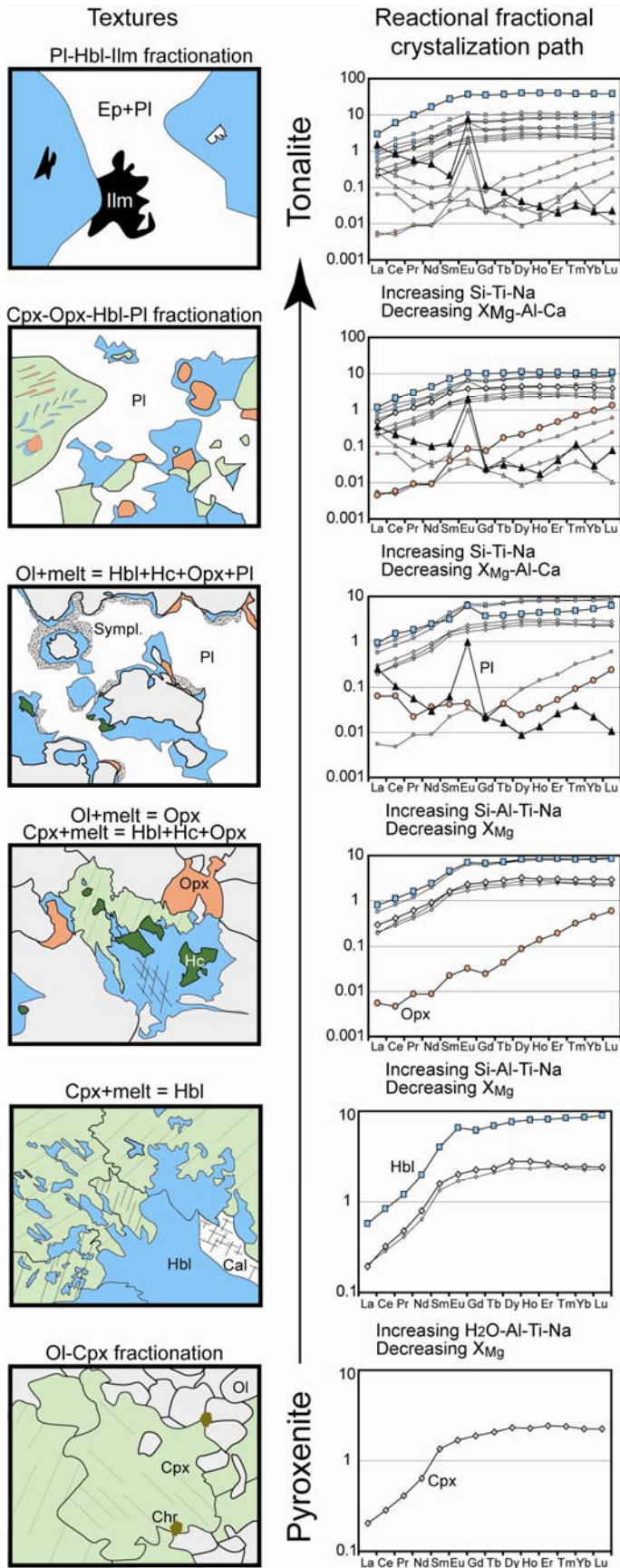
Figure III.38: Synthetic reconstitution of the Reactional-Fractional Crystallization (RFC) path that the melt follow in Pipe2. Left column: typical texture observed with on the right the corresponding REE chondrite normalized content of the minerals.

The most primitive (highest X_{Mg}) cpx leads to the most depleted calculated melt compositions (chondrite normalized, Fig. III.37c), with a flat M-HREE segment and a convex-up LREE segment. The calculated melt in equilibrium with hornblende associated with these clinopyroxenes has the same pattern, but is ≈ 1.5 times more enriched. Clinopyroxenes from hbl-gabbronorites are much more evolved than those from pyroxenites (lower X_{Mg}, higher Al_2O_3 and TiO_2) and the calculated melt has a flat chondrite normalized REE pattern. This melt has HREE values comparable to the melt in equilibrium with the hornblende in pyroxenites, but LREE are more enriched.

Edenite of the hbl-gabbronorite has similar X_{Mg} than the cpx from the same rock, and the edenite calculated melt shows a slightly fractionated flat pattern (La_N/Yb_N = 1.12 and 1.38) with a Eu positive anomaly This calculated melt is more enriched in REE than the cpx calculated melt but show the same patterns.

We observed a small (1.5) discrepancy between melts calculated from cpx and from amphiboles in pyroxenite. This discrepancy is also observed for hbl-gabbronorite with amphibole calculated melt being two times more enriched than cpx calculated melt. The enrichment observed in melt compositions derived from amphiboles are thus likely to be due to the sets of partition coefficient employed. It is especially true for the hbl-gabbronorite for which the Kd's of Hart and Dunn (1993) are used to calculated melts in equilibrium with cpx, whereas the these Kd's are for basaltic composition.

Edenites in the tonalitic rocks are the most evolved amphiboles of all lithologies. They have equilibrated with a melt having a flat REE pattern with a positive Eu anomaly. REE concentrations are 2 times that of melts in equilibrium with edenites from hbl-gabbronorites.

The Sr anomaly evolves from positive in the pyroxenite, to nonexistent in the hbl-gabbronorite, to negative in the hbl-tonalite calculated melt (primitive mantle normalized diagram Fig. III.37d). This shift in Sr anomaly shows that the Sr concentration in the residual melt is controlled by plagioclase appearance, and once plagioclase appears and dominates the fractional crystallization process Sr becomes negative in the residual melt. This interpretation should be confirmed by a negative Eu anomaly in the most differentiated melts, but it is not observed. On the contrary, Eu shows a slight positive anomaly in the calculated melt from edenite of the hbl-tonalite. This could be due to the oxidation state of Eu, which would remain under the form of Eu^{3+} in an oxidizing melt.

As observed in pipe 1, HFSE anomalies become much stronger with differentiation. The melt calculated from the pyroxenite has a small to inexistent negative Ti anomaly, whereas Nb-Ta and Zr-Hf show a wide range of concentration. Nb-Ta can be depleted or enriched compared to La, and Zr-Hf anomalies maybe depleted or not compare to Nd. The calculated melt from the hbl-gabbronorite has slight negative Ti and Nb-Ta anomalies, whereas in average Zr and Hf do not show any anomaly. The calculated melt from the hbl-tonalite shows the strongest negative Ti, Nb-Ta and Zr-Hf anomalies.

III.2.7.2.2. *Differentiation process*

As in pipe 1, the major element compositions of minerals in pipe 2 reflect melt enrichment during its evolution and the decrease in bulk X_{Mg}. Crystallization of olivine and clinopyroxene leads to the enrichment of H_2O in the residual melt Hornblende becomes stable through a peritectic reaction between the residual melt and clinopyroxene

leading to partial replacement of clinopyroxene. The stabilization of low silica (low Na, Ti) hornblende and its crystallization induce an enrichment in Si, Na, and Ti in the residual melt. Concomitantly olivine reacts with the Si-rich melt and producing aluminous low Ti orthopyroxene and hercynite. With increasing differentiation hornblende becomes richer in Na and Ti, reflecting magma enrichment in these elements. These reactions started with the increase in H_2O and stabilization of hornblende and reaches their paroxysms in the fully reacted pyroxenites in which hbl + opx + pl ± hc crystallized from the invading melt. In these former pyroxenites, cpx is completely consumed and plagioclase occurs for the first time in the crystallization sequence. Symplectites in these "consumed" pyroxenites are constituted by the minerals that have been present throughout the reaction sequence, which together with their equilibrated REE patterns indicates their magmatic origin. The stabilization and fractionation of anorthite-rich plagioclase leads to a continued increase the Si content of the melt. This melt further follows a more classical fractional crystallization processes with the formation of hbl-gabbronorite and hbl-gabbro leading to tonalitic compositions.

III.2.8. Pipes and mantle relationships

The most differentiated clinopyroxenes of pipe 1 are in equilibrium with the same melt as clinopyroxenes of the background pipe 2 pyroxenites and pipe1 clinopyroxenes pertain to the differentiation trend documented by Ti and Al in clinopyroxene compositions of both pipes. The calculated melts from hornblende show that hornblende from pipe1 pyroxenites are in equilibrium with the same melt than hornblende from pipe 2 pyroxenite and hornblende of both pipes 1 and 2 pertain to the same differentiation trend as defined by major elements. Olivines from pipes 1 and 2 also result from the same differentiation trend. From these lines of evidence, and together with the fact that both pipes are linked by pegmatitic metagabbros, pipes 1 and 2 seem to be cogenetic, both deriving from the same melt. Rock associations suggest that pipe1 was a major conduit, where most of the melt passed through, whereas pipe 2 represents a minor conduit, possibly an offshoot of pipe 1 in which the melt has evolved.

The melt in equilibrium with the most primitive clinopyroxene in pipe1 is similar to the calculated melt in equilibrium with the most primitive clinopyroxene of the crust-mantle transition zone in the mantle of Sapat (sample D17, Fig. III.37a). On the other hand, most of the melt in equilibrium with clinopyroxene from the crust mantle transition zone has the same M-HREE segment as the calculated melt from both the most evolved pipe1 clinopyroxene and clinopyroxene from pipe2 pyroxenite. The LREE segment of the mantle-equilibrated clinopyroxene melts is higher than that from pipe clinopyroxenes. Moreover, olivines from the pipes are the continuation of the differentiation trend identified in mantle rocks (Fig. III.31). Clinopyroxene in the crust mantle transition zone has been interpreted to form by magma percolation, leaving clinopyroxene. Following this line of argument, we interpret the pipes as crustal conduits in which the same melt that percolated through the mantle ascended in the crust. The LREE difference between calculated melt in the pipes and the calculated melt of the crust mantle transition zone is explained by the crystallization of LREE depleted clinopyroxene in the mantle leading to LREE enriched clinopyroxene in the conduit.

Consequently, pipes 1 and 2 are not only cogenetic, but are also linked to the magma percolation process recognized in the mantle part of Sapat.

III.2.9. Conclusions

This work reaches two conclusions: one concerns the mode of melt migration through the crust, the other concerns magmatic fractionation and differentiation.

Structural observations indicate that the Sapat pyroxenite bodies have a dual relationship with the host metagabbros: they intruded the fine grained metagabbros and were co-magmatic with the pegmatitic metagabbros. This relationship indicates that the investigated pyroxenite bodies grew at the expense of, while participating in the formation of their host. The subvertical magmatic structures such as dykes and impregnation features within the bodies reveal the upward migration of several melt batches These structures and features define the pyroxenite bodies as deep magmatic conduits. Crystallization and cooling of the different melt batches released fluids that further reacted with previously formed magmatic minerals. This process of melts crystallizing and reacting with their own cumulative products implies that fluid-assisted re-equilibration in amphibolite facies conditions was unrelated to late Himalayan metamorphism. These conclusions answer the general question on how melts migrate within the arc crust: they follow sub-vertical pipes that are more or less cogenetic with their surroundings.

Within investigated pyroxenite bodies, continuous melt percolation and crystallization of primitive melt supplied from the mantle led to reactional-fractional crystallization somehow similar than described by Kelemen and Ghiorso (1986). During that process, the melt became more silicic and reached tonalitic compositions. Hornblende played a key role by enhancing the enrichment in silica and trace element in the residual transferred melt. Amphibole is mainly a peritectic phase within the magmatic conduits and would not be traced on the residual transferred melt using classical ratios such as Dy/Yb. Therefore the cryptic amphibole fractionation identified in Sapat would not be responsible for the Dy/Yb change reported in lavas (Davidson et al., 2007). It probably takes place higher in the crust. The melt transferred through pipe 2 would deliver tonalitic intrusions in the crust and dacitic lavas at the surface, and melt transferred through pipe 1 would likely supply High-Al basaltic volcanoes. Indeed, experimental work performed on dacitic compositions reproduces the mineralogy involved in both pipes and, moreover, emphasizes the high water content of the melts necessary for dacite generation (Prouteau and Scaillet, 2003; Rodriguez et al., 2007).

Magmatic conduits similar to the investigated pyroxenite bodies at Sapat may thus be considered as analogue to deep-seated magmatic "chambers" in which the melt is transferred from the crust mantle transition zone towards higher crustal levels, and in which reactional-fractional crystallization leads to the differentiation from primitive to evolved melt. This study shows that silicic melts are generated in lower crustal magmatic conduits. These results complement those from the Jijal and Chilas lithospheric sections of the Kohistan Paleo-Island arc, and place intra-crustal processes as being very important for the evolution of arc-magmas.

III.3. <u>Geochronology</u>

III.3.1. Introduction

Sills of metagabbros and metahornblendites intruded by magmatic pyroxenite bodies represent the lower crust above the mantle-derived, ultrabasic rocks of the Sapat Complex (Chapter II, III). Tonalite-trondhjemite rocks are found in all of these lithologies, thus defining three main structural settings. From bottom to top: (i) as dykes in the mantle rocks (ii) interlayered and as dykes cross cutting the crustal metagabbros and (iii) as dykes within the pyroxenite bodies. Within the crustal section, locally foliated tonalite sills often exhibit primary magmatic textures. In some places, tonalite veins cross-cut foliated metagabbros whereas in other places metagabbros cut foliated, interlayered tonalites. These complex structural relationships call for chronological constraints in order to consolidate petrological considerations that link all these rocks to a common magmatic event. None of the interlayered tonalites (Chapter III.1) contains zircons. Zircons were found in the tonalite-trondhjemite dykes only. These minerals have been dated with the U-Pb methods in order to give a geochronological constraint on the formation of the Sapat Complex and their Hf isotopic composition has been measured to characterize the source evolution during the formation of the Complex. Results show that all rocks crystallized within a narrow time span, between 105 and 99 Ma, that links all rocks to the Kohistan Arc system during its intra-oceanic history. .

III.3.2. Sample Description

The petrography and detailed mineralogical description of the dated samples is given in the chapters referenced in the text. All of these tonalite-trondhjemite dykes are the ultimate products from the differentiation of the Sapat parental melt (Chapter III.1)

Sample D101 (Fig. III.8; Table II.5, 6) comes from the crust-mantle transition zone, where melt infiltration led to the formation of amalgamated metagabbros and pyroxenite (Bouilhol et al., 2008). It is one of the tonalites found as patches with diffuse boundaries in the core of metagabbros, a feature indicating that tonalites assimilated the metagabbros.

Sample G12 (Fig. III.8; Table II.5, 6) is a plagioclase-rich trondhjemite representing a segregated crystal mush from the pegmatitic metagabbro connecting the pyroxenite pipes 1 and 2 (see Chapter III.1).

Sample G13 (Fig. III.8; Table II.5, 6) represents a garnet-bearing leuco-tonalite dyke cross cutting both fine-grained and pegmatitic metagabbros. This dyke is contemporaneous with ductile shearing.

Sample P63 (Fig. III.8; Table II.5, 6) is a leucocratic hornblende-tonalite (see Chapter III.1) found in the pipe 2 pyroxenite . It is interpreted as the crystallized product from the ultimate residual liquid derived from reactional-fractional crystallization.

Sample P8 (Fig. III.8; Table II.5, 6) is a hornblende-trondhjemite dyke cross cutting pipe 1 (see chapter III.1 and III.2).

III.3.3. U/Pb ages and Hf isotope results

Rock samples have been crushed using a disk mill and sieved to retain the fraction below 250µm. Heavy minerals were then separated using a Wilfley table and methylene iodide. The fraction heavier than 3.3 g.cm^{-3} was further separated using a Frantz magnetic separator. Euhedral and clear zircons without inclusions and cracks were hand-picked under a binocular microscope from the non-magnetic (<1.5 A.) fraction. The chemistry procedures and analytical methods for zircon analysis have been described in Galfetti et al. (Galfetti et al., 2007). Hf chemistry and measurement procedure can be found in Schaltegger et al. (Schaltegger and Brack, 2007). U-Pb ages on zircon have been obtained in the Department of Mineralogy at Univ. of Geneva. Hf isotopic compositions have been measured in the Institute of Isotope Geology and Mineral Resources at ETH. Calculation of ages is done with PbMacDat in Excel, only plotting and calculation of averages is done in Isoplot (Ludwig, 2003)

III.3.3.1. *Ages*

Zircons have very low U concentrations (5 < U ppm < 64). Radiogenic Pb is also extremely low (0.07 < Pb$_{rad}$ ppm < 1.07), leading to very low radiogenic / common lead ratio (Table III.16).

Zircons from sample G12, and P8 yield overlapping concordant ages at 104.38 ± 0.78 Ma and 104.83 ± 0.30 Ma, respectively (Fig. III.III.39).

For sample G13, fractions 1 to 6 are concordant or near-concordant but show a considerable spread in their ^{206}Pb/^{238}U ages. They are very likely biased by multiplier nonlinearity effects at very low count rates of <100 cps (as a consequence of smallest radiogenic Pb quantities), as well as potential interferences at masses 204, 205 and/or 207. The points at lower ^{206}Pb/^{238}U ages have extremely low Pb$_{rad}$ /Pb$_{com}$ (fraction 1, 3 and 4 with Pb$_{rad}$ /Pb$_{com}$ ≈ 0.2) relative to the concordant one (fraction 2, 5 and 6). We therefore consider the age of G13 has being similar that of G12 and P8, at 103.0 ± 1.1 Ma, calculated with analyses 5 and 6.

Sample P63 yielded a group of 4 concordant or near-concordant analyses (except fraction 1) which yield a mean ^{206}Pb/^{238}U age of 99.48 ± 0.69 Ma. Fraction number 6 yields an age of 103.16 ± 0.41 Ma, which is significantly older than the age obtained with the other fractions. This older age is similar to the ages of sample G13, G12 and P8. The deviation of analysis 1 from the concordia is believed to result from inaccurate common or blank lead correction.

Sample D101 provides two groups of ages, at 106.83 ± 0.24 Ma and at 104.3 ± 1.3 Ma. The latter age is similar to ages of G13, G12, P8 and the older age of fraction 6 of P63.

III.3.3.2. *Hf results*

Hafnium isotopic compositions (Table III.16) of some of the dated zircons (Fig. III.39) have been analyzed. Owing to typically very low ^{176}Lu $/$ ^{177}Hf isotopic ratios of c. 0.005 in zircon, they represent initial Hf isotopic compositions at the time of melt crystallization. The measured ^{176}Hf/^{177}Hf is corrected by the zircon age to further constrain the zircon isotopic composition at crystallization time (εHf). The εHf values of all analyzed fractions overall show a restricted range (14.34 ± 0.5 <εHf<16.16 ± 0.5). The hafnium isotopic composition of the dated zircons shows in the overall the same MORB-like mantle source (Nowell et al., 1998; Chauvel and Blichert-Toft, 2001).

No	U (ppm)	Pb (ppm)	Pb rad (ppm)	Pb com. (pg)	Th/U$_d$	$^{206}Pb/^{238}Pb_{bc}$	error 2s (%)	$^{207}Pb/^{235}Pb_b$	error 2s (%)	$^{207}Pb/^{206}Pb_{bc}$	error 2s (%)	Age $^{206}Pb/^{238}Pb_{bc}$	$^{176}Hf/^{177}Hf_e$	±2s$_e$	εHf(T)$_g$	±2s
Tonalite (G13)																
G-13/1	6	0.40	0.09	1.38	0.00	0.01547	1.01	0.13398	13.70	0.06283	12.91	98.94				
G-13/2	10	0.57	0.15	2.09	0.13	0.01598	0.61	0.11436	8.40	0.05192	7.90	102.18	0.283142	8	**15.4**	0.5
G-13/3	5	0.30	0.08	1.22	0.08	0.01574	0.76	0.11566	8.96	0.05331	8.40	100.65	0.283129	8	**15.0**	0.5
G-13/4	5	0.33	0.07	1.19	0.01	0.01544	0.91	0.11578	12.78	0.05440	12.05	98.75				
G-13/5	6	0.20	0.10	1.50	0.12	0.01611	0.37	0.10671	4.53	0.04805	4.32	103.00				
G-13/6	9	0.34	0.14	1.88	0.14	0.01624	0.38	0.10784	4.49	0.04817	4.27	103.83				
Tonalite (P63)																
P63/1	17	0.29	0.29	0.75	0.65	0.01560	0.28	0.11446	4.68	0.05320	4.55	99.81	0.283125	51	**14.8**	0.5
P63/2	8	0.15	0.15	0.69	0.94	0.01546	0.53	0.09690	16.80	0.04545	16.45	98.92				
P63/3	22	0.39	0.39	0.82	0.92	0.01566	0.28	0.10541	5.99	0.04881	5.85	100.19	0.283133	14	**15.1**	0.5
P63/4	6	0.12	0.12	0.72	1.21	0.01546	0.36	0.09545	8.99	0.04477	8.78	98.91	0.283111	4	**14.3**	0.5
P63/6	6	0.17	0.12	0.93	1.22	0.01613	0.40	0.10672	12.13	0.04798	11.93	103.16	0.283146	12	**15.6**	0.5
Tonalite (D101)																
D101/1	24	0.77	0.54	0.49	1.66	0.01672	0.31	0.11186	3.84	0.04852	3.66	106.90				
D101/2	9	0.46	0.24	0.90	2.59	0.01678	0.64	0.11224	11.39	0.04853	10.86	107.24				
D101/3	16	0.73	0.48	0.55	3.14	0.01667	0.39	0.11302	5.05	0.04917	4.81	106.59				
D101/4	11	0.52	0.27	0.84	1.95	0.01646	0.53	0.12131	7.70	0.05345	7.29	105.24	0.283119	11	**14.6**	0.5
D101/5	16	0.44	0.44	0.58	2.42	0.01610	1.98	0.12234	45.24	0.05510	43.65	102.98				
D101/6	8	0.14	0.14	0.53	0.53	0.01625	0.60	0.11653	13.82	0.05202	13.37	103.89	0.283150	10	**15.7**	0.5
Trondhjemite (G12)																
G12/1	14	0.30	0.23	1.52	0.22	0.01640	1.11	0.10900	15.89	0.04822	14.89	104.84	0.283132	17	**15.1**	0.5
G12/2	42	1.89	0.65	2.74	0.21	0.01621	1.14	0.10834	15.49	0.04849	14.48	103.63	0.283163	14	**16.2**	0.5
G12/3	15	1.32	0.24	2.09	0.25	0.01651	2.31	0.10875	34.22	0.04778	32.15	105.53				
Trondhjemite (P8)																
P8/1	30	0.47	0.24	0.63	0.24	0.01645	0.34	0.11106	4.48	0.04898	4.20	105.15	0.283155	19	**15.9**	0.5
P8/2	64	1.08	1.07	0.62	0.41	0.01639	0.13	0.10888	1.55	0.04819	1.45	104.77				

(a) Isotopic ratios were measured on Thermo TRITON mass spec. using ion counting. The ion counting system was calibrated by repeated analyses of the NBS 982 standard. The procedural Pb blank was 1.5 ± 0.75 pg; common lead in excess was corrected with depleted mantle isotopic compositions.
(b) Corrected for fractionation, spike, blank and common lead.
(c) Corrected for initial Th disequilibrium, using an estimated Th/U ratio of 4 for the melt.
(d) Calculated on the basis of radiogenic 208Pb/206Pb ratios, assuming concordance.
(e) Calculated with an estimated 176Lu/177Hf=0.005. The Hf fraction was isolated using Eichrom□ Ln-spec resin, and measured in static mode on a NuPlasma multicollector ICP-MS using a MCN-6000 nebulizer for sample introduction. Zircons were not corrected for in-situ radiogenic ingrowth from 176Lu, because corrections for the 100-Ma-old zircons are within the analytical uncertainty of the measured 176Hf/177Hf ratios. The Hf isotopic ratios were corrected for mass fractionation using a 179Hf/177Hf value of 0.7325 and normalized to 176Hf/177Hf ¼ of 0.282160 of the JMC-475 standard (Blichert-Toft et al., 1997). Mean isotopic values are at the 95% confidence level.
(f) Numbers refer to the last digits.
(g) Calculated with present-day DM values of 176Hf/177Hf=0.283252, 176Lu/177Hf=0.04145 and a crustal 176Lu/177Hf=0.017

Table III.16: Isotopic composition of zircons
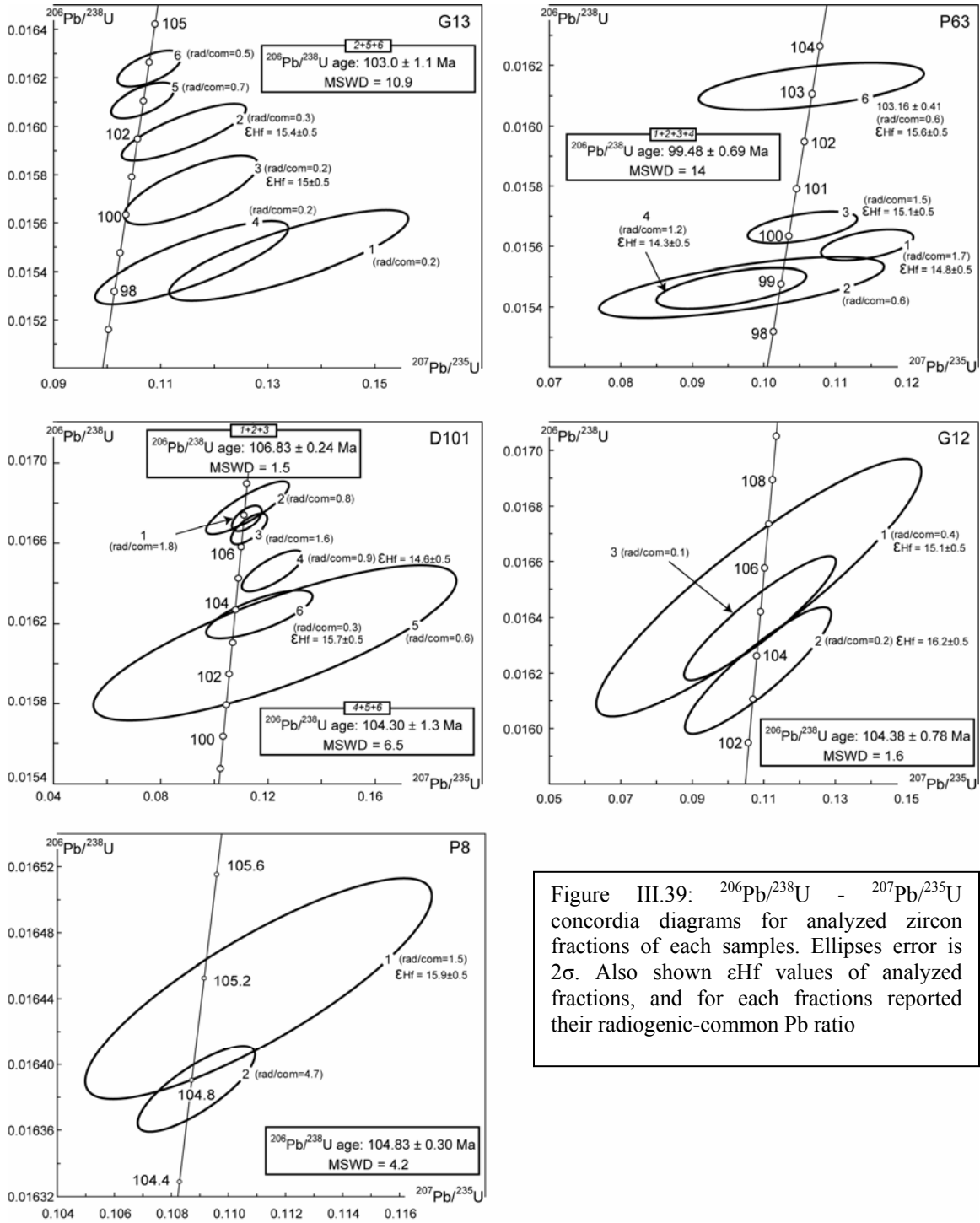
Figure III.39: $^{206}Pb/^{238}U$ - $^{207}Pb/^{235}U$ concordia diagrams for analyzed zircon fractions of each samples. Ellipses error is 2σ. Also shown εHf values of analyzed fractions, and for each fractions reported their radiogenic-common Pb ratio

III.3.4. Evolution of the Sapat complex

III.3.4.1. *Timing of the Sapat Complex formation*

The dated samples were collected from the three main structural positions of the Sapat Complex (mantle, lower crust, and mantle crust transition zone). Therefore, the obtained ages show that both the mantle and the crust of the Sapat Complex have been built during a magmatic continuum lasting for approximately 7 Ma. The crystallization age of samples G12, G13 and P8 is well constrained at around 103 Ma. The two groups of ages identified in samples P63 and D101 are interpreted as follows:

The oldest age of P63 (fraction 6, 103.16 ± 0.5 Ma) is very close to the crystallization age of samples G12, G13 and P8 (between 103.0 ± 1.1 and 104.83 ± 0.30 Ma). Considering that the pyroxenite in which P63 has been sampled is co-magmatic with G12, G13 and P8, we interpret this zircon age as that of an inherited zircon assimilated by magma at beginning stage of the pyroxenite intrusion. The younger age resulting from the other P63 zircon fractions reflects the latest stage of magma percolation and magmatic activity in the Sapat Complex.

The youngest age of sample D101 corresponds to the crystallization ages of samples G12, G13, P8, and P63$_{(6)}$. This age is therefore considered to be the magmatic age. The oldest age group would represent zircons that have been assimilated during the contemporaneous crystallization of D101 , G12, G13, P8, and P63$_{(6)}$. Since D101 is found within metagabbros of the crust-mantle transition zone, and since metagabbro pieces have been identified within the sample, we interpret the oldest zircon as pertaining to the host metagabbro.

These interpretations have several implications: (i) The entire age dataset shows that magmatism was continuous between 106 (crystallization of the metagabbro protolith) and 99 Ma (the last melt percolation in pipe 2) (ii) The lower-crustal metagabbros were the first lithologies to be emplaced within the Sapat Complex; (iii) The tonalites associated with metagabbros (D101-G12) are issued from the near in-situ crystal segregation of differentiated melt from metagabbro protolith (see also Chapter III.1); iv) In agreement with field observation, the pyroxenite bodies intruded later, but still in the same magmatic episode as the metagabbros, v) melt transfer in pipe 2 lasted much longer than in pipe 1 vi) The crust-mantle transition zone in which metagabbros and tonalite dykes are observed is at least 106 Ma old. This implies that the unidentified mantle processes inherited by meta-harzburgites (Bouilhol et al., 2008), and responsible for its U shaped REE pattern are necessarily older than 106 Ma and the formation of the crust mantle transition zone.

III.3.4.2. *Evolution of the source*

Even if hafnium isotopic concentrations show a restricted MORB-like mantle source, the high level of precision of ages and $^{176}Hf/^{177}Hf$ determination shows micro-scale variations between zircon ages and their εHf (Fig. III.40), assuming that none of the age variations is due to lead loss effects (reasonable because of the very low U concentration): The observed trend corresponds to a sharp εHf increase between 106 and 104 Ma (D101-fraction 4 to P8-fraction 1), and a linear εHf decrease with decreasing zircon age, from P8$_{(1)}$ (εHf = 15.88 ± 0.5 at 105.15 ± 0.35 Ma) to P63$_{(4)}$ (εHf = 14.34 ± 0.5 at 98.91 ± 0.36 Ma).

Comparing εHf of zircons with the bulk rock Pb-Nd-Sr isotopic compositions shows correlation with ages (Fig. III.40). Surprisingly, all measured isotopes show the same behavior as εHf with respect to age, except Nd. $^{206}Pb/^{204}Pb$ and $^{208}Pb/^{204}Pb$ sharply decrease from 18.671 and 38.847 to 18.333 and 38.445, respectively, at 105 Ma and increase back to D101 values at 99 Ma. $^{207}Pb/^{204}Pb$ also shows a sharp decrease from 15.630 to 15.596 at 105 Ma, but large errors do not allow further constraining the behavior of ^{207}Pb expected to follow the two other Pb isotopes. The Sr isotopic ratio also sharply decreases from 0.7044 to 0.7037 at 105 Ma and increases drastically to 0.7050 at 99 Ma. All of these correlations corroborate a strong and sharp change in the melting source region towards more depleted values at 105 Ma. They further indicate that the onset of the source-region melting affected a depleted mantle and that the source evolved towards more enriched compositions during continuing melting. Like the other isotopic systems, Nd isotopes show a sharp evolution at 105 Ma, but they decreases from 0.51288 to 0.51278, i.e they tend towards enriched components instead of more depleted sources. Like the other isotopic systems, $^{143}Nd/^{144}Nd$ decreases from 0.51284 to 0.51278 between 103 and 99 Ma indicating enrichment of the source.

Overall, the Pb-Sr-Hf isotopic systems show a sharp peak of depleted components at 105 Ma and evolve toward a more enriched source after 105 Ma. Conversely, Nd isotopes show a linear increase of source enrichment with a sharp enriched component peak at 105 Ma. This decoupled behavior of Hf-Pb-Sr and Nd isotopes may indicate that the more depleted mantle component where melting began in Sapat was somewhat heterogeneous and may have contained an old Nd-enriched component that quickly vanished after the onset of melting (e.g., pyroxenite strips). This observation is in agreement with the isotopic dataset (chapter III.1) which shows that the melting source was heterogeneous and comprised a depleted member little affected by slab signature and a Nd enriched component. The isotopic evolution toward enriched values after onset of melting at 105 Ma is attributed to an increasing slab contribution to the melting region, and would reflect the whole trends observed in the lithologies of Sapat (chapter III.1).

III.3.4.3.   *Sapat in the Kohistan arc*

Several lithologies of the Kohistan Arc have been sampled and analyzed for zircon U-Pb ages and Hf isotopic compositions (Schaltegger et al., 2002; Schaltegger et al., 2003; Heuberger et al., 2007). This dataset allows tracking of the evolution of the arc source with time (Fig. III.41). Schaltegger et al. (2003) showed that the Kohistan Arc existed 155 Ma ago with a melting of oceanic crust indicated by the high εHf value of +21. In the present-day knowledge on Kohistan, there is no data to which we may refer to trace the εHf evolution toward the older documented value of εHf ≈14 at 110 Ma. However, we suggest that the εHf values quickly dropped to mantle ratios with stabilization of the subduction regime. From 110 Ma to 80 Ma, the Kohistan base line εHf composition is defined at a constant εHf of +14. From this base line, two events can be pointed out:

(1) Intrusion of the Chilas Complex at 85 Ma is marked by a decrease in εHf values marking a change in the composition of the source attributed to the influx of new mantle from the rear-arc (Schaltegger et al. 2002).
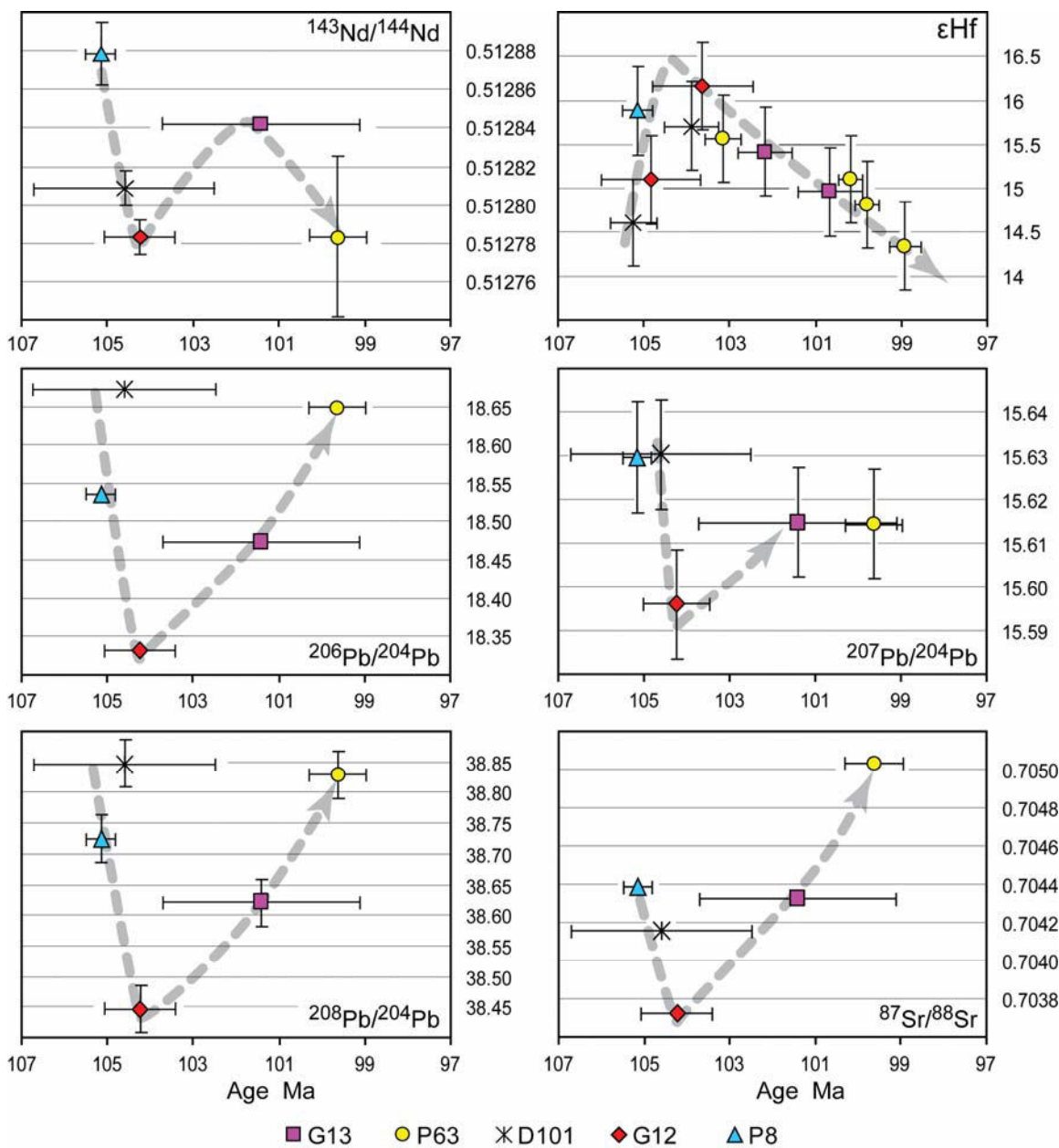
Figure III:40: 7 Ma isotopic evolution in Sapat. For Hf, single zircon fractions are plotted. For Pb, Sr and Nd, bulk rock isotopic ratios are shown. Ages of each sample have been recalculated with the zircon fractions on which Hf has been measured (error recalculated accordingly). For sample P63, fraction 6 has not been considered in the calculated age. All errors are 2sigma based on reproducibility (Appendix 1) and when bigger than the plot sign.

(2) Formation of the Sapat Complex at 105 Ma records an increase in εHf values toward a more depleted mantle source, with evolution toward the Kohistan base line 7Ma after onset of melting. This evolution is regarded as representing the migration of the melting region towards the trench, in a forearc position, which is consistent with the chemistry of the Sapat mantle rocks (Bouilhol et al., 2008). This interpretation agrees with the range of εHf values linked to the initiation of the Marianas arc system (Pearce et al., 1999), considering that subduction initiation involves the same mantle processes as forearc magmatism.

After the onset of collision with the Indian continent (57±1 Ma, Leech et al., 2005) εHf values point to a less depleted melt source (+11; +9), but inherited zircons within the samples yield εHf values down to -6 indicating that melts have sampled and assimilated different types of crust (Heuberger et al., 2007).

In summary, tracking precisely the εHf evolution of the Kohistan Arc, from 110 Ma to 80 Ma allows conclusions on the geodynamical evolution of the Kohistan subduction system. It shows two successive events, a trenchward melt source migration with the formation of the Sapat Complex at 104 Ma, and splitting of the arc with mantle replenishment and the formation of the Chilas Complex at 85 Ma.
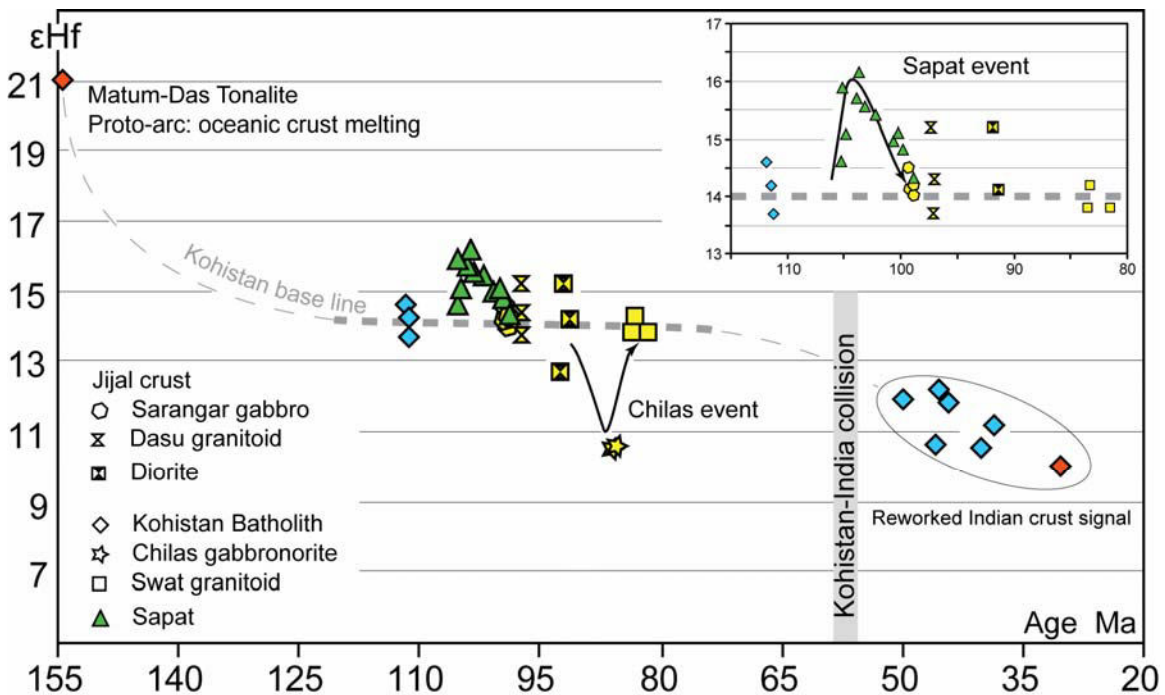

Figure III.41: εHf versus age for zircons dated from different Kohistan lithologies. Symbols type represent lithologies, symbol color literature source: Yellow from Schaltegger et al. 2002; red from Schaltegger et al. 2003; blue from Heuberger et al., 2007; green = Sapat (this study). Onset of collision from Leech et al. (2005)

III.3.5. **Conclusions**

The Sapat Complex formed during a 7 Ma long magmatic event during Cretaceous times. As such, it documents arc-building processes. Hf isotopes show that the onset of melting occurred in a mantle wedge portion more depleted than the Kohistan base line mantle source (εHf ≈ 14). This indicates that melting occurred in a portion of the mantle wedge that was earlier slightly overprinted by the slab signal, and therefore would indicate a melting regime in the forearc mantle, in accordance with the chemistry of the Sapat mantle rocks and the whole isotopic dataset (chapter II.1 and III.1). Moreover, the Nd isotopic system might indicates that the onset of melting occurred in a heterogeneous portion of the mantle wedge as suggested by the isotopic dataset (chapter III.1). The evolution of the isotopic system during the formation of the Sapat Complex shows an increasing slab component with time, after initial onset of melting.

IV. Summary-Conclusions

Among the few places in the world where arc lithospheric sections can be studied, the Kohistan offers the possibility to study deep processes within an arc. This study showed that the Sapat Complex can be added to the list of exhumed arc-root zones, with all the benefit for understanding deep-arc processes. Before this study, the Sapat Complex was very little documented, to the point that even the most reachable part of it (the ultramafic rocks) did not have a clear origin. Most of the Complex was not explored and most of this study is pioneer work in this area. Much remains to be explored. If one of the major contributions of this work is to describe Sapat (map, samples, ages, structures, petro-chemistry) it also brings several conclusions concerning the history of the Kohistan Arc and deep-arc processes. As such, this work contributes to our understanding of the "subduction factory".

(1) An important finding is that the Sapat Complex does not represent a crustal magmatic layered complex, in which the ultramafic rocks would represent the lower most depleted cumulative part. Instead, it represents an upper-mantle / lower crustal arc section (Fig. IV.1).

(2) The exhumed mantle rocks of Sapat are mainly composed of meta-hazburgites in which $10\text{-}100m^2$ zones of dunite are found. Within these dunites, clinopyroxenites and associated gabbroic dykes attest for melt percolation (Fig. IV.1). The meta-harzburgites recorded a complex history. Their chemical composition denotes their highly depleted character but they suffered at least one metasomatic event of unknown origin (U-shaped REE pattern) prior to the dunite formation at the expense of the meta-harzburgites from the same parental melt as the clinopyroxenites. This parental melt was a highly depleted arc-melt. We concluded that the mantle part of Sapat is of arc to forearc origin (Fig. IV.2).

(3) The forearc origin of the mantle rocks is confirmed by the presence of fluid-derived veins that contain one of the best worldwide gem olivine and that are found exclusively in the dunites. These veins contain ol + cal + chl as a primary paragenesis. The major, trace and isotopic compositions of the vein-filling minerals show that they formed from a CO_2-bearing fluid of subduction origin and not by a late "Himalayan" metamorphic event. Moreover, the peculiar trace element concentration (Nb/Ta ≈ 0.1) and B isotopic composition of both olivine and borate inclusions ($\delta^{11}B_{fluid}$ ≈ -23) indicate that carbonate fluids allow Nb-Ta and $\delta^{11}B$ to fractionate within the mantle, not only during slab dehydration.

(4) The peculiarity of the relationships between dunite and meta-harzburgites on the one hand and between clinopyroxenites-gabbroic dykes and dunites on the other hand revealed the migration mode of the parental melt within the mantle. The continuum of melt migration mode from porous to channelized flow indicates that the parental melt migrated into dunitic channels formed thanks to porosity waves at the expense of harzburgites (Fig. IV.1). Porosity waves induced dunitic conduits with a porosity contrast with the surrounding; the low porosity in the conduits concentrated further porosity waves into these channels, so producing a "melt highway" in the mantle. Numerical modeling of such conduits successfully reproduces the observation made in Sapat and strengthens such a process as of major importance for melt transfer in arc lithosphere.
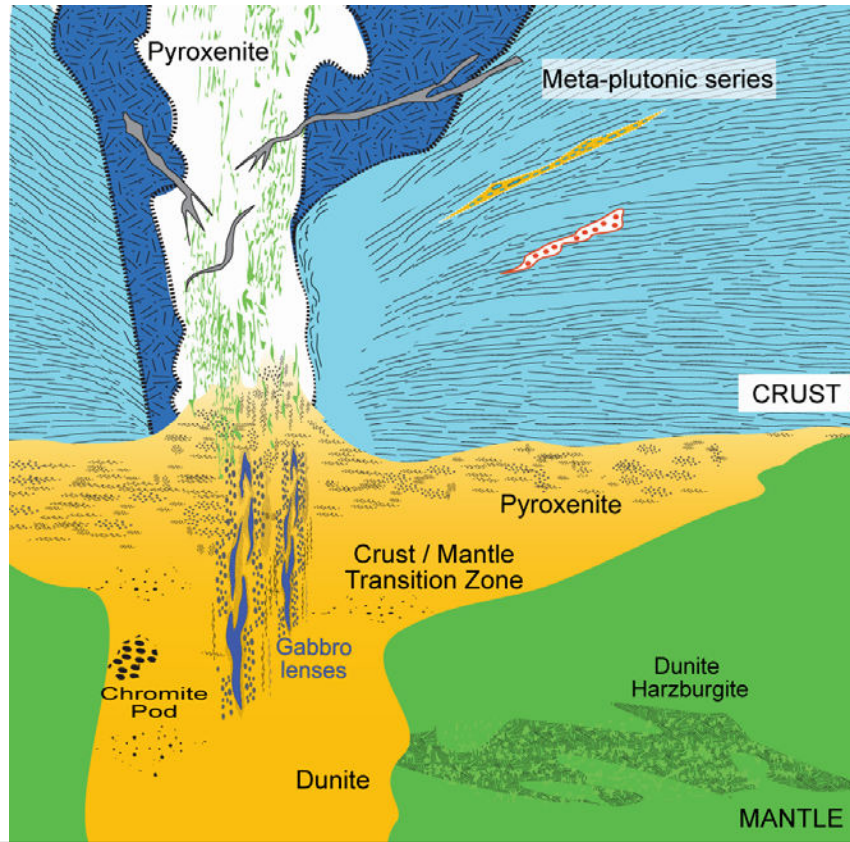
Figure IV.1: Schematic representation of the magmatic plumbing of the Sapat Complex at the time of its formation, ca. 100 Ma ago. Ascending porosity waves of primitive melts reacted with a depleted previously metasomatised harzburgitic mantle and formed dunitic channels. These channels allowed further melt percolation and the transfer in the mantle toward the crust of arc magmas. Within the crust, these primitive melts formed magmatic pipes that grew at the expanse of their host but also participated to its formation. In the pipes, primitive melts fractionated to form the observed pyroxenite bodies. These magmatic conduits were feeder pipes of higher crustal levels, silicic, more evolved tonalitic compositions testifyed by tonalitic dykes.

(5) The lower crustal part of the Sapat Complex, overlying the ultramafic mantle rocks, is principally made of amphibolite facies hornblende-bearing metagabbros enclosing mafic-ultramafic pyroxenite bodies (Fig. IV.1). Tonalite sills and dykes are derived from fractional crystallization of the melt parental to the meta-gabbros. All of these rocks are cumulates derived from a common parental melt through fractional crystallization. Isotopic and trace element data show that all the lithologies are cogenetic and derive from a common source (Fig. IV.1), but also show that the melt that percolated through the mantle is cogenetic with the crustal series. These series suffered extensive metasomatism by fluids that percolated during on-going subduction and therefore are not due to a late Himalayan metamorphism. The isotopic data also show that the mantle source region was heterogeneous, with a depleted component attributed to a 150 Ma Tethysian lithosphere. The Sapat Complex does not resemble any of the other known Kohistan series. It is interpreted to have originated in a forearc region (Fig. IV.2).

(6) Structural and petrological relationships indicate that pyroxenite bodies grew at the expense of, while participating to the formation of their host meta-plutonic series (Fig. IV.1). Subvertical magmatic structures and impregnation features within the pyroxenite bodies document the upward migration of several melt batches. These structures and features define the pyroxenite bodies as deep magmatic conduits (Fig. IV.1). Their identification as such answers the general question on how melts migrate within the arc crust: they follow pipes that are more or less cogenetic with their surroundings. Within the pipes, continuous melt percolation and crystallization of primitive melt supplied from the mantle lead to reactional-fractional crystallization. During that process, the melt became more silicic and reached tonalitic compositions (Fig. IV.1). Magmatic conduits similar to the investigated pyroxenite bodies at Sapat may thus be considered as analogue to deep-seated magmatic "chambers" in which the melt is transferred from the crust mantle transition zone towards higher crustal levels, and in which reactional-fractional crystallization leads to the differentiation from primitive to evolved melt.

(7) The Sapat Complex formed between 106 and 99 Ma (Fig. IV.2). The high precision Hf isotopic composition of dated zircons show that the onset of melting tapped a source region more depleted (εHf $\approx$ +16) than the Kohistan base line source (εHf $\approx$ +14). Just after the onset, εHf values decreased steadily toward Kohistan values of +14. These observations are in accordance with a forearc (Fig. IV.2) origin of the melting source region (highly depleted) which became richer in slab component with time. The Sapat Complex magmatic event was followed by splitting of the arc and formation of the Chilas complex at 85 Ma.
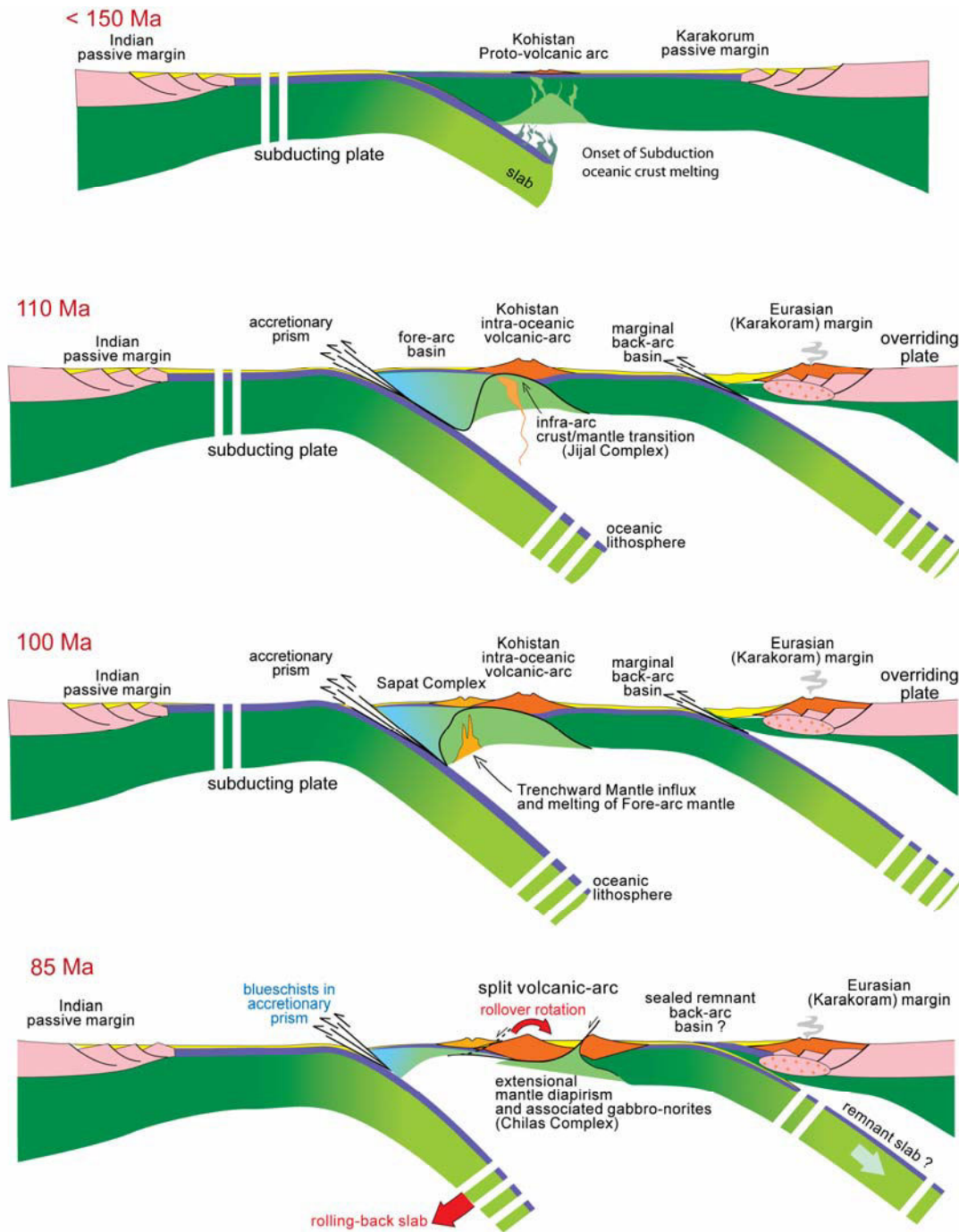
Figure IV.2: Schematic evolution of the Kohistan arc through time. The study of the Sapat Complex bridges the Kohistan geodynamical history gap between 110 Ma and 85 Ma. Inspired from Burg et al. (1998). The Sapat Complex at 100 Ma is placed on the forearc region. A trenchward influx of asthenospheric mantle may be responsible for melting of this forearc region. This event may reflect either trenchward growth and expansion of the arc or the premises of slab roll back later expressed by splitting at 85 Ma, while the Chilas Complex formed.

Appendix 1

Sampling-Mapping

All the field data have been collected during 4 summer field seasons. 2004 has been an explorative season (15 days). 2005 and 2006 have produced most of the work (4.5 months in total). Due to political situation, I could not go in 2007, and JPB did the 2008 field season by himself. Field work consisted on setting-up high altitude (> 4000m) autonomous base camp, moved to different locations when the reachable surrounding has been explored. Field work could not be done without the "blessed" help of a Shaffik Mohammad (cooking+logistic) who became, with time, irreplaceable and moreover a true friend. Also a helper was hired for day-by-day work, without whom the > 1 ton of samples could not be collected. Materials have been carried up the mountains thank to mules. Samples and material brought down the valley the same way. Also, the people from the mines are greatly thanks for their assistance or, their ability to put pressure on me, which gave me more strength to stay with them and dive into Kohistan remote valley's culture and habits. Samples have been collected using a 6kg Pakistani hammer coupled to a home made Kaghan valley chisel for recalcitrant samples. The usual "Eastwing technique" has been in most case inefficient. Samples have been numbered depending on their main lithological belonging (D for ultramafic - G for metaplutonics - P for pyroxenite bodies). All samples have been positioned by satellite coordinates. All data points (measurements-observations-photos) have been GIS referenced. The geological map has been built on Arc-Gis software, with the combination of field observation, SPOT and Landsat 7ETM+ satellite images. Landsat 7ETM+ images have been processed with the software ENVI, allowing spectral determination and enhancement. Illustrator helped to re-process the map for a better visualization.

Whole rock analysis-major and traces

Sixty three samples represent all rock types composing the Sapat Complex have been analysed. They were chosen independently of their metamorphic grade. Samples were reduced in grain size with a hydraulic press in a stainless-steel beaker, and grinded to powder with an agate mill. Powders were fired for XRF analysis. Standard analyses are performed on fused glass-beads prepared from rock powder mixed with Lithium-Tetraborate (1:5 mixture) using a Claisse M4® fluxer. Typically, we used 1.5 g of rock powder and 7.5 g of Lithium-Tetraborate. The machine is a Panalytical Axios wavelength dispersive XRF spectrometer (WDXRF, 2.4 KV). For this study the current setup includes 10 major (SiO_2, TiO_2, Al_2O_3, Fe_2O_3, MnO, MgO, CaO, Na_2O, K_2O, P_2O_5) elements. The calibration bases on ca. 40 certified international standards with emphasize on igneous and metamorphic rock compositions. Minor and trace elements (Sc, V, Co, Ni, Ti, Cu, Zn, Cs, Rb, Ba, Th, , Nb, Ta, La, Ce, Pb, Pr, Sr, Nd Sm, Zr, Hf, Eu, Gd, Tb, Dy, Y, Ho, Er, Tm, Yb, Lu,) in whole rocks were analyzed by solution- ICP-MS. We used the $HF-HClO_4-HNO_3$ digestion procedure described by Ionov et al. (1992) for sample dissolution. The analyses were run on an Element XR high-resolution ICP-MS at Géosciences Montpellier (France). Concentrations were determined by external calibration for most elements except Nb and Ta which were calibrated by using Zr and Hf, respectively, as internal standards. This technique is an adaptation of the ICP-MS

analytical method described by Jochum et al. (1990) for the determination of Nb by spark-source mass spectrometry. This method avoids memory effects due to the introduction of concentrated Nb-Ta solutions in the instrument. Detection limits obtained by long-term analyses of chemical blanks can be found in Ionov et al. (1992) and Garrido et al. (2000).

Whole rock analyses-isotopes

Rocks were also analyzed for Pb, Sr and Nd isotopic compositions. Between 100 and 150 mg of powdered rock fractions (<70 µm) were dissolved on a hot plate at 140°C in closed Teflon vials during 7 days with a mixture of 4 ml conc. HF and 1 ml HNO3 15 M. The sample was then dried on a hot plate, and redissolved in 3 ml of 15M HNO3 in closed Teflon vials at 140°C and dried down again. Sr, Nd and Pb separation was carried out using cascade columns with Sr-spec, TRU-spec and Ln-spec resins following a modified method after Pin et al. (1996). Pb was further purified with a AG-MP1-M anion exchange resin in hydrobromic medium. Pb, Sr and Nd isotope ratios were measured on a Thermo TRITON mass spectrometer on Faraday cups in static mode. Pb was loaded on Re filaments using the silica gel technique and all samples (and standards) were measured at a pyrometer controlled temperature of 1220°C. Pb isotope ratios were corrected for instrumental fractionation by a factor of 0.07% per amu based on more than 90 measurements of the SRM981 standard and using the standard values of Todt et al. (1996). External reproducibility (2σ) of the standard ratios are 0.05% for $^{206}Pb/^{204}Pb$, 0.08% for $^{207}Pb/^{204}Pb$ and 0.10% for $^{208}Pb/^{204}Pb$. Sr was loaded on single Re filaments with a Ta oxide solution and measured at a pyrometer-controlled temperature of 1490°C. $^{87}Sr/^{86}Sr$ values were internally corrected for fractionation using a $^{88}Sr/^{86}Sr$ value of 8.375209. Raw values were further corrected for external fractionation by a value of +0.03‰, determined by repeated measurements of the SRM987 standard ($^{87}Sr/^{86}Sr$ = 0.710250). External reproducibility (2σ) of the SRM987 standard is <7 ppm. Nd was loaded on double filaments with 1M HNO3. $^{143}Nd/^{144}Nd$ values were internally corrected for fractionation using a $^{146}Nd/^{144}Nd$ value of 0.7219 and the ^{144}Sm interference on ^{144}Nd was monitored on the mass ^{147}Sm and corrected by using a $^{144}Sm/^{147}Sm$ value of 0.206700. External reproducibility (2σ) of the JNdi-1 standard (Tanaka et al., 2000) is 4 ppm.

Mineral analysis-major and traces

Major elements analyses of minerals have been done at the ETH Zurich using a "JEOL-8200 WDS/EDS microanalyser" microprobe. Beam conditions were an acceleration voltage of 15 Kv and $2*10^{-8}$ A during analysis. Counting time was 40 s on the peak for each element except for Fe and Mn (20 s). The detection limit is better than 0.01 wt% for each element. In-situ trace elements analyses were performed by Laser ablation (LA-) ICP-MS analyses have been performed at the Montpellier II University with the help of Bruguier Olivier. Analyses acquired using a single collector double-focusing sector field Element XR (eXtended Range) ICP-MS, coupled with a Geolas (Microlas) automated platform housing a ArF 193 nm Compex 102 laser from LambdaPhysik. Ablation experiments were conducted in an ablation cell of ca. 30 cm^3 in a He atmosphere, which enhances sensitivity and reduces inter-element fractionation (Gunther and Heinrich, 1999). The helium gas stream and particles from the sample were then mixed with Ar

before entering the plasma. Data were acquired in the fast E-scan mode at low resolution (M/DM = 300). Signals were measured in Time Resolved Acquisition (TRA), devoting 2 minutes for the blank, and 1 minute for measurement of the analyses. The laser was fired using an energy density of 15 J cm^{-2} at a frequency of 10Hz and using a spot size of 120 µm for olivine, orthopyroxene and plagioclase, and 7Hz / 77µm for clinopyroxene and hornblende. Oxyde level, measured using the ThO/Th ratio, was below 0.7%. ^{29}Si was used as an internal standard for olivine orhtopyroxene and plagioclase, and ^{43}Ca for clinopyroxene and hornblende, and analyte concentrations were calibrated against the NIST 612 rhyolitic glass using the values given in Pearce et al. (1997). Data were subsequently reduced using the GLITTER software (van Achterbergh et al., 2001) by carefully inspecting the time-resolved analysis to check for lack of heterogeneities (inclusions or fractures) in the analysed volume. Four-five grains core have been analysed for each sample, taking care of avoiding visible inclusions.

Mineral analysis-isotopes

Twelve calcite and ten gem-olivine grains with different shapes and mineral associations were selected for stable isotope analysis. From these, three calcites have been analyzed for Sr isotopes and two gem-olivine hosting borates for B isotopes. Oxygen isotope compositions of the calcites were determined on a Thermo Delta V Plus mass spectrometer equipped with a Kiel IV carbonate preparation module at ETH Zurich. Samples were reacted in 100% phosphoric acid at 70°C. The δ^{18}O is reported in the conventional delta-notation with respect to VPDB, as defined by the measurement of NBS 19 with δ^{13}C= 1.95‰ and δ^{18}O= -2.2‰. Analytical reproducibility of duplicate standard measurements (Carrara marble) is better than 0.1‰. Oxygen isotopes of olivine and magnetite have been done at the University of Lausanne with the help of Benita Putlitz. Samples have been crushed in small chips of 1-2 mg and carefully chosen to avoid inclusions with a binocular. Samples have been loaded in a Pt-trail in a F_2 saturated chamber 12 hours prior to CO_2 Laser extraction. The CO2-laser fluorination line is equipped with a Finnigan MAT 253 for normal dual inlet and carrier gas analyses.

Boron isotopes have been analysed in Nancy (France) using a SIMS IMS 1270. Samples were gold coated and measurement where standardize with a NBS boric acid standard SRM 951.

Strontium analyses have been made at ETH Zurich with the help of de Souza Gregory. Approximately 20 mg of calcite has been taken from the samples. Errors on strontium analyses are given in 2 standard deviations. The data is normalised to NBS987 = 0.710248.

Appendix 2

E.P.M.A. analyses of orthopyroxene from two meta-harzburgite samples

rock	Meta-harzburgite				Meta-harzburgite			
Sample	D89				D88			
opx	core	n=29	rim	n=23	core	n=15	rim	n=9
	Average	2σ	Average	2σ	Average	2σ	Average	2σ
SiO2	56.35	1.00	56.49	0.29	57.09	0.25	57.28	0.25
TiO2	0.009	0.007	0.010	0.007	0.022	0.008	0.019	0.010
Cr2O3	0.549	0.059	0.494	0.042	0.558	0.039	0.508	0.100
Al2O3	1.65	0.12	1.57	0.06	1.67	0.10	1.57	0.13
FeO	6.02	0.43	6.06	0.21	5.90	0.33	5.91	0.37
MnO	0.148	0.017	0.148	0.017	0.147	0.017	0.150	0.017
NiO	0.086	0.015	0.076	0.017	0.066	0.019	0.073	0.025
MgO	34.47	0.67	34.42	0.39	34.52	0.25	34.62	0.39
CaO	0.757	0.270	0.584	0.140	0.484	0.123	0.512	0.116
Total	100.04	0.54	99.86	0.48	100.48	0.30	100.76	0.41
Si	1.941	0.034	1.949	0.010	1.958	0.006	1.958	0.015
Ti	0.000	0.000	0.000	0.000	0.001	0.000	0.000	0.000
Cr	0.015	0.002	0.013	0.001	0.015	0.001	0.014	0.003
Al	0.067	0.005	0.064	0.002	0.068	0.004	0.063	0.005
Fe3+	0.031	0.041	0.025	0.018	0.004	0.006	0.002	0.006
Fe2+	0.142	0.032	0.150	0.021	0.165	0.012	0.167	0.014
Mn	0.004	0.001	0.004	0.000	0.004	0.001	0.004	0.000
Ni	0.002	0.000	0.002	0.000	0.002	0.001	0.002	0.001
Mg	1.769	0.029	1.770	0.013	1.765	0.009	1.764	0.012
Ca	0.028	0.010	0.022	0.005	0.018	0.004	0.019	0.004
xMg(Fetot)	0.911	0.005	0.910	0.004	0.912	0.005	0.913	0.006

Representative E.P.M.A analyses of amphibole. Analyses recalculated assuming no Na on M4 site.

rock	Meta-harzburgite		Meta-gabbro		impregnated dunite	
Sample			D25		D21	
amph		n=69		n=13	in cpx	n=5
	Average	2σ	Average	2σ	Average	2σ
SiO2	57.84	0.69	44.06	0.27	47.33	1.30
TiO2	0.010	0.009	0.073	0.030	0.290	0.059
Cr2O3	0.238	0.177	0.721	0.439	1.482	0.391
Al2O3	0.637	0.450	15.080	0.507	9.646	1.129
FeO	1.53	0.27	4.48	0.12	3.12	0.23
MnO	0.055	0.027	0.074	0.014	0.056	0.015
NiO	0.075	0.017	0.047	0.017	0.063	0.008
MgO	23.71	0.42	16.88	0.22	19.31	0.67
CaO	12.44	0.76	12.78	0.29	12.83	0.08
Na2O	1.117	0.758	3.155	0.197	2.688	0.212
K2O	0.017	0.011	0.156	0.013	0.002	0.002
Total	97.673	0.634	97.506	0.363	96.813	0.875
Si	7.972	0.074	6.285	0.036	6.740	0.129
Ti	0.001	0.001	0.008	0.003	0.031	0.006
Cr	0.026	0.019	0.081	0.049	0.167	0.046
Al	0.104	0.073	2.536	0.084	1.620	0.192
Fe3+	0.000	0.000	0.007	0.026	0.008	0.016
Fe2+	0.176	0.030	0.527	0.028	0.363	0.031
Mn	0.006	0.003	0.009	0.002	0.007	0.002
Ni	0.008	0.002	0.005	0.002	0.007	0.001
Mg	4.870	0.073	3.588	0.039	4.099	0.131
Ca	1.836	0.104	1.953	0.038	1.957	0.020
Na	0.300	0.207	0.873	0.056	0.742	0.060
K	0.003	0.002	0.028	0.002	0.000	0.000
xMg(Fetot)	0.965	0.005	0.870	0.004	0.917	0.008

Appendix 3

Trace element concentrations of gem olivine and calcite, of olivine from the dunite, and of chromium clinochlore of the veins.

Mineral	gem-ol.	gem-ol.	gem-ol.	gem-ol.	gem-calcite	olivine	olivine	olivine	olivine
Sample:	OG	Ogi	OGM	OG1	CAP	kj_1	kj_2	kj_3	kj_4
Cs	0.0028	0.0027	0.0035	0.0025	0.0100	<0.00156	0.0045	<0.00136	<0.00144
Rb	0.0027	0.0013	0.0052	0.0011	0.0093	<0.0027	<0.0024	<0.0023	<0.0024
Ba	0.0455	0.0634	0.0430	0.1077	5.5787	0.0029	0.0026	<0.0152	<0.00158
Th	0.0042	0.0088	0.0186	0.0008	0.0005	<0.00005	0.0025	<0.00005	0.0001
U	0.0007	0.0012	0.0029	0.0004	0.0003	0.0014	<0.00003	0.0010	0.0004
Nb	0.00633	0.01124	0.00563	0.01314	0.00277	<0.00042	<0.00039	<0.00035	<0.00035
Ta	0.00038	0.12885	0.00100	0.11673	0.01498	<0.00022	<0.00020	<0.00015	<0.00018
La	0.00188	0.22297	0.00144	0.16641	0.17700	<0.00023	<0.00018	<0.00015	<0.00020
Ce	0.00258	0.67494	0.00182	0.48622	0.55957	<0.00023	<0.00022	<0.00014	<0.00026
Pb	0.0520	0.1701	0.0548	0.2040	0.2345	0.0129	0.0101	0.0084	0.0095
Pr	0.00030	0.00104	0.00026	0.00072	0.00737	<0.00011	0.00198	0.00894	<0.00011
Sr	0.01820	0.06744	0.02372	0.07204	36.585	<0.00163	<0.00151	0.00248	0.0284
Nd	0.00343	0.06097	0.00358	0.04512	0.11253	<0.00048	0.00075	<0.00038	<0.00050
Sm	0.00142	0.00186	0.00090	0.00139	0.05500	<0.00125	<0.00118	<0.00117	<0.00099
Zr	0.0424	0.0686	0.0507	0.0473	0.0264	0.00544	0.00979	0.00879	0.00784
Hf	0.00131	0.00144	0.00109	0.00126	0.00023	0.00058	0.00061	<0.00021	<0.00026
Eu	0.00043	0.00045	0.00034	0.00047	0.03520	<0.00020	<0.00017	<0.00019	<0.00019
Gd	0.00079	0.00061	0.00096	0.00035	0.11411	<0.00132	<0.00093	<0.00106	<0.00113
Tb	0.00008	0.00027	0.00007	0.00020	0.02337	0.00028	<0.00013	<0.00012	<0.00016
Dy	0.0028	0.0072	0.0014	0.0038	0.2293	0.00156	0.0027	0.00113	0.00347
Y	0.0467	0.1646	0.0073	0.0522	1.7595	0.0626	0.0612	0.0247	0.0922
Ho	0.0015	0.0051	0.0002	0.0018	0.0569	0.0015	0.0019	0.0008	0.0022
Er	0.0163	0.0503	0.0022	0.0180	0.1867	0.0143	0.014	0.0054	0.0234
Ti	8.79	3.47	3.12	5.12	2.64	1.81	2.32	2.03	2.31
Tm	0.00590	0.01583	0.00099	0.00694	0.02501	0.00679	0.00706	0.00311	0.00968
Yb	0.0671	0.1380	0.0101	0.0811	0.1434	0.0977	0.0904	0.0428	0.1246
Lu	0.0147	0.0244	0.0027	0.0186	0.0199	0.0208	0.0234	0.0102	0.0316
Li	5.67	2.12	2.14	11.02	0.32	18.91	19.14	8.2	22.92
Cu	0.78	207.61	8.08	181.52	210.97	<0.0072	<0.0069	<0.0065	0.0162
Zn	16.47	139.14	17.02	151.98	127.20	6.67	6.15	6.45	6.5
Nb/Ta	16.49	0.09	5.66	0.11	0.18				
Zr/Hf	32.39	47.73	46.31	37.71	112.73	9.38	16.05		

Mineral	olivine	olivine	olivine	olivine	olivine	olivine	olivine	olivine	olivine
Sample:	ic_1	ic_2	ic_3	ic_4	ic_5	ih_1	ih_2	ih_3	ih_4
Cs	<0.00144	<0.00140	0.0075	0.0031	0.0023	<0.0021	<0.0021	0.0048	0.0047
Rb	<0.0030	0.0060	0.0062	0.0116	<0.0025	0.0042	<0.0040	0.0125	0.0096
Ba	0.0070	<0.0029	0.0096	<0.0020	0.0046	0.0094	0.0113	0.0146	0.0483
Th	<0.00009	0.0000	<0.00007	0.0075	<0.00	<0.00	<0.00009	<0.00008	<0.00003
U	<0.00007	0.0009	0.0000	0.0000	<0.00002	0.0002	0.0001	0.0002	0.0000
Nb	0.00197	0.00047	0.00177	<0.00049	<0.00046	<0.00074	0.00139	0.00133	0.0008
Ta	<0.00031	<0.00026	0.00047	<0.00024	0.00031	<0.00054	<0.00046	<0.00041	0.00084
La	<0.00029	<0.00018	<0.00019	<0.00017	0.00056	0.00177	0.00086	0.00095	0.0005
Ce	<0.00032	0.00047	0.00072	0.00061	0.00055	0.002	0.00314	0.00269	0.00175
Pb	0.0132	0.0127	1.0660	0.1243	0.0085	0.0683	0.0380	0.0422	0.0365
Pr	0.00042	<0.00020	0.00022	<0.00009	0.00029	0.00064	0.00038	0.00075	0.00043
Sr	0.00218	<0.00161	0.0078	<0.00134	0.00125	0.0369	0.0692	0.492	0.411
Nd	0.00062		0.00184	<0.00059	<0.00053	0.0027	0.0017	0.0049	0.00065
Sm	0.00252	<0.00131	0.0032	0.00226	<0.00131	<0.0024	0.0102	<0.0021	<0.0023
Zr	0.00144	0.00261	0.00741	0.00263	0.00164	0.0202	0.0137	0.0177	0.00321
Hf	0.00099	0.00086	0.00156	<0.00031	<0.00014	0.00123	0.00139	0.00059	<0.00073
Eu	0.00029	0.0004	0.00145	<0.00020	<0.00019	0.002	0.00057	0.00094	0.00036
Gd	<0.00193	<0.00113	0.00243	<0.00091	<0.00077	<0.0021	<0.0018	0.0085	<0.00143
Tb	<0.00027	<0.00024	0.00054	0.00034	<0.00017	0.00097	0.00054	0.00055	0.00059
Dy	<0.00046	<0.00	0.00492	0.00066	0.00208	0.0124	0.00296	0.00743	0.00237
Y	0.0029	0.0053	0.0328	0.0052	0.0099	0.0580	0.0442	0.0634	0.0186
Ho	0.0002	0.0003	0.0014		0.0005	0.0022	0.0011	0.0022	0.0003
Er	0.00056	0.00039	0.00443	0.00036	0.00137	0.0111	0.00617	0.00793	0.00121
Ti	9.05	8.02	7.74	8.11	7.37	7.88	8.56	10.31	6.40
Tm	<0.00031	0.00022	0.0003	<0.00017	<0.00023	0.00138	0.0015	0.00093	<0.00035
Yb	<0.00048	0.0019	0.0042	0.0027	0.0025	0.0096	0.0089	0.0095	0.0035
Lu	0.0004	0.0005	0.0009	0.0008	0.0005	0.0026	0.0015	0.0020	0.0015
Li	1.369	1.433	1.527	1.647	1.557	1.09	1.243	1.196	1.501
Cu	<0.0097	0.0138	0.0282	<0.0086	<0.0080	1.962	0.126	0.444	0.0382
Zn	26.95	26.5	32.12	27.1	30.18	32.58	30.8	36.03	31.54
Nb/Ta			3.77						0.95
Zr/Hf	1.45	3.03	4.75			16.42	9.86	30.00	

Mineral	olivine	olivine	olivine	olivine	olivine	olivine	Chlorite	Chlorite	Chlorite	Chlorite
Sample:	ih_5	ii_1	ii_2	ii_3	ii_4	ii_5	kk_1	kk_2	kk_3	kk_4
Cs	0.0061	<0.0021	<0.0022	<0.0023	0.0026	0.0064	0.0105	0.0054	<0.0055	0.0113
Rb	0.0076	<0.0039	<0.0040	0.0051	0.0126	0.0038	0.0197	<0.0091	0.0239	<0.0100
Ba	0.0116	0.0422	<0.0032	0.0095	0.0744	0.0127	<0.0070	<0.0071	0.016	<0.0074
Th	<0.00004	<0.00008	0.0000	0.0381	<0.00007	0.0001	<0.00017	<0.00012	<0.00018	<0.00024
U	<0.00	0.0001	0.0001	0.0216	0.0009	<0.00	<0.00	<0.00010	0.00013	0.00019
Nb	<0.00072	<0.00067	<0.00069	0.00076	<0.00078	<0.00062	0.0143	0.0116	0.0121	0.0128
Ta	<0.00046	0.00055	<0.00041	<0.00044	<0.00045	0.00334	<0.00080	<0.00081	<0.00073	0.00143
La	0.0009	<0.00031	<0.00030	0.00078	<0.00031	<0.00024	<0.00075	<0.00068	<0.00068	0.00104
Ce	0.00267	0.00067	<0.00047	<0.00044	0.00113	<0.00038	<0.00093	<0.00092	0.00796	0.00145
Pb	0.0399	0.0048	0.0066	0.0083	0.0057	0.0048	0.0114	0.00143	0.0082	0.0378
Pr	0.00038	<0.00021	<0.00022	<0.00018	0.00061	0.00042	<0.00047	<0.00042	0.00071	0.00231
Sr	0.1276	0.0058	0.0032	<0.0020	0.0035	0.0022	0.0105	<0.0059	0.0074	0.0087
Nd	<0.00047	0.00061	<0.00080	<0.00098	0.00192	0.00056	<0.00195	0.00164	0.0028	<0.00179
Sm	<0.0027	<0.0019	<0.0018	<0.0028	<0.0018	<0.00148	<0.0040	<0.0040	<0.0044	<0.0038
Zr	0.01134	0.00891	<0.00066	0.0009	0.00436	0.00328	0.0172	0.024	0.0207	0.0127
Hf	<0.00050	0.00068	0.00068	0.00074	<0.00049	<0.00026	<0.00128	0.00038	0.00216	0.0023
Eu	<0.00044	0.00048	<0.00033	0.00096	<0.00031	<0.00018	0.00143	0.00109	<0.00091	<0.00068
Gd	0.0057	<0.0018	<0.00150	0.0023	0.00202	0.0056	<0.0041	<0.0036	0.0063	<0.0050
Tb	0.00058	<0.00026		<0.00031	0.00061	0.00056	<0.00053	<0.00039	<0.00050	<0.00062
Dy	0.00379	0.00445	0.00154	0.00198	0.00094	0.00053	<0.00131	<0.00131	<0.00037	<0.00140
Y	0.0322	0.0392	0.0048	0.0101	0.0141	0.0099	<0.00126	<0.00108	<0.00136	0.00301
Ho	0.0009	0.0014	<0.00013	0.0004	0.0003	<0.00	0.0002	0.00029	<0.00030	<0.00025
Er	0.00346	0.008	0.00117	0.00057	0.00085	0.00058	<0.00118	<0.00108	<0.00100	<0.00152
Ti	10.82	5.23	9.45	6.11	7.41	7.26	56.51	56.47	59.37	91.41
Tm	0.00071	0.00063	0.00042	0.00059	0.00178	0.00184	<0.00066	<0.00055	<0.00059	<0.00053
Yb	0.0100	0.0094	0.0052	0.0056	0.0069	0.0046	<0.0015	<0.0018	<0.0019	0.0038
Lu	0.0022	0.0026	0.0020	0.0026	0.0017	0.0020	0.00072	<0.00043	0.00095	0.00057
Li	1.821	1.308	1.621	1.548	1.79	1.612	<0.023	<0.022	<0.023	0.677
Cu	0.0839	<0.0101	<0.0098	<0.0100	<0.0103	0.0186	4.79	5.64	3.39	3.84
Zn	35.43	16.38	18.28	18.69	17.72	17.91	1.219	1.2	1.66	0.693
Nb/Ta										8.95
Zr/Hf		13.10		1.22				63.16	9.58	5.52

159

Sr isotopic values, C and O isotopic compositions and MgO content of calcites
Errors in brackets are given in 2 standard deviations.

Calcite	MgO wt %	δ18O SMOW ‰	δ13C VPDB ‰	87Sr/86Sr
CAZ rim	0.151	15.78	4.65	0.705539 (22)
CAZ core	0.296	10.78	-1.86	0.705610 (65)
CA2	0.364	9.45	-2.27	0.705626 (9)
CAP	n.d	11.8	-3.98	0.705449 (40)

Appendix 4

Some recalculated epidote analyses, and LA-ICPMS data on epidote.
Left Mn poor epidote, Right Mn rich epidote

Wt.% Recalculated				Sample P14			
SiO2	37.83	38.04	37.56	37.95	37.81	37.43	37.74
TiO2	0.00	0.14	0.01	0.00	0.00	0.00	0.00
Cr2O3	0.01	0.00	0.00	0.00	0.00	0.02	0.00
Al2O3	28.06	29.70	27.29	29.29	28.33	28.05	28.50
Fe2O3	6.75	4.09	7.36	5.02	6.05	6.08	6.17
FeO	0.00	0.00	0.00	0.00	0.00	0.00	0.00
MnO	0.07	0.08	0.08	0.32	0.27	0.23	0.11
NiO	0.01	0.00	0.02	0.00	0.01	0.02	0.01
MgO	0.00	0.02	0.00	0.00	0.00	0.00	0.00
CaO	24.00	24.32	23.79	23.68	23.93	23.67	23.95
Na2O	0.00	0.00	0.00	0.00	0.01	0.00	0.00
K2O	0.00	0.00	0.00	0.00	0.00	0.00	0.00
H2O	1.91	1.92	1.89	1.91	1.90	1.89	1.91
Total	98.63	98.31	98.00	98.17	98.30	97.38	98.39
Xep	0.40	0.25	0.44	0.29	0.36	0.37	0.36

	ig_2	ig_3	**Avrg**	ig_1	ig_4	ig_5	**Avrg**
Cs	<0.0059	<0.0061		0.0101	<0.0058	0.0087	0.0094
Rb	0.0153	<0.0088	0.0153	0.059	0.0318	0.0219	0.037567
Ba	5.5	2.4	3.9	3.8	6.8	4.8	5.1
Th	0.00097	0.0007	0.000835	0.00879	0.0634	0.0196	0.030597
U	0.001	0.003	0.002	0.010	0.040	0.008	0.020
Nb	<0.00148	0.0222	0.0222	0.0117	0.0158	<0.00149	0.01375
Ta	<0.00114	0.00241	0.00241	<0.00087	<0.00093	<0.00103	
La	0.225	0.114	0.169	0.018	0.029	0.007	0.018
Ce	0.420	0.294	0.357	0.030	0.082	0.019	0.044
Pb	15.5	22.1	18.8	3.8	3.9	3.4	3.7
Pr	0.050	0.050	0.050	0.004	0.015	0.007	0.009
Sr	256.0	137.6	196.8	338.1	479.7	511.8	443.2
Nd	0.236	0.272	0.254	0.0081	0.074	0.0266	0.036233
Sm	0.0336	0.1266	0.0801	<0.0043	0.0105	<0.0047	0.0105
Zr	1.296	1.108	1.202	0.892	0.925	1.105	0.974
Hf	0.0227	0.0305	0.0266	0.0223	0.0183	0.0240	0.0215
Eu	0.4120	0.3390	0.3755	0.0031	0.0204	0.0115	0.0117
Gd	0.0351	0.1440	0.0896	0.0028	0.0065	0.0032	0.0042
Tb	0.0031	0.0180	0.0106	0.0005	0.0021	<0.00034	0.0013
Dy	0.0179	0.1262	0.0721	0.0029	0.0068	0.0090	0.0062
Y	0.0912	0.5430	0.3171	0.0154	0.0382	0.0636	0.0391
Ho	0.0014	0.0252	0.0133	0.0005	0.0015	0.0023	0.0014
Er	0.004	0.053	0.028	0.003	0.004	0.020	0.009
Ti	412.3	864.4	638.4	854.1	672.6	565.4	697.4
Tm	0.003	0.006	0.004	0.002	0.001	0.005	0.002
Yb	0.018	0.030	0.024	0.017	0.026	0.031	0.025
Lu	0.004	0.005	0.004	0.005	0.005	0.007	0.005

The Entire DATASET
(Microprobe, ICPMS)
Can be asked to the Author

Bibliography

Anczkiewicz, R., Burg, J.P., Hussain, S., Dawood, H., Ghazanfar, M., Chaudry, M.N., 1998. Stratigraphy and structure of the Indus suture in the Lower Swat, Pakistan, NW Himalaya. Journal of Asian Earth Sciences, 16(2-3): 225-238.

Annen, C., Blundy, J.D. and Sparks, R.S.J., 2006. The genesis of intermediate and silicic magmas in deep crustal hot zones. Journal of Petrology, 47(3): 505-539.

Argles, T., Foster, G., Whittington, A., Harris, N. and George, M., 2003. Isotope studies reveal a complete Himalayan section in the Nanga Parbat syntaxis. Geology, 31(12): 1109-1112.

Arif, M. and Jan, M.Q., 2006. Petrotectonic significance of the chemistry of chromite in the ultramafic-mafic complexes of Pakistan. Journal of Asian Earth Sciences, 27(5): 628-646.

Bard, J.P., 1983. Metamorphism of an obducted Island-arc - Example of the Kohistan sequence (Pakistan) in the himalayan collided range. Earth and Planetary Science Letters, 65(1): 133-144.

Barnes, S.J. and Roeder, P.L., 2001. The range of spinel compositions in terrestrial mafic and ultramafic rocks. Journal of Petrology 42(12): 2279-2302.

Bedard, J.H., 1999. Petrogenesis of boninites from the Betts Cove Ophiolite, Newfoundland, Canada: Identification of subducted source components. Journal of Petrology 40(12): 1853-1889.

Bedini, R.M. and Bodinier, J.L., 1999. Distribution of incompatible trace elements between the constituents of spinel peridotite xenoliths: ICP-MS data from the East African Rift. Geochimica Et Cosmochimica Acta 63(22): 3883-3900.

Benothman, D., White, W.M. and Patchett, J., 1989. The Geochemistry of Marine-Sediments, Island-Arc Magma Genesis, and Crust Mantle Recycling. Earth and Planetary Science Letters, 94(1-2): 1-21.

Bodinier, J-L., Garrido C.J., Chanefo, I., Bruguier O., Gervilla, F., 2008. Origin of pyroxenite-peridotite veined mantle by metl-rock reactions: evidence from the Ronda peridotite. Journal of Petrology, 49(5): 999-1025.

Bodinier, J.L. and Godard, M., 2005. Orogenic, Ophiolitic, and Abyssal Peridotites. In, R.W. Carlson (Ed.), Treatise on Geochemistry. Elsevier.

Bodinier, J.L., Merlet, C., Bedini, R.M., simien, F., Remaidi, M., Garrido, C.J., 1996. Distribution of niobium, tantalum, and other highly incompatible trace elements in the lithospheric mantle: The spinel paradox. Geochimica et Cosmochimica Acta 60(3), 545-550.

Bouilhol, P., Burg, J.P., Bodinier, J.L., Schmidt, M.W., Dawood, H., Hussain, S., 2008. Magma and fluid percolation in arc to forearc mantle: Evidence from Sapat (Kohistan, Northern Pakistan). Lithos, doi:10.1016/j.lithos.2008.07.004.

Braun, M.G. and Kelemen, P.B., 2002. Dunite distribution in the Oman ophiolite: Implications for melt flux through porous dunite conduits. Geochemistry Geophysics Geosystems, 3: 21.

Brophy, J.G., 2008. A study of rare earth element (REE)-SiO2 variations in felsic liquids generated by fractionation and amphibolite melting: a potential test for

discriminating the two different processes. Contributions to Mineralogy and Petrology, 155(3).

Burg, J.P., Chaudhry, M.N., Ghazanfar, M., Anczkiewicz, R. and Spencer, D., 1996. Structural evidence for back sliding of the Kohistan arc in the collisional system of northwest Pakistan. Geology 24(8): 739-742.

Burg, J.P., Bodinier, J.L., Chaudhry, S., Hussain, S. and Dawood, H., 1998. Infra-arc mantle-crust transition and intra-arc mantle diapirs in the Kohistan Complex (Pakistani Himalaya): petro-structural evidence. Terra Nova 10(2): 74-80.

Burg, J.P., Arbaret, L., Chaudry, M.N., Dawood, H., Hussain, S., Zeilinger, G., 2005. Shear strain localization from the upper mantle to the middle crust of the Kohistan Arc (Pakistan). In: D. Brunhn and L. Burlini (Editors), High-Strain Zones: Structures and Physical properties. Geological society of London, Special Publications, London, pp. 25-38.

Burg, J.P., Jagoutz, O., Dawood, H. and Hussain, S.S., 2006. Precollision tilt of crustal blocks in rifted island arcs: Structural evidence from the Kohistan Arc. Tectonics, 25(5): 13.

Cawthorn, R.G. and Ohara, M.J., 1976. Amphibole Fractionation in Calc-Alkaline Magma Genesis. American Journal of Science, 276(3): 309-329.

Chaussidon, M. and Jambon, A., 1994. Boron Content and Isotopic Composition of Oceanic Basalts - Geochemical and Cosmochemical Implications. Earth and Planetary Science Letters, 121(3-4): 277-291.

Chauvel, C. and Blichert-Toft, J., 2001. A hafnium isotope and trace element perspective on melting of the depleted mantle. Earth and Planetary Science Letters, 190(3-4): 137-151.

Condie, K.C., 1997. Plate tectonics and crustal evolution. Butterworth-Heinemann, Oxford, 282 pp.

Connolly, J.A.D. and Podladchikov, Y.Y., 2007. Decompaction weakening and channeling in ductile porous media: Implications for asthenospheric melt segregation. Journal of Geophysical Research, 112: doi:10.1029/2005JB004213

Coward, M.P. and Butler, R.W., 1985. Thrust tectonics and the deep structure of the Pakistan Himalaya. Geology, 13(6): 417-420.

Coward, M.P., Butler, R.W.H., Khan, M.A. and Knipe, R.J., 1987. The tectonic history of Kohistan and its implications for himalayan structure. Journal of the Geological Society, 144: 377-391.

Crawford, M.B. and Searle, M.P., 1992. Field Relationships and Geochemistry of Pre-Collisional (India-Asia) Granitoid Magmatism in the Central Karakoram, Northern Pakistan. Tectonophysics, 206(1-2): 171-192.

Crawford, A.J., Falloon, T.J. and Green, D.H., 1989. Classification, petrogenesis and tectonic settings of boninites. In, A.J. Crawford (Ed.), Boninites and related rocks. University press, Cambridge, London.

Daines, M.J. and Kohlstedt, D.L., 1994. The Transition from Porous to Channelized Flow Due to Melt/Rock Reaction During Melt Migration. Geophysical Research Letters, 21(2): 145-148.

Dalpe, C. and Baker, D.R., 2000. Experimental investigation of large-ion-lithophile-element, high-field-strength-element and rare-earth-element-partitioning between

calcic amphibole and basaltic melt: the effects of pressure and oxygen fugacity. Contributions to Mineralogy and Petrology, 140(2): 233-250.

Davidson, J., Turner, S., Handley, H., Macpherson, C. and Dosseto, A., 2007. Amphibole "sponge" in arc crust? Geology, 35(9): 787-790.

de Haas, G., Nijland, T.G., Valbracht, P.J., Maijer, C., Verschure, R., Andersen, T., 2002. Magmatic versus metamorphic origin of olivine-plagioclase coronas. Contributions to Mineralogy and Petrology, 143(5): 537-550.

Debari, S.M. and Coleman, R.G., 1989. Examination of the deep levels of an Island-arc - Evidence from the Tonsina ultramafic-mafic assemblage, Tonsina, Alaska. Journal of Geophysical Research 94(B4): 4373-4391.

Debari, S.M. and Sleep, N.H., 1991. High-Mg, Low-Al Bulk Composition Of The Talkeetna Island-Arc, Alaska - Implications For Primary Magmas And The Nature Of Arc Crust. Geological Society of America Bulletin, 103(1): 37-47.

Defant, M.J., Richerson, P.M., Deboer, J.Z., Stewart, R.H., Maury, R.C., Bellon, H., Drummond, M.S., Feigenson, M.D., Jackson, T.E., 1991. Dacite Genesis Via Both Slab Melting and Differentiation - Petrogenesis of La-Yeguada Volcanic Complex, Panama. Journal of Petrology, 32(6): 1101-1142.

Dessimoz, M., Muntener, O., Jagoutz, O. and Hussein, D., 2008. Epidote forming reactions in calc-alkaline rocks monitored by trace elements. Geochimica Et Cosmochimica Acta, 72(12): A213-A213.

Dhuime, B., Bosch, D., Bodinier, J-L., Garrido, C.J., Bruguier, O. Hussain, S.S., Dawood, H., 2007. Multistage evolution of the Jijal ultramafic-mafic complex (Kohistan, N Pakistan): Implications for building the roots of island arcs. Earth and Planetary Science Letters 261 (1-2): 179-200.

Dodony, I. and Weiszburg, T., 1983. The Real Structure of Ludwigite. Mikroskopie, 40(5-6): 146-146.

Drummond, M.S. and Defant, M.J., 1990. A Model for Trondhjemite-Tonalite-Dacite Genesis and Crustal Growth Via Slab Melting - Archean to Modern Comparisons. Journal of Geophysical Research-Solid Earth and Planets, 95(B13): 21503-21521.

Galfetti, T., Bucher, H., Ovtcharova, M., Schaltegger, U., Brayard, A., Brühwiler, T., Goudemand, N., Weissert, H., Hochuli, P.A., Cordey, F., Guodun, K., 2007. Timing of the Early Triassic carbon cycle perturbations inferred from new U–Pb ages and ammonoid biochronozones. Earth and Planetary Science Letters, 258: 593-604.

Gaetani, G.A. and Grove, T.L., 1998. The influence of water on melting of mantle peridotite. Contributions to Mineralogy and Petrology, 131(4): 323-346.

Gansser, A., 1980. The significance of the Himalayan suture zone. Tectonophysics, 62: 37-52.

Garrido, C.J., Bodinier, J.L. and Alard, O., 2000. Incompatible trace element partitioning and residence in anhydrous spinel peridotites and websterites from the Ronda orogenic peridotite. Earth and Planetary Science Letters 181(3), 341-358.

Garrido, C.J., Bodinier, J-L., Burg, J-P., Zeilinger, G., Hussain, S.S., Dawood, H., Chaudhry, M.N., Gervilla, F., 2006. Petrogenesis of mafic garnet granulite in the lower crust of the Kohistan paleo-arc complex (Northern Pakistan): Implications

for intra-crustal differentiation of island arcs and generation of continental crust. Journal of Petrology 47(10): 1873-1914.

Garrido, C.J., Bodinier, J-L., Dhuime, B., Bosch, D., Chanefo, I., Bruguier, O., Hussain, S.S., Dawood, H., Burg, J.P., 2007. Origin of the island arc Moho transition zone via melt-rock reaction and its implications for intracrustal differentiation of island arcs: Evidence from the Jijal complex (Kohistan complex, northern Pakistan). Geology 35(8): 683-686.

Gazis, C.A., Blum, J.D., Chamberlain, C.P. and Poage, M., 1998. Isotope systematics of granites and gneisses of the Nanga Parbat Masssif, Pakistan Himalaya. American Journal of Science, 298(8): 673-698.

Godard, M., Jousselin, D. and Bodinier, J.L., 2000. Relationships between geochemistry and structure beneath a palaeo-spreading centre: a study of the mantle section in the Oman ophiolite. Earth and Planetary Science Letters 180(1-2), 133-148.

Green, T.H., 1995. Significance of Nb/Ta as an Indicator of Geochemical Processes in the Crust-Mantle System. Chemical Geology, 120(3-4): 347-359.

Green, T.H. and Adam, J., 2003. Experimentally-determined trace element characteristics of aqueous fluid from partially dehydrated mafic oceanic crust at 3.0 GPa, 650-700 degrees C. European Journal of Mineralogy, 15(5): 815-830.

Greene, A.R., DeBari, S.M., Kelemen, P.B., Blusztajn, J. and Clift, P.D., 2006. A detailed geochemical study of island arc crust: the Talkeetna Arc section, south-central Alaska. Journal of Petrology 47(6): 1051-1093.

Grove, T.L., Chatterjee, N., Parman, S.W. and Medard, E., 2006. The influence of H2O on mantle wedge melting. Earth and Planetary Science Letters, 249(1-2): 74-89.

Grove, T.L., DonnellyNolan, J.M. and Housh, T., 1997. Magmatic processes that generated the rhyolite of Glass Mountain, Medicine Lake volcano, N California. Contributions to Mineralogy and Petrology, 127(3): 205-223.

Grove, T.L., Elkins-Tanton, L.T., Parman, S.W., Chatterjee, N., Müntener, O., Gaetani, G.A., 2003. Fractional crystallization and mantle-melting controls on calc-alkaline differentiation trends. Contributions To Mineralogy And Petrology, 145(5): 515-533.

Gunther, D. and Heinrich, C.A., 1999. Enhanced sensitivity in laser ablation-ICP mass spectrometry using helium-argon mixtures as aerosol carrier - Plenary lecture. Journal of Analytical Atomic Spectrometry 14(9): 1363-1368.

Hart, S.R. and Dunn, T., 1993. Experimental Cpx Melt Partitioning of 24 Trace-Elements. Contributions to Mineralogy and Petrology 113(1): 1-8.

Harte, B., Hunter, R.H. and Kinny, P.D., 1993. Melt Geometry, Movement and Crystallization, in Relation to Mantle Dykes, Veins and Metasomatism. Philosophical Transactions of the Royal Society of London Series a-Mathematical Physical and Engineering Sciences 342(1663): 1-21.

Hervig, R.L., Moore, G.M., Williams, L.B., Peacock, S.M., Holloway, J.R., Roggensack, K., 2002. Isotopic and elemental partitioning of boron between hydrous fluid and silicate melt. American Mineralogist, 87(5-6): 769-774.

Heuberger, S., Schaltegger, U., Burg, J.P., Villa, I.M., Frank, M., Dawood, H., Hussain, S., Zanchi, A., 2007. Age and isotopic constraints on magmatism along the Karakoram-Kohistan Suture Zone, NW Pakistan: evidence for subduction and

continued convergence after India-Asia collision. Swiss Journal of Geosciences, 100(1): 85-107.

Holtzman, B.K., Groebner, N.J., Zimmerman, M.E., Ginsberg, S.B. and Kohlstedt, D.L., 2003. Stress-driven melt segregation in partially molten rocks. Geochemistry Geophysics Geosystems, 4: 26.

Ionov, D.A., Savoyant, L. and Dupuy, C., 1992. Application of the Icp-Ms Technique to Trace-Element Analysis of Peridotites and Their Minerals. Geostandards Newsletter 16(2): 311-315.

Jackson, M.D., Gallagher, K., Petford, N. and Cheadle, M.J., 2005. Towards a coupled physical and chemical model for tonalite-trondhjemite-granodiorite magma formation. Lithos, 79(1-2): 43-60.

Jagoutz, J., 2004. zoned Ultramafic Complexes of the Kohistan Paleo-Island Arc. Petrological, Structural and Geochemical evidence for kilometre-scale melt-conduits, ETH Zurich, 223pp.

Jagoutz, O., Muntener, O., Burg, J.P., Ulmer, P. and Jagoutz, E., 2006. Lower continental crust formation through focused flow in km-scale melt conduits: The zoned ultramafic bodies of the Chilas complex in the Kohistan island arc (NW Pakistan). Earth and Planetary Science Letters, 242(3-4): 320-342.

Jagoutz, O., Müntener, O., Ulmer, P., Pettke, T., Burg, J.P., Dawood, H., Hussain, S., 2007. Petrology and mineral chemistry of lower crustal intrusions: the Chilas Complex, Kohistan (NW Pakistan). Journal of Petrology, 48(10): 1895-1953.

Jan, M.Q. and Howie, R.A., 1981. The Mineralogy and Geochemistry of the Metamorphosed Basic and Ultrabasic Rocks of the Jijal Complex, Kohistan, NW Pakistan. Journal of Petrology 22(1): 85-126.

Jan, M.Q. and Windley, B.F., 1990. Chromian Spinel Silicate Chemistry in Ultramafic Rocks of the Jijal Complex, Northwest Pakistan. Journal of Petrology, 31(3): 667-715.

Jan, Q., Khan, A. and Qazi, S., 1993. The Sapat mafic-ultramafic complex, Kohistan arc, North Pakistan. In: P.J. Treloar and M.P. Searle (Editors), Himalayan tectonics. Special Publication. Geological Society, London, pp. 113-121.

Jochum, K.P., Seufert, H.M., Spettel, B. and Palme, H., 1986. The Solar-System Abundances of Nb, Ta, and Y, and the Relative Abundances of Refractory Lithophile Elements in Differentiated Planetary Bodies. Geochimica Et Cosmochimica Acta, 50(6): 1173-1183.

Jochum, K.P., Seufert, H.M. and Thirlwall, M.F., 1990. High-Sensitivity Nb Analysis by Spark-Source Mass-Spectrometry (Ssms) and Calibration of Xrf Nb and Zr. Chemical Geology 81(1-2): 1-16.

Jull, M. and Kelemen, P.B., 2001. On the conditions for lower crustal convective instability. Journal of Geophysical Research-Solid Earth, 106(B4): 6423-6446.

Kane, R.E., 2004. The creation of a magnificent suite of peridot jewelry: From the Himalayas to fifth avenue. Gems & Gemology, 40(4): 288-302.

Kay, S.M. and Kay, R.W., 1985. Role of Crystal Cumulates and the Oceanic-Crust in the Formation of the Lower Crust of the Aleutian Arc. Geology, 13(7): 461-464.

Kelemen, P.B., Ghiorso, M.S., 1986. Assimilation of peridotite in zoned Calc-alcaline Plutonic Complexes-Evidence from the Big Jim Complex, Washington Cascades. Contributions to Mineralogy and Petrology, 94(1):12-28.

Kelemen, P.B., 1995. Genesis of High Mg-Number Andesites and The Continental-Crust. Contributions to Mineralogy and Petrology, 120(1): 1-19.

Kelemen, P.B., Whitehead, J.A., Aharonov, E. and Jordahl, K.A., 1995. Experiments On Flow Focusing In Soluble Porous-Media, With Applications To Melt Extraction From The Mantle. Journal of Geophysical Research 100(B1): 475-496.

Kelemen, P.B., Hirth, G., Shimizu, N., Spiegelman, M. and Dick, H.J.B., 1997. A review of melt migration processes in the adiabatically upwelling mantle beneath oceanic spreading ridges. Philosophical Transactions of the Royal Society of London, Series A, 355(1723): 283-318.

Kelemen, P.B., Hanghøj, K. and Greene, A.G., 2003. One view of the geochemistry of subduction-related magmatic arcs, with an emphasis on primitive andesite and lower crust. In: R.L. Rudnick (Editor), The crust, Treatise on geochemistry. Elsevier, Amsterdam, pp. 593-659.

Kent, A.J.R. and Rossman, G.R., 2002. Hydrogen, lithium, and boron in mantle-derived olivine: The role of coupled substitutions. American Mineralogist, 87(10): 1432-1436.

Khan, M.A., Stern, R.J., Gribble, R.F. and Windley, B.F., 1997. Geochemical and isotopic constraints on subduction polarity, magma sources, and palaeogeography of the Kohistan intra-oceanic arc, northern Pakistan Himalaya. Journal of the Geological Society, 154: 935-946.

Khan, M.A., Treloar, M.A., Khan, M.A., Khan, T., Qazi, M.S., Jan, M.Q., 1998. Geology of the Chalt-Babusar transect, Kohistan terrane, N. Pakistan: implications for the constitution and thickening of island-arc crust. Journal of Asian Earth Sciences, 16(2-3): 253-268.

Khan, T., Khan, M.A., Jan, M.Q. and Naseem, M., 1996. Back-arc basin assemblages in Kohistan, northern Pakistan. Geodinamica Acta, 9(1): 30-40.

Khan, T., Murata, M., Ozawa, H., Kausar, A.B., 2004. Origin of dunite of the Sapat Complex, Himalaya, North Pakistan, 19Th Himalayan-Karakoram-Tibet Workshop. Himalayan Journal of Sciences.

Klein, M., Stosch, H.G. and Seck, H.A., 1997. Partitioning of high field-strength and rare-earth elements between amphibole and quartz-dioritic to tonalitic melts: An experimental study. Chemical Geology, 138(3-4): 257-271.

Kodaira, S., Sato, T., Takahashi, N., Itao, A., Tamura, Y., Tatsumi, Y., Kaneka, Y., 2007. Seismological evidence for variable growth of crust along the Izu intraoceanic arc. Journal of Geophysical Research-Solid Earth, 112(B5): 25.

Koga, K.T., Kelemen, P.B., and Shimizu ,N., 2001. Petrogenesis of the crust-mantle transition zone and the origin of the lower wehrlite in the Oman ophiolite. Geochemistry Geophysics Geosystems 2, 34.

Kretz, R., 1983. Symbols for rock-forming minerals. American Mineralogist 68, 277-279.

Laurora, A., Mazzucchelli, M., Rivalenti, G., Vannucci, R., Zanetti, A., Barbieri, M.A., Cingolani, C.A., 2001. Metasomatism and melting in carbonated peridotite xenoliths from the mantle wedge: The Gobernador Gregores case (Southern Patagonia). Journal of Petrology, 42(1): 69-87.

Ludwig, K.R., 2003. Isoplot/3.0: A geochronological Toolkit for Microsoft Excel. Berkeley Geochronology Center Special Publication(4).

Leech, M.L., Singh, S., Jain, A.K., Klemperer, S.L. and Manickavasagam, R.M., 2005. The onset of India-Asia continental collision: Early, steep subduction required by the timing of UHP metamorphism in the western Himalaya. Earth and Planetary Science Letters, 234(1-2): 83-97.

Mahoney, J.J., Frei, R., Tejada, M .L.G., Mo, X.X., Leat, P.T., Nagler, T.F., 1998. Tracing the Indian Ocean mantle domain through time: Isotopic results from Old West Indian, East Tethyan, and South Pacific seafloor. Journal of Petrology, 39(7): 1285-1306.

Martel, C., Pichavant M., Holtz, F., Scaillet, B., Bourdier, J.L, Traineau, H., 1999. Effects of f(O2) and H2O on andesite phase relations between 2 and 4 kbar. Journal of Geophysical Research-Solid Earth, 104(B12): 29453-29470.

Mattey, D., Lowry, D. and Macpherson, C., 1994. Oxygen-Isotope Composition of Mantle Peridotite. Earth and Planetary Science Letters, 128(3-4): 231-241.

McDonough, W.F. and Sun, S.S., 1995. The Composition of the Earth. Chemical Geology, 120(3-4): 223-253.

McGetchi, Tr., Nikhanj, Y.S. and Chodos, A.A., 1973. Carbonatite-Kimberlite Relations in Cane Valley Diatreme, San-Juan County, Utah. Journal of Geophysical Research 78(11): 1854-1869.

McInnes, B.I.A. and Cameron, E.M., 1994. Carbonated, Alkaline Hybridizing Melts from a Sub-Arc Environment - Mantle Wedge Samples from the Tabar-Lihir Tanga-Feni Arc, Papua-New-Guinea. Earth and Planetary Science Letters, 122(1-2): 125-141.

Miller, D.J., Loucks, R.R. and Ashraf, M., 1991. Platinum-Group Element Mineralization in the Jijal Layered Ultramafic-Mafic Complex, Pakistani Himalayas. Economic Geology and the Bulletin of the Society of Economic Geologists, 86(5): 1093-1102.

Molina, J.F. and Poli, S., 2000. Carbonate stability and fluid composition in subducted oceanic crust: an experimental study on H2O-CO2-bearing basalts. Earth and Planetary Science Letters, 176(3-4): 295-310.

Morris, J.D., Leeman, W.P. and Tera, F., 1990. The Subducted Component In Island-Arc Lavas - Constraints From Be Isotopes And B-Be Systematics. Nature, 344(6261): 31-36.

Munker, C., 1998. Nb/Ta fractionation in a Cambrian arc back arc system, New Zealand: source constraints and application of refined ICPMS techniques. Chemical Geology, 144(1-2): 23-45.

Müntener, O., Hermann, J. and Trommsdorff, V., 2000. Cooling history and exhumation of lower crustal granulite and Upper Mantle (Malenco, Eastern Central Alps). Journal of Petrology 41(2): 175-200.

Müntener, O., Kelemen, P.B. and Grove, T.L., 2001. The role of H2O during crystallization of primitive arc magmas under uppermost mantle conditions and genesis of igneous pyroxenites: an experimental study. Contributions to Mineralogy and Petrology, 141(6): 643-658.

Müntener, O. and Ulmer, P., 2006. Experimentally derived high-pressure cumulates from hydrous arc magmas and consequences for the seismic velocity structure of lower arc crust. Geophysical Research Letters, 33(21): 5.

Müntener, O., Ulmer, P. and Perez, R.A., 2008. Role of garnet and amphibole fractionation in the genesis of high Mg# granitoids. Geochimica Et Cosmochimica Acta, 72(12): A665-A665.

Nicolas, A., Boudier, F., Koepke, J., France, L., Ildefonse, B., Mevel, C., 2008. Root zone of the sheeted dike complex in the Oman ophiolite. Geochemistry Geophysics Geosystems, 9: 29.

Niida, K. and Green, D.H., 1999. Stability and chemical composition of pargasitic amphibole in MORB pyrolite under upper mantle conditions. Contributions to Mineralogy and Petrology, 135(1): 18-40.

Nowell, G.M., Kempton, P.D., Noble, S.R., Fitton, J.G., Saunders, A.D., Mahoney, J.J., Taylor, R.N., 1998. High precision Hf isotope measurements of MORB and OIB by thermal ionisation mass spectrometry: insights into the depleted mantle. Chemical Geology, 149(3-4): 211-233.

Palmer, M.R., London, D., Morgan, G.B. and Babb, H.A., 1992. Experimental-Determination of Fractionation of B-11/B-10 between Tourmaline and Aqueous Vapor - a Temperature-Dependent and Pressure-Dependent Isotopic System. Chemical Geology, 101(1-2): 123-129.

Parkinson, I.J. and Pearce, J.A., 1998. Peridotites from the Izu-Bonin-Mariana forearc (ODP leg 125): Evidence for mantle melting and melt-mantle interaction in a supra-subduction zone setting. Journal of Petrology 39(9): 1577-1618.

Pearce, J.A., Kempton, P.D., Nowell, G.M. and Noble, S.R., 1999. Hf-Nd Element and Isotope Perspective on the Nature and Provenance of Mantle and Subduction Components in Western Pacific Arc-Basin Systems. Journal of Petrology, 40(11): 1579-1611.

Pearce, J.A., Barker, P.F., Edwards, S.J., Parkinson, I.J. and Leat, P.T., 2000. Geochemistry and tectonic significance of peridotites from the South Sandwich arc-basin system, South Atlantic. Contributions to Mineralogy and Petrology 139(1): 36-53.

Pearce, N.J.G., Perkins, W.T., Westgate, J.A., Gorton, M.P., Jackson, S.E., Neal, C.R., Chenery, S.P., 1997. A compilation of new and published major and trace element data for NIST SRM 610 and NIST SRM 612 glass reference materials. Geostandards Newsletter-the Journal of Geostandards and Geoanalysis 21(1): 115-144.

Pearcy, L.G., Debari, S.M. and Sleep, N.H., 1990. Mass balance calculations for two sections of island-arc crust and implications for the formation of continents. Earth and Planetary Science Letters, 96: 427-442.

Petford, N. and Gallagher, K., 2001. Partial melting of mafic (amphibolitic) lower crust by periodic influx of basaltic magma. Earth and Planetary Science Letters, 193(3-4): 483-499.

Petterson, M.G., Crawford, M.B. and Windley, B.F., 1993. Petrogenetic Implications of Neodymium Isotope Data from the Kohistan Batholith, North Pakistan. Journal of the Geological Society, 150: 125-129.

Petterson, M.G. and Windley, B.F., 1985. Rb-Sr Dating of the Kohistan Arc-Batholith in the Trans-Himalaya of North-Pakistan, and Tectonic Implications. Earth and Planetary Science Letters, 74(1): 45-57.

Petterson, M.G. and Windley, B.F., 1991. Changing Source Regions of Magmas and Crustal Growth in the Trans-Himalayas - Evidence from the Chalt Volcanics and Kohistan Batholith, Kohistan, Northern Pakistan. Earth and Planetary Science Letters, 102(3-4): 326-341.

Pfiffner, M.A., 1999. Genese der Hochdruckmetamorphen ozeanishen Abfolge des Cima Lunga-Einheit (Zentralalpen), E.T.H Zurich, 310 pp.

Prouteau, G. and Scaillet, B., 2003. Experimental constraints on the origin of the 1991 Pinatubo dacite. Journal of Petrology, 44(12): 2203-2241.

Ray, J.S. and Ramesh, R., 1999. Evolution of carbonatite complexes of the Deccan flood basalt province: Stable carbon and oxygen isotopic constraints. Journal of Geophysical Research-Solid Earth, 104(B12): 29471-29483.

Richter, F.M. and McKenzie, D., 1984. Dynamical Models for Melt Segregation from a Deformable Matrix. Journal of Geology, 92(6): 729-740.

Ringuette, L., Martignole, J. and Windley, B.F., 1999. Magmatic crystallization, isobaric cooling, and decompression of the garnet-bearing assemblages of the Jijal sequence (Kohistan terrane, western Himalayas). Geology, 27(2): 139-142.

Rodriguez, C., Selles, D., Dungan, M., Langmuir, C. and Leeman, W., 2007. Adakitic dacites formed by intracrustal crystal fractionation of water-rich parent magmas at Nevado de Longav volcano (36.2 degrees S; Andean Southern Volcanic Zone, central Chile). Journal of Petrology, 48(11): 2033-2061.

Romick, J.D., Kay, S.M. and Kay, R.W., 1992. The Influence of Amphibole Fractionation on the Evolution of Calc-Alkaline Andesite and Dacite Tephra from the Central Aleutians, Alaska. Contributions to Mineralogy and Petrology, 112(1): 101-118.

Rose, E.F., Shimizu, N., Layne, G.D. and Grove, T.L., 2001. Melt production beneath Mt. Shasta from boron data in primitive melt inclusions. Science, 293(5528): 281-283.

Rosner, M., Erzinger, J., Franz, G. and Trumbull, R.B., 2003. Slab-derived boron isotope signatures in arc volcanic rocks from the Central Andes and evidence for boron isotope fractionation during progressive slab dehydration. Geochemistry Geophysics Geosystems, 4: 25.

Rudnick, R.L., McDonough, W.F. and Chappell, B.W., 1993. Carbonatite Metasomatism in the Northern Tanzanian Mantle - Petrographic and Geochemical Characteristics. Earth and Planetary Science Letters, 114(4): 463-475.

Rudnick, R.L., 1995. Making Continental-Crust. Nature 378(6557): 571-578.

Rudnick, R.L. and Fountain, D.M., 1995. Nature and Composition of the Continental-Crust - a Lower Crustal Perspective. Reviews of Geophysics, 33(3): 267-309.

Rudnick, R.L. and Gao, S., 2003. The composition of the continental crust. In: R.L. Rudnick (Editor), The Crust, Treatise on Geochemistry. Elsevier, Oxford, pp. 1-64.

Sanchez-Valle, C., Reynard, B., Daniel, I., Lecuyer, C., Martinez, I., Chervin, J.C., 2005. Boron isotopic fractionation between minerals and fluids: New insights from in situ high pressure-high temperature vibrational spectroscopic data. Geochimica Et Cosmochimica Acta, 69(17): 4301-4313.

Schaltegger, U., Zeilinger, G., Frank, M. and Burg, J.P., 2002. Multiple mantle sources during island arc magmatism: U-Pb and Hf isotopic evidence from the Kohistan arc complex, Pakistan. Terra Nova, 14(6): 461-468.

Schaltegger, U., Frank, M. and Burg, J.P., 2003. A 120 Million years record of magmatism and crustal melting in the Kohistan Batholith, E.G.U. Geophysical Research Abstracts.

Schaltegger, U. and Brack, P., 2007. Crustal-scale magmatic systems during intracontinental strike-slip tectonics: U, Pb and Hf isotopic constraints from Permian magmatic rocks of the Southern Alps. International Journal of Earth Sciences, 96(6): 1131-1151.

Scott, D.R. and Stevenson, D.J., 1984. Magma Solitons. Geophysical Research Letters, 11(11): 1161-1164.

Searle, M.P., Khan, M.A., Fraser, J.E., Gough, S.J. and Jan, M.Q., 1999. The tectonic evolution of the Kohistan-Karakoram collision belt along the Karakoram Highway transect, north Pakistan. Tectonics, 18(6): 929-949.

Sisson, T.W. and Grove, T.L., 1993. Experimental Investigations of the Role of H2o in Calc-Alkaline Differentiation and Subduction Zone Magmatism. Contributions to Mineralogy and Petrology, 113(2): 143-166.

Smellie, J.L., Stone, P. and Evans, J., 1995. Petrogenesis of boninites in the Ordovician Ballantrae Complex ophiolite, southwestern Scotland. Journal of Volcanology and Geothermal Research 69(3-4): 323-342.

Smith, D.R. and Leeman, W.P., 1987. Petrogenesis of Mount St-Helens Dacitic Magmas. Journal of Geophysical Research-Solid Earth and Planets, 92(B10): 10313-10334.

Sobolev, A.V. and Danyushevsky, L.V., 1994. Petrology and Geochemistry of Boninites from the North Termination of the Tonga Trench - Constraints on the Generation Conditions of Primary High-Ca Boninite Magmas. Journal of Petrology 35(5): 1183-1211.

Spiegelman, M., Kelemen, P.B. and Aharonov, E., 2001. Causes and consequences of flow organization during melt transport: The reaction infiltration instability in compactible media. Journal of Geophysical Research 106(B2): 2061-2077.

Spiegelman, M. and Kelemen, P.B., 2003. Extreme chemical variability as a consequence of channelized melt transport. Geochemistry Geophysics Geosystems, 4.

Stevenson, D.J., 1989. Spontaneous Small-Scale Melt Segregation in Partial Melts Undergoing Deformation. Geophysical Research Letters, 16(9): 1067-1070.

Stolz, A.J., Jochum, K.P., Spettle, B. and Hofmann, A.W., 1996. Fluid- and melt-related enrichment in the subarc mantle: Evidence from Nb/Ta variations in island-arc basalts. Geology, 24(7): 587-590.

Sun, S.-S. and McDonough, W.F., 1989. Chemical and isotopic systematics of oceanic basalts: implications for mantle composition and processes. In: A.D. Saunders and M.J. Norry (Editors), Magmatism in the Ocean Basins. Geological Society Special Publication, pp. 313-345.

Tahirkheli, R.A., 1979. Geology of Kohistan and adjoining Eurasian and Indo-Pakistan continents, Pakistan. Geological Bulletin, University of Peshawar, 11: 1-30.

Tahirkheli, R.A.K., Mattauer, M., Proust, F. and Tapponnier, P., 1979. The India Eurasia Suture Zone in Northern Pakistan: Synthesis and interpretation of recent data at plate scale. In: A. Farah and K.A. De Jong (Editors), Geodynamics of Pakistan. Geological Survey of Pakistan, Quetta, pp. 125-130.

Takahashi, N., Kodaira, S., Tatsumi, Y., Kaneda, Y. and Suyehiro, K., 2008. Structure and growth of the Izu-Bonin-Mariana arc crust: 1. Seismic constraint on crust and mantle structure of the Mariana arc-back-arc system. Journal of Geophysical Research-Solid Earth, 113(B1): 18.

Tatsumi, Y., Sakuyama, M., Fukuyama, H. and Kushiro, I., 1983. Generation of Arc Basalt Magmas and Thermal Structure of the Mantle Wedge in Subduction Zones. Journal of Geophysical Research, 88(NB7): 5815-5825.

Taylor, S.R. and McLennan, S.M., 1985. The continental crust : its composition and evolution : an examination of the geochemical record preserved in sedimentary rocks. Blackwell, Oxford, 312 pp.

Taylor, S.R. and McLennan, S.M., 1996. The evolution of continental crust. Scientific American, 274(1): 76-81.

Tiepolo, M., Vanucci, R., Oberti, R., Foley, S., Botazzi, P., Zanetti, A., 2000. Nb and Ta incorporation and fractionation in titanian pargasite and kaersutite: crystal-chemical constraints and implications for natural systems. Earth and Planetary Science Letters, 176(2): 185-201.

Treloar, P.J., Brodie, K.H., Coward, M.P., Jan, M.Q., Khan, M.A., Knipe, R.P., Rex, D.C., Williams, M.P., 1990. The evolution of the Kamila Shear Zone, Kohistan, Pakistan. In: M.H. Sallisbury and D.M. Fountain (Editors), Exposed cross-sections of the continental crust. Kluwer Academic Press, Amsterdam, pp. 175-214.

Treloar, P.J., Petterson, M.G., Jan, M.Q. and Sullivan, M.A., 1996. A re-evaluation of the stratigraphy and evolution of the Kohistan arc sequence, Pakistan Himalaya: Implications for magmatic and tectonic arc-building processes. Journal of the Geological Society, 153: 681-693.

Turner, S., Hawkesworth, C., Rogers, N., Bartlett, J., Worthington, T., Hergt, J., Pearce, J., Smith, I., 1997. U-238-Th-230 disequilibria, magma petrogenesis, and flux rates beneath the depleted Tonga-Kermadec island arc. Geochimica Et Cosmochimica Acta, 61(22): 4855-4884.

Ulmer, P., 1989. The Dependence of the Fe-2+-Mg Cation-Partitioning between Olivine and Basaltic Liquid on Pressure, Temperature and Composition - an Experimental-Study to 30 Kbars. Contributions to Mineralogy and Petrology 101(3): 261-273.

Ulmer, P., 2001. Partial melting in the mantle wedge - the role of H_2O in the genesis of mantle-derived 'arc-related' magmas. Physics of the Earth and Planetary Interiors, 127(1-4): 215-232.

Ulmer, P., 2007. Differentiation of mantle-derived calc-alkaline magmas at mid to lower crustal levels: experimental and petrologic constraints. Periodico Di Mineralogia, 76(2-3): 309-325.

van Achterbergh, E., Ryan, C.G., Jackson, S.E. and Griffin, W.L., 2001. Data reduction software for LA-ICP-MS. In, S. P. (Ed.), Laser ablation ICP-MS in the Earth Science. Mineralogical Association of Canada.

Vernieres, J., Godard, M. and Bodinier, J.L., 1997. A plate model for the simulation of trace element fractionation during partial melting and magma transport in the Earth's upper mantle. Journal of Geophysical Research-Solid Earth 102(B11): 24771-24784.

Vince, K.J. and Treloar, P.J., 1996. Miocene north-vergent extensional displacements along the Main Mantle Thrust, NW Himalaya, Pakistan. Journal of the Geological Society of London, 153: 677-680.

Woodhead, J.D., Hergt, J.M., Davidson, J.P. and Eggins, S.M., 2001. Hafnium isotope evidence for 'conservative' element mobility during subduction zone processes. Earth and Planetary Science Letters, 192(3): 331-346.

Workman, R.K. and Hart, S.R., 2005. Major and trace element composition of the depleted MORB mantle (DMM). Earth and Planetary Science Letters, 231(1-2): 53-72.

Yamamoto, H. and Nakamura, E., 1996. Sm-Nd dating of garnet granulites from the Kohistan complex, northern Pakistan. Journal of the Geological Society, 153: 965-969.

Yamamoto, H. and Yoshino, T., 1998. Superposition of replacements in the mafic granulites of the Jijal complex of the Kohistan arc, northern Pakistan: dehydration and rehydration within deep arc crust. Lithos 43(4): 219-234.

Yamamoto, H., Kobayashi, K., Nakamura, E., Kaneko, Y. and Kausar, A.B., 2005. U-Pb zircon dating of regional deformation in the lower crust of the Kohistan arc. International Geology Review, 47(10): 1035-1047.

Yoshino, T. and Satish-Kumar, M., 2001. Origin of scapolite in deep-seated metagabbros of the Kohistan Arc, NW Himalayas. Contributions to Mineralogy and Petrology, 140(5): 511-531.

Zeilinger, G., Burg, J.P., Chaudhry, N., Dawood, H. and Hussain, S., 2000. Fault systems and Paleo-stress tensors in the Indus Suture Zone (NW Pakistan). Journal of Asian Earth Sciences, 18(5): 547-559.

Zeilinger, G., 2002. Structural and geochronological study of the Lowest Kohistan Complex, Indus Kohistan region in Pakistan, NW Himalaya. PhD Thesis, ETH, Zürich, 243 pp.

Zhou, M.F., Robinson, P.T., Malpas, J., Edwards, S.J. and Qi, L., 2005. REE and PGE geochemical constraints on the formation of dunites in the Luobusa ophiolite, Southern Tibet. Journal of Petrology 46(3), 615-639.Aharonov, E., Whitehead, J.A., Kelemen, P.B. and Spiegelman, M., 1995. Channeling Instability Of Upwelling Melt In The Mantle. Journal of Geophysical Research, 100(B10): 20433-20450.

Acknowledgements

A difficult part of the Thesis to write... Writing down four years of Science took me more than 100 pages, and I would have needed at least the double to resume four years of human relationships. I would like first to thank Jean-Pierre Burg without whom all of these would have not been possible. He offered me the possibility to do what I was looking for since my beginnings at the university: working in the Himalayas; and for this I will always be grateful. Also, working with him has been a daily pleasure, and I did learn a lot from him, and not only about science. My second thought comes to Max Schmidt, who dedicated a lot of his time. He teaches me many aspect of petrology, and not the least pragmatism… I will for sure remember the good times spent in the field at Sapat or in conferences... Both of them have strongly built my future scientific foundations. I also would like to acknowledge Peter Kelemen to be part of my Jury.

I would like to thanks all the people who participated to this study: Peter Ulmer, Othmar Müntener, "Jamie" Connolly, Bernard Bourdon, Carmen Sanchez-Vella., Gretchen and Stephano Bernasconi, Diane Seaward, Mark James Caddick., Oliver Jagoutz, Eric Reusser, Lydia Zehnder, Gregory De souza, Jean-Louis Bodinier, Marguerite Godard, Olivier Bruguier, Simone Pourtales, Urs Schaltegger, Massimo Chiaradia, Benita Pullitz, Margrith Bischof and Pirovino Frowin. Also I would like to thanks my past teacher of Montpellier André Leyreloup and Jean-Marie Dautria who greatly imprinted my scientific education.
Working at ETH has been a pleasure for many reasons, and one of them has been the fantastic human environment that drives you through your PhD. Thanks go to all of those who welcomed me and left: Weronicka and Claudio, Alex and Elena, James, Erwan, Krughy, Oli and Raquel, Christian, Tonny, Chiara, Giulio, Samuel, Ansgar, Manu, Helen, Darel, Morten, Markus, Andrew, Bastian, Pauline and Gerald, Adélie, Sonia, Federica, Ben etc… and to those who still there: SuperSeb and Zarina, Leo, Eli and Jorg, Sabine, Ashgar, Marina, Marcel, Beatrice, Mark, Brian, Bettina, Luigi, Neil, Stephan, Janne, Mathieu, the tiny master who grow quickly, Clemens, Daniela, Barbara and Antoine, etc… Of course the people from IMP cannot be forgotten as they have adopted me in their institute: Luca, Paola, Maarten, Estelle+Arnaud, Alessandro, Ettore, Huong, Peter N., the super post-doc Mark, Alistair, Etienne... Special thanks to the Friday beer crew (Maarten Jessica and Marion) and to the Institute's Mum Regula (Sorry to all that I forgot). Thanks also to Adliswil crew for keeping me fit…

A particular attention goes to my family who supported me all along these years. Also I cannot forget the whole Clapiers crew and particulary the "Closades streets" members: Richard-Emi, Simon-Laurence and Sylvain-Julie[Margot], but also Freddy and Laure who always encouraged me. A special consideration goes to my love Marion without whom I would not be what I am.